THE UNIVERSITY of ADELAIDE

New Generation of 2D Materials for Ionizing Electromagnetic Radiation Shielding Applications

By

Le Yu

A thesis is submitted for the degree of

Doctor of Philosophy

In

School of Chemical Engineering and Advanced Materials

The University of Adelaide, Australia

March 2022

This page is left blank intentionally

TABLE OF CONTENTS

ABSTRACT

The hazards from the use of X-ray have been recognized by International Committee on Radiological Protection (ICPR), showing that it is detrimental for human health, including the damage to human cells and is a carcinogenic hazard. The use of X-ray shielding apparel is therefore of great significance to protect workers from risk of excessive exposure towards harmful X-ray. Lead (Pb) has been used as an ideal radiation shielding material, owing to its high Z at 81 and high density of 11.3 g/cm^3, which is commonly for sale on the market. However, the concerns have been growing recently that using Pb has caused safety and health issues. The toxicity, heaviness, and inflexibility of the Pb-based garments pose a great risk to practitioners, which can harm their biochemical system. The substitution of Pb is thus momentous for the development of lightweight, non-toxic, and Pb-free X-ray shielding materials, where several high-Z metals (including bismuth (Bi), tungsten (W), and barium (Ba), tin (Sn), and antimony (Sb)) and their derivates were explored.

The aim of this thesis is to develop a new generation of lightweight, Pb-free, and highly efficient materials using a series of nanosized and layered 2D materials with their laminated structures and composites. Three key aspects are addressed in this thesis: firstly, the synergistic effect of the particle size and morphology on X-ray shielding performance have been investigated, showing that the nanomaterials with higher surface-to-volume ratio provide a significant effect on X-ray attenuation. Adapted this idea, successful synthesis of bismuth titanate (BTO) nanocomposite provides superior X-ray shielding ability (0.35 mm Pb equivalent attenuation).

Secondly, development of the 2D layered material using few-layer molybdenum MoS_2 provides an insight study for superior low-energy X-ray shielding application. Further, the design of the laminated 2D layered structure composed of few-layer MoS_2, antimonene, Mxene and their heterolaminates combinations (MoS_2 +Mxene) shows a promising enhancement for low-energy X-ray shielding, which could be a new radiation shielding technology.

Thirdly, the addition of graphene and hexagonal boron nitride (hBN) has a significant impact on reinforcement of polymer-based composites, leading to improved X-ray

shielding ability of MoS_2 nanocomposite. On the other hand, the laminated polymer-based composite with the few-layer antimonene exhibits enhanced X-ray shielding ability.

The superior X-ray shielding performance obtained from these studies suggests that these lightweight, non-toxic, and environmentally friendly materials could pave the development of a new generation of highly efficient Pb-free shielding materials, which is urgently needed across the broad sectors.

PREFACE

This thesis is submitted as a "*thesis by publication*" in accordance to the "*Specifications for Thesis 2020*" of The University of Adelaide. This thesis contains the following list of publications during 4 years of my PhD candidature. The outcomes generated during my PhD candidature include 14 published, under reviewed or under final prepared journal articles (7 first-authored; 7 co-authored), 1 AU patent (provisional approval), 5 conference presentations and 5 awards.

LIST OF JOURNAL PAPERS (Published/ Under Review as first author)

1. **Yu, L.**, Nine, M. J., Tran, T., Pereira, A. C., Hassan, k., Tran, D., . . . Losic, D. (2022). Layered 2D materials films and their heterolaminates for enhanced low-energy X-Ray radiation shielding. *Advanced Materials*. **Submitted**. (**IF: 30.85**)

2. **Yu, L.**, Douglass, M., Santos, A., Tran, D., & Losic, D. (2022). Two-dimensional (2D) layered molybdenum disulfide (MoS_2) films for high-performing low-energy X-ray radiation shielding. *2D Materials*. **To be submitted** (**IF: 8.161**)

3. **Yu, L.**, Yap, P. L., Santos, A., Tran, D., & Losic, D. (2022). Lightweight polyester fabric with elastomic bismuth titanate composite for high-performing lead-free X-ray shielding. *Advanced Engineering Materials*. **Under review** (**IF: 3.862**)

4. **Yu, L.**, Yap, P. L., Santos, A., Tran, D., Hassan, k., & Losic, D. (2022). Synergistic effect of graphene and hexagonal boron nitride for significant X-ray shielding enhancement of molybdenum disulfide-epoxy composites. *ACS Applied Materials & Interfaces*. **Under review** (**IF: 9.229**)

5. Nine, M. J., **Yu, L.**, Pereira, A. L. C., Batmunkh, M., Hassan, K., Santos, A. M. C., . . . Losic, D. (2022). Laminated antimonene as an alternative and efficient shielding strategy against X-ray radiation. *Applied Materials Today, 29*, 101556-64. doi:10.1016/j.apmt.2022.101566 **(IF: 10.041)**

6. **Yu, L.**, Yap, P. L., Santos, A., Tran, D., & Losic, D. (2021). Lightweight bismuth titanate ($Bi_4Ti_3O_{12}$) nanoparticle-epoxy composite for advanced lead-free X-ray radiation shielding. *ACS Applied Nano Materials, 4*(7), 7471-7478. doi:10.1021/acsanm.1c01475 (**IF: 5.097**)

7. **Yu, L.**, Yap, P. L., Tran, D. N. H., Santos, A. M. C., & Losic, D. (2021). High-yield preparation of edge-functionalized and water dispersible few-layers of hexagonal boron nitride (hBN) by direct wet chemical exfoliation. *Nanotechnology, 32*(40). doi:10.1088/1361-6528/ac0931 (**IF: 3.874**)

8. **Yu, L.**, Pereira, A. L. C., Tran, D. N. H., Santos, A. M. C., & Losic, D. (2021). Bismuth Oxide Films for X-ray shielding: Effects of particle size and structural morphology. *Materials Chemistry and Physics, 260,* 124084-91. doi:10.1016/j.matchemphys.2020.124084 (**IF: 4.094**)

LIST OF CONTRIBUTING JOURNAL PAPERS (Published/ Under preparation as co-author)

1. Tran, T., **Yu, L.**, Santos, A. M. C., Hassan, k., & Losic, D. (2022). Nanolayered Mxene films for highly efficient X-ray shielding, under preparation.

2. Wilkinson, K. L., Ristic, R., Szeto, C., Capone, D. L., **Yu, L.**, & Losic, D. (2022). Novel use of activated carbon fabric to mitigate smoke taint in grapes and wine. *Australian Journal of Grape and Wine Research*. doi:10.1111/ajgw.12548 **(IF: 3.137)**

3. Rastin, H., Mansouri, N., Tung, T. T., Hassan, K., Mazinani, A., Ramezanpour, M., **Yu, L.**, Losic, D. (2021). Converging 2D Nanomaterials and 3D Bioprinting Technology: State-of-the-Art, Challenges, and Potential Outlook in Biomedical Applications. *Adv Healthc Mater, 10*(22), e2101439. doi:10.1002/adhm.202101439 **(IF: 9.933)**

4. Hassan, K., Stanley, N., Tung, T. T., Yap, P. L., Rastin, H., **Yu, L.**, & Losic, D. (2021). Extrusion-Printed CNT–Graphene Sensor Array with Embedded MXene/PEDOT:PSS Heater for Enhanced NO_2 Sensing at Low Temperature. *Advanced Materials Interfaces, 8*(24). doi:10.1002/admi.202101175 **(IF: 6.147)**

5. Wang, H., Tran, D., Moussa, M., Stanley, N., Tung, T. T., **Yu, L.**, . . . Losic, D. (2020). Improved preparation of MoS_2/graphene composites and their inks for supercapacitors applications. *Materials Science and Engineering: B, 262*. doi:10.1016/j.mseb.2020.114700 **(IF: 4.051)**

6. Hassan, K., Nine, M. J., Tung, T. T., Stanley, N., Yap, P. L., Rastin, H., **Yu, L.**, Losic, D. (2020). Functional inks and extrusion-based 3D printing of 2D materials: a review of current research and applications. *Nanoscale, 12*(37), 19007-19042. doi:10.1039/d0nr04933f **(IF: 7.790)**

LIST OF CONFERENCE/WORKSHOP PRESENTATIONS

1. **Yu, L.**, Pereira, A. L. C., Tran, D. N. H., Santos, A. M. C., & Losic, D. (2021). *Bismuth Oxide Films for X-ray shielding: Effects of particle size and structural morphology*, 2021 Third ARC Graphene Research Hub Workshop, 26 Mar 2021, Adelaide, Australia (Oral Presentation).

2. **Yu, L.**, Yap, P. L., Santos, A., Tran, D., & Losic, D. (2021). *Lightweight bismuth titanate ($Bi_4Ti_3O_{12}$) nanoparticle-epoxy composite for advanced lead-free X-ray radiation shielding*, ARPS 2020-Radiation Protection Changes and Challenges, 01-02 Oct 2020, Adelaide, Australia (Oral Presentation).

3. **Yu, L.**, Yap, P. L., Tran, D. N. H., Santos, A. M. C., & Losic, D. (2021). *High-yield preparation of edge-functionalized and water dispersible few-layers of hexagonal boron nitride (hBN) by direct wet chemical exfoliation*, 2020 Second

ARC Graphene Research Hub Workshop, 13-14 Mar 2020, Melbourne, Australia (Poster Presentation).

4. **Yu, L.**, Pereira, A. L. C., Tran, D. N. H., Santos, A. M. C., & Losic, D. (2021). *Bismuth Oxide Films for X-ray shielding: Effects of particle size and structural morphology,* ICRP 2019 5th International Symposium on the System of Radiological Protection, 17-21 Nov 2019, Adelaide, Australia (Poster Presentation).

5. **Yu, L.**, Yap, P. L., Tran, D. N. H., Santos, A. M. C., & Losic, D. (2021). *High-yield preparation of edge-functionalized and water dispersible few-layers of hexagonal boron nitride (hBN) by direct wet chemical exfoliation,* 2019 First ARC Graphene Research Hub Workshop, 28-29 Mar 2019, Adelaide, Australia (Poster Presentation).

PATENT

1. **Yu, L.**, Losic, D., Santos, A. M. C., Tran, D. N. H., Tran, T. T. & Nine, M. J. Radiation shielding using 2D materials, AU patent approved (No. AU 2021902612).

LIST OF AWARDS

1. **Student Representative** for the School of Chemical Engineering and Advanced Materials 2020 Staff Student Liaison Committee, 18 Mar 2021, Adelaide, Australia.

2. **Certificate of Workshop Committee Member**, 2021 Third ARC Graphene Research Hub Workshop, 26 Mar 2021, Adelaide, Australia.

3. **Certificate of Workshop Committee Member**, 2020 Second ARC Graphene Research Hub Workshop, 13-14 Mar 2020, Adelaide, Australia.

4. **Learning Enhancement Ambassador**, Learning Enhancement & Innovation, 18 Dec 2019, The University of Adelaide, Adelaide, Australia.

5. **Full Fee Scholarship**, ARC Grant Funded Scholarship, 2019

HDR THESIS DECLARATION

I certify that this work contains no material which has been accepted for the award of any other degree or diploma in my name, in any university or other tertiary institution and, to the best of my knowledge and belief, contains no material previously published or written by another person, except where due reference has been made in the text. In addition, I certify that no part of this work will, in the future, be used in a submission in my name, for any other degree or diploma in any university or other tertiary institution without the prior approval of the University of Adelaide and where applicable, any partner institution responsible for the joint award of this degree.

I acknowledge that copyright of published works contained within the thesis resides with the copyright holder(s) of those works.

I give permission for the digital version of my thesis to be made available on the web, via the University's digital research repository, the Library Search and also through web search engines, unless permission has been granted by the University to restrict access for a period of time.

I acknowledge the support I have received for my research through the provision of an Australian Government Research Training Program Scholarship.

Le Yu **Date: 12.03.2022**

ACKNOWLEDGEMENTS

I would like to express my deep appreciation to the following people and organizations, without whom this thesis would have not been possible.

My principal supervisor **Professor Dusan Losic** for his massive support, inspiration, guidance, and outstanding leadership during my entire Ph.D. journey. I have felt so grateful as one of this professional research group, where I am honoured to have an opportunity for gaining such valuable knowledge and experiences and receiving the endless assistance throughout my Ph.D. life. In addition, his encouragement and enthusiasm towards exploration of novel ideas always kept me motivated for the research. I am so indebted to him that no words can express my sincere gratitude for his dedication.

My co-supervisor **Dr. Diana Tran** and **Dr. Alexandre Santos** for their highly helpful advice, selfless support and encouragement that always lighten me up in my Ph.D. journey. They are such great supervisors who constantly provide me with scientific thoughts and constructive inspiration. I am so grateful to have them as my mentors during my Ph.D. study.

I would like to warmly deliver my great appreciation to **Dr. Pei Lay Yap**, **Dr. Kamrul Hassan, Dr. Jacqui McRae, Dr. Tung Tran, Dr. Julker Nine, Dr. Farzaneh Farivar, Dr. Kamrul Mahnaz Dadkah Jazi,** for sharing their scientific insights and knowledge to help shaping a better version of myself each day.

My sincere gratitude also goes to School of Chemical Engineering and Advanced Materials supporting staff members (**Dr. Qiuhong Hu, Dr. Ay Ching Hee, Ms. Michelle Fitton and Ms. Leanne Haller**), ECMS technical staff (**Mr. Jason Peak, Mr. Jozef Kumberger, and Mr. Tom Wilson**), and Adelaide Microscopy experts (**Mr. Ken Neubauer and Dr. Ashley Slattery**) for providing the support and facilities to proceed with this research.

Finally, this research journey cannot have been smoothly sailed without the immense love, the strong support and the constant encouragement from my beloved family members, especially father (**Zhongwei Yu**), mother (**Huijun Zheng**) and grandmother (**Aju, Xu**), and my caring friends. Last but not the least, deeply thanks to **Mr. Mobai Chen** for his unconditional love, patience, and everlasting support to have brought me this far.

Le Yu **Date: 12.03.2022**

This page is left blank intentionally

CHAPTER 1

INTRODUCTION AND MOTIVATION

Chapter 1 Introduction

1.1. Background, research motivation and significance

According to its capability to ionize the materials, radiation is commonly classified into two major groups: (1) non-ionizing radiation, and (2) ionizing radiation.[1] Non-ionizing radiation possesses insufficient energy to eject electrons from one atom, and therefore it cannot generate ions. Microwaves, radio waves, infrared, and visible lights belong to this category.[2] On the other hand, ionizing radiation is able to eject the electrons from one atom by producing both negative and positive charged ions, due to its high energy.[3] Electromagnetic radiation mainly composes of X-ray, and gamma (γ)-ray from radioactive materials.[4] With the development of industries including power plants, medical care industries as well as aerospace, various high energy radiation sources such as X-ray, gamma ray, neutron particles are mostly employed.[5] Neutron particles are generally uncharged and applied to nuclear reactors for generating nuclear power.[6] γ-ray is generated from the radioactive decay or nuclear explosion, which contains the smallest wavelength with the greatest energy among any waves from the electromagnetic spectrum.[7] While X-ray is a pure energy of the photons, it is generally less penetrating and lower in energy than γ-ray.[7]

During the last decade of the 21st century, the hazards caused from ionizing radiation were extensively recognized by the International Commission on Radiological Protection (ICPR), due to their high penetration ability that is harmful for the human health and heredity.[8] Long-exposure to X-ray is detrimental to human body, including poor haematopoiesis, nerve system dysfunction, spermatogenesis disorder, and lens turbidity.[9] In addition, the radiosensitive organs (e.g. lymph, spleen), skin, brain and cardiovascular system can be significantly affected during X-ray irradiation.[10] **Figure 1** illustrated the radiosensitivity level of organs and tissues.[11]

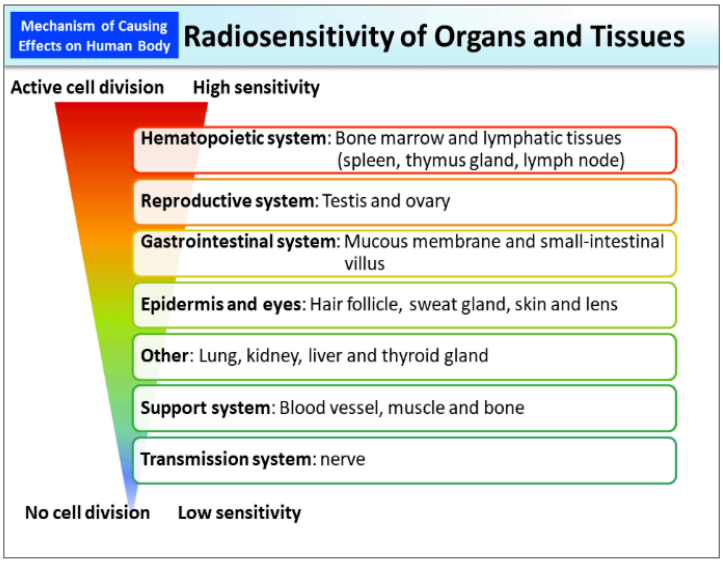

Figure 1. Radiosensitivity level of the organs and tissues.[11]

During the last decade, X-ray is widely applied to the medical field, including medical radiotherapy and diagnosis.[12] It is reported that the employment rate of radiology occupation has been estimated to increase by 9 % between 2014 and 2024.[13] To protect the practitioners from the risk of the X-ray radiation, the Australian Radiation Protection and Nuclear Safety Agency (ARPANSA) has been monitoring the medical exposure dose for each worker over the decade. Regards to the doctors, nurses, radiographers and radiologists, the most receiving dose is 1 mSv per annum (max.). For personnel whose works are related to nuclear medicine and cardiology, the occupational receiving dose is 3 mSv per annum (max.).[14] The possible health effects caused from X-ray radiation is shown in **Table 1**. To achieve "as low as reasonably achievable" (ALARA) principle for reducing the receiving radiation dose,[15] radiation protection is therefore paramount to prevent the related workers from the risk of X-ray sources.

Table 1. Possible health effects caused from X-ray exposure.[14]

Dose range (mSv)	Dose level	Health effects
<10	Very low	None observed
10-100	Low	Plausible health effect
100-100	Moderate	Increased risk of cancer or acute effect at the highest dose
>1000	High	Acute effect (vomiting or burn) Death caused at the highest dose

There are three ways to minimize the effect from radiation hazards: (1) reducing the exposure time, (2) keeping a certain (longer) distance from the radiation source, and (3) use of shielding. Among the three options, application of the radiation shielding material is the most effective practice to prevent the personnel from hazardous radiations (as shown in **Figure 2**).[16, 17] The attenuation of the incident X-ray photons are largely dependent on the photoelectric effect and Compton scattering effect, where the photoelectric effect is one of the most important mechanisms during the X-ray photons interaction with the shielding material at low energy (< 100 keV). The probability of the photoelectric effect can be enhanced with the increased Z and density of the shielding material.[18]

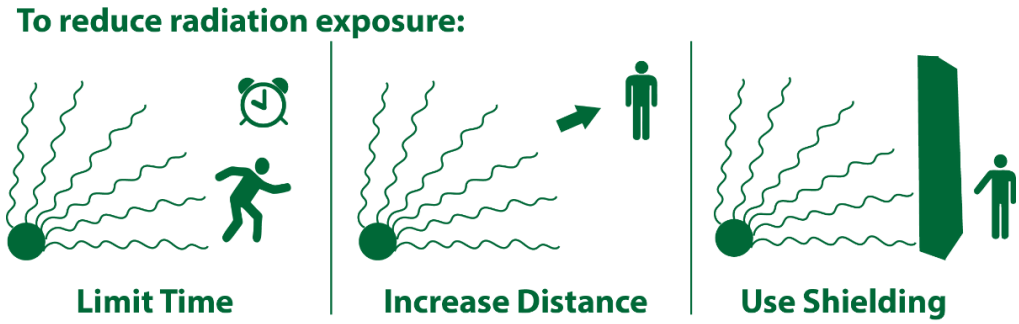

Figure 2. Three ways to minimize the hazardous effects from X-ray radiation.[19]

Metallic Pb is therefore widely used as a dominant shielding material, owing to its high density and high Z that enhances the photoelectric effect by providing more electrons and photon absorption edges.[20-22] Pb glass, one of the best-known products is applied not only to provide visibility of the observation room in the laboratory but also to protect the practitioners from X-ray.[23] Pb bricks are often blended with concrete to add the extra shielding within the room construction, which is an efficient approach to reduce the thickness of the wall and maintain X-ray shielding effectiveness.[24] Importantly, the conventional X-ray shielding apparels are made of layered Pb-based vinyl sheets enveloped with polyester fabrics. **Figure 3** presented the four main Pb-based products for X-ray protection.

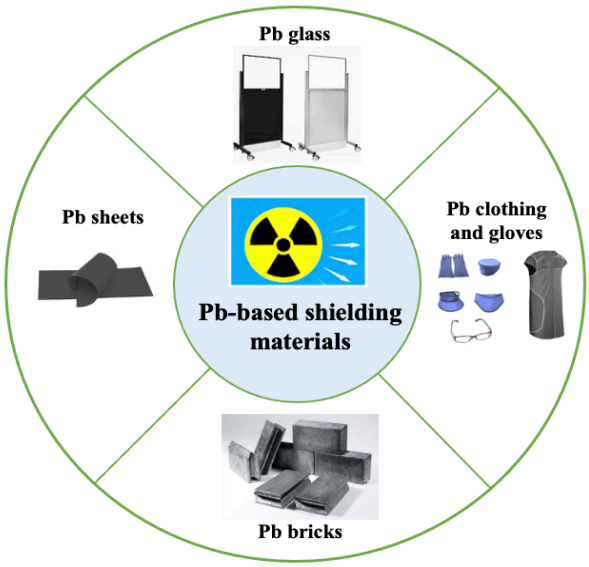

Figure 3. Four main Pb-based products for X-ray protection.

However, the use of Pb-based shielding products (e.g. Pb bricks and Pb sheets) could generate Pb dust from their surfaces.[25] This airborne Pb dust can be inhaled into the lungs or upper respiratory system, which can be absorbed into the human blood vessels.[26] Moreover, Pb is neither biodegradable nor rapidly excreted from the body, which increases the probability of having chronic or cumulative diseases.[27] Human exposure to Pb could induce irreversible toxic hazards on the nervous, haematological, cardiovascular, and reproductive system.[28] Furthermore, Pb-equivalent shields are often referred to Pb-based aprons, which is used for protecting the workers from the hazardous radiation.[29] However, toxicity, poor flexibility, heaviness, and discomfort wearing experience of using Pb-based protective apparels have caused health and environmental concerns,[30, 31] which has been banned for use in Europe since 2014.[32] With their long-term use, the inner Pb-sheets and the outer covering layer may be separated, due to their repetitive bending and folding.[29] This leads to reduced X-ray shielding effectiveness and lost in capability against scattered radiation.[33] To guarantee the safe use of the shielding aprons, they need to undergo a regular assessments to check for gaps and cracks within the aprons.[34] Another major issue of wearing Pb-based shielding apparel is severe low-back pain resulted from the continuously overuse of the back muscles. To solve the listed-above problems, there is an urgent need for the development of lightweight, non-toxic, environmentally friendly, Pb-free X-ray shielding materials.

In the past, metals that contain other high-Z elements (including bismuth (Bi), tungsten (W), and barium (Ba), tin (Sn), and antimony (Sb)) were explored to replace Pb

as effective X-ray attenuating materials.[35-42] To reduce the weight of shielding materials, polymers and their composites are introduced to provide benefits for X-ray shielding applications, owing to their lightweight, flexibility, durability and low manufacturing cost.[43] However, polymer-based composites are often low in mechanical properties. To overcome this problem, the mechanical properties of polymer can be improved via the reinforcement mechanism.[44] To be specific, polymers can be reinforced by adding inorganic particles that are tailored by reducing particle size (nanosized), changing shape, and increasing weight faction.[45, 46] Polymer-based nanocomposites are thus widely applied to X-ray protection application, due to high surface-to-volume ratio of the nanofillers that improves the composite's properties.[3]

Previously, metal oxides have been commonly selected as effective components for the formation of shielding nanocomposites, due to their low manufacturing cost, high chemical stability, and low toxicity.[47] Nanosized WO_3, SnO_2, Bi_2O_3, and Gd_2O_3 are often employed with different polymers for X-ray shielding applications.[26, 48, 49] **Table 2** summarized several major polymer-based shielding nanocomposites and their attenuation performance. Among these studies, it was found that the dispersion ability within the composite began to significantly be affected (decreased) when the addition of the filler content was above 30 wt.%, resulting from the low compatibility of the filler-polymer composite.

Table 2. X-ray shielding performance comparison between different polymer-based nanocomposites

Active component	Polymers	Thickness (mm)	Density (g/cm^3)	Attenuation performance	Ref.
Nanosized Bi_2O_3	PLA	0.8	1.77	38 wt.% Bi_2O_3 achieved 55 cm^{-1} of linear attenuation coefficient at 20.8 keV	48
Nanosized Bi_2O_3	PVA/Epoxy	2	1.5	50 wt.% of Bi_2O_3 achieved 0.51 mm Pb-equivalent X-ray shielding	50
Nanosized Bi_2O_3 and SiO_2	Silicone polymer	-	-	50 wt.% of Bi_2O_3 and 0.025 wt.% of SiO_2 achieved 7.19 cm^2/g of μ_m, and 0.78 cm of HVL at 66 keV.	51
Nanosized ZrO_2	P(VDF-TrFE)	1	-	10 wt.% of ZrO_2 achieved 60 % X-ray attenuation at 40 keV	52
Nanosized Gd_2O_3	Epoxy	8	-	14 vol.% Gd_2O_3 achieved 0.5 mm Pb-equivalent X-ray at 100 kVp.	49

In the wonder materials of 21st century, graphene has been found to possess a variety of excellent electrical properties applied to many fields, such as electronic and optoelectronic industries.[53] Current research reported that graphene oxide (GO) was employed as a reinforcement into the Pb_3O_4-epoxy composite for X-ray radiation shielding.[54] The lightweight GO could be a good carrier for the homogeneous dispersion of Pb_3O_4 particles, leading to improved X-ray attenuation at a variety of energies.[54] Another study also claimed that graphene, as a good mobility carrier could improve the absorption and reflection at high energies.[55] In addition, graphene with its excellent properties including light weight, higher thermal and chemical stability and higher specific surface area could potentially act as a reinforcement within the polymer-based nanocomposites for X-ray shielding enhancement.[53] Recently, the 'beyond graphene' 2D material groups were established: the graphene family, hexagonal boron nitride (hBN), 2D chalcogenides like transition metal dichalcogenides (TMDCs) and 2D oxides including transition metal oxides.[56]

Hexagonal boron nitride (hBN, recognized as white graphene) having a hexagonal crystal structure similar to graphene was applied for improving the mechanical and chemical properties of the polymer-based composite, due to its stiffness and high thermal stability.[58] So far, hBN has gained numerous interests on neutron shielding applications, owing to its high absorption cross-section (~ 760 b).[59-61] However, with its excellent thermal and mechanical properties, the effect of hBN as a reinforcement on X-ray shielding enhancement has not been explored yet.

Transition metal dichalcogenides (TMDCs) with the formula of MX_2 (X-M-X layer), where M = Mo, Bi, V, Ti, Nb, W, and Zr and X = S, Se, and Te, have been studied systematically, especially for molybdenum disulfide (MoS_2) and tungsten disulfide (WS_2).[62] The exfoliated TMDCs exhibited distinct properties compared to their bulk forms, and the single- or few-layer of TMDCs with their outstanding electrical, chemical, and mechanical properties are applied to numerous applications, including sensors, semiconductors, energy storage, and thermo-electric devices.[63-65] So far, only few studies have explored the effect of MoS_2 and WS_2 on X-ray attenuation performance.[66, 67] The findings from the previous studies brought potential for using exfoliated MoS_2 (few-layer) or other high-Z TMDCs for not only improving X-ray attenuation but also to enhance the mechanical properties.

Metal oxides with their layered structure can be considered as the new 2D material group, including molybdenum oxides, vanadium oxides, phosphorus oxides, lead oxides and other transition metal oxides.[68] Although many 2D oxides with layered structures may have promising properties after exfoliation, the effect of the exfoliated high-Z 2D oxide nanosheets on X-ray shielding have not yet been extensively studied.[69]

Perovskites as new developed 2D metal oxides have attracted interests in many fields such as solar cell and building construction, due to their high optical absorption, ferroelectric, dielectric, and catalytical properties.[47] The hybrid perovskites with the formula of ABO_3 are often fabricated using the layers of a metal halide intercalated with the layers of the organic chains.[70] Few-layer perovskites can be generated by mechanical exfoliation, which are highly stable.[70] For the first time, Morad et al. explored the effect of Ni substitution on X-ray shielding efficiency of $Nd_{0.6}Sr_{0.4}Mn_{1-y}Ni_yO_3$ (perovskite structure).[71] This study opened a pathway for use of hybrid perovskites for X-ray shielding application. A recent study compared the effect of Bi_2O_3 and Yb_2O_3 additives on the shielding effectiveness of a $BaTiO_3$ composite. The obtained result indicated the addition of Bi_2O_3 provided greater shielding effectiveness than Yb_2O_3, owing to the increased composite's density and the higher Z value (83) of the Bi element.[72] However, the effect of the synthesized $BaTiO_3$ for X-ray shielding efficiency was not clearly explained. Moreover, there are still more hybrid perovskite-structure materials that need to be explored for the design of Pb-alternative shielding materials. The mechanical properties, thermal and chemical stability of the perovskites-based materials are not yet studied, which can be crucial for the new generation of Pb-free X-ray shielding materials.

The commercial Pb-based X-ray aprons composed of multilayered Pb-vinyl sheets as an inner layer enveloped with a polyester fabric as an outer layer.[73] These Pb-based garments contain ~ 0.5 m^2 of the shielding material with a total weight of 4.5 kg, which provide 0.50 mm Pb-equivalent X-ray shielding ability for diagnostic X-ray (60 kVp-120 kVp).[73] However, the inflexibility of these X-ray shielding aprons easily develops cracks and gaps, due to the long-term wear and bending. Recently, many studies have focused on the fabrication of a lightweight, durable, and flexible textile material for X-ray shielding to replace Pb aprons. According to the standard of the International Commission on Radiological Protection,[74-76] the X-ray protection ability of Pb-free X-ray shielding garments need to achieve no less than 0.25 mm Pb-equivalent X-ray shielding ability at the same energy range. Polyester, cottons, nylons, and leather are often used as coating

substrates, due to their good strength, durability and lightweightness.[41] Bismuth and its oxide (Bi_2O_3) are the most promising shielding candidate for coating on different types of textiles.[41, 77-79] Although these textile materials achieved 0.25 mm Pb-equivalent shielding ability at 80 kVp and 100 kVp, the one-side coating technique has its limits for long-term use, due to less resistant to laundry and folding. The manufacturing technique for the coated textile thus needs to be improved, and the complete laboratory examinations are necessary before commercializing any Pb-free shielding products.

To summarize, the future challenges of 2D nanomaterials as emerging X-ray protection components listed below are to be addressed:

(1) There are limited studies on the effect of various nanostructured materials in terms the impact of their particle sized and morphology towards X-ray attenuation improvement.

(2) Effect of carbon-based materials, such as graphene, CNT as reinforcements for X-ray shielding composites are still not clear.

(3) The use of high-Z 2D materials with high density, non-toxicity and low manufacturing costs is not explored for X-ray shielding applications.

(4) Sustainability and durability of the X-ray shielding textiles needs to be evaluated for the development of commercial Pb-free shielding apparels.

(5) Complete exploratory examinations are recommended for commercializing any novel Pb-alternative X-ray shielding materials.

The successfully addressing these problems with understanding the knowledge of the material design constraints will provide the guidance for the development of new generation of the Pb-free X-ray shielding materials, which brings great potential for engineering the X-ray shielding apparels.

1.2. Thesis outlines

This thesis compiles the comprehensive outcomes of my PhD research structured into seven chapters including introduction with significance, literature review, four chapters adapted from the original research work and publications, and final chapter of conclusion. The details are summarized in the following sections:

Chapter 1 Introduction

This chapter presents a brief overview on the ionizing electromagnetic radiation and their hazards, especially for X-ray radiation, followed by the significance of applying radiation shielding. The health concerns of using conventional Pb-based materials are discussed,

followed by significance of developing Pb-free X-ray shielding composite materials and their limits. The research gaps and challenges of this research is highlighted, showing the significance of employing 2D materials to design a new generation of lightweight, non-toxic, and advanced X-ray shielding materials.

Chapter 2 Literature review

This chapter provides a comprehensives literature review on the Pb-free shielding materials, introduction of 2D materials, and their potential applications for a new generation of Pb-free X-ray shielding materials. This section also introduces the fundamental principles of X-rays attenuation, including the definition and classification of X-ray energy, shielding mechanisms, properties of designing shielding materials. Moreover, the chapter focuses on the development of both Pb and non-Pb X-ray shielding composite materials, followed by the problems related to their formulation. Finally, the benefits of introducing 2D materials are discussed for a new generation of Pb-alternative X-ray shielding materials, followed by research gaps, aims and objectives, and hypothesis for this thesis.

Chapter 3 Effect of particle size and morphology of 2D oxides for X-ray shielding enhancement

This chapter investigates the synergistic effect of particle size distribution and structural morphology on X-ray shielding improvement of the metal oxide materials. The key finding from this work has been adapted to the next study on the development of a 2D metal oxide nanocomposite for the lightweight, non-Pb and high-performing X-ray shielding application. The outcomes from this chapter achieve **aim 1** with two published peer-reviewed articles:

(1) **Yu, L.**, Pereira, A. L. C., Tran, D. N. H., Santos, A. M. C., & Losic, D. (2021). Bismuth Oxide Films for X-ray shielding: Effects of particle size and structural morphology. *Materials Chemistry and Physics, 260,* 124084-91. **(Published)**

(2) Yu, L., Yap, P. L., Santos, A., Tran, D., & Losic, D. (2021). Lightweight bismuth titanate ($Bi_4Ti_3O_{12}$) nanoparticle-epoxy composite for advanced lead-free X-ray radiation shielding. *ACS Applied Nano Materials, 4*(7), 7471-7478. **(Published)**

Chapter 4 Development of 2D layered materials for low-energy X-ray shielding improvement

This chapter aims to explore the impact of applying 2D layered materials on X-ray attenuation improvement. Multilayered (bulk) and few-layer (exfoliated, FL) 2D materials including antimony, Mxene and MoS_2 are prepared for the comparison of the low-energy X-ray shielding effectiveness. The outcomes regarding to the significant effect of the layer-structure materials on X-ray attenuation enhancement provide great potential for the new design of FL-2D materials for radiation shielding application. The key contribution of this chapter achieves **aim 2,** and two prepared manuscripts are under provisional patent approval (No. AU2021902612):

(1) **Yu, L.**, Douglass, M., Santos, A., Tran, D., & Losic, D. (2022). Two-dimensional (2D) layered molybdenum disulfide (MoS_2) films for high-performing low-energy X-ray radiation shielding. *2D Materials*. **(To be submitted)**

(2) **Yu, L.**, Nine, M. J., Tran, T., Pereira, A. C., Hassan, k., Tran, D., . . . Losic, D. (2022). Layered 2D materials films and their heterolaminates for enhanced low-energy X-Ray radiation shielding. *Advanced Materials*. **(Submitted)**

Patent: Yu L, Losic D, Santos A, Tran D, Tran T and Nine M J (2021). Improved radiation shielding. *University of Adelaide,* No.72309AU.

Chapter 5 Development of polymer-based 2D nanocomposites for enhanced X-ray shielding performance

The first part of this chapter is to study the synergistic effect of using 2D nanomaterials (graphene and hBN) as reinforcements for polymer-based shielding materials. This work involves the fabrication of FL-hBN via wet chemical exfoliation, preparation of graphene and hBN reinforced MoS_2 nanocomposites for evaluation of X-ray attenuation enhancement as well as their mechanical properties and thermal stability. The second part is to investigate laminated polymer-based composite reinforced with exfoliated 2D antimony for improved shielding ability. The results from this chapter achieve **aim 3:**

(1) **Yu, L.**, Yap, P. L., Tran, D. N. H., Santos, A. M. C., & Losic, D. (2021). High-yield preparation of edge-functionalized and water dispersible few-layers of hexagonal boron nitride (hBN) by direct wet chemical exfoliation. *Nanotechnology, 32*(40). **(Published)**

(2) **Yu, L.**, Yap, P. L., Santos, A., Tran, D., Hassan, k., & Losic, D. (2022). Synergistic effect of graphene and hexagonal boron nitride for significant X-ray shielding

enhancement of molybdenum disulfide-epoxy composites. *ACS Applied Materials & Interfaces*. **(Under review)**

(3) Nine, M. J., **Yu, L**., Pereira, A. L. C., Batmunkh, M., Hassan, K., Santos, A. M. C., . . . Losic, D. (2022). Laminated antimonene as an alternative and efficient shielding strategy against X-ray radiation. *Applied Materials Today, 29*, 101556-64. **(Published)**

Chapter 6 Application of the designed polymer-based 2D oxide coated textile for X-ray shielding

This chapter introduces the best shielding materials selected from the previous studies in chapter 3, 4, and 5 to fabricate a lightweight, Pb-free coated textile for X-ray protection. The study on the structure design of the 2D metal oxide composite coated textile provides a new solution to the fabrication of light, flexible and effective Pb-free shielding fabrics. The key findings from this chapter achieve **aim 4:**

(1) Yu, L., Yap, P. L., Santos, A., Tran, D., & Losic, D. (2022). Lightweight polyester fabric with elastomic bismuth titanate composite for high-performing lead-free X-ray shielding. *Advanced Engineering Materials*. **(Under review)**

Chapter 7 Conclusion and future challenges

This chapter includes the summary of the development of 2D composite materials for advanced X-ray shielding application, and it also highlights the future challenges of engineering a lightweight, non-toxic, and environmentally friendly Pb-free shielding materials for commercializing X-ray shielding apparels.

1.3. Format

The thesis entitled “New Generation of 2D materials for ionizing electromagnetic radiation shielding applications” has been prepared as a combination of publications, submitted and prepared manuscripts based on the requirements of The University of Adelaide. The printed and online versions of this thesis are identical.

1.4. Reference

[1] S. A. K. Thibeault, Jin Ho; Sauti, Godfrey; Park, Cheol; Fay, Catharine C.; King, Glen C., MRS Bulletin 2015, 40, 836.
[2] S. A. M. Issa, M. I. Sayyed, A. M. A. Mostafa, G. Lakshminarayana, I. V. Kityk, Journal of Materials Science: Materials in Electronics 2019, 30, 12140.

[3] C. V. More, Z. Alsayed, M. S. Badawi, A. A. Thabet, P. P. Pawar, Environ Chem Lett 2021, 19, 2057.
[4] A. Kumar, Radiation Physics and Chemistry 2017, 136, 50.
[5] S. Geetha, K. K. Satheesh Kumar, C. R. K. Rao, M. Vijayan, D. C. Trivedi, Journal of Applied Polymer Science 2009, 112, 2073.
[6] S. A. Thibeault, J. H. Kang, G. Sauti, C. Park, C. C. Fay, G. C. King, MRS Bulletin 2015, 40, 836.
[7] ICRP, Vol. 49, 2020, 4.
[8] M. L. Monje, H. Toda, T. D. Palmer, Science 2003, 302, 1760.
[9] M. Mercuri, T. Sheth, M. K. Natarajan, CMAJ 2011, 183, 413.
[10] M. o. t. Environment, Ministry of the Environment Japan 2013.
[11] Z. Li, W. Zhou, X. Zhang, Y. Gao, S. Guo, Sci Rep 2021, 11, 4384.
[12] U. S. D. o. Labor, *Occupational outlook handbook*, Radiologic and MRI Technologists 2015.
[13] ARPANSA, Australia 2022.
[14] Y. Wang, P. Ding, H. Xu, Q. Li, J. Guo, X. Liao, B. Shi, ACS Appl Mater Interfaces 2020, 12, 19916; N. Z. N. Azman, S. A. Siddiqui, R. Hart, I. M. Low, Journal of Applied Polymer Science 2013, 128, 3213.
[15] J. Rooyen, *Transport and shielding of ionizing radiation* South African Nuclear Energy Corporation, South Africa 2020.
[16] E. P. Agency, United States 2022.
[17] D. I. Tishkevich, S. S. Grabchikov, S. B. Lastovskii, S. V. Trukhanov, T. I. Zubar, D. S. Vasin, A. V. Trukhanov, A. L. Kozlovskiy, M. M. Zdorovets, ACS Applied Energy Materials 2018, 1, 1695; N. Z. Azman, S. A. Siddiqui, I. M. Low, Mater Sci Eng C Mater Biol Appl 2013, 33, 4952; J. P. McCaffrey, F. Tessier, H. Shen, Med Phys 2012, 39, 4537.
[18] I. M. Low, N. Z. Noor Azman, *Polymer Composites and Nanocomposites for X-Rays Shielding*, 2020.
[19] A. A. Plionis, S. R. Garcia, E. R. Gonzales, D. R. Porterfield, D. S. Peterson, Journal of Radioanalytical and Nuclear Chemistry 2009, 282, 239.
[20] S. M. Hulbert, K. A. Carlson, J Nucl Med Technol 2009, 37, 170.
[21] M. M. Movahedi, A. Abdi, A. Mehdizadeh, N. Dehghan, E. Heidari, Y. Masumi, M. Abbaszadeh, Indian J Nucl Med 2014, 29, 18.
[22] L. M. Heath, K. L. Soole, M. L. McLaughlin, G. T. McEwan, J. W. Edwards, Rev Environ Health 2003, 18, 231.
[23] S. V. Verstraeten, L. Aimo, P. I. Oteiza, Arch Toxicol 2008, 82, 789.
[24] K. M. Burns, J. M. Shoag, S. S. Kahlon, P. J. Parsons, P. E. Bijur, B. H. Taragin, M. Markowitz, J Am Coll Radiol 2017, 14, 641.
[25] Q. Li, Q. Wei, W. Zheng, Y. Zheng, N. Okosi, Z. Wang, M. Su, ACS Appl Mater Interfaces 2018, 10, 35510; K. K. Kadyrzhanov, D. I. Shlimas, A. L. Kozlovskiy, M. V. Zdorovets, Journal of Materials Science: Materials in Electronics 2020, 31, 11729.
[26] H. A. Maghrabi, A. Vijayan, F. Mohaddes, P. Deb, L. Wang, Fibers and Polymers 2017, 17, 2047.
[27] J. Clements, J. Moirano, C. Sherry, P. Barr, J. Berg, J Am Coll Radiol 2015, 12, 531.
[28] S. Smith, J. Zhang, L. Anaskevich, B. P. Lemieux, M. E. Oates, J Am Coll Radiol 2016, 13, 1223.
[29] B. M. Abunahel, I. S. Mustafa, N. Z. Noor Azman, Applied Physics A 2018, 124; H. O. Tekin, V. P. Singh, T. Manici, Appl Radiat Isot 2017, 121, 122; K. Verdipoor, A. Alemi, A. Mesbahi, Radiation Physics and Chemistry 2018, 147, 85; M. Lopresti, L. Palin, G. Alberto, S. Cantamessa, M. Milanesio, Materials Today Communications 2021, 26; A.

J. Mieszawska, W. J. Mulder, Z. A. Fayad, D. P. Cormode, Mol Pharm 2013, 10, 831; Q. Zhang, Q. Liang, Z. Zhang, Z. Kang, Q. Liao, Y. Ding, M. Ma, F. Gao, X. Zhao, Y. Zhang, Advanced Functional Materials 2018, 28; A. M. Elsied, P. K. Diwakar, M. Polek, A. Hassanein, Journal of Applied Physics 2016, 120.
[30] S. Pulford, M. Fergusson, The Journal of The Textile Institute 2016, 107, 1610.
[31] M. R. Ambika, N. Nagaiah, S. K. Suman, Journal of Applied Polymer Science 2017, 134.
[32] S. Nambiar, J. T. Yeow, ACS Appl Mater Interfaces 2012, 4, 5717.
[33] Y. T. Park, Y. Qian, C. Chan, T. Suh, M. G. Nejhad, C. W. Macosko, A. Stein, Advanced Functional Materials 2015, 25, 575; A. Zandiatashbar, G. H. Lee, S. J. An, S. Lee, N. Mathew, M. Terrones, T. Hayashi, C. R. Picu, J. Hone, N. Koratkar, Nat Commun 2014, 5, 3186.
[34] P. Kumbhakar, C. Chowde Gowda, P. L. Mahapatra, M. Mukherjee, K. D. Malviya, M. Chaker, A. Chandra, B. Lahiri, P. M. Ajayan, D. Jariwala, A. Singh, C. S. Tiwary, Materials Today 2021, 45, 142.
[35] N. Z. Noor Azman, S. A. Siddiqui, H. J. Haroosh, H. M. Albetran, B. Johannessen, Y. Dong, I. M. Low, J Synchrotron Radiat 2013, 20, 741.
[36] L. B. T. La, C. Leatherday, Y.-K. Leong, H. P. Watts, L.-C. Zhang, Composites Science and Technology 2018, 163, 89.
[37] A. K. Singh, R. K. Singh, B. Sharma, A. K. Tyagi, Radiation Physics and Chemistry 2017, 138, 9.
[38] S. Jayakumar, T. Saravanan, J. Philip, Journal of Applied Polymer Science 2020, 137.
[39] C. C. P. Fontainha, A. T. Baptista Neto, A. P. Santos, L. O. d. Faria, Materials Research 2016, 19, 426.
[40] S. Das, M. Kim, J.-w. Lee, W. Choi, Critical Reviews in Solid State and Materials Sciences 2014, 39, 231.
[41] S. A. Hashemi, S. M. Mousavi, R. Faghihi, M. Arjmand, S. Sina, A. M. Amani, Radiation Physics and Chemistry 2018, 146, 77.
[42] E. Drakakis, M. Suchea, V. Tudose, G. Kenanakis, D. Stratakis, K. Dangakis, A. Miaoudakis, D. Vernardou, E. Koudoumas, Thin Solid Films 2018, 651, 152.
[43] K. Shavanova, Y. Bakakina, I. Burkova, I. Shtepliuk, R. Viter, A. Ubelis, V. Beni, N. Starodub, R. Yakimova, V. Khranovskyy, Sensors (Basel) 2016, 16, 223.
[44] Z. Liu, J. Li, X. Liu, ACS Appl Mater Interfaces 2020, 12, 6503.
[45] A. Güngör, I. K. Akbay, T. Özdemir, Radiation Physics and Chemistry 2019, 165; S. N. Yılmaz, İ. K. Akbay, T. Özdemir, Radiation Physics and Chemistry 2021, 180; Y. Shang, G. Yang, F. Su, Y. Feng, Y. Ji, D. Liu, R. Yin, C. Liu, C. Shen, Composites Communications 2020, 19, 147.
[46] J. A. Wilson, A. D. Yoffe, Advances in Physics 1969, 18, 193.
[47] Q. H. Wang, K. Kalantar-Zadeh, A. Kis, J. N. Coleman, M. S. Strano, Nat Nanotechnol 2012, 7, 699; B. Poudel, Q. Hao, Y. Ma, Y. Lan, A. Minnich, B. Yu, X. Yan, D. Wang, A. Muto, D. Vashaee, X. Chen, J. Liu, M. S. Dresselhaus, G. Chen, Z. Ren, Science 2008, 320, 634; T. Wang, L. Liu, Z. Zhu, P. Papakonstantinou, J. Hu, H. Liu, M. Li, Energy Environ. Sci. 2013, 6, 625.
[48] M. Afshar, J. Morshedian, S. Ahmadi, Polymer Composites 2019, 40, 149; A. M. Deliormanlı, M. Ensoylu, S. A. M. Issa, W. Elshami, A. M. Al-Baradi, M. S. Al-Buriahi, H. O. Tekin, Ceramics International 2021, 47, 29739.
[49] R. Ma, T. Sasaki, Acc Chem Res 2015, 48, 136.

[50] S. K. Radha, K. Crowley, B. A. Holler, X. P. A. Gao, W. R. L. Lambrecht, H. Volkova, M.-H. Berger, E. Pentzer, K. G. Pachuta, A. Sehirlioglu, Journal of Applied Physics 2021, 129.
[51] H. Xie, Z. Li, L. Cheng, A. A. Haidry, J. Tao, Y. Xu, K. Xu, J. Z. Ou, iScience 2022, 25, 103598.
[52] M. K. Hamad, M. H. A. Mhareb, Y. S. Alajerami, M. I. Sayyed, G. Saleh, Y. Maswadeh, K. Ziq, Radiation Physics and Chemistry 2020, 174.
[53] M. H. A. Mhareb, Y. Slimani, Y. S. Alajerami, M. I. Sayyed, E. Lacomme, M. A. Almessiere, Ceramics International 2020, 46, 28877.
[54] J. P. McCaffrey, H. Shen, B. Downton, E. Mainegra-Hing, Med Phys 2007, 34, 530.
[55] ICPR, Vol. 103, ICPR 2007; G. J. Scuderi, G. V. Brusovanik, D. R. Campbell, R. P. Henry, B. Kwon, A. R. Vaccaro, Spine J 2006, 6, 577; ICRP, Ann. ICRP 2007, 37, 2.
[56] Y. Wang, R. Zhong, Q. Li, J. Liao, N. Liu, N. S. Joshi, B. Shi, X. Liao, J. Guo, Advanced Materials Technologies 2020, 5; Q. Li, R. Zhong, X. Xiao, J. Liao, X. Liao, B. Shi, ACS Appl Mater Interfaces 2020, 12, 54117; H. A. Maghrabi, A. Vijayan, P. Deb, L. Wang, Textile Research Journal 2015, 86, 649.

CHAPTER 2

LITERATURE REVIEW

Chapter 2 Literature review

2.1. Introduction

The current development in the medical, mining, agricultural, nuclear- and defence-energy sectors are largely related to electromagnetic radiation.[1] Ionizing electromagnetic radiation composed of X-ray and gamma (γ)-ray is extensively applied to many non-destructive materials testing applications, including medical diagnosis and geological exploration, due to its high penetration ability.[2] Unguarded ionizing radiation exposure to human can have severe harm to living cells, break the DNA chains, and cause many other health problems, including carcinogenesis, damage to the nervous system and cardiac diseases. So far, the growing demand of applying X-ray radiation, especially in the medical field has brought potential harm for practitioners, due to their frequent exposure to X-ray, which requires more efficient protection.[3] The employment rate of radiology occupation has been estimated to increase by 9 % between 2014 and 2024.[4] Previous reports from the International Commission on Radiological Protection (ICRP) revealed that the long-term exposure to high-energy radiation led to irreversible health issues (e.g., carcinogenetic disease),[5] thus the use of X-ray protective material is inevitable for protecting personnel from the detrimental effects of X-ray.

There are three ways to minimize the effect from radiation hazards: (1) reducing the exposure time, (2) keeping a certain (longer) distance from the radiation source, and (3) wearing protection garments. Among the three options, application of the radiation shielding garment is the most effective practice to prevent the personnel from hazardous radiations. Attenuation of the X-ray photon energy is achieved due to the dominant photoelectric effect (mainly dependent on the atomic number (Z) and density).[6-7] Lead (Pb) is therefore widely used as an important shielding material, owing to its high density and high Z that enhances the photoelectric effect by providing more electrons and photon absorption edges.[8-10] However, the heaviness of these Pb-based aprons hinders physical movement and causes discomfort for the wearer.[11] Moreover, the severe toxicity of these Pb integrated materials is detrimental to the human body and leads to environmental pollution, thus limiting their extensive application.[12] Recently, Pb has been reported as the second most hazardous material out of the top 20 materials by the Comprehensive Environmental Response, Compensation and Liability Act (CERCLA), as it is highly toxic and a cancer causing agent.[13] There is thus an urgent demand for the development

of lightweight, non-toxic, Pb-free materials, which can replace or minimize the Pb usage for shielding applications. To address the aforesaid problems, polymer is often introduced as a supporting component to form a lightweight and durable X-ray shielding composite, owing to its unique properties, such as low density, durability, low manufacturing cost, and flexibility in fabrication.[14] The polymer-based nanocomposites are widely used in the new design of lightweight radiological protective garments.

On the other hand, two-dimensional (2D) materials have been applied extensively to many promising fields including optical devices, sensors, biomedicine and electromagnetic interference (EMI) shielding, owing to their unique mechanical, chemical, electrical and structural properties.[15] Moreover, these 2D materials exhibit a wide range of thicknesses from atomic-layer (few microns) to lateral size of a few centimetres, leading to variations in their properties.[16] Applying high-Z 2D nanomaterials can be a great potential to generate lightweight, environmentally friendly and high-performing X-ray shielding materials.

In this review, the fundamental principles of the ionizing electromagnetic radiation shielding, including classifications of radiation, the mechanism of radiation attenuation and properties of the shielding materials are explicitly explained. The conventional Pb-based materials with their advantages are discussed, followed by introducing the development of the Pb-alternative shielding materials. The review also focuses on introducing the high-Z 2D nanomaterials for the new design of X-ray shielding enhancement and highlights the application of an X-ray shielding textile compared to the commercial Pb-based apparels. Finally, the challenges and opportunities of high-Z 2D nanomaterials as emerging X-ray protection materials are addressed.

2.2. Classification of radiation

Radiation is defined as an energy that originates from a source and travels through a variety of materials.[17] According to its capability to ionize the materials, radiation is commonly classified into two major groups: (1) non-ionizing radiation, and (2) ionizing radiation.[17] Non-ionizing radiation possesses insufficient energy to eject the electrons from one atom, and it therefore cannot generate ions. Microwaves, radio waves, infrared and visible lights belong to this category.[18] On the other side, ionizing radiation is able to eject the electrons from one atom by producing both negative and positive charged ions, due to its high energy.[19] Ionizing electromagnetic radiation can be divided in several

classes including X-ray, gamma (γ)-ray as well as alpha (α) and beta (β) particles from the radioactive materials.[20] γ-ray is generated from the radioactive decay or nuclear explosion, which contains the smallest wavelength with the greatest energy among any waves from the electromagnetic spectrum.[21] While X-ray is a pure energy of the photons, which is generally less penetrating and lower energy than γ-ray.[21] α particles are emitted from the decay of the heaviest radioactive nuclei, like uranium and radium, and β particles are negative charged electron-like particles.[21] α particles can be easily attenuated by a piece of paper, and β particles are shielded by only a layer of thin sheet of aluminium.[22] However, attenuation of both X-ray and γ-ray requires the proper shielding materials (e.g., Pb sheet).[22] **Figure 1** shows the diagram of the required shielding materials for α and β particles, γ-ray and neutron.[23]

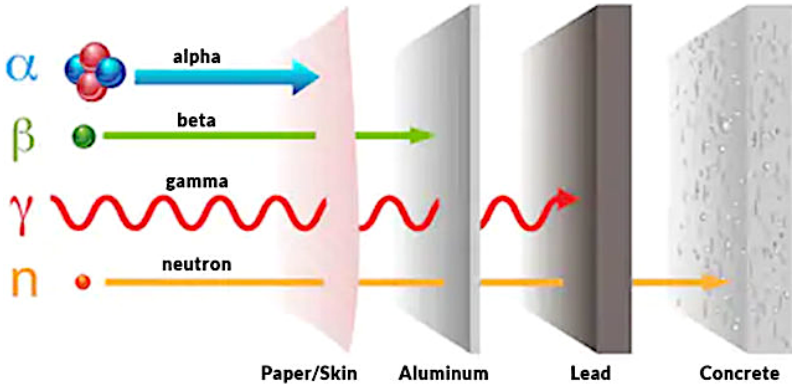

Figure 1. Diagram of the required shielding materials for alpha and beta particles, gamma-ray and neutron.[23]

2.3. History of X-ray shielding

Since X-ray was first discovered in 1895 by Wilhelm Roentgen (a German physicist), it has been extensively applied to many non-destructive material testing applications, including medical diagnosis, geological exploration, food irradiation, biological studies, space exploration and etc.[24] However, inadvertent exposure to X-ray has drawn a great concern, as it is detrimental to human health and the environment.[25] Hazards from X-ray have been recognized by the International Committee on Radiological Protection (ICRP), indicating that overexposure to X-ray can engender the carcinogenic effect to organs, radiation sickness, cell mutation and other illnesses.[26-27] With the development of medical care industries, the employment rate of radiology occupation has been estimated to increase by 9 % between 2014 and 2024.[4, 27] Protection from harmful effects of radiation is therefore of paramount importance for the related practitioners. Applying the principle

– *as low as reasonably achievable* (ALARA) can effectively minimize the radiation dose when the specialists are working closely with radiation sources.[28] To minimize the X-ray exposure, it depends on three key factors: (1) reducing the exposure time, (2) increasing the working distance, and (3) applying shielding materials.[29] Among all factors, shielding is considered as the most preferred radiation protection, owing to its independent efficiency within the required working circumstance. X-ray shielding towards the practitioners is thus highly in demand for the safe operation and healthy working environment.

2.4. Classification of X-ray energy

X-ray is one of the ionizing radiations that can be emitted by the excitement of atoms, where the outer-shell electrons fill the vacancy in the inner-shell atoms by releasing X-ray (called as characteristic or fluorescence X-ray).[30] Moreover, X-ray can be generated by gamma-ray interaction with the matter.[31] In general, X-ray can be categorized into five groups based on the energy ranges as listed in **Table 1**.[32]

Table 1. Classification of X-ray based on the energy ranges.[32]

Group	Energy range
Low-energy or soft X-ray	0.1-20 keV
Diagnostic X-ray	20-40 keV
Orthovoltage X-ray	140-300 keV
Intermediate-energy X-ray	300 keV-1 meV
Upward megavoltage X-ray	> 1 meV

In addition, X-ray based on the energy ranges is classified into two types, that is monochromatic and polychromatic X-ray.[33] The former one is a type of X-ray with a single wavelength, while the polychromatic X-ray possesses a broad spectrum of energy with several wavelengths, which is commonly used in clinic practice.[33]

2.5. X-ray attenuation

X-ray attenuation is the process of X-ray intensity reduction via either absorption or scattering when X-ray passes through the shielding material.[34] There are several methods to study the X-ray attenuation ability of a shielding material including: (1) X-ray transmission, (2) mass attenuation coefficient and (3) linear mass coefficient, (4) half-value layer, and (5) radiation protection efficiency.[35] For instance, when a narrow beam

of X-ray generated from X-ray tube goes through a attenuating material, some of them will be scattered directly from the surface of the material. Some of the X-ray photons will be absorbed completely by its interaction with the material, and then the low energy of electrons will be generated and received by the ionization chamber.[36]

(1) For a narrow beam of mono-energy photons, the change in X-ray intensity at a certain distance within a shielding material can be expressed as equation (1),[37]

$$I = I_0\, e^{-\mu x} \qquad (1)$$

where I is the X-ray intensity transmitted across a certain distance of a shielding material. I_0 is the initial X-ray intensity that mainly depends on distance from the source to the detector, the mAs setting and detector calibration, μ is linear attenuation coefficient of the shielding material (cm^{-1}), and x is the distance travelled (cm).[37] The X-ray transmission rate after the attenuation can be integrated as equation (2),

$$T = I / I_0 \times 100\% \qquad (2)$$

(2) Linear attenuation coefficient (μ) and mass attenuation coefficient (μ_m) are two major coefficients for determining the quantity of X-ray shielding ability. The linear coefficient expresses the fraction of X-ray that is absorbed or scattered per unit thickness of a shielding material.[37] According to Beer Lambert's law, it can be expressed as equation (3),[38]

$$\mu = (-\ln (I / I_0)) / x \qquad (3)$$

(3) Mass attenuation coefficient is used to evaluate the X-ray shielding ability of the developed shielding materials with different densities.[2, 39] More specifically, it describes a rate between X-ray attenuation capacity per unit thickness (cm^{-1}) of a shielding material and the density (g/cm^3) of this material, which can be expressed as equation (4), [40]

$$\mu/\rho = -\ln (I / I_0) / \rho t \qquad (4)$$

where ρ is the density of the material (g/cm^3).

(4) Half-value layer (HVL) is the layer (thickness) of a shielding material that reduces the intensity of X-ray by a factor of one half of the initial intensity (as shown in equation 5),[34]

$$HVL = \ln (2) / \mu \qquad (5)$$

(5) Radiation protection efficiency (RPE) is commonly used to evaluate the X-ray attenuation ability of a shielding material, which is determined as equation (6),[41]

$$RPE = (1- I / I_0) \times 100\% \qquad (6)$$

2.6. X-ray interaction with the shielding materials

In general, when the incident X-ray travels through a shielding material, three possible interactions may occur within the material as listed below:[38]

(1) **Absorption**: X-ray photons encounter the atoms from the attenuating material and then lose all their energies to the atoms.

(2) **Scattering**: X-ray photons encounter the atoms from the attenuating material, and the photons are directly deflected with or without energy loss.

(3) **No interaction**: X-ray photons travel through the attenuating material without any interaction with any atoms from the material.

These three interactions can be classified into five main mechanisms of the X-ray interactions towards the shielding material including: (1) photoelectric effect, (2) Compton scattering, (3) pair production, (4) Rayleigh scattering, and (5) photonuclear interactions.[31] The above-listed interaction mechanisms when the incident X-ray is travelling through the attenuating material are shown in **Figure 2**. Among the five types, photoelectric effect, Compton scattering, and pair production are three of the most critical interaction types, since they can effectively deliver the photon energy to the electrons.[42]

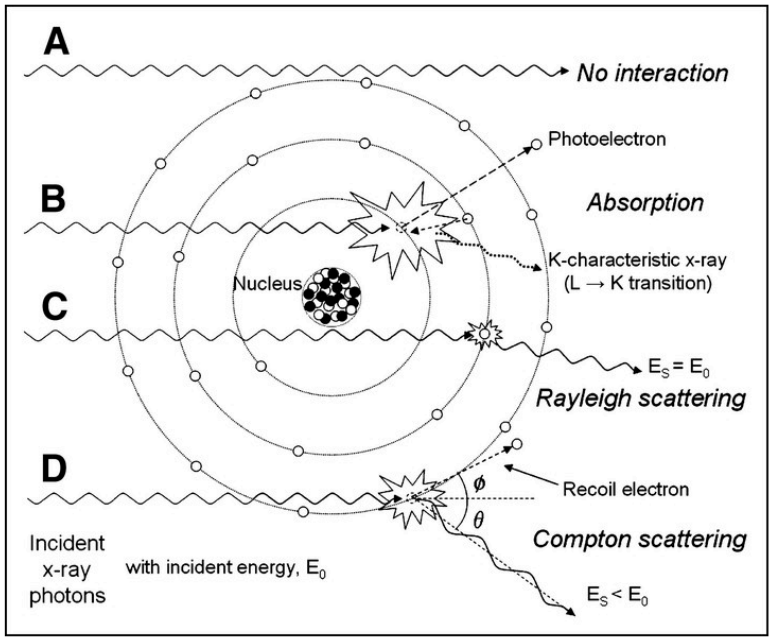

Figure 2. Five interaction mechanisms when the incident X-ray is travelling through the attenuating material. Reproduced with permission.[43] Copyright (2005) JNMT.

2.6.1 Photoelectric effect

Photoelectric effect is one of the most important interactions during the X-ray photons interaction with the shielding material at the low energy (< 100 keV). When the inelastic collision occurs between the incoming X-ray photons and the inner shell electron from the material, these photons will disappear with giving up all their energies.[44] If the photon energy is greater than the binding energy from the core electron, the ejection of this electron will occur with the remaining photon energy converted to kinetic energy of this ejected photoelectron (**Figure 3**).[45-46] The photoelectric effect is dominant at the X-ray energy range between 1-100 keV, and the probability of the photoelectric effect enhances with the increasing atomic number (Z) of the shielding material.[47] The cross section of the interaction via the photoelectric effect is directly proportional to Z^3 of the absorbing material, and inversely proportional to the X-ray energy ($1 / E^3$).[42] (Note: the cross section is used to describe the X-ray absorption ability of the shielding material, which evaluate the probability of photons interacted with the material).[42]

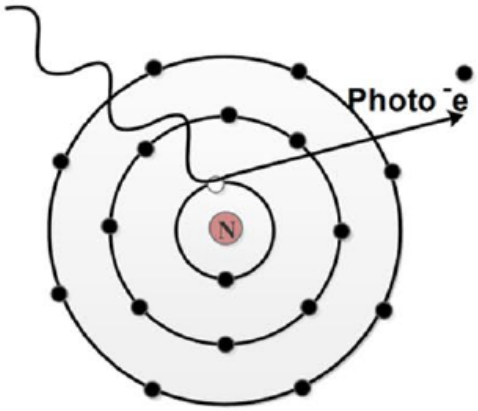

Figure 3. Schematic illustration of the photoelectric effect within the attenuating material. Reproduced with permission.[48] Copyright (2021) Springer Nature.

2.6.2 Compton scattering

Most of the scattered photons from the interaction within the absorbing material result from Compton scattering.[32] During this process, the high-energy X-ray photons strike the outer-shell electrons, leading to the ejection of low-energy electrons from the orbit. At the same time, the photons are directly deflected and travel to a new direction with the reduced energy.[46] The predominant Compton scattering effect occurs when the X-ray

energy ranges from 100 keV-10 meV, which is directly proportional to Z of the shielding material.[49] **Figure 4** depicts the process of Compton scattering effect occurring.

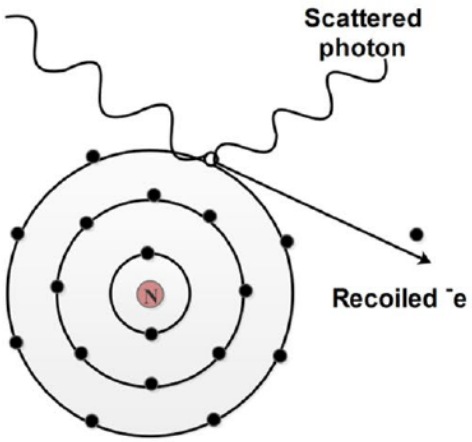

Figure 4. Schematic illustration of the Compton scattering within the attenuating material. Reproduced with permission.[48] Copyright (2021) Springer Nature.

2.6.3 Pair production

Pair production occurs when the X-ray photon energy is two times higher than the rest mass of the electron. (Note: rest mass of the electron is the mass measured when the electron is in its stationary status).[45] As the rest mass of an electron is 0.511 meV, pair production will only happen when the X-ray energy reaches above 1.02 meV, where a pair of particles (an electron and a positron) are ejected from the nucleus of the shielding material, and the extra energy from the photons will then be transferred to this pair of particles (as shown in **Figure 5**).[31] The probability of the pair production mainly relies on Z^2 of the material.[30]

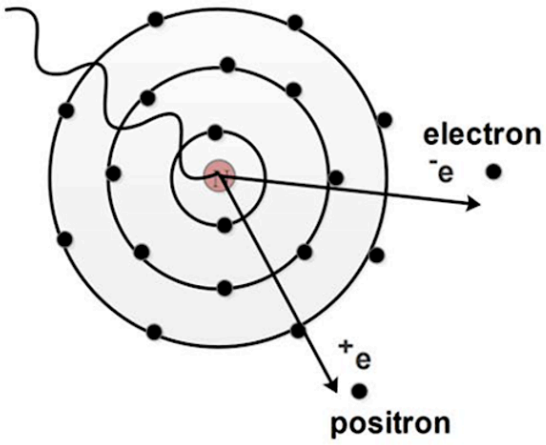

Figure 5. The process of pair production occurred within the nucleus. Reproduced with permission.[48] Copyright (2021) Springer Nature.

As discussed above, the relationship of the main attenuation mechanisms with the photon energy (E) and the atomic number (Z) during the absorption and scattering are summarized in **Table 2**.[50]

Table 2. Summary of the relationship between the main attenuation mechanisms and the photon energy and the atomic number.[50]

Mechanism	Relationship with E	Relationship with Z	Energy range
Photoelectric effect	$1 / E^3$	Z^3	1-100 keV
Compton scattering	Decreases gradually with E	Independent	100 keV-10 meV
Pair production	Increases gradually with E	Z^2	> 1.02 meV

2.7. Properties of materials for X-ray shielding

2.7.1 Atomic number (Z)

A compound containing high Z has its alluring property for the development of an X-ray shielding material, since predominant photoelectric effect is significantly dependent on Z of the absorbing material.[51] Moreover, the Z dependent K absorption edge of each element is another critical parameter for radiation absorption, especially for the diagnostic X-ray energy. The elements can effectively absorb the radiation energy above their K absorption edges. The important high-Z elements with their densities and corresponding K absorption edges are summarized in **Table 3**.[52]

Table 3. High-Z elements with their densities and corresponding K absorption edges.[52]

Elements	Z value	Density (g/cm^3)	K absorption edge (keV)
Bismuth (Bi)	83	9.8	90.5
Lead (Pb)	82	11.4	88.0
Tungsten (W)	74	19.3	69.5
Gadolinium (Gd)	64	7.9	50.2
Cerium (Ce)	58	6.7	40.4
Barium (Ba)	56	3.5	37.4
Cesium (Cs)	55	1.8	36.0
Antimony (Sb)	51	6.7	30.5
Tin (Sn)	50	7.3	29.2
Cadmium (Cd)	48	8.6	26.7
Molybdenum (Mo)	42	10.3	20.0

2.7.2 Density of shielding materials

Density (ρ) is one of the key parameters for the design of a shielding material, which is a measure of mass per unit volume of a substrate.[53] According to Beer Lambert's law related to the X-ray absorption of the shielding material, the density is directly proportional to the X-ray intensity, showing that by increasing the density of a shielding substrate, it can effectively improve the probability of X-ray interaction between the incoming X-ray and the shielding material.[54] Moreover, density determines the quantity of the electrons within the given thickness of the attenuating material, which is related to interaction with the photon energies.[55] A dense material with a higher atomic number is beneficial to improve X-ray attenuation. The recent study investigated on the effect of adding bismuth oxide (Bi_2O_3) within the glass composite for X-ray shielding enhancement, proved that the addition of 14 % Bi_2O_3 was able to achieve a 15 % increase in the density of the glass composite, leading to 50 % improvement of the X-ray attenuation ability at 60 kVp.[56] The density of the material can be calculated using equation (7),

$$\rho = M / V \qquad (7)$$

where M is mass (g) of the material and V (cm^3) is volume of the material.

2.7.3 Thickness

The photon intensity of X-ray, especially for low energy can be attenuated by the photoelectric absorption, which is significantly dependent on the thickness of the shielding material.[57] Optimization of the material thickness is thus of great importance with the aim of designing a X-ray shielding composite.[58] Previous study investigated on the enhanced X-ray shielding performance of neodymium oxide (Nd_2O_3) imbedded with natural rubber (NR) composites at 60 keV. With the increment of the composite thicknesses from 0.2 cm to 1.0 cm, X-ray shielding rate of the NR composite with 60 wt.% of Nd_2O_3 loading increased from 80 % to 100 %.[59]

2.7.4 Effective atomic number of shielding materials

The effective atomic number (Zeff) is a critical parameter for determination of an X-ray absorbing material, especially for diagnostic X-ray (35-60 keV).[60] The effectiveness of diagnostic X-ray shielding ability significantly depends on the probability of the predominant photoelectric effect, which is directly proportional to the atomic number of

the absorbing material.[61] An effective Z (called as average Z) of the materials is considered, when various compounds, mixtures, and multilayered materials containing different Z are developed for X-ray shielding.[60] The effective Z can be calculated using equation (8),[62]

$$Z_{eff} = \sigma_a / \sigma_e \qquad (8)$$

where σ_a and σ_e are total atomic cross section and electronic cross section, respectively.

2.7.5 Key parameters of X-ray shielding using composite materials

X-ray is a high-energy electromagnetic radiation that can penetrate many materials, and a short wavelength with high frequency of radiation. X-ray is widely applied in radiotherapy, medical imaging, and material characterization, due to its high penetration ability.[2] At the same time, X-ray is biologically unsafe for the human body, leading to irreversible health issues, such as carcinogenetic diseases.[5] The use of X-ray protective apparel is thus of great importance to the practitioners working with X-ray. The mechanism of X-ray attenuation is mainly based on the probability of the photoelectric and Compton scattering effects between the incident photons and the shielding materials.[6] Lead (Pb) is therefore widely used as an important shielding material, owing to its high density and high Z that enhances the photoelectric effect by providing more electrons and photon absorption edges.[8-10] However, Pb-based materials normally lack flexibility, mechanical strength, and chemical stability.[63] Moreover, the heaviness of these Pb-based aprons hinders the physical movement and causes discomfort wearing experience.[11] To reduce the weight of these Pb-free shielding materials, polymer is often introduced as a supporting component to form a lightweight and durable X-ray shielding composite, owing to its unique properties, such as low density, durability, low manufacturing cost, and flexibility in fabrication.[14] Many researchers have explored a wide range of polymetric matrices (e.g., polyvinyl chloride (PVC), polymethyl methacrylate (PMMA), and natural rubber (NR)) filled with different high-Z metals and metal oxides to fabricate polymer-based composites for X-ray shielding.[64] Some of the widely used polymers are summarised in **Table 4**.[65] To synthesize a polymer-based radiation shielding material, several key parameters are discussed in the following sections.

Table 4. Polymers with their chemical formula and densities.[65]

Polymer name	Formula	Density (g/cm^3)
Polyacrylonitrile (PAN)	C_3H_3N	1.18
Polyaniline (PANi)	C_6H_4NH	1.63
Polyethylene terephthalate (PET)	$C_{10}H_8O_4$	1.38
Polyphenylenesulfide (PPS)	C_6H_4S	1.35
Polyamide (Nylon 6) (PA-6)	$C_6H_{11}NO$	1.13
Polytetrafluoroethylene (PTFE)	C_2F_4	2.20

2.7.6 Particle size effect

Particle size distribution of the radiation protective materials (fillers) is of great significance that impacts on radiation shielding performance of the polymer-based composite materials.[66] The incorporation of the nanomaterials (nanofillers) into the polymeric matrix could significantly improve the properties of the composite.[66] Generally, the filler can be bonded with the polymer by the intermolecular forces or weak chemical forces.[19] However, the molecular interaction between polymers and nanofillers can be enhanced by chemical bonding, which elevates the mechanical and physical properties.[19] Moreover, the addition of the nanofillers into the polymeric matrix could gain some promising features, such as elevated mechanical strength and stiffness, heat resistance, and radiation resistance.[67] Importantly, the loading requirement of nanofillers towards the polymers is lower than their microsized counterpart, which can be beneficial for the dispersibility within the matrix.[67]

Currently, the use of nanomaterials for development of Pb-free radiation protection composites have gained immense attention, owing to their unique properties. Previous work carried out by Botelho et al. investigated the effect of nanostructured copper oxide (CuO, 13.4 nm) on X-ray shielding performance compared to its microsized counterpart (56 μm).[67] The outcome showed that X-ray attenuation of nanosized CuO had 14 % improvement, compared to the microsized CuO at low-energy X-ray (26 keV and 30 keV), at the same filler loading (5 wt.%). However, it has also proved that there was no significant difference between the two at the higher energy (60 keV and 120 keV).[67] The study concluded that the nanostructured materials were more effective towards low-energy X-ray absorption, due to the predominate photoelectric effect. Another study performed by Azman et al. confirmed that the nanosized tungsten oxide (WO_3, 100 nm)-epoxy composite had 1.1-2.3 times higher attenuation ability at the lower energy (10-25

keV), respectively, compared to the microsized WO_3-epoxy composite at the same filler content (10 vol.%).[9] However, there was no apparent size effect on X-ray attenuation at 30-40 keV. The work also concluded that nanosized WO_3 consisted of a higher number of particles per gram compared to its microsized WO_3 composite, leading to increased probability of the photon absorption by the WO_3 nanoparticles. In addition, the reduced size filler could provide more uniform dispersion within the polymer.[9] Several similar studies have been investigated on the particle size effect towards X-ray attenuation improvement using other metal oxides, such as Bi_2O_3, PbO, confirming the same findings.[68-70] However, there is no study that investigates the effect of particle size and morphology on X-ray shielding performance, since the shape variations of the nanomaterials may influence on radiation shielding effectiveness.

2.7.7 Thermal stability

Generally, more than 99 % of kinetic energy from the X-ray beam is converted to heat at the anode target. For instance, a 50 W X-ray tube can generate approximately 49.8 W energy transferred to heat.[71] The materials containing good thermal stability are able to withstand the high energy bombardment caused by X-ray.[7] Alternatively, the materials with good thermal conductivity can effectively remove the heat from their inner layer structure.[47]

2.7.8 Radiation damage resistance and other factors

Radiation damage resistance is a necessary requirement for the design of an X-ray shielding garment, due to a significant deleterious effect on the mechanical properties of the X-ray absorbing materials.[13] Moreover, the balance between the durability, processing cost, and flexibility of the shielding materials should be considered for manufacturing effective X-ray protection materials.

2.8. Pb as a conventional X-ray shielding material

2.8.1. Pb properties

Pb has excellent properties including high density (11.30 g/cm^3), high Z (82), ease of fabrication, cheap and high level of stability, which is ideal for both X-ray and γ-ray protection.[13] In addition, when Pb is applied to neutron shielding, Pb itself cannot be radioactive after neutron irradiation, due to low level of neutron absorption. For this

reason, Pb can also be used in neutron shielding without emitting any significant amount of harmful secondary radiation.[72] Despite that Pb is not the densest metal compared with tungsten or thorium, it is more readily available and lower in manufacturing cost compared to other high-density metals.[73] Historically, Pb-based shields have been used frequently for radiation protection purpose. The application includes a Pb lined wall, and Pb lined plywood for the construction of the laboratory or nuclear industries.[72] The Pb-based shielding materials are discussed in the following sections.

2.8.2. Pb sheets, foils, and plates

Pb sheets can be easily shaped and formed for use in many different applications, and the thickness of the commercially available Pb sheets is in a range from 0.007 cm to many centimeters.[48] Its advantages include soundproofing, waterproofing and highly resistance to chemical corrosion and environmental changes. Moreover, Pb foils are referred to less than 0.08 cm of Pb sheets and Pb plates are defined as greater than 1.27 cm of Pb sheets.[72]

2.8.3. Pb bricks

Pb bricks commonly contain 4 % of antimony (Sb)-Pb alloy with interlocking styles in a wide size range, where the 4 % of antimony-Pb alloy can provide extra resistance to the damage, compared with pure Pb, and the interlocking style can prevent leakage caused from radiation irradiation.[74] The smooth surface of these Pb bricks is manufactured to prevent the contamination from radiation dust.[74] In addition, the standard sizes for a Pb brick can be set as 7-33 cm in length, 7-12 cm in width, and 5 cm in depth for the room build-up in the industry plants or hospital.[51] However, Pb dust is created from the movement of the Pb bricks, which potentially causes hazardous effect on the lung and upper respiratory tract via inhalation.[75]

2.8.4. Pb glass

To view the patients without exposure to X-ray, Pb-glass commonly provides the visibility and effective X-ray and γ-ray shielding for the observation rooms in laboratories.[76] The standard Pb glass is produced in the thickness of 0.63 cm, which has 1.5 mm Pb-equivalent shielding ability.[38] To achieve different levels of the Pb-equivalent shielding ability, Pb glass can be installed with a multilayered structure in the wall.

Pb glass composes of 65 % of lead oxide into a high-quality optical grade glass during the manufacturing process, which contains a high refractive index to allow light

transmission with little or no distortion.[77] It is also scratch-resistant as the result of the polished effect on both surfaces of the glass. At the same time, there is one major concern of using Pb-glass, that is the cause of eye strain to the medical users due to the light reflections created.[78]

2.8.5. Pb-based acrylic/vinyl sheet

Pb acrylic sheet is made of an acrylic copolymer blended with a Pb salt compound (30 %), which is a versatile and transparent plastic with a refractive index of 1.54.[79] It has excellent light transmission with effective radiation protection, which is extensively used for Pb glass substitution as observation windows, mobile shielding protection and door glazing purposes.[80] The details of different Pb acrylic sheets are summarized in **Table 5**.[38]

Table 5. Details of different Pb acrylic sheets.[38]

Thickness of Pb acrylic sheet (mm)	Weight (lb./ft)	Pb equivalency (mm)
7	2.3	0.3
12	3.9	0.5
22	7.2	1.0
35	11.5	1.5
46	13.7	2.0

Pb vinyl sheet is made more suitably for use in X-ray and low-energy γ-ray shielding purposes.[81] It is often applied to a wide range of applications, such as Pb vinyl aprons or curtains, owing to its flexibility, durability, and uniform density.[38] In addition, the conventional Pb-based shielding aprons are made from the multilayered Pb vinyl sheets because of their high abrasion resistance and acid/alkali resistance.[81] **Table 6** presented the different thicknesses of Pb vinyl sheets with their respective Pb-equivalent shielding values.[82]

Table 6. Thicknesses of Pb vinyl sheets with their respective Pb-equivalent shielding values.[82]

Thickness of Pb vinyl sheet (mm)	Pb-equivalent shielding value (mm)
0.8	0.25
1.6	0.50
3.2	1.0

The Pb apron with 0.50 mm equivalent protection and its inside filler of the Pb vinyl sheets are presented in **Figure 6**.

Figure 6. 0.50 mm Pb equivalent X-ray protection apron composed of the Pb vinyl sheets.

2.9. Disadvantage of using Pb as shielding material

Despite the merits of using Pb as a conventional shielding material, the Pb-based shields are notorious for their environmental contamination, heaviness, low flexibility, chemical stability as well as toxicity.[79] The dust generated from Pb is a highly potential hazard causing air pollution and provides harmful consequences to related practitioners when they breathe in the dust.[78] Moreover, Pb is neither biodegradable nor fast at excretion from the human body. Constant exposure to high toxic Pb can give rise to several health concerns, such as cardiovascular and haematological diseases, which has been extensively recognized by the International Committee on Radiological Protection (ICRP).[5] The heaviness and inflexibility of the Pb-based shielding aprons have brought about a significant health problem, such as back pain. Since 2014, Pb has been banned for use in European countries, and there is an urgent need for the design of a lightweight, non-toxic, Pb-free and effective X-ray shielding material.[77] Furthermore, the good mechanical property, high chemical and thermal stability, improved flexibility and low manufacturing cost are considered as other critical qualities for the generation of Pb-free alternatives.[51]

2.10. Development of Pb compounds-based shielding composites

To reduce the toxicity and heaviness of metallic Pb, the compound and composite forms of Pb have been extensively studied to provide Pb-equivalent radiation (X-ray) shielding performance. Initially, Aziz et al. used lead oxide (Pb_3O_4) filled in styrene-

butadiene rubber (SBR), and the use of Pb_3O_4 was first surface modified with stearic acid for compatibility improvement with SBR. The linear attenuation coefficient of Pb_3O_4-SBR composite increased with the increment of Pb_3O_4 up to 5.6 vol.% at 30 kGy, which achieved 63 % radiation shielding ability of pure Pb.[11] However, the mechanical properties decreased with the increment of the Pb_3O_4 loading. During the last decade, research on lead oxide composites for radiation shielding has gained momentum. In 2009, iso-phthalate resin was mixed with lead mono oxide (PbO) using a mold casting technique, and the composite with 50 wt.% provided the best radiation attenuation at 0.662 meV, showing its mass attenuation coefficient at 0.0948 cm^2/g.[7, 63] Azman et al. (2013) began to employ epoxy resin as the supporting component; a thermosetting polymer that can also withstand the heat from the high-energy X-ray. Microsized Pb_3O_4 particles were used to blend with the epoxy resin where the X-ray attenuation of the prepared composite was then tested under energy at 0.662 meV, indicating 0.0974 cm^2/g of mass attenuation coefficient when Pb_3O_4 loading increased up to 50 wt.%.[7] In another study, ethylene-propylene-diene monomer (EPDM) were first introduced for high-energy X-ray shielding, owing to its good radiation resistance that is often used as a base matrix for the X-ray beam accelerator,[83] and microsized $PbWO_4$ particles was then employed to form a $PbWO_4$-EPDM composite. Shielding capacity was measured at the energies of 0.086 meV and 0.105 meV, suggesting that X-ray attenuation at 0.105 meV was achieved by both elements (W and Pb), and interestingly X-ray attenuation at 0.086 meV was governed by W only. This result proved that Pb has its weakness of attenuating the radiation energy below 0.105 meV, and W could be complementary towards Pb below 0.105 meV.[84] Importantly to notice, aggregation appeared within the $PbWO_4$-EPDM composite, indicating the low compatibility between the polymer and the particles. This suggested that reduced-size filler particles or surface modifications in the composite for greater dispersion performance might need to be addressed. To improve the compatibility, the comparative study demonstrated that microsized and nanosized PbO particles individually mixed with a high-density polyethylene (HDPE) matrix showed that the nanosized PbO-HDPE composite had 12.5 % attenuation improvement at 1332 keV with improved mechanical and thermal properties, compared to its microsized counterpart.[84] With this proved finding, PbO nanoparticles with different loadings (5, 10, 20 wt.%) were applied to the EPDM matrix for enhancing the dispersion. The PbO-EPDM composite with 20 wt. % loading (thickness at 6 mm) provided 60.7 % attenuation ability at 120

kGy.[85] In 2020, lead chloride ($PbCl_2$) was first introduced for radiation shielding purposes where an orthophthaic unsaturated polyester resin was used as the supporting matrix. The radiation shielding ability of the $PbCl_2$ composites with different weight fractions (10-20 %) was measured under the energy range of 59.5 keV to 1408 keV. The key results found that the $PbCl_2$ composite (thickness at 5 cm) with 20 wt.% addition showed 244 % radiation protection efficiency at 59.5 keV, compared to the neat polyester resin. With the increment of the radiation energies, the improvement effect of the $PbCl_2$ loading on radiation shielding became insignificant.[86] So far, many studies on high-energy X-ray shielding have been reported to incorporate non-toxic/low-toxic Pb compounds with various polymeric matrixes for replacing toxic Pb. **Table 7** summarized the details of the Pb compound-based composites for high-energy X-rays shielding applications.

Table 7. Details of the Pb compound-based composites for high-energy X-rays shielding

Effective filler	Polymers	Density (g/cm^3)	Thickness (mm)	Attenuation performance	Ref.
Pb_3O_4	Styrene-butadiene rubber	4.73	2	87 wt.% Pb_3O_4 showed 0.424 cm^{-1} of μ at 0.663 meV	11
PbO	Isopthalate resin	2.17	2	50 wt.% PbO showed 0.0948 g/cm^2 of μ_m at 0.663 meV	63
Microsized Pb_3O_4 and PbO	Epoxy resin	2.83 for (Pb_3O_4) 2.93 for (PbO)	5	70 wt.% of both fillers showed 0.105 g/cm^2 of μ_m for PbO, and 0.102 g/cm^2 of μ_m for Pb_3O_4	7
$PbWO_4$	ethylene-propylene-diene monomer	1.24	5	30 wt.% of $PbWO_4$ showed 0.070 g/cm^2 of μ_m at 1836 keV	87
Microsized and nanosized PbO	High density polyethylene	1.75	2	Nanosized PbO composite provided 12.5 % attenuation improvement at, compared to the microsized PbO composite	84
$PbCl_2$	Orthophthaic unsaturated polyester resin	1.33	10	20 wt.% of $PbCl_2$ showed 0.748 g/cm^2 of μ_m at 59.5 keV	86

2.11. Development of new Pb-free X-ray shielding materials

Previous studies have explored a variety of high-Z metal (e.g., Bi, W, Gd, Sn) oxides for X-ray and -ray shielding applications. In 2012, Kunzel et al. used an epoxy matrix filled with micro- and nanosized copper oxide (CuO) for low-energy X-ray shielding, indicating that X-ray attenuation of nanosized CuO (30 wt.%) had 40 % improvement compared with their microsized counterpart, at 25 kVp and 30 kVp, while there was no

obvious difference in the attenuation when the energy increased above 60 kVp.[88] Mocahedi et al. prepared a combination of nanosized tungsten trioxide (15 wt.%, WO_3) and tin dioxide (85 wt.% SnO_2) particles within an epoxy paint, showing that this WO_3-SnO_2-epoxy composite (density at 4.16 g/cm^3) achieved 5.8 % of X-ray transmission at 100 kVp, which is lower than a nanosized Pb-epoxy composite (9 %) with a density of 4.79 g/cm^3.[89] Despite that the density of the prepared epoxy composite was slightly lighter than the Pb composite, this WO_3-SnO_2-epoxy composite still could be a potential lightweight, erosion-resistance, non-toxic material for Pb substitution. In 2016, Fontainha et al. used another 2D metal oxide (ZrO_2 nanoparticles) integrated with poly(vinylidene fluoride tryfluorethylene) (P(VDF-TrFE)).[90] The ZrO_2 nanoparticles were first modified using methyl methacrylate (MMA) for dispersion improvement. The as-prepared ZrO_2 composite with a thickness of 1 mm achieved 60 % attenuation at 40 keV, proving that the enhanced dispersion ability using surface modification on the metal oxide nanoparticles could be beneficial for X-ray attenuation.[90] Belgin et al. used an isophthalic polyester filled with natural ilmenite (titanium-iron oxide) for the first time, and μ_m of the prepared composite was measured at 60 keV.[91] The ilmenite (50 wt.%)-based composite with a density of 1.86 g/cm^3 achieved ~ 0.44 cm^2/g of μ_m, showing 80 % of X-ray attenuation performance of the Pb at 60 keV. The scanning electron microscope (SEM) image confirmed that the nanosized filler particles exhibited uniform dispersion within the matrix. Singh et al. investigated on the X-ray attenuation efficiency of nanosized Bi_2O_3 integrated with polyvinyl chloride (PVC). The synthesis of the Bi_2O_3-PVC composite is shown in **Figure 7**.[92] The outcome showed that the Bi_2O_3-PVC composite with a thickness of 1.5 mm achieved 0.51 mm Pb-equivalent X-ray shielding at 100 kVp, and its weight was 25 % lighter than a Pb sheet at the same dimension. It was also found that increasing the Bi_2O_3 loading could improve the thermal stability of the composite but reduced its mechanical strength due to the formation of micro cracks in the matrix.[92]

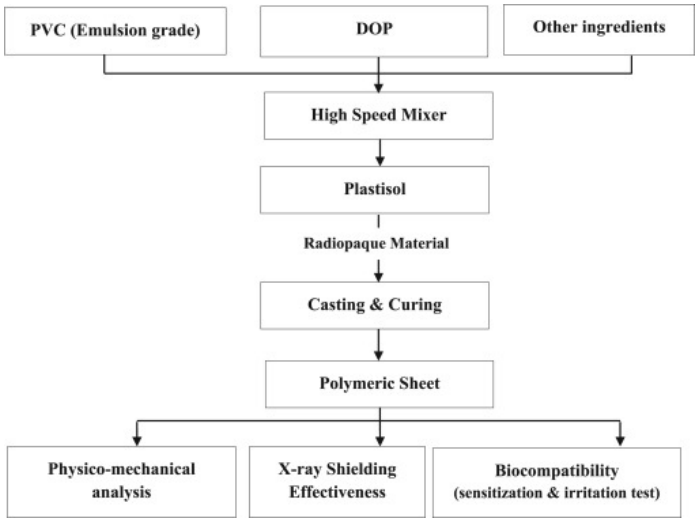

Figure 7. Process diagram of synthesis of the Bi_2O_3-PVC composite. Reproduced with permission.[92] Copyright (2017) Elsevier.

Later, Abunahel et al. studied the attenuation ability of epoxy-polyvinyl alcohol (PVA) filled with 12 wt.% of Bi_2O_3 nanoparticles towards the low-energy X-ray (23 keV and 35 keV), indicating that the prepared composite with a thickness of 2 mm could attenuate nearly 100 % X-ray photons. This result suggested that the composite filled with more than 12 wt.% of Bi_2O_3 may be used as a Pb-free low-energy (< 35 keV) X-ray shielding material.[93] Jayakumar et al. investigated on the X-ray attenuation efficiency of silicone filled with a combination of Bi_2O_3 and SiO_2 nanoparticles.[94] The prepared composite with 50 wt.% of Bi_2O_3 and 0.025 wt.% of SiO_2 provided the best X-ray attenuation, showing 7.19 cm^2/g of μ_m, and 0.78 cm of HVL at 66 keV. It was also found that the addition of the Bi_2O_3 and SiO_2 nanoparticles could increase the thermal stability compared to the polymer itself.[94] **Table 8** summarized all the listed-above studies of the non-Pb metal oxide-polymer composites for X-ray radiation shielding.

Table 8. Development of Pb-free metal oxide composites for X-ray shielding.

Active component	Polymer	Density (g/cm^3)	Thickness (mm)	X-ray energy	Attenuation performance	Ref.
Micro- and nanosized CuO	Epoxy	-	9	25, 30 and 60 kVp	30 wt.% of nanosized CuO had 40 % improvement, compared to microsized CuO at 25 and 30 kVp	88
Nanosized WO_3 and SnO_2	HDPE	4.16	-	100 kVp	15 wt.% WO_3 and 85 wt.% of SnO_2 achieved 8.5 % X-ray transmission and 0.23 mm of HVL	89
Nanosized ZrO_2	P(VDF-TrFE)	-	1	40 keV	10 wt.% of ZrO_2 achieved 60 % X-ray attenuation	90
TiO_2 and Fe_2O_3	Isophthalic polyester	1.86	-	60 keV	50 wt.% of TiO_2 and Fe_2O_3 achieved 0.44 cm^2/g of μ_m, and 80 % of X-ray attenuation as Pb sheet	95
Nanosized Bi_2O_3	PVC	-	1.5	100kVp	50 wt.% of Bi_2O_3 achieved 0.51 mm Pb-equivalent X-ray shielding	92
Nanosized Bi_2O_3	PVA/epoxy	1.5	2	23 keV and 35 keV	>12 wt.% of Bi_2O_3 achieved 100 % X-ray attenuation at both X-ray energies.	93
Nanosized Bi_2O_3 and SiO_2	Silicone polymer	-	-	66 keV	50 wt.% of Bi_2O_3 and 0.025 wt.% of SiO_2 achieved 7.19 cm^2/g of μ_m, and 0.78 cm of HVL	94

2.12. 2D materials and their potentials for X-ray shielding applications

Since 2004, the first two-dimensional (2D) material - graphene was synthesized by isolating high oriented graphite; it has raised an interest in many disciplines, such as physics, chemistry, and material science.[96-97] Other 2D materials, such as hexagonal boron nitride (hBN) and transition metal dichalcogenides (TMDCs) have also been applied extensively to many promising fields including optical devices, sensors, biomedicine, and electromagnetic interference (EMI) shielding, owing to their unique mechanical, chemical, electrical and structural properties.[15] Moreover, these 2D materials exhibited a wide range of thicknesses from atomic-layer (few microns) to lateral size of a few centimetres, leading to the variations in their properties.[16] The developed 2D materials are classified into three categories and are summarised in **Figure 8**.[15] The yellow shaded materials from the majority of the graphene family are constant at ambient temperature for their monolayers. The light green shaded materials are mostly stable in air, while the blue shaded materials are only stable in the inert atmosphere. The materials under the purple shade require further characterization on their exfoliated monolayers.[98] Recently, 2D materials has gained an increased attention on radiation shielding applications, due to excellent chemical, thermal and mechanical properties.

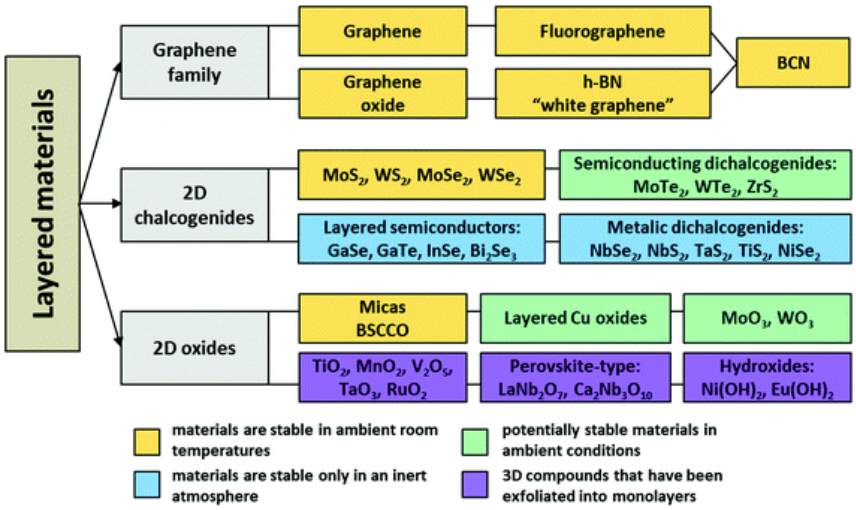

Figure 8. Classification of the developed 2D (layered) materials. Reproduced with permission.[15] Copyright (2020) RSC.

2.12.1. Graphene

Graphene sheets composed of a single layer of sp^2-hybridized carbon atoms with a hexagonal lattice structure are covalently bound together (shown in **Figure 9**).[99] It is also the most desirable nanomaterial, owing to its zero bandgap and high specific surface area (2630 m^2/g).[100] Graphene is 100 times stronger than a steel film and its conductivity of graphene is up to 15000 $cm^2/v{\cdot}s$ at room temperature (RT). In addition, it is reported that graphene can withstand the greater stress than other 2D nanomaterials.[101] One of the notable properties of graphene is to improve the thermal conductivity of the composites. leading to improved electromagnetic radiation absorption.[102] For example, a single layer of graphene can absorb ~ 2.3 % of the visible light.[103] Graphene-based materials have also showed promising results for EMI shielding, indicating a shielding effectiveness at 21 dB with only 15 % of graphene addition, due to its high specific surface area and high electric conductivity.[104] So far, graphene has attracted research and industrial attentions, as it can significantly improve the mechanical or chemical properties of the nanocomposites using only low filler loadings.[105]

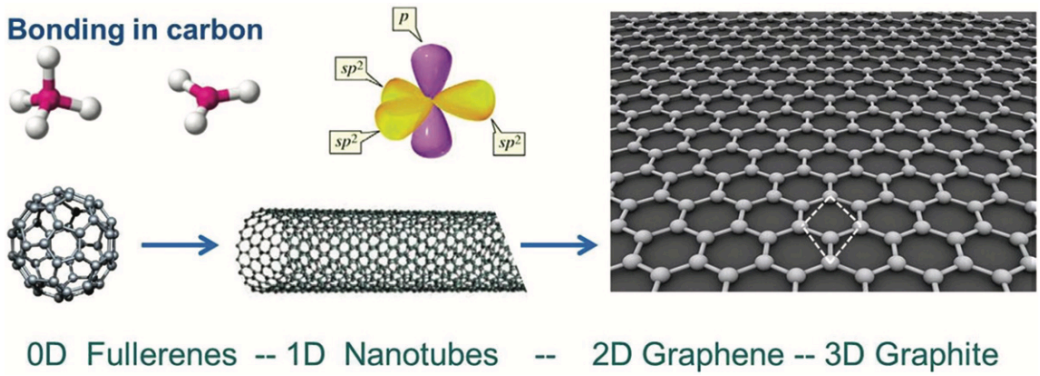

Figure 9. Hexagonal lattice structure of a single graphene sheet, fullerenes (0D), nanotubes (1D), and graphite (3D) are all carbon-based allotropes. Reproduced with permission.[15] Copyright (2020) RSC.

Currently, several studies have explored graphene oxide (GO) to form graphene-based composites for X-ray shielding applications, as they can be acted as reinforcements towards the polymeric matrices for shielding enhancement. In 2017, graphene oxide (GO) was first considered as a potential two-dimensional (2D) material to be applied as an effective reinforcement, since it can be integrated easily with many high-density materials (e.g., Pb) to assist the homogeneous distribution of these materials within the polymers. The effect of the graphene oxide (GO)/polyvinylidene fluoride (PVDF) nanocomposite on X-ray attenuation coefficient was investigated at X-ray energy of 6.9 keV. For comparison, PVDF-based composites filled with other two graphitic materials (graphite (PG) and multiwalled carbon nanotubes (MWCNT)) were prepared in the same weight fractions as GO. The results demonstrated that the addition of GO (1.88 wt.%) into PVDE matrix had four times higher value of X-ray attenuation coefficient at 6.9 keV, compared to PVDF only. This result suggested that GO containing carboxyl (COOH) and hydroxyl (OH) bonds can improve the interaction with the PVDF main chain, leading to an increase in the homogenous dispersion.[106] Importantly, the presence of GO in a polymeric matrix can effectively improve the radiation resistance of PVDF by preventing it from the radiation-oxidation reaction.[106] Further comparison with PVDF/PG and PVDF/MWCNT revealed that a significant improvement was observed in the PVDF/GO composite, and the PVDF/PG and PVDF/MWCNT composites shared similar shielding ability, which was slightly higher than PVDF itself as shown in **Figure 10**.

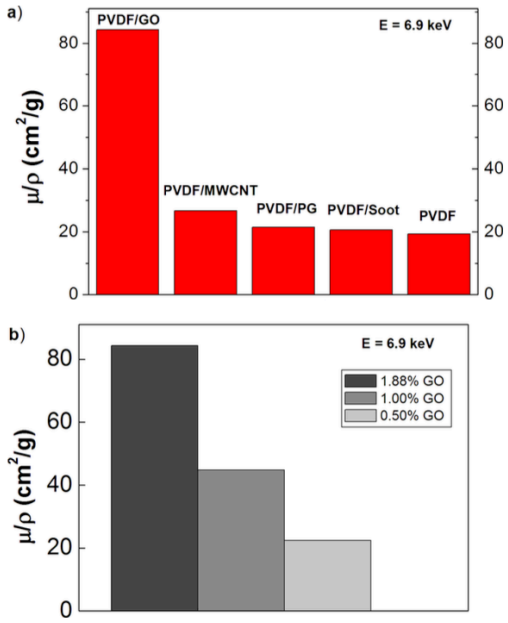

Figure 10. (a) Mass attenuation coefficients of PVDF based composites filled with GO, MWCNT, Soot with the same weight fraction (1.88 %), compared with PVDF at 6.9 keV, (b) PVDF/GO composites with increased GO loadings. Reproduced with permission.[106] Copyright (2017) American Chemical Society.

With this idea, Pb_3O_4 decorated GO-EP composites towards X-ray shielding performance were studied with different filler loadings (5 wt.% and 10 wt.% of GO). The reinforced composites containing GO-Pb_3O_4 were fabricated using a vacuum shock technique and the X-ray effectiveness of each composite was evaluated using an equivalent aluminium (Al) thickness. The outcomes proved that the Pb_3O_4-EP composite containing 10 wt.% GO (thickness of 6 mm) achieved 4.1 mm, 4.8 mm, and 3.9 mm equivalent Al thickness, showing 124.3, 124.6 and 103.6% improvement in the X-ray attenuation at 40 kVp, 60 kVp and 80 kVp, respectively, compared to neat EP. It is proved that the molecular attachment between GO and Pb_3O_4 transformed as a carrier for the Pb_3O_4 particles, thus resulting in the homogenous dispersion within the composite. Moreover, the addition of GO can enhance the mechanical properties of the Pb_3O_4-EP composites, showing improved hardness (0.9 kg·f/mm^2), contact angle (27.8 °) and glass transition temperature (53.2 ℃).[69] Interestingly, the reinforcement effect of GO towards X-ray shielding of the Pb_3O_4 composite diminished with the increment of the X-ray energies.[69]

Another study reported that reinforced polyaniline (PANi) composites with different loading of GO-iron tungsten nitride ($FeWN_2$, ITN) flakes for the X-ray shielding effectiveness at 30-60 kVp. The outcomes revealed that the PANi composite with 50 wt.%

of GO-ITN addition (the thickness at 1.2 mm) achieved 44.99 % X-ray attenuation at 60 kVp. This final composite also presented 5.77 S/cm of the electrical conductivity, which had 131.75 % improvement compared to the neat PANi. Importantly, it is claimed that the enhancement in the electrical conductivity with the higher-charge carrier on the surface of the composite provided a benefit for X-ray absorption.[107]

The latest work aimed at generating a novel reinforced PANi using GO nanoflakes decorated with the complex of the tungsten-bismuth-tin (TBT). X-ray attenuation property of these nanocomposites were examined under the energy range of 40-120 kVp. The final composite with a thickness of 9 mm and a density of 5.48 g/cm^3 achieved 44.99 % X-ray attenuation and 0.43 cm^2/g of μ_m value at 120 kVp. Importantly, it is claimed that the individually applied metals (Bi, W and Sn) had weak X-ray absorption edges at certain energy ranges, while the Bi-W-Sn hybrid complemented each other to enhance the X-ray attenuation at the region of 40 -120 kVp.[108]

As discussed above, GO as a 2D carbonaceous material has extensively been used as an effective carrier to support the composite-based materials for shielding applications, due to its functional groups (COOH and OH). It has been approved from the studies that GO can not only integrate with the heavy metals (such as Bi, Pb and W), but also provide molecular attachment for homogenous distribution of various nanoparticles.[109] In addition, the presence of GO within the polymer-based materials can improve their mechanical properties, as well as the chemical stability.[110] Importantly to note, use of GO synthesized by Hummer's method is not sustainable, due to generation of ionic wastewater streams during production process. Currently, the GO production process is significantly improved with minor waste, since the wastewater streams are treated using chemical precipitation, and the insoluble precipitates are then filtered.[111] **Table 9** summarized the polymer-based composites with the addition of GO for X-ray attenuation improvement.

Table 9. Polymer-based composites with the GO additive for X-ray attenuation

Active component	Polymer	Additive	Density (g/cm^3)	Thickness (mm)	X-ray energy	Attenuation performance	Ref.
GO	PVDF	-	-	-	6.9 keV	1.88 wt.% of GO showed 84.3 g/cm^2 of μ_m	106
Pb_3O_4	EP	GO	1.57	6	80 kVp	10 wt.% GO achieved 3.9 mm equivalent Al thickness	69
$FeWN_2$ (ITN)	PANi	GO	2.21	1.2	60 kVp	10 wt.% GO achieved 44.99 % X-ray attenuation	107
W-Bi-Sn (TBT)	PANi	GO	5.48	9	120 kVp	10 wt.% GO achieved 98.1 % X-ray attenuation and 0.43 cm^2/g of μ_m	108

2.12.2. Hexagonal boron nitride (hBN)

Hexagonal boron nitride (hBN) is recognized as 'white graphene' that has a structure like graphene but with a different stack ordering. Layered hBN composes of hexagonal rings of boron (B) and nitrogen (N) atoms connected with the strong covalent sp^2 bonds.[112] **Figure 11(a)** showed the schematic illustration of the hBN structure and its lattice constants of a = b =2.5 Å, c = 6.6 Å with a bond length of 1.45 Å and interlayer spacing of 3.3 Å.[113] **Figure 11(b)** provides an example of the hBN monolayer. Among other 2D materials, h-BN has drawn considerable attention recently due to its exceptional properties, including high thermal conductivity (550 W/m·K), remarkable oxidation resistance, non-toxicity, excellent mechanical strength (up to 239 N/m). Its outstanding chemical stability can be applied as lubricants, light-emitting devices, surface coatings and a platform for graphene electronics.[114-117]

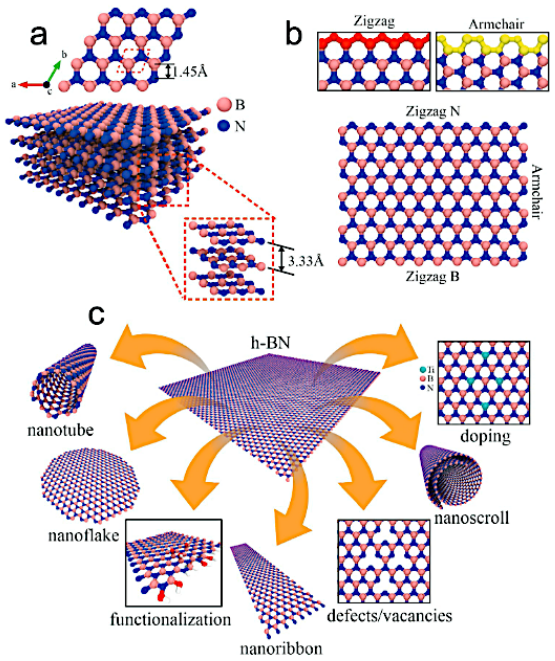

Figure 11. (a) Schematic illustration of hBN structure, (b) the atomic distribution of B and N atoms in different orientation, (c) illustration of possible nanostructures of hBN. Reproduced with permission.[113] Copyright (2021) Wiley-VCH.

Currently, hBN has also gained great attention in the radiation shielding application, owing to its high thermal stability (up to 1000 °C), low density, high thermal conductivity, and stiffness.[98] The mechanism of neutron shielding mainly depends on neutron absorption and scattering, and the thermalized neutron particles can be absorbed effectively by the boron-based composites, such as hBN, due to its high absorption cross-section (~ 760 b).[118] Many studies performed to fabricate hBN composites with various polymers for neutron shielding, as it not only provides the benefit for the shielding purposes, but also enhances the thermal stability and mechanical properties (strength and stiffness) of the polymer-based composites.[118-120] Despite hBN not being a promising candidate (an effective component) for X-ray shielding due to its low Z number, it may have great potential to act as a reinforcement for a polymer-based X-ray shielding composites.

2.12.3. Transition metal dichalcogenides (TMDCs)

Transition metal dichalcogenides (TMDCs) with the formula of MX_2 (X-M-X layer), where M = Mo, Bi, V, Ti, Nb, W, and Zr and X = S, Se, and Te, have been studied systematically, especially for molybdenum disulfide (MoS_2) and tungsten disulfide (WS_2).[121] The symmetry of the MX2 structure can be anti-prismatic or trigonal-prismatic

with a coordination number of 6 (**Figure 12**). Metal dichalcogenides (MDCs) have strong interlayer covalent bonding between M-X and weak interlayer van der Waals bonding, which can be exfoliated into mono- or few-layer TMDCs depending on their surface energies.[98] For example, both MoS_2 and WS_2 have surface energies between 65-75 mJ/m^2, which is similar to graphene.[98] Importantly to note, the exfoliated TMDCs can exhibit distinct properties compared to their bulk forms, and the single- or few-layer of TMDCs containing outstanding electrical, chemical, and mechanical properties are applied to numerous applications, including sensors, semiconductors, energy storage, and thermo-electric devices.[122-124]

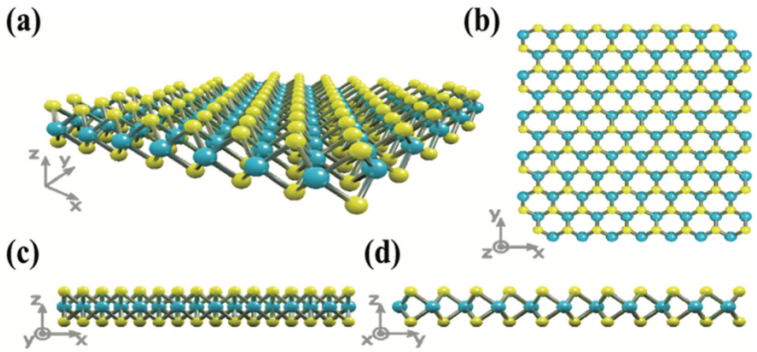

Figure 12. The 3D view of the crystal structure of a single-layer MoS_2, and the planar view of MoS_2 structure from (b) Z axis, (c) Y axis and (d) X axis. Reproduced with permission.[116] Copyright (2021) Wiley-VCH.

MoS_2 as one of the well-studied TMDCs is widely applied to biomedicine, biosensing, and drug delivery, due to its biocompatibility and antibacterial activity.[125] A recent work explored a MoS_2 composite for high-energy X-ray shielding, due to its high density (5 g/cm^3) and high-Z (Mo = 42) metal compound.[52] A microsized MoS_2-HDPE composite was prepared where its X-ray attenuation ability was further compared with a microsized W-HDPE composite at 40 keV. The outcome revealed that the MoS_2-HDPE composite (thickness of 2 mm) provided slightly higher X-ray photon transmission (3927) than that (3887) from the W-HDPE composite with the same loading (45 wt.%). This result was attributed to the poor dispersion between the microsized MoS_2 powder and HDPE matrix, leading to the negative effect on the X-ray shielding performance.[126] The finding also showed that both MoS_2 and W additives could enhance the thermal stability of the HDPE-based composites.[126] On the other hand, one previous study has proved that monolayered WS_2 was effective for detecting a low dose γ-ray, which is commonly used for the development of radiation sensors.[127] Moreover, WS_2 nanoparticles have been applied as a scaffold towards porous bioactive glass composites, showing an increase in the

compression strength.[128] However, the effect of WS_2 nanoparticles (as a biocompatible and high-Z metal compound) on the high-energy X-ray attenuation of the bioactive glass-based material has yet to be investigated. WS_2-glass based composites (1180.8 cm^2/g) were therefore prepared using the different filler loadings (0.1-4 wt.%), achieving X-ray attenuation coefficient 1.5 times higher than that of a glass-based composite (784.3 cm^2/g) at 15 keV. The compression strength was also improved by 55.7 % with the addition (4 wt.%) of WS_2 nanoparticles.[129] This result suggested that the nanosized WS_2 can not only achieved excellent X-ray attenuation ability, but also enhanced the mechanical property as an effective reinforcement towards the glass-based composite.[129] This study has allowed the potential for applying WS_2 or other high-Z TMDCs to form a non-toxic, Pb-free, and superior X-ray shielding material. In conclusion, there is only few works reported using high-Z TMDCs for radiation protection. So far, the effect of the exfoliated MoS_2 and WS_2 (nanosheets) towards the X-ray shielding capacity is not yet explored, which may bring about a new pathway for the development of lightweight, Pb-free, and non-toxic radiation protective materials.

2.12.4. 2D metal oxides

The layer-structure metal oxides can be considered as a new group of 2D material, including molybdenum oxides, vanadium oxides, phosphorus oxides, lead oxides and other transition metal oxides. These 2D metal oxides often have a layered structure by covalent bonds or are intercalated with other elements that are normally stoichiometric, thus showing the polycrystalline phase. Most of these 2D oxides can be exfoliated using intercalation with ions and molecules, which allows it to combine with different layers or form alloys. This feature can be used in the material design that is suitable for many applications, such as battery cathode materials, superconductors, and radiation shielding materials.

Perovskites as new developed 2D metal oxides have attracted interests in many fields such as solar cell and building construction, due to their high optical absorption, ferroelectric, dielectric, and catalytical properties. The hybrid perovskites with the formula of ABO_3 are often fabricated using the layers of a metal halide intercalated with the layers of organic chains. Few-layer perovskites can be generated by mechanical exfoliation, which are highly stable. Recently, a few studies have explored the radiation protective properties of the synthesized perovskites. Morad et al. explored the effect of Ni substitution on X-ray shielding efficiency of $Nd_{0.6}Sr_{0.4}Mn_{1-y}Ni_yO_3$ (a perovskite

structure).[130] With the increment of nickel (Ni) loading up to 20 wt.%, the μ_m value of the composite increased from 49.8 cm^2/g to 51.1 cm^2/g at 0.015 meV, due to the elevated density of the composite from 5.18 g/cm^3 to 6.25 g/cm^3.[130] This result opened a new pathway to investigate the use of perovskites for the shielding applications. Mhareb et al. explored the effect of both Bi_2O_3 and Yb_2O_3 on the radiation shielding performance of a $BaTiO_3$ material using ball milling technique.[131] The μ_m value of $BaTiO_3$ with 20 wt.% Bi_2O_3 loading was 0.065 cm^2/g at 1 meV, which was slightly higher than that (0.062 cm^2/g) from $BaTiO_3$ with the same Yb_2O_3 loading. The obtained result indicated the addition of Bi_2O_3 had more shielding effectiveness than Yb_2O_3, owing to the increased composite's density and the higher Z value (83) of Bi element.[131] Slimani et al. employed $BaTiO_3$ nanoparticles within a PVA matrix for high-energy X-ray shielding application. The prepared $BaTiO_3$ (3.57 wt.%)-PVA with a thickness of 2 cm provided 0.25 cm/g of μ_m value at 81 keV.[132] The radiation shielding performance of the listed-above perovskite-structure materials are summarized in **Table 10**.

Table 10. Development of the perovskite-structure materials for high-energy X-ray shielding.

Active component	Density (g/cm^3)	Thickness (mm)	X-ray energy (meV)	Attenuation performance	Ref.
$Nd_{0.6}Sr_{0.4}Mn_{1-y}Ni_yO_3$	6.25	-	0.015	20 wt.% of Ni content achieved 51.1 cm^2/g	130
Bi_2O_3 and Yb_2O_3 individually mixed with $BaTiO_3$	-	-	1	20 wt.% of Bi_2O_3 addition achieved 0.065 cm^2/g of μ_m, and 20 wt.% of Yb_2O_3 addition achieved 0.062 cm^2/g of μ_m	131
$BaTiO_3$ (+ polymer = PVA)	1.86	20	0.081	50 wt.% of TiO_2 and Fe_2O_3 achieved 0.44 cm^2/g of μ_m, and 80 % of X-ray attenuation as Pb sheet	95

The outstanding radiation attenuation performance of these perovskites showed their great potential to become Pb-alternative shielding materials for the various energy ranges. The tuneable property of the different perovskites is a motivation to explore other promising materials, which could provide valuable insight for the design of the effective radiation shielding materials.

2.13. Applications for X-ray shielding textile

Pb equivalence is a measure for radiation attenuation ability of non-Pb shielding materials compared to that of Pb with specific thicknesses (0.25 mm, 0.35 mm and 0.50 mm).[133] These values are commonly used for comparison with garment (or textiles)

materials, and the attenuation abilities of radiation shielding garments (textiles) can be specified as 0.25 mm Pb equivalent, 0.35 mm Pb equivalent, etc.[52] To synthesize a lightweight X-ray protective apparel with comparable Pb-equivalent X-ray shielding performance, incorporation of Pb-free metal powders into the polymeric yarn was first developed. Earlier study tended to use Sn (80 wt.%) and Bi (20 wt.%) embedded in a protective clothing for evaluation of X-ray shielding effectiveness at 60 kVp and 120 kVp. However, the Sn-Bi combination embedded clothing (at the thickness of 0.41 mm) provided 32 % less protection compared with 0.35 mm Pb sheet at 120 kVp.[134] In addition, it was found that adequately higher amount of metal powders were used within the polymeric fabric to achieve effective attenuation as Pb, which was much costly. Another study has been reported using barium sulphate ($BaSO_4$)-silicon rubber (SR) composite coated cotton fabric for X-ray shielding performance, compared to Bi-SR and W-SR composites coated cotton fabrics. It was found that $BaSO_4$-SR coated fabric with a thickness of 2.81 mm only showed 90 % X-ray attenuation at 100 kVp, which was less effective than the Bi-SR (99 %) and W-SR (95 %) composites coated fabrics.[135] Bi_2O_3 was then introduced as a Pb-alternative to develop an X-ray protective textile, showing that Bi_2O_3 (50 wt.%) coated polyester fabric with a thickness of 1.33 mm provided 92 % X-ray attenuation at 80 kVp.[136] The latest study prepared La_2O_3 and Bi_2O_3 nanoparticles co-impregnated in natural leather (NL), followed by additional Bi_2O_3 coating at the bottom side of the NL (shown in **Figure 13**).[26]

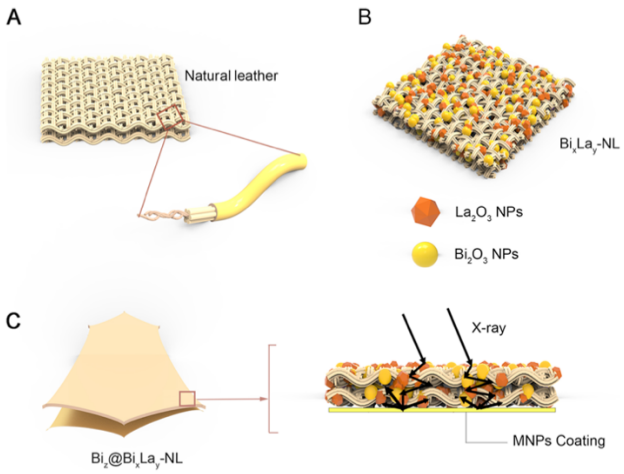

Figure 13. (a) Scheme of natural leather (NL) structure, (b) the Bi_xLa_y impregnated NL, (c) schematic illustration of X-ray pathway within the $Bi_z@Bi_xLa_y$-NL material. Reproduced with permission.[26] Copyright (2020) American Chemical Society.

The X-ray attenuation abilities of the synthesized material were 65-100 % at 20-120 keV, respectively, with 30 % reduced scattered secondary radiation.[26] It was found that the bottom-side coated layer played a key role in X-ray shielding improvement, as well as minimizing the scattered secondary radiation via deflection and reflection of the incoming X-ray. The mechanical properties of this synthesized NL were significantly improved, showing 15.39 MPa of tensile strength and 25.81 N/mm of tearing load. However, the unsealed coating technique made this X-ray protective textile less resistant to laundry and less durable for long-term wearing purposes. The details of the X-ray attenuation performance of the synthesized textiles are summarized in **Table 11**.

Table 11. The development of the synthesized X-ray shielding textiles at 80 kVp.

High Z materials	Textile matrix	Thickness (mm)	Mass per unit area (g/m^2)	Major results	Ref.
Bi_2O_3	Polyester	1.33	2907.0	X-ray transmission of 8 %	136
$Bi_2O_3/BaSO_4$	Polyester/ viscose	1.8	Reduced 30 % of 0.35 mm Pb	equivalent to 0.35 mm Pb	137
Bi_2O_3/La_2O_3	Leather	1.4	-	mass attenuation coefficient at 16.9 cm^2/g	26
$Bi_2O_3/BaSO_4$	Nylon	1.46	2321.8	X-ray transmission of 55.6 %, mass attenuation coefficient at 9.6 cm^2/g	77
Bi/I	Leather	2.0	-	mass attenuation coefficient at 28 cm^2/g, equivalent to 0.25 mm Pb	3

Based on previous studies on generation of lightweight X-ray shielding materials, most researchers mainly focused on synthesis of X-ray attenuating materials using metal oxides, including Bi_2O_3, WO_3 as well as Pb_3O_4. 2D materials with excellent chemical and physical properties have not been studied extensively for potential X-ray shielding applications. In particular, there is no specific research on the synergistic effect of size and morphology towards X-ray attenuation improvement. Moreover, there is no investigation on design of the layered structure for X-ray shielding improvement, which could provide a new prospective for design of Pb-free X-ray protection garments. So far, several works have focused on fabrication of a textile-based material for engineering Pb-free X-ray apparels. However, the durability and scalability of these non-Pb textile-based materials remain to be addressed. With the consideration of all constrains, development of new generation of lightweight, durable, Pb-free, and advanced X-ray shielding materials is urgently needed.

2.14. Research gaps

According to the comprehensive literature review presented here, there are many challenges associated with the development of the Pb-free shielding materials need to be addressed as follows:

- The effect of particle size and shape variations of the materials on X-ray shielding performance needs to be investigated.
- Influence of other key parameters (such as filler loading, thickness, and density of the materials, etc.) on X-ray shielding performance needs to be studied.
- The promising concept of the use of layered or laminated structure 2D materials on X-ray shielding enhancement needs to be explored and proved.
- The X-ray shielding performance comparison between few-layered and bulk 2D materials needs to be investigated for new generation of Pb-free shielding materials.
- The reinforcement of 2D materials (such as graphene and hBN) towards polymer-based materials needs to be explored, and the properties of the reinforced composites including thermal stability, mechanical properties and dispersion ability needs to be determined.
- The X-ray interaction between the layered-structure coated materials needs to be studied, which can provide important evidence for the new design of Pb-free shielding materials.
- An urgent demand for developing a textile-based material for engineering Pb-free shielding garments with advanced X-ray shielding property is needed.

2.15. Aims and research questions

The aim of this PhD work is to develop a new generation of 2D and their composite materials for X-ray radiation shielding. By introducing 2D materials based on their unique physical and chemical properties, these 2D materials-based composites will provide the fundamental principles for designing lightweight, non-toxic, environmentally friendly and Pb-alternative X-ray radiation shielding materials, which can bring forward a new pathway to develop a high-performing Pb-free X-ray shielding garment.

To achieve this goal, the objectives are articulated as the following:

- **Objective 1:** To investigate the effect of the particle size and structural morphology on X-ray shielding enhancement using the metal oxide film, which

provided the guidance for the development of the 2D metal oxide composite for superior Pb-free X-ray shielding performance.

- **Objective 2:** To understand the low-energy X-ray shielding improvement of the layered-structure materials using the representative 2D materials including MoS_2, Mxene and antimony.
- **Objective 3:** To explore specific 2D materials including graphene, hBN and antimony as the reinforcement towards the polymer-based nanocomposites for the X-ray shielding enhancement.
- **Objective 4:** To design a polymer-based 2D oxide coated textile for the development of a lightweight, non-toxic, flexible Pb-free X-ray protection material, which is related to the practical application.

This thesis attempts to address the following questions in separate chapters:

- **Question 1:** How did particle size and structure morphology have impact on X-ray shielding?
- **Question 2:** How did the layered-structure materials influence on X-ray shielding improvement?
- **Question 3:** How did 2D materials (graphene and hBN) reinforce the polymer-based composites for X-ray shielding enhancement?
- **Question 4:** How to design a polymer-based 2D oxide coated textile for the development of a lightweight, flexible, and highly efficient Pb-free shielding material?

2.16. Hypothesis

To address the above-mentioned aims and questions, the following hypothesis is made:

- **(1):** Nanostructured materials with a high-aspect ratio are favorable for X-ray shielding.
- **(2):** The layered 2D material sheets can enhance the X-ray shielding by absorption and internal scattering multiple times within the layered structure, which could lead to the discovery of a novel concept.
- **(3):** 2D nanomaterials (graphene and hBN) act as carriers to improve the dispersion performance within the polymer-based composites, leading to

enhanced X-ray shielding efficiency with reinforced thermal and mechanical properties.

- **(4):** The sandwiched 2D metal oxide composite coated textile offers its flexibility and durability for superior X-ray shielding effectiveness, which provide the new pathway for the development of the commercial X-ray shielding apparel.

2.17. Reference

(1) Guo, K.; Baidak, A.; Yu, Z. Recent advances in green synthesis and modification of inorganic nanomaterials by ionizing and non-ionizing radiation. *Journal of Materials Chemistry A* **2020,** *8* (44), 23029-23058, DOI: 10.1039/d0ta06742c.
(2) Li, Z.; Zhou, W.; Zhang, X.; Gao, Y.; Guo, S. High-efficiency, flexibility and lead-free X-ray shielding multilayered polymer composites: layered structure design and shielding mechanism. *Sci Rep* **2021,** *11* (1), 4384, DOI: 10.1038/s41598-021-83031-4.
(3) Wang, Y.; Zhong, R.; Li, Q.; Liao, J.; Liu, N.; Joshi, N. S.; Shi, B.; Liao, X.; Guo, J. Lightweight and Wearable X-Ray Shielding Material with Biological Structure for Low Secondary Radiation and Metabolic Saving Performance. *Advanced Materials Technologies* **2020,** *5* (7), DOI: 10.1002/admt.202000240.
(4) Labor, U. S. D. o. *Occupational outlook handbook*, Radiologic and MRI Technologists 2015.
(5) ICRP *Radiological protection of people and the enviroment in the event of a large nuclear accident*; 2020; p 4.
(6) Wang, Y.; Ding, P.; Xu, H.; Li, Q.; Guo, J.; Liao, X.; Shi, B. Advanced X-ray Shielding Materials Enabled by the Coordination of Well-Dispersed High Atomic Number Elements in Natural Leather. *ACS Appl Mater Interfaces* **2020,** *12* (17), 19916-19926, DOI: 10.1021/acsami.0c01663.
(7) Azman, N. Z. N.; Siddiqui, S. A.; Hart, R.; Low, I. M. Microstructural design of lead oxide-epoxy composites for radiation shielding purposes. *Journal of Applied Polymer Science* **2013,** *128* (5), 3213-3219, DOI: 10.1002/app.38515.
(8) Tishkevich, D. I.; Grabchikov, S. S.; Lastovskii, S. B.; Trukhanov, S. V.; Zubar, T. I.; Vasin, D. S.; Trukhanov, A. V.; Kozlovskiy, A. L.; Zdorovets, M. M. Effect of the Synthesis Conditions and Microstructure for Highly Effective Electron Shields Production Based on Bi Coatings. *ACS Applied Energy Materials* **2018,** *1* (4), 1695-1702, DOI: 10.1021/acsaem.8b00179.
(9) Azman, N. Z.; Siddiqui, S. A.; Low, I. M. Characterisation of micro-sized and nano-sized tungsten oxide-epoxy composites for radiation shielding of diagnostic X-rays. *Mater Sci Eng C Mater Biol Appl* **2013,** *33* (8), 4952-7, DOI: 10.1016/j.msec.2013.08.023.
(10) McCaffrey, J. P.; Tessier, F.; Shen, H. Radiation shielding materials and radiation scatter effects for interventional radiology (IR) physicians. *Med Phys* **2012,** *39* (7), 4537-46, DOI: 10.1118/1.4730504.
(11) Abdel-Aziz, M. M.; Badran, A. S.; Abdel-Hakem, A. A.; Helaly, F. M.; Moustafa, A. B. Styrene–butadiene rubber/lead oxide composites as gamma radiation shields. *Journal of Applied Polymer Science* **1991,** *42* (4), 1073-1080, DOI: 10.1002/app.1991.070420420.
(12) Shao, P.; Liang, D.; Yang, L.; Shi, H.; Xiong, Z.; Ding, L.; Yin, X.; Zhang, K.; Luo, X. Evaluating the adsorptivity of organo-functionalized silica nanoparticles towards

heavy metals: Quantitative comparison and mechanistic insight. *J Hazard Mater* **2020,** *387*, 121676, DOI: 10.1016/j.jhazmat.2019.121676.
(13) AbuAlRoos, N. J.; Baharul Amin, N. A.; Zainon, R. Conventional and new lead-free radiation shielding materials for radiation protection in nuclear medicine: A review. *Radiation Physics and Chemistry* **2019,** *165*, DOI: 10.1016/j.radphyschem.2019.108439.
(14) Harish, V.; Nagaiah, N.; Prabhu, T. N.; Varughese, K. T. Thermo-mechanical analysis of lead monoxide filled unsaturated polyester based polymer composite radiation shields. *Journal of Applied Polymer Science* **2010**, n/a-n/a, DOI: 10.1002/app.32265.
(15) Tyagi, D.; Wang, H.; Huang, W.; Hu, L.; Tang, Y.; Guo, Z.; Ouyang, Z.; Zhang, H. Recent advances in two-dimensional-material-based sensing technology toward health and environmental monitoring applications. *Nanoscale* **2020,** *12* (6), 3535-3559, DOI: 10.1039/c9nr10178k.
(16) Vlassiouk, I. V.; Stehle, Y.; Pudasaini, P. R.; Unocic, R. R.; Rack, P. D.; Baddorf, A. P.; Ivanov, I. N.; Lavrik, N. V.; List, F.; Gupta, N.; Bets, K. V.; Yakobson, B. I.; Smirnov, S. N. Evolutionary selection growth of two-dimensional materials on polycrystalline substrates. *Nat Mater* **2018,** *17* (4), 318-322, DOI: 10.1038/s41563-018-0019-3.
(17) Thibeault, S. A. K., Jin Ho; Sauti, Godfrey; Park, Cheol; Fay, Catharine C.; King, Glen C. Nanomaterials for radiation shielding. *MRS Bulletin* **2015,** *40* (10), 836-841, DOI: 10.1557/mrs.2015.225.
(18) Issa, S. A. M.; Sayyed, M. I.; Mostafa, A. M. A.; Lakshminarayana, G.; Kityk, I. V. Investigation of mechanical and radiation shielding features of heavy metal oxide based phosphate glasses for gamma radiation attenuation applications. *Journal of Materials Science: Materials in Electronics* **2019,** *30* (13), 12140-12151, DOI: 10.1007/s10854-019-01572-x.
(19) More, C. V.; Alsayed, Z.; Badawi, M. S.; Thabet, A. A.; Pawar, P. P. Polymeric composite materials for radiation shielding: a review. *Environ Chem Lett* **2021,** *19* (3), 2057-2090, DOI: 10.1007/s10311-021-01189-9.
(20) Kumar, A. Gamma ray shielding properties of PbO-Li 2 O-B 2 O 3 glasses. *Radiation Physics and Chemistry* **2017,** *136*, 50-53, DOI: 10.1016/j.radphyschem.2017.03.023.
(21) Donya, M.; Radford, M.; ElGuindy, A.; Firmin, D.; Yacoub, M. H. Radiation in medicine: Origins, risks and aspirations. *Glob Cardiol Sci Pract* **2014,** *2014* (4), 437-48, DOI: 10.5339/gcsp.2014.57.
(22) claus, G. *Astroparticle physics*, Spinger: 2005.
(23) MarShield Choosing the right radiation shielding: Factors considered by a shielding materials expert. https://marshield.com/choosing-the-right-radiation-shielding-factors-considered-by-a-shielding-materials-expert/.
(24) Archer; Benjamin, R.; Thornby, J.; Bushong, S. C. Diagnostic X-ray shielding design based on an empirical model of photon attenuation. *Health Physics* **1983,** *44* (5), 507-17.
(25) Yu, L.; Yap, P. L.; Santos, A.; Tran, D.; Losic, D. Lightweight Bismuth Titanate (Bi4Ti3O12) Nanoparticle-Epoxy Composite for Advanced Lead-Free X-ray Radiation Shielding. *ACS Applied Nano Materials* **2021,** *4* (7), 7471-7478, DOI: 10.1021/acsanm.1c01475.
(26) Li, Q.; Zhong, R.; Xiao, X.; Liao, J.; Liao, X.; Shi, B. Lightweight and Flexible Bi@Bi-La Natural Leather Composites with Superb X-ray Radiation Shielding Performance and Low Secondary Radiation. *ACS Appl Mater Interfaces* **2020,** *12* (48), 54117-54126, DOI: 10.1021/acsami.0c17008.
(27) ICPR, The 2007 Recommendations of International Commission on Radiological Protection. ICPR 2007; Vol. 103.

(28) Yu, L.; Pereira, A. L. C.; Tran, D. N. H.; Santos, A. M. C.; Losic, D. Bismuth Oxide Films for X-ray shielding: Effects of particle size and structural morphology. *Materials Chemistry and Physics* **2021,** *260*, DOI: 10.1016/j.matchemphys.2020.124084.
(29) Howard, B. J.; Beresford, N. A.; Andersson, P.; Brown, J. E.; Copplestone, D.; Beaugelin-Seiller, K.; Garnier-Laplace, J.; Howe, P. D.; Oughton, D.; Whitehouse, P. Protection of the environment from ionising radiation in a regulatory context--an overview of the PROTECT coordinated action project. *J Radiol Prot* **2010,** *30* (2), 195-214, DOI: 10.1088/0952-4746/30/2/S01.
(30) Evans, R. D. *The atomic nucleus*, Krieger: 1982.
(31) Podgorsak, E. B. *Radiation oncology physics*, International Atomic Energy Agency: Vienna, 2005.
(32) Attix, F. *Introduction to radiological physics and radiation dosimetry*, Wiley: New York, 1986.
(33) Hoheisel, M.; Bernhardt, P.; Lawaczeck, R.; Pietsch, H. Comparison of polychromatic and monochromatic X-ray for imaging *Proceedings of the SPIE* **2006,** *6142*, 71-78, DOI: 10.1117/12.651037.
(34) Baltaş, H.; Çelik, Ş.; Çevik, U.; Yanmaz, E. Measurement of mass attenuation coefficients and effective atomic numbers for superconductor using X-ray energies. *Radiation Measurements* **2007,** *42* (1), 55-60, DOI: 10.1016/j.radmeas.2006.08.005.
(35) McKetty, M. H. The AAPM/RSNA physics tutorial for residents. X-ray attenuation. *Radiographics* **1998,** *18* (1), 151-63; quiz 149, DOI: 10.1148/radiographics.18.1.9460114.
(36) Mowery, M. L.; Singh, V. *X-ray production technical evaluation*, StatPearls: 2021.
(37) Swinehart, D. F. The Beer-Lambert law. *Journal of Chemical Education* **1962,** *39*, 333-35.
(38) Low, I. M.; Noor Azman, N. Z. *Polymer Composites and Nanocomposites for X-Rays Shielding*, 2020.
(39) He, D.; Ma, Y.; Zhao, R.; Qiu, J.; Sun, B.; Wang, H.; Yang, M.; Jia, X.; Li, X.; Li, Y.; Lu, X.; Wang, C. Complete - Lifecycle - Available, Lightweight and Flexible Hierarchical Structured Bi2WO6/WO3/PAN Nanofibrous Membrane for X - Ray Shielding and Photocatalytic Degradation. *Advanced Materials Interfaces* **2021,** *8* (7), DOI: 10.1002/admi.202002131.
(40) *Power Plant Instrumentation and Control Handbook*, 2015.
(41) More, C. V.; Lokhande, R. M.; Pawar, P. P. Effective atomic number and electron density of amino acids within the energy range of 0.122–1.330 MeV. *Radiation Physics and Chemistry* **2016,** *125*, 14-20, DOI: 10.1016/j.radphyschem.2016.02.024.
(42) Palmer, C. Interaction of radiation with the matter. *Health Physics* **2013,** *104* (2), 234.
(43) Seibert, J. A.; Boone, J. M. X-Ray Imaging Physics for Nuclear Medicine Technologists. Part 2: X-Ray Interactions and Image Formation. *Journal of Nuclear Medicine Technology* **2005,** *33*, 3-18.
(44) Nambiar, S.; Yeow, J. T. Polymer-composite materials for radiation protection. *ACS Appl Mater Interfaces* **2012,** *4* (11), 5717-26, DOI: 10.1021/am300783d.
(45) Liang, D. Absorption of X-ray photon. http://personal.cityu.edu.hk/liangdai/post/absorption-of-x-ray-photon/.
(46) Abdel-Rahman, W.; Podgorsak, E. B. Energy transfer and energy absorption in photon interactions with matter revisited: A step-by-step illustrated approach. *Radiation Physics and Chemistry* **2010,** *79* (5), 552-566, DOI: 10.1016/j.radphyschem.2010.01.007.

(47) Rooyen, J. *Transport and shielding of ionizing radiation* South African Nuclear Energy Corporation: South Africa 2020.
(48) Bijanu, A.; Arya, R.; Agrawal, V.; Tomar, A. S.; Gowri, V. S.; Sanghi, S. K.; Mishra, D.; Salammal, S. T. Metal-polymer composites for radiation protection: a review. *Journal of Polymer Research* **2021,** *28* (10), DOI: 10.1007/s10965-021-02751-3.
(49) Jaeger, R. G.; Blizard, E. P.; CHilton, A. B.; Grotenhuis, M.; Honig, A.; Jaeger, T. A.; Eisenlohr, H. H. *Engineering compendium on radiation shielding*, Springer Berlin Heidelberg, 1975; Vol. 2.
(50) Leroy, C.; Rancoita, P.-G. *Principles of Radiation Interaction in Matter and Detection*, 2009.
(51) Mann, H. S.; Brar, G. S.; Mudahar, G. S. Gamma-ray shielding effectiveness of novel light-weight clay-flyash bricks. *Radiation Physics and Chemistry* **2016,** *127*, 97-101, DOI: 10.1016/j.radphyschem.2016.06.013.
(52) McCaffrey, J. P.; Shen, H.; Downton, B.; Mainegra-Hing, E. Radiation attenuation by lead and nonlead materials used in radiation shielding garments. *Med Phys* **2007,** *34* (2), 530-7, DOI: 10.1118/1.2426404.
(53) Hellström, K.; Diószegi, A.; Diaconu, L. A Broad Literature Review of Density Measurements of Liquid Cast Iron. *Metals* **2017,** *7* (5), DOI: 10.3390/met7050165.
(54) APRANSA, Aprons for Protection Against X-rays. 2015.
(55) Curry, T. S.; Dowdey, J. E.; Murry, R. C. *Christensen's physics of diagnostic radiology*, Lippincott Williams & Wilkins: USA, 1990.
(56) Sayyed, M. I.; Almuqrin, A. H.; Kurtulus, R.; Javier-Hila, A. M. V.; Kaky, K.; Kavas, T. X-ray shielding characteristics of P2O5–Nb2O5 glass doped with Bi2O3 by using EPICS2017 and Phy-X/PSD. *Applied Physics A* **2021,** *127* (4), DOI: 10.1007/s00339-021-04405-z.
(57) Sharon, M.; Sharon, M. Interaction of Radiation with Matter. In *Nuclear Chemistry*; 2021; Chapter Chapter 4, pp 45-51.
(58) Noor Azman, N. Z.; Siddiqui, S. A.; Haroosh, H. J.; Albetran, H. M.; Johannessen, B.; Dong, Y.; Low, I. M. Characteristics of X-ray attenuation in electrospun bismuth oxide/polylactic acid nanofibre mats. *J Synchrotron Radiat* **2013,** *20* (Pt 5), 741-8, DOI: 10.1107/S0909049513017871.
(59) Wang, Y.; Wang, G.; Hu, T.; Wen, S.; Hu, S.; Liu, L. Enhanced photon shielding efficiency of a flexible and lightweight rare earth/polymer composite: A Monte Carlo simulation study. *Nuclear Engineering and Technology* **2020,** *52* (7), 1565-1570, DOI: 10.1016/j.net.2019.12.028.
(60) Langeveld, W. G. J. Effective Atomic Number, Mass Attenuation Coefficient Parameterization, and Implications for High-Energy X-Ray Cargo Inspection Systems. *Physics Procedia* **2017,** *90*, 291-304, DOI: 10.1016/j.phpro.2017.09.014.
(61) Spiers, F. W. Effective atomic number and energy absorption in tissues. *Br. J. Radiol.* **1946,** *19*.
(62) Sayyed, M. I.; Lakshminarayana, G.; Mahdi, M. A. Evaluation of radiation shielding parameters for optical material. *Chalcogenide Letters* **2017,** *14*, 43-47.
(63) Harish, V.; Nagaiah, N.; Prabhu, T. N.; Varughese, K. T. Preparation and characterization of lead monoxide filled unsaturated polyester based polymer composites for gamma radiation shielding applications. *Journal of Applied Polymer Science* **2009,** *112* (3), 1503-1508, DOI: 10.1002/app.29633.
(64) More, C. V.; Alsayed, Z.; Badawi, M. S.; Thabet, A. A.; Pawar, P. P. Polymeric composite materials for radiation shielding: a review. *Environ Chem Lett* **2021**, 1-34, DOI: 10.1007/s10311-021-01189-9.

(65) Stawarz, S.; Witek, N.; Kucharczyk, W.; Bakar, M.; Stawarz, M. Thermo-protective properties of polymer composites with nano-titanium dioxide. *International Journal of Mechanics and Materials in Design* **2018,** *15* (3), 585-599, DOI: 10.1007/s10999-018-9432-7.
(66) Kumar, A. P.; Depan, D.; Singh Tomer, N.; Singh, R. P. Nanoscale particles for polymer degradation and stabilization—Trends and future perspectives. *Progress in Polymer Science* **2009,** *34* (6), 479-515, DOI: 10.1016/j.progpolymsci.2009.01.002.
(67) Botelho, M. Z.; Kunzel, R.; Okuno, E.; Levenhagen, R. S.; Basegio, T.; Bergmann, C. P. X-ray transmission through nanostructured and microstructured CuO materials. *Appl Radiat Isot* **2011,** *69* (2), 527-30, DOI: 10.1016/j.apradiso.2010.11.002.
(68) Noor Azman, N. Z.; Musa, N. F. L.; Nik Ab Razak, N. N. A.; Ramli, R. M.; Mustafa, I. S.; Abdul Rahman, A.; Yahaya, N. Z. Effect of Bi2O3 particle sizes and addition of starch into Bi2O3–PVA composites for X-ray shielding. *Applied Physics A* **2016,** *122* (9), DOI: 10.1007/s00339-016-0329-8.
(69) Hashemi, S. A.; Mousavi, S. M.; Faghihi, R.; Arjmand, M.; Sina, S.; Amani, A. M. Lead oxide-decorated graphene oxide/epoxy composite towards X-Ray radiation shielding. *Radiation Physics and Chemistry* **2018,** *146*, 77-85, DOI: 10.1016/j.radphyschem.2018.01.008.
(70) Asari Shik, N.; Gholamzadeh, L. X-ray shielding performance of the EPVC composites with micro- or nanoparticles of WO3, PbO or Bi2O3. *Appl Radiat Isot* **2018,** *139*, 61-65, DOI: 10.1016/j.apradiso.2018.03.025.
(71) Li, X.; Wang, X.; Li, Y.; Liu, Y. Production and Heat Properties of an X-ray Reflective Anode Based on a Diamond Heat Buffer Layer. *Materials (Basel)* **2020,** *13* (1), DOI: 10.3390/ma13010241.
(72) Hulbert, S. M.; Carlson, K. A. Is lead dust within nuclear medicine departments a hazard to pediatric patients? *J Nucl Med Technol* **2009,** *37* (3), 170-2, DOI: 10.2967/jnmt.109.062281.
(73) R, A. A. S.; Abdelal, N.; Alsabbagh, A.; Al-Jarrah, M.; Al-Jawarneh, F. Radiation Shielding of Fiber Reinforced Polymer Composites Incorporating Lead Nanoparticles-An Empirical Approach. *Polymers (Basel)* **2021,** *13* (21), DOI: 10.3390/polym13213699.
(74) Plionis, A. A.; Garcia, S. R.; Gonzales, E. R.; Porterfield, D. R.; Peterson, D. S. Replacement of lead bricks with non-hazardous polymer-bismuth for low-energy gamma shielding. *Journal of Radioanalytical and Nuclear Chemistry* **2009,** *282* (1), 239-242, DOI: 10.1007/s10967-009-0245-x.
(75) Weiss, M. D.; Wasdell, M. B.; Bomben, M. M.; Rea, K. J.; Freeman, R. D. Sleep Hygiene and Melatonin Treatment for Children and Adolescents With ADHD and Initial Insomnia. *Journal of the American Academy of Child & Adolescent Psychiatry* **2006,** *45* (5), 512-519, DOI: 10.1097/01.
(76) Rammah, Y. S.; Mahmoud, K. A.; Sayyed, M. I.; El-Agawany, F. I.; El-Mallawany, R. Novel vanadyl lead-phosphate glasses: P2O5–PbO–ZnO Na2O–V2O5: Synthesis, optical, physical and gamma photon attenuation properties. *Journal of Non-Crystalline Solids* **2020,** *534*, DOI: 10.1016/j.jnoncrysol.2020.119944.
(77) Maghrabi, H. A.; Vijayan, A.; Mohaddes, F.; Deb, P.; Wang, L. Evaluation of X-ray radiation shielding performance of barium sulphate-coated fabrics. *Fibers and Polymers* **2017,** *17* (12), 2047-2054, DOI: 10.1007/s12221-016-5850-z.
(78) Lewis, R. D.; Ong, K. H.; Emo, B.; Kennedy, J.; Brown, C. A.; Condoor, S.; Thummalakunta, L. Do new wipe materials outperform traditional lead dust cleaning methods? *J Occup Environ Hyg* **2012,** *9* (8), 524-33, DOI: 10.1080/15459624.2012.695975.

(79) Wani, A. L.; Ara, A.; Usmani, J. A. Lead toxicity: a review. *Interdiscip Toxicol* **2015,** *8* (2), 55-64, DOI: 10.1515/intox-2015-0009.
(80) Archer, B. R.; Fewell, T. R.; Conway, B. J.; Quinn, P. W. Attenuation properties of diagnostic x-ray shielding materials. *Med Phys* **1994,** *21* (9), 1499-507, DOI: 10.1118/1.597408.
(81) Hubbert, T. E.; Vucich, J.; Armstrong, M. Lightweight aprons for protection against scattered radiation during fluoroscopy. *Technical Note* **1993,** *161*, 1079-81.
(82) Products, R. P. Sheet lead capabilities.
(83) Hacıoğlu, F.; Özdemir, T.; Çavdar, S.; Usanmaz, A. Possible use of EPDM in radioactive waste disposal: Long term low dose rate and short term high dose rate irradiation in aquatic and atmospheric environment. *Radiation Physics and Chemistry* **2013,** *83*, 122-130, DOI: 10.1016/j.radphyschem.2012.10.011.
(84) Mahmoud, M. E.; El-Khatib, A. M.; Badawi, M. S.; Rashad, A. R.; El-Sharkawy, R. M.; Thabet, A. A. Fabrication, characterization and gamma rays shielding properties of nano and micro lead oxide-dispersed-high density polyethylene composites. *Radiation Physics and Chemistry* **2018,** *145*, 160-173, DOI: 10.1016/j.radphyschem.2017.10.017.
(85) Özdemir, T.; Güngör, A.; Akbay, I. K.; Uzun, H.; Babucçuoglu, Y. Nano lead oxide and epdm composite for development of polymer based radiation shielding material: Gamma irradiation and attenuation tests. *Radiation Physics and Chemistry* **2018,** *144*, 248-255, DOI: 10.1016/j.radphyschem.2017.08.021.
(86) Özkalaycı, F.; Kaçal, M. R.; Agar, O.; Polat, H.; Sharma, A.; Akman, F. Lead(II) chloride effects on nuclear shielding capabilities of polymer composites. *Journal of Physics and Chemistry of Solids* **2020,** *145*, DOI: 10.1016/j.jpcs.2020.109543.
(87) Eren Belgin, E.; Aycik, G. A. Preparation and radiation attenuation performances of metal oxide filled polyethylene based composites for ionizing electromagnetic radiation shielding applications. *Journal of Radioanalytical and Nuclear Chemistry* **2015,** *306* (1), 107-117, DOI: 10.1007/s10967-015-4052-2.
(88) Kunzel, R.; Okuno, E. Effects of the particle sizes and concentrations on the X-ray absorption by CuO compounds. *Appl Radiat Isot* **2012,** *70* (4), 781-4, DOI: 10.1016/j.apradiso.2011.12.040.
(89) Movahedi, M. M.; Abdi, A.; Mehdizadeh, A.; Dehghan, N.; Heidari, E.; Masumi, Y.; Abbaszadeh, M. Novel paint design based on nanopowder to protection against X and gamma rays. *Indian J Nucl Med* **2014,** *29* (1), 18-21, DOI: 10.4103/0972-3919.125763.
(90) Fontainha, C. C. P.; Baptista Neto, A. T.; Santos, A. P.; Faria, L. O. d. P(VDF-TrFE)/ZrO2 Polymer-Composites for X-ray Shielding. *Materials Research* **2016,** *19* (2), 426-433, DOI: 10.1590/1980-5373-mr-2015-0576.
(91) Eren Belgin, E.; Aycik, G. A.; Kalemtas, A.; Pelit, A.; Dilek, D. A.; Kavak, M. T. Usability of natural titanium-iron oxide as filler material for ionizing electromagnetic radiation shielding composites; preparation, characterization and performance. *Journal of Radioanalytical and Nuclear Chemistry* **2015**, DOI: 10.1007/s10967-015-4643-y.
(92) Singh, A. K.; Singh, R. K.; Sharma, B.; Tyagi, A. K. Characterization and biocompatibility studies of lead free X-ray shielding polymer composite for healthcare application. *Radiation Physics and Chemistry* **2017,** *138*, 9-15, DOI: 10.1016/j.radphyschem.2017.04.016.
(93) Abunahel, B. M.; Mustafa, I. S.; Noor Azman, N. Z. Characteristics of X-ray attenuation in nano-sized bismuth oxide/epoxy-polyvinyl alcohol (PVA) matrix composites. *Applied Physics A* **2018,** *124* (12), DOI: 10.1007/s00339-018-2254-5.
(94) Jayakumar, S.; Saravanan, T.; Philip, J. Polymer nanocomposites containing β-Bi2O3 and silica nanoparticles: Thermal stability, surface topography and X-ray

attenuation properties. *Journal of Applied Polymer Science* **2020,** *137* (36), DOI: 10.1002/app.49048.
(95) Belgin, E. E.; Aycik, G. A. Effect of particle size of mineral fillers on polymer-matrix composite shielding materials against ionizing electromagnetic radiation. *Journal of Radioanalytical and Nuclear Chemistry* **2017,** *311* (3), 1953-1961, DOI: 10.1007/s10967-016-5156-z.
(96) Chang, H.; Wu, H. Graphene-based nanocomposites: preparation, functionalization, and energy and environmental applications. *Energy & Environmental Science* **2013,** *6* (12), DOI: 10.1039/c3ee42518e.
(97) Perreault, F.; Fonseca de Faria, A.; Elimelech, M. Environmental applications of graphene-based nanomaterials. *Chem Soc Rev* **2015,** *44* (16), 5861-96, DOI: 10.1039/c5cs00021a.
(98) Gupta, A.; Sakthivel, T.; Seal, S. Recent development in 2D materials beyond graphene. *Progress in Materials Science* **2015,** *73*, 44-126, DOI: 10.1016/j.pmatsci.2015.02.002.
(99) Castro Neto, A. H.; Guinea, F.; Peres, N. M. R.; Novoselov, K. S.; Geim, A. K. The electronic properties of graphene. *Reviews of Modern Physics* **2009,** *81* (1), 109-162, DOI: 10.1103/RevModPhys.81.109.
(100) Chen, J. H.; Jang, C.; Xiao, S.; Ishigami, M.; Fuhrer, M. S. Intrinsic and extrinsic performance limits of graphene devices on SiO2. *Nat Nanotechnol* **2008,** *3* (4), 206-9, DOI: 10.1038/nnano.2008.58.
(101) Bonaccorso, F.; Colombo, L.; Yu, G.; Stoller, M.; Tozzini, V.; Ferrari, A. C.; Ruoff, R. S.; Pellegrini, V. 2D materials. Graphene, related two-dimensional crystals, and hybrid systems for energy conversion and storage. *Science* **2015,** *347* (6217), 1246501, DOI: 10.1126/science.1246501.
(102) Kumar, P.; Yu, S.; Shahzad, F.; Hong, S. M.; Kim, Y.-H.; Koo, C. M. Ultrahigh electrically and thermally conductive self-aligned graphene/polymer composites using large-area reduced graphene oxides. *Carbon* **2016,** *101*, 120-128, DOI: 10.1016/j.carbon.2016.01.088.
(103) Nair, R. R.; Blake, P.; Grigorenko, A. N.; Novoselov, K. S.; Booth, T. J.; Stauber, T.; Peres, N. M.; Geim, A. K. Fine structure constant defines visual transparency of graphene. *Science* **2008,** *320* (5881), 1308, DOI: 10.1126/science.1156965.
(104) Liang, J.; Wang, Y.; Huang, Y.; Ma, Y.; Liu, Z.; Cai, J.; Zhang, C.; Gao, H.; Chen, Y. Electromagnetic interference shielding of graphene/epoxy composites. *Carbon* **2009,** *47* (3), 922-925, DOI: 10.1016/j.carbon.2008.12.038.
(105) Rubrice, K.; Castel, X.; Himdi, M.; Parneix, P. Dielectric Characteristics and Microwave Absorption of Graphene Composite Materials. *Materials (Basel)* **2016,** *9* (10), DOI: 10.3390/ma9100825.
(106) Viegas, J.; Silva, L. A.; Batista, A. M. S.; Furtado, C. A.; Nascimento, J. P.; Faria, L. O. Increased X-ray Attenuation Efficiency of Graphene-Based Nanocomposite. *Industrial & Engineering Chemistry Research* **2017,** *56* (41), 11782-11790, DOI: 10.1021/acs.iecr.7b02711.
(107) Hashemi, S. A.; Mousavi, S. M.; Faghihi, R.; Arjmand, M.; Rahsepar, M.; Bahrani, S.; Ramakrishna, S.; Lai, C. W. Superior X-ray Radiation Shielding Effectiveness of Biocompatible Polyaniline Reinforced with Hybrid Graphene Oxide-Iron Tungsten Nitride Flakes. *Polymers (Basel)* **2020,** *12* (6), DOI: 10.3390/polym12061407.
(108) Zarei, M.; Sina, S.; Hashemi, S. A. Superior X-ray radiation shielding of biocompatible platform based on reinforced polyaniline by decorated graphene oxide with interconnected tungsten–bismuth–tin complex. *Radiation Physics and Chemistry* **2021,** *188*, DOI: 10.1016/j.radphyschem.2021.109588.

(109) Hashemi, S. A.; Mousavi, S. M.; Bahrani, S.; Ramakrishna, S.; Babapoor, A.; Chiang, W. H. Coupled graphene oxide with hybrid metallic nanoparticles as potential electrochemical biosensors for precise detection of ascorbic acid within blood. *Anal Chim Acta* **2020,** *1107*, 183-192, DOI: 10.1016/j.aca.2020.02.018.
(110) Azhdari, R.; Mousavi, S. M.; Hashemi, S. A.; Bahrani, S.; Ramakrishna, S. Decorated graphene with aluminum fumarate metal organic framework as a superior non-toxic agent for efficient removal of Congo Red dye from wastewater. *Journal of Environmental Chemical Engineering* **2019,** *7* (6), DOI: 10.1016/j.jece.2019.103437.
(111) Lowe, S. E.; Zhong, Y. L. Challenges of Industrial-Scale Graphene Oxide Production. In *Graphene Oxide*; 2016; pp 410-431.
(112) Zhang, K.; Feng, Y.; Wang, F.; Yang, Z.; Wang, J. Two dimensional hexagonal boron nitride (2D-hBN): synthesis, properties and applications. *Journal of Materials Chemistry C* **2017,** *5* (46), 11992-12022, DOI: 10.1039/c7tc04300g.
(113) Roy, S.; Zhang, X.; Puthirath, A. B.; Meiyazhagan, A.; Bhattacharyya, S.; Rahman, M. M.; Babu, G.; Susarla, S.; Saju, S. K.; Tran, M. K.; Sassi, L. M.; Saadi, M.; Lai, J.; Sahin, O.; Sajadi, S. M.; Dharmarajan, B.; Salpekar, D.; Chakingal, N.; Baburaj, A.; Shuai, X.; Adumbumkulath, A.; Miller, K. A.; Gayle, J. M.; Ajnsztajn, A.; Prasankumar, T.; Harikrishnan, V. V. J.; Ojha, V.; Kannan, H.; Khater, A. Z.; Zhu, Z.; Iyengar, S. A.; Autreto, P.; Oliveira, E. F.; Gao, G.; Birdwell, A. G.; Neupane, M. R.; Ivanov, T. G.; Taha-Tijerina, J.; Yadav, R. M.; Arepalli, S.; Vajtai, R.; Ajayan, P. M. Structure, Properties and Applications of Two-Dimensional Hexagonal Boron Nitride. *Adv Mater* **2021,** *33* (44), e2101589, DOI: 10.1002/adma.202101589.
(114) Wang, Z.; Tang, Z.; Xue, Q.; Huang, Y.; Huang, Y.; Zhu, M.; Pei, Z.; Li, H.; Jiang, H.; Fu, C.; Zhi, C. Fabrication of Boron Nitride Nanosheets by Exfoliation. *The Chemical Record* **2016,** *16* (3), 1204-1215, DOI: 10.1002/tcr.201500302.
(115) Yuan, C.; Li, J.; Lindsay, L.; Cherns, D.; Pomeroy, J. W.; Liu, S.; Edgar, J. H.; Kuball, M. Modulating the thermal conductivity in hexagonal boron nitride via controlled boron isotope concentration. *Communications Physics* **2019,** *2* (1), DOI: 10.1038/s42005-019-0145-5.
(116) Falin, A.; Cai, Q.; Santos, E. J. G.; Scullion, D.; Qian, D.; Zhang, R.; Yang, Z.; Huang, S.; Watanabe, K.; Taniguchi, T.; Barnett, M. R.; Chen, Y.; Ruoff, R. S.; Li, L. H. Mechanical properties of atomically thin boron nitride and the role of interlayer interactions. *Nat Commun* **2017,** *8*, 15815, DOI: 10.1038/ncomms15815.
(117) Chen, J.; Chen, J.; Zhang, H.; Hu, M.; Li, M. Microstructure and mechanical properties of h-BN/Yb4Si2O7N2 composites. *Journal of Advanced Ceramics* **2018,** *7* (4), 317-324, DOI: 10.1007/s40145-018-0281-5.
(118) Güngör, A.; Akbay, I. K.; Özdemir, T. EPDM Rubber with hexagonal Boron Nitride: A Thermal Neutron Shielding Composite. *Radiation Physics and Chemistry* **2019,** *165*, DOI: 10.1016/j.radphyschem.2019.108391.
(119) Yılmaz, S. N.; Akbay, İ. K.; Özdemir, T. A metal-ceramic-rubber composite for hybrid gamma and neutron radiation shielding. *Radiation Physics and Chemistry* **2021,** *180*, DOI: 10.1016/j.radphyschem.2020.109316.
(120) Shang, Y.; Yang, G.; Su, F.; Feng, Y.; Ji, Y.; Liu, D.; Yin, R.; Liu, C.; Shen, C. Multilayer polyethylene/ hexagonal boron nitride composites showing high neutron shielding efficiency and thermal conductivity. *Composites Communications* **2020,** *19*, 147-153, DOI: 10.1016/j.coco.2020.03.007.
(121) Wilson, J. A.; Yoffe, A. D. The transition metal dichalcogenides discussion and interpretation of the observed optical, electrical and structural properties. *Advances in Physics* **1969,** *18* (73), 193-335, DOI: 10.1080/00018736900101307.

(122) Wang, Q. H.; Kalantar-Zadeh, K.; Kis, A.; Coleman, J. N.; Strano, M. S. Electronics and optoelectronics of two-dimensional transition metal dichalcogenides. *Nat Nanotechnol* **2012,** *7* (11), 699-712, DOI: 10.1038/nnano.2012.193.
(123) Poudel, B.; Hao, Q.; Ma, Y.; Lan, Y.; Minnich, A.; Yu, B.; Yan, X.; Wang, D.; Muto, A.; Vashaee, D.; Chen, X.; Liu, J.; Dresselhaus, M. S.; Chen, G.; Ren, Z. High-thermoelectric performance of nanostructured bismuth antimony telluride bulk alloys. *Science* **2008,** *320* (5876), 634-8, DOI: 10.1126/science.1156446.
(124) Wang, T.; Liu, L.; Zhu, Z.; Papakonstantinou, P.; Hu, J.; Liu, H.; Li, M. Enhanced electrocatalytic activity for hydrogen evolution reaction from self-assembled monodispersed molybdenum sulfidenanoparticles on an Au electrode. *Energy Environ. Sci.* **2013,** *6* (2), 625-633, DOI: 10.1039/c2ee23513g.
(125) Kaur, J.; Singh, M.; Dell'Aversana, C.; Benedetti, R.; Giardina, P.; Rossi, M.; Valadan, M.; Vergara, A.; Cutarelli, A.; Montone, A. M. I.; Altucci, L.; Corrado, F.; Nebbioso, A.; Altucci, C. Biological interactions of biocompatible and water-dispersed MoS2 nanosheets with bacteria and human cells. *Sci Rep* **2018,** *8* (1), 16386, DOI: 10.1038/s41598-018-34679-y.
(126) Afshar, M.; Morshedian, J.; Ahmadi, S. Radiation attenuation capability and flow characteristics of HDPE composite loaded with W, MoS2
, and B4C. *Polymer Composites* **2019,** *40* (1), 149-158, DOI: 10.1002/pc.24620.
(127) Felix, J. F.; da Silva, A. F.; da Silva, S. W.; Qu, F.; Qiu, B.; Ren, J.; de Azevedo, W. M.; Henini, M.; Huang, C.-C. A comprehensive study on the effects of gamma radiation on the physical properties of a two-dimensional WS2monolayer semiconductor. *Nanoscale Horizons* **2020,** *5* (2), 259-267, DOI: 10.1039/c9nh00414a.
(128) Ensoylu, M.; Atmaca, H.; Deliormanlı, A. M. Fabrication and in vitro characterization of macroporous WS2/ bioactive glass scaffolds for biomedical applications. *Journal of the Australian Ceramic Society* **2022**, DOI: 10.1007/s41779-021-00696-w.
(129) Deliormanlı, A. M.; Ensoylu, M.; Issa, S. A. M.; Elshami, W.; Al-Baradi, A. M.; Al-Buriahi, M. S.; Tekin, H. O. WS2/bioactive glass composites: Fabrication, structural, mechanical and radiation attenuation properties. *Ceramics International* **2021,** *47* (21), 29739-29747, DOI: 10.1016/j.ceramint.2021.07.146.
(130) Hamad, M. K.; Mhareb, M. H. A.; Alajerami, Y. S.; Sayyed, M. I.; Saleh, G.; Maswadeh, Y.; Ziq, K. Radiation shielding properties of Nd0.6Sr0.4Mn1−yNiyO3 substitute with different concentrations of nickle. *Radiation Physics and Chemistry* **2020,** *174*, DOI: 10.1016/j.radphyschem.2020.108920.
(131) Mhareb, M. H. A.; Slimani, Y.; Alajerami, Y. S.; Sayyed, M. I.; Lacomme, E.; Almessiere, M. A. Structural and radiation shielding properties of BaTiO3 ceramic with different concentrations of Bismuth and Ytterbium. *Ceramics International* **2020,** *46* (18), 28877-28886, DOI: 10.1016/j.ceramint.2020.08.055.
(132) Issa, S. A. M.; Zakaly, H. M. H.; Pyshkina, M.; Mostafa, M. Y. A.; Rashad, M.; Soliman, T. S. Structure, optical, and radiation shielding properties of PVA–BaTiO3 nanocomposite films: An experimental investigation. *Radiation Physics and Chemistry* **2021,** *180*, DOI: 10.1016/j.radphyschem.2020.109281.
(133) Jayakumar, S.; Saravanan, T.; Philip, J. Thermal Stability and X-ray Attenuation Studies on alpha-Bi(2)O(3), beta-Bi(2)O(3) and Bi Based Nanocomposites for Radiopaque Fabrics. *J Nanosci Nanotechnol* **2018,** *18* (6), 3969-3981, DOI: 10.1166/jnn.2018.15237.
(134) Schlattl, H.; Zankl, M.; Eder, H.; Hoeschen, C. Shielding properties of lead-free protective clothing and their impact on radiation doses. *Med Phys* **2007,** *34* (11), 4270-80, DOI: 10.1118/1.2786861.

(135) Aral, N.; Banu Nergis, F.; Candan, C. An alternative X-ray shielding material based on coated textiles. *Textile Research Journal* **2015,** *86* (8), 803-811, DOI: 10.1177/0040517515590409.
(136) Maghrabi, H. A.; Vijayan, A.; Deb, P.; Wang, L. Bismuth oxide-coated fabrics for X-ray shielding. *Textile Research Journal* **2015,** *86* (6), 649-658, DOI: 10.1177/0040517515592809.
(137) Pulford, S.; Fergusson, M. A textile platform for non-lead radiation shielding apparel. *The Journal of The Textile Institute* **2016,** *107* (12), 1610-1616, DOI: 10.1080/00405000.2015.1131402.

CHAPTER 3

EFFECT OF PARTICLE SIZE AND MORPHOLOGY OF 2D OXIDES FOR X-RAY SHIELDING ENHANCEMENT

Chapter 3 Effect of particle size and morphology of 2D oxides for X-ray shielding enhancement

Overview and significance of work

Chapter 3 investigates the effect of particle size distribution and structural morphology on X-ray shielding improvement of the metal oxide materials. The microsized and nanosized Bi_2O_3 films with different structural morphologies are prepared, followed by X-ray transmission measurement compared with the theoretical values from XCOM database. The key finding from this work proved that the synergistic effect of particle size and shape variations are significant for the X-ray shielding improvement at the energy range of 30, 50 and 80 kVp. The nanomaterials having high SA/V aspect ratio benefit the X-ray attenuation, which has been adapted to the development of a 2D metal oxide ($Bi_4Ti_3O_{12}$) nanocomposite for the lightweight, non-Pb and high-performing X-ray shielding application. The results from this chapter achieve **aim 1**, with two published research papers:

(1) **Yu, L.**, Pereira, A. L. C., Tran, D. N. H., Santos, A. M. C., & Losic, D. (2021). Bismuth Oxide Films for X-ray shielding: Effects of particle size and structural morphology. *Materials Chemistry and Physics, 260,* 124084-91. **(Published)**

(2) Yu, L., Yap, P. L., Santos, A., Tran, D., & Losic, D. (2021). Lightweight bismuth titanate ($Bi_4Ti_3O_{12}$) nanoparticle-epoxy composite for advanced lead-free X-ray radiation shielding. *ACS Applied Nano Materials, 4*(7), 7471-7478. **(Published)**

Statement of Authorship

Title of Paper	Bismuth oxide film for X-ray shielding: effects of particle size and structural morphology
Publication Status	☑ Published ☐ Accepted for Publication ☐ Submitted for Publication ☐ Unpublished and Unsubmitted work written in manuscript style
Publication Details	Yu, L., Pereira, A. L. C., Tran, D. N. H., Santos, A. M. C., & Losic, D. (2021). Bismuth Oxide Films for X-ray shielding: Effects of particle size and structural morphology. *Materials Chemistry and Physics, 260.*

Principal Author

Name of Principal Author (Candidate)	Le Yu		
Contribution to the Paper	Prepared and characterized on all the samples, and interpreted all the data as well as wrote the manuscript.		
Overall percentage (%)	85 %		
Certification:	This paper reports on original research I conducted during the period of my Higher Degree by Research candidature and is not subject to any obligations or contractual agreements with a third party that would constrain its inclusion in this thesis. I am the primary author of this paper.		
Signature		Date	03/03/2022

Co-Author Contributions

By signing the Statement of Authorship, each author certifies that:

i. the candidate's stated contribution to the publication is accurate (as detailed above);

ii. permission is granted for the candidate in include the publication in the thesis; and

iii. the sum of all co-author contributions is equal to 100% less the candidate's stated contribution.

Name of Co-Author	Ana L. C. Pereira		
Contribution to the Paper	Edited and revised the manuscript.		
Signature		Date	03/03/2022

Name of Co-Author	Diana, N. H. Tran		
Contribution to the Paper	Co-supervised and revised the manuscript.		
Signature		Date	03/03/2022

Please cut and paste additional co-author panels here as required.

Statement of Authorship

Title of Paper	Bismuth oxide film for X-ray shielding: effects of particle size and structural morphology
Publication Status	☑ Published ☐ Accepted for Publication ☐ Submitted for Publication ☐ Unpublished and Unsubmitted work written in manuscript style
Publication Details	Yu, L., Pereira, A. L. C., Tran, D. N. H., Santos, A. M. C., & Losic, D. (2021). Bismuth Oxide Films for X-ray shielding: Effects of particle size and structural morphology. *Materials Chemistry and Physics, 260.*

Principal Author

Name of Principal Author (Candidate)	Le Yu		
Contribution to the Paper	Prepared and characterized on all the samples, and interpreted all the data as well as wrote the manuscript.		
Overall percentage (%)	85 %		
Certification:	This paper reports on original research I conducted during the period of my Higher Degree by Research candidature and is not subject to any obligations or contractual agreements with a third party that would constrain its inclusion in this thesis. I am the primary author of this paper.		
Signature		Date	03/03/2022

Co-Author Contributions

By signing the Statement of Authorship, each author certifies that:

i. the candidate's stated contribution to the publication is accurate (as detailed above);

ii. permission is granted for the candidate in include the publication in the thesis; and

iii. the sum of all co-author contributions is equal to 100% less the candidate's stated contribution.

Name of Co-Author	Alexandre M. C. Santos		
Contribution to the Paper	Co-supervised, performed X-ray irradiations and revised the manuscript.		
Signature		Date	03/03/2022

Name of Co-Author	Dusan Losic		
Contribution to the Paper	Supervised the development of the work, edited, revised the manuscript and acted as the corresponding author.		
Signature		Date	03/03/2022

Please cut and paste additional co-author panels here as required.

Materials Chemistry and Physics 260 (2021) 124084

Contents lists available at ScienceDirect

Materials Chemistry and Physics

journal homepage: www.elsevier.com/locate/matchemphys

Bismuth Oxide Films for X-ray shielding: Effects of particle size and structural morphology

Le Yu [a,b], Ana L.C. Pereira [a,b,c], Diana N.H. Tran [a,b], Alexandre M.C. Santos [d,e], Dusan Losic [a,b,*]

[a] School of Chemical Engineering and Advanced Materials, University of Adelaide, Adelaide, SA, 5005, Australia
[b] ARC Research Hub for Graphene Enabled Industry Transformation, University of Adelaide, Adelaide, SA, 5005, Australia
[c] School of Applied Sciences, University of Campinas (UNICAMP), Limeira, 13484-350, Brazil
[d] School of Physical Sciences, University of Adelaide, Adelaide, South Australia, 5005, Australia
[e] Department of Medical Physics, Royal Adelaide Hospital, Adelaide, South Australia, 5000, Australia

HIGHLIGHTS

- Bi2O3 films with different particle morphologies such as spherical, wires, flowers were synthesized.
- Synergy effects of particle size and morphologies have impact on X-ray attenuation.
- Nanoflower of Bi_2O_3 provide better X-ray attenuation than microwires and nanoparticles.
- Large surface to volume ratio and smaller particle size are key parameters for X-ray attenuation.

ARTICLE INFO

Keywords:
Bismuth oxide X-ray attenuation morphology particle size

ABSTRACT

Lead (Pb) as a traditional shielding material is limited due to its toxicity and heaviness. Recently, nanomaterials in different forms have attracted considerable attention for radiation shielding applications, due to their prominent chemical and physical properties. This work aims to evaluate the effects of size and morphology on the X-ray shielding performance. Both micro- and nano-sized Bi_2O_3 films with different morphologies (e.g. particles, wires, flowers) were synthesized via a ball milling process and a hydrothermal treatment, respectively. X-ray transmission tests were conducted using a superficial X-ray unit at energies of 30, 50 and 80 kVp (effective energies converted as 14, 24 and 29 keV), which were then compared with mass attenuation coefficient of Bi_2O_3 obtained from XCOM database. The results showed that the nanoflower (388 ± 30 nm) Bi_2O_3 film gave the best X-ray shielding performance among all three energies (60.49% improvement at 30 kVp, especially) compared to the bulk Bi_2O_3 film, indicating the synergy effects of both particle size and morphologies impact on low energies of X-ray attenuation. Moreover, the nanoparticle (830 ± 30 nm) Bi_2O_3 film enhanced the X-ray attenuation, up to 13.27% at 30 kVp relative to microparticle (1.21 ± 0.14 μm) films. However, the nanoflower (388 ± 30 nm) Bi_2O_3 film gave the best X-ray shielding performance (45.93% and 47.49% improvement at 30 kVp, respectively) compared to the microwire (1.30 ± 0.13 μm) and nanoparticle (830 ± 30 nm) Bi_2O_3 film, due to its large surface-to-volume ratio, showing that morphological variations can significantly impact the X-ray transmission to enhance the radiation shielding performance compared to the particle size. Theoretical data from XCOM database compared with experimental measurements showed the limitation of simulation as it can only calculate the ideal condition of regular distributions in materials with standardized geometry. This work concluded that the synergy effect of the particle size and morphology should be considered when designing effective radioprotective garments.

1. Introduction

Ionizing radiation, (such as X- and γ-ray) are found in many operating environments, such as medical diagnosis and therapy, nuclear power plants and space exploration [1]. These radiation sources can be extremely harmful for human health by causing mutagenic and

* Corresponding author. School of Chemical Engineering and Advanced Materials, University of Adelaide, Adelaide, SA, 5005, Australia.
E-mail address: dusan.losic@adelaide.edu.au (D. Losic).

https://doi.org/10.1016/j.matchemphys.2020.124084
Received 11 September 2020; Received in revised form 19 November 2020; Accepted 20 November 2020
Available online 25 November 2020

carcinogenetic effects on bodily -organs [2]. Therefore, applying the rule – *as low as reasonably achievable* (ALARA) can minimize the radiation exposure of specialists, who are working closely within the radiation fields [3]. According to Beer-Lambert law, X-ray attenuation performance can be significantly affected by atomic number (Z), density and thickness of the X-ray absorbing materials [4]. However, the use of lead (Pb) as a traditional shielding material has limitations due to its toxicity and heaviness. [5,6], Recent studies have reported to use non-Pb, light-weighted and effective radiation protection garments with high Z. Typical metal oxide (containing high Z) materials, especially, Pb, bismuth (Bi), tungsten (W) and barium (Ba) were used as effective shielding fillers to form composites with different kinds of polymers [5]. For example, Maghrabi et al. [6] reported that 66.67 wt% bismuth oxide (Bi_2O_3) coated fabrics with 1.33 mm thickness were comparable with X-ray attenuation (92%) of a 0.17 mm Pb sheet at a X-ray energy of 80 kVp (at peak energy). Another study conducted by Haahemi et al. [2] discovered that 10 wt% lead oxide (PbO) decorated graphene oxide (GO)/epoxy composite with 6 mm thickness could provide X-ray attenuation equal to 3.91 mm equivalent aluminium thickness under 80 kVp. Recently, nanomaterials in different forms have attracted a considerable attention for radiation shielding applications, due to their prominent chemical and physical properties [7]. In 2012, Kunzel et al. [8] investigated 5, 10 and 30 wt% micro- and nano-sized copper oxide (CuO) particles incorporated with a polymeric resin. As a result, nano-sized CuO-resin composites were more effective than microsized composites at a low energy range of 25 and 30 keV, however, there was no change in the X-ray attenuation at high energies (60 and 120 keV). Noor Azman et al. [7] reported that 35 wt% nanosized (<100 nm) tungsten oxide (WO_3)-epoxy composites were able to attenuate a further 8 % of X-rays compared with microsized (20 μm) composites under an energy range of 25–35 keV, but the effects of particle size on X-ray attenuation were insignificant under high energy ranges (40–120 keV). Recently, Tekin et al. [3] investigated the effect of particle size on mass attenuation coefficients using simulation on MCNPX code, for concrete samples doped with both microsized (1 μm) and nanosized (100 nm) WO_3 simulated under theoretical conditions at an energy range of 663–1330 keV. The simulation concluded that nanosized particles can be another key parameter for improving the radiation attenuation [3]. All of these similar investigations on nanoparticles aimed to understand the impacts on X-ray shielding performance for particle sizes less than 100 nm, and it is extensively acknowledged that nanosized particles (1–100 nm) can be more regular and less agglomerated in the formation of material composites, and thus resulting in their good radiation attenuation at low energies (<35 keV) [1,3,7,9,10].

Importantly to note, the limit of all these previous works is their use of polymers (only used to hold the materials together but provide no benefits to X-ray shielding) within the composite structures for X-ray shielding applications. Moreover, these studies only explored the particle size effect on metal oxide composites for radiation shielding performance. However, they neglected that the morphological variations among different nanomaterials can be another key effect on the radiation absorption. Considering the fact that the surface-to-volume ratios on various geometrical shapes (such as a sphere and cube) are different, it is expected to have a greater impact on their radiation shielding performance [11].

In this work, Bi_2O_3 was explored without the use of polymers, relying only on itself as the active component for X-ray shielding performance. So far, there has been no reports examining the synergy effect of particle-size and morphological differences of Bi_2O_3 on the X-ray attenuation performance, thus, this study will provide a significant contribution. Two simple processes were used to synthesize Bi_2O_3 samples. The ball milling process was applied to fabricate Bi_2O_3 powders in various nano-meter scales at room temperature without any post-annealing [12]. The hydrothermal treatment used is a simple 'one-pot' reaction method, which can provide structural transformation and size reduction under thermal annealing [13]. Therefore, this study aims to fabricate micro- and nano-sized Bi_2O_3 films with different morphologies via the two methods, and the results will reveal the particle size and structural effects on X-ray attenuation performance.

2. Materials and methods

2.1. Materials

Bismuth oxide powder (Bi_2O_3, 99.90 %, 10 μm) was provided by Sigma-Aldrich (Australia). Potassium sulphate (K_2SO_4) and dimethylformamide (DMF, AR) were purchased from Chem-Supply (Australia). Hydrophilic PTFE membrane filter (pore size: 0.45 μm, diameter: 47 mm, thickness: 25 μm) was purchased from Rowe Scientific (Australia).

2.2. Methods

2.2.1. Two-step ball milling (BM) synthesis

The ball milling method was adapted from Ref. [14]. In the first stage, bulk Bi_2O_3 powder was ball-milled for 3 h using a Planetary Ball Mill PM 200 (Retsch, Australia) with zirconium balls (3 mm in diameter) under dry conditions. Grinding balls (75 g) were added to the process with a ball-to-material ratio at 15: 1, and then the as-prepared Bi_2O_3 was washed with deionized (DI) water and dried at 50 °C overnight. The second stage involved re-grinding the dried Bi_2O_3 under the same ball milling conditions to further reduce the particle size, and the obtained products from both stages were collected for further use.

2.2.2. Hydrothermal (HT) synthesis

The hydrothermal synthesis method was adapted from Ref. [15]. K_2SO_4 (1.60 g) was gently mixed with 80 ml DI water, and 0.16 g bulk Bi_2O_3 powder was then added into the as-prepared solution followed by pH adjustment to 4. This mixture was magnetically stirred before transferring to a Teflon-lined stainless-steel autoclave heated at 160 °C for 4 and 24 h, respectively. The obtained products were rinsed with DI water and dried overnight at 50 °C.

2.2.3. Bi_2O_3 films preparation

BM (or HT) (0.10 g) products were dissolved in DMF and constantly stirred for 2 h followed by bath sonication for 1 h. The as-prepared mixture was then transferred to a vacuum filtration system for removal of DMF, and the yellow Bi_2O_3 films were formed onto the PTFE membranes and dried overnight at room temperature (22°C ±2).

2.2.4. Characterization of Bi_2O_3 films

The obtained Bi_2O_3 films were characterized by a scanning electron microscope (SEM, FEI Quanta 450, US) for the morphology identification and film-thickness measurements. Elemental analysis of synthesized Bi_2O_3 films was measured using energy dispersive X-ray spectroscopy (EDS) in conjunction with SEM. The morphology and structure of BM and HT Bi_2O_3 samples were also confirmed using a FEI Tecnai G2 Spirit transmission electron microscope (TEM) operating at an accelerating voltage of 100 kV. Particle size distribution (PSD) of all samples was measured using a Zetasizer Nano-ZS (Malvern Analytical Australia, Australia). X-ray diffractometer (XRD, Rigaku Miniflex 600, Japan) for the measurements of the crystalline forms of each sample were collected in the range of $2\theta = 20–80°$ (scan rate of 10°C min^{-1}).

2.2.5. X-ray transmission testing

X-ray transmissions of the controls (air and PTFE membrane) and Bi_2O_3 films were measured by a Gulmay D3150 superficial X-ray (SXR) unit as shown in Fig. S1. The detector used to measure the transmission was a NE 2571 farmer type ionization chamber (Phoenix Dosimetry Ltd, UK). The testing distance between X-ray tube and the sample holder, and the material sample to the detector were both set to 50 cm. The composite films were placed over a collimator of diameter 1 cm, and exposed

to the X-ray voltage range at 30, 50 and 80 kVp for 0.50 min. Before the X-ray transmission measurement for each prepared sample, the X-ray transmission measurements for the control (air, without samples) were conducted three times to obtain the average, and then this was re-performed before the end of the measurement to know the uncertainty of the system. Therefore, this uncertainty has been included into the following X-ray transmission measurement for each sample. Moreover, for each sample, the measurements were performed three times for obtaining the meaningful readings. The X-ray transmission (T) was calculated as the charge collected by the ionization chamber with the sample (I) divided by the transmission dose without the sample (I_0). The equation is expressed as (1) [16],

$$T = I / I_0 \quad (1)$$

2.2.6. Simulations on XCOM program

XCOM photon cross section database is widely applied to obtain the total cross-sections and mass attenuation coefficients (μ/ρ) of elements, compounds and mixtures with the energy range from 1 KeV to 100 GeV [17]. According to the experimental measurements of X-ray transmission (T), the density (ρ) and the thickness (t) of each prepared Bi_2O_3 sample, their mass attenuation coefficients were calculated using equation (2) based on Lambert-Beer law [18], as shown,

$$\mu / \rho = -\ln(T)/\rho t \quad (2)$$

3. Results and discussion

For clarity, the prepared samples (BM-1.21 μm Bi_2O_3 particles, BM-0.83 μm Bi_2O_3 particles, HT-1.30 μm Bi_2O_3 wires, and HT-0.40 μm Bi_2O_3 flowers) will be denoted as BM-MP1.2, BM-NP0.8, HT-MW1.3 and HT-NF0.4, respectively, depending on their particle sizes and shapes. The shapes, particle sizes and surface-to-volume ratios (SAVR) analysis (PSD analysis presented in Fig. S2) of each sample are displayed in Table 1.

3.1. Structural characterization of synthesized Bi_2O_3

The morphological differences of the synthesized powders and prepared samples were investigated using SEM. In Fig. 1(a), the bulk Bi_2O_3 powder typically showed agglomeration of irregular and semi-spherical particles with size of 10 μm [19]. The benefit of ball milling is its ability to reduce particle size without changing the particle's shape by optimizing the milling time, ball-to-material ratio and milling speed [20]. Since Bi_2O_3 is a highly brittle metal oxide and significantly susceptible to particle breakage, the ball milling conditions were optimized to obtain particles with minimal sizes (830 ±30 nm) [14]. Synthesized BM-MP1.2 showed smaller microsized particles stacked closely together (Fig. 1(b)), whereas BM-NP0.8 powder showed agglomeration of Bi_2O_3 nanoparticles during 6-h of ball milling as expected (Fig. 1(c)), due to Brownian motion (the particles collide and re-stack together) [21]. This indicated that the threshold milling condition for nanoparticle synthesis of Bi_2O_3 was 350 r/min with 6-h grinding time. Further milling provided no benefit to the particle size reduction hence, the BM method can only provide particle size reduction (to extend) and no structural transformation. Fig. 1(d and e) illustrated the morphological variations of hydrothermally synthesized Bi_2O_3 via the two heating times. During the hydrothermal process, the hydrolysis reaction would occur when Bi_2O_3 dissolved in an acid solution, and a $Bi(SO_4)_n^{3-2n}$ complex (n = 1–6) was formed by Bi^{3+} reaction with SO_4^{2-}. On the other hand, $K(H_2O)_n^+$ clusters (n = 1–6) were formed in solution by hydrogen bonds. The crystallization of bismuthal species was generated to construct the nanostructures [15]. For example, when n = 1, the chemical equation of the hydrolysis reaction is shown as below:

$$Bi_2O_3 + 2K_2SO_4 + H_2O + 6H^+ \rightleftharpoons 4K(H_2O)^+ + 2Bi(SO_4)^-$$

The as-synthesis HT-MW1.3 in Fig. 1(d) showed wire-like microstructures with a length of approximately 1.08 μm (± 0.10 μm) as confirmed with TEM (Fig. S3). After 24-h heating treatment, HT-NF0.4 (Fig. 1(e)) was completely transformed to flower-shaped nanostructures with a particle size of 388 nm (±30 nm) (Fig. S2). The HT method is able to produce nanosized products (< 800 nm) from the microsized Bi_2O_3. TEM images of each sample showed good agreement with the SEM images (noted: as HT-NF0.4 appeared as packed nanoflower shapes in SEM, agglomeration of flower-shaped appearances is observed in Fig. S3(d)).

Table 1
Shapes, particle sizes and surface-to-volume ratios (SAVR) of synthesized Bi_2O_3 samples via BM and HT methods.

Method	Sample name	Shape	Particle size (μm)	SAVR (μm^{-1})
BM	BM-MP1.2	Particle (micro)	1.21 ± 0.14	4.99±1.13
	BM-NP0.8	Particle (nano)	0.83 ± 0.03	12.85±2.14
HT	HT-MW1.3	Wires (micro)	1.30 ± 0.13	20.47±4.62
	HT-NF0.4	Flowers (nano)	0.40 ± 0.02	22.07±2.36

3.2. XRD analysis of synthesized Bi_2O_3

Fig. 2 showed XRD patterns of bulk Bi_2O_3 (control) and the obtained samples after BM and HT synthesis, respectively. Bulk Bi_2O_3 was composed of α(monoclinic)-Bi_2O_3, where three main peaks were observed at 2θ = 27.95°, 33.71° and 46.86° corresponding to (120), (200) and (041) reflection, respectively, with several minor peaks indicated in Fig. 2 [22]. The intensity of (120) and (200) reflections in BM-MP1.2 decreased sharply with the disappearance of (041) reflection, due to microparticles breakage (showed in Fig. 2) occurred by increasing the milling time after 3 h Bi_2O_3 is mostly susceptible to particle breakage under the effect of mechanical force, and the prolonged ball-milling resulted in agglomeration due to interparticle interactions with a longer ball milling time, which largely impacted on the crystallite size of Bi_2O_3 [23]. Based on XRD peak broadening, the crystallite size (t) can be calculated using Debye-Scherrer equation (3) [24],

$$t = 0.9\,\lambda / \beta_{hkl} \cos\theta_{hkl} \quad (3)$$

where t is crystallite size (nm) of (hkl) phase, λ is X-ray wavelength of radiation for Cu Kα, β_{hkl} is full-width at the half maximum (FWHM) at (hkl) peak in radian and θ_{hkl} is diffraction angle of (hkl) phase.

The increase of crystallite size of (120) reflection (t_{120}) of BM-NP0.8 (47.07 nm) from 8.08 nm of BM-MP1.2 resulted in an increase of intensity of the peak at 27.95°, due to the agglomeration of the nanoparticles changing the surface area and crystallite lattice [23]. All three peaks of the as-synthesized HT-MW1.3 and bulk Bi_2O_3 are in good agreement, indicating that it is α-Bi_2O_3 wires with increasing t_{120} (63.17 nm). The HT synthesized Bi_2O_3 wires are of high crystallinity and have well-controlled morphology [25]. Increasing the hydrothermal reaction time (24 h) had a significant impact on the crystal structure of the material. A decrease intensity of the (120) and (200) reflections with the disappearance of the (041) reflection in HT-NF0.4 reflection corresponded to a broadening peak [26].

3.3. Characterization of synthesized Bi_2O_3 films

Fig. 3 showed the top-sectional SEM images of the bulk Bi_2O_3 and four synthesized Bi_2O_3 films. The bulk Bi_2O_3 film represented a smooth-surface appearance with randomly stacked and well-dispersed particles as illustrated in Fig. 3(a). The BM-NP0.8 film provided much denser coverage of the surface structure compared to the BM-MP1.2 film (Fig. 3 (b and c)), due to particle size reduction via the BM process. From Fig. 3 (d and e), HT-MW1.3 was intensely packed with irregular wire-breakage debris, while HT-NF0.4 exhibited a nanoflower-like and randomly

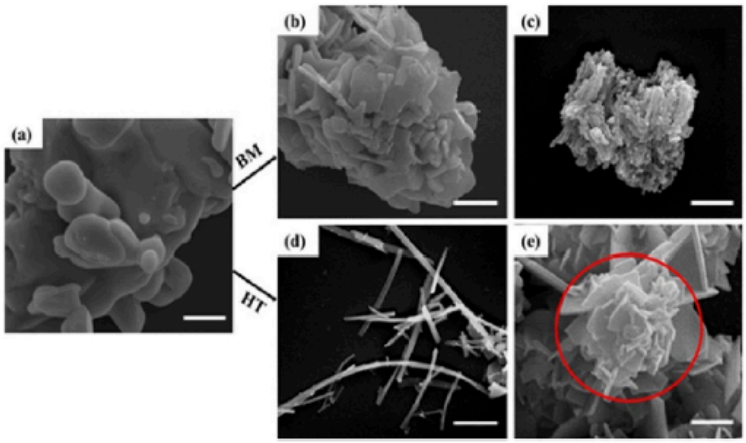

Fig. 1. SEM images of (a) bulk Bi_2O_3 (10 μm), (b–c) BM-MP1.2, BM-NP0.8, and (d–e) HT-MW1.3 (scale bar = 1 μm), HT-NF0.4 (scale bar = 500 nm) (red circle in (e) is the individual flower-shape structure) in their powdered from after synthesis (BM and HT). (For interpretation of the references to colour in this figure legend, the reader is referred to the Web version of this article.)

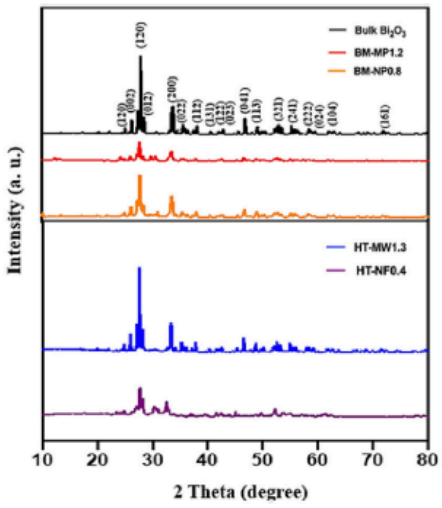

Fig. 2. XRD patterns of bulk Bi_2O_3, BM-MP1.2, BM-NP0.8, HT-MW1.3 and HT-NF0.4.

stacked surface. Noticeably, the morphology of each prepared film remained largely the same as their powdered form but only their particle sizes decreased, due to the effect of bath sonication. EDS analysis showed that the presence of Na in the spectrum resulted from the preparation procedure for the commercial Bi_2O_3 production which required heating alkali-metal (e.g. sodium) hydroxides [27] and there were no presence of impurities on all prepared films via both BM and HT methods compared to the bulk Bi_2O_3 film (Fig. 3(f)). Typical peak elements were detected as 2.08, 2.42 and 2.54 KeV for Bi, 1.06 KeV for Na and 0.53 KeV for O, as expected.

3.4. X-ray transmission characterization

The X-ray transmission testing of each film was conducted using three different peak energies at 30, 50 and 80 kVp which had effective energies of 14, 24 and 29 keV, respectively [28]. The overall trend was observed that by increasing X-ray energies from 14 to 29 keV, there was a decrease in X-ray transmission of each sample (Fig. 4). For example, comparison between micro and nano particles produced using BM method, the differences of X-ray transmission between BM-MP1.2 and BM-NP0.8 were less than 3.30%. However, comparison between microwires and nanoflowers synthesized by HT process, HT-NF0.4 had approximately 10% lower X-ray transmission (11.20–53.51%) than HT-MW1.3 (20.91–61.43%) at all three energies. Moreover, HT-NF0.4 showed its lowest transmission among all samples, indicating synergy effects of both morphological differences with particle size reduction had significant impacts on X-ray attenuation, when the same Bi_2O_3 mass loading was provided.

Fig. 5 presented a graph showing enhancement rates of X-ray attenuation of all prepared films compared with bulk Bi_2O_3. Further increasing the X-ray energy from 14 to 29 keV showed a reduced improvement for all synthesized samples. For example, at the low energy of 14 keV, significant increases of enhancement of each sample compared to bulk Bi_2O_3 showed that 13.29 % for BM-MP1.2 (microparticles), 24.83 % for BM-NP0.8 (nanoparticles), 26.92 % for HT-MW1.3 (microwires) and 60.49% for HT-NF0.4 (nanoflowers). It is noticeable that X-ray attenuation improvement of BM-NP0.8 was almost double than BM-MP1.2, since nanoparticles provided more homogenous and less agglomerated coverage but less cracking films, which can be seen in SEM mage of Fig. 3(c). On the other hand, HT-NF0.4 provided more than double X-ray attenuation improvement than HT-MW1.3, indicating that nanoflowers with its lowest particle size (388 ±30 nm) and largest SAVR (22.07± 2.36 $m^{-1}\mu$) benefited the surface absorption than microwires (20.47± 4.62 $m^{-1}\mu$), which elevated the photon-to-electron conversion efficiency, especially at low X-ray energies [28]. It is proved that structural variation with particle size reduction should be both evaluated significantly when designing a X-ray shielding material.

Fig. 6 presented compares the enhancement rates of each sample based on different shapes and particle sizes at three X-ray energies (14, 24 and 29 keV). Comparison between particle size reduction from micro to nano level, improvement of X-ray attenuation of microparticles (BM-MP1.2, 1.21 ± 0.14 μm) towards bulk Bi_2O_3 (10 μm) was almost equal to the enhancement between microparticles and nanoparticles (BM-NP0.8, 830 ±30 nm), which provided the lowest improvement of X-ray attenuation performance among all. Moreover, it is interesting to notice that both BM-MP1.2 and HT-MW1.3 had approximately a similar range of

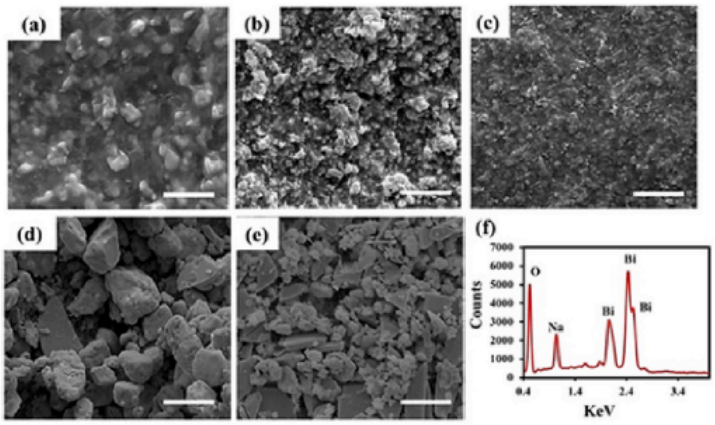

Fig. 3. SEM images of the prepared films: (a–f) top-section (scale bar = 5 μm) of (a) bulk Bi_2O_3 (10 μm), (b-c) BM- MP1.2, BM-NP0.8, and (d-e) HT-MW1.2 and HT-NF0.4. Fig. 3(f) is the EDX analysis of bulk Bi_2O_3 (a).

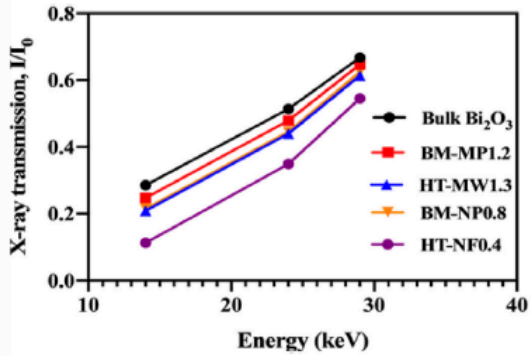

Fig. 4. X-ray transmission of bulk Bi_2O_3, BM- MP1.2, HT-MW1.3, BM-NP0.8 and HT-NF0.4 (experimental data is extremely reproducible with a standard deviation ± 0.001).

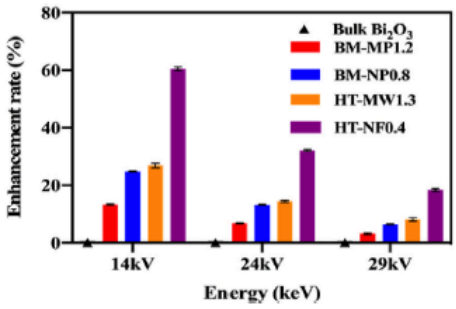

Fig. 5. Enhancement rate of BM-MP1.2, BM-NP0.8, HT-MW1.3 and HT-NF0.4 compared to bulk Bi_2O_3.

particle sizes (1.21 ± 0.14 μm and 1.30 ± 0.14 μm, respectively), but X-ray attenuation performance of microwires (HT-MW1.3) was able to improve up to 15.68 % compared to microparticles (BM-MP1.2) at 14 keV. This is due to the fact that photoelectric effect (one of three energy-

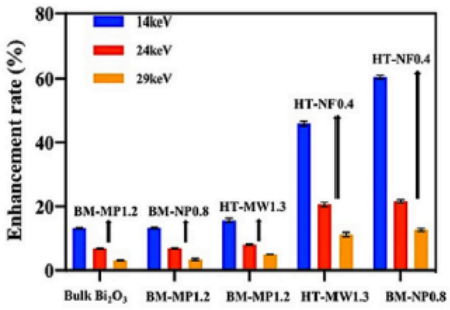

Fig. 6. Enhancement rate of each sample compared based on different shapes and particle sizes at three X-ray energies (14, 24 and 29 keV).

dissipative mechanism for X-ray attenuation) is predominant at the low energies (less than 200 keV) when X-ray interacts with the shielding materials [4]. Moreover, Compton scattering is independent of X-ray energy and Z, which is dominant when the energy is increasing above 100 keV, and pair production only occurs when the energy is above 611 keV. Thus, both of these two effects are not considered in this study of the energy range (less than 30 keV) [7,29]. Wire-shape structures can be applied to photoconverter, which has a great impact on photon-to-electron conversion efficiency due to its high SAVR (20.47± 4.62 $m^{-1}\mu$) [30]. This finding proves that structural differences have a greater impact on low energy of X-ray attenuation than size reduction. Comparison between different shapes (particle, wires and flowers) with particle size reduction (from micro to nano), nanoflowers (HT-NF0.4) provided the greatest X-ray attenuation enhancement (45.99–11.20 % and 60.49–12.69 %, respectively) towards microwires (HT-MW1.3) and nanoparticles (BM-NP0.8). Since the nanoflower structures have the highest SAVR compared to all prepared samples, this enhances the surface absorption and increases the efficiency of photon-to-electron conversion, and thus is beneficial for the X-ray energy attenuation [31].

3.5. *Mass attenuation coefficient analysis*

Mass attenuation coefficient (MAC) is used to evaluate the X-ray attenuation ability of the absorbing materials [32]. Further investigations were conducted to compare between theoretical MAC of

Bi_2O_3 from XCOM database and the calculated MACs (μ_m) of each sample from the experimental data, including X-ray transmission of each film, their thicknesses (μm) obtained from SEM (shown in Fig. S4) and their densities (g/cm^3) calculated using equation (4) (data shown in table S1),

$$\rho = m/V \quad (4)$$

where m is the weight of the Bi_2O_3 films (g), and V is the volume of the sample (cm^3). The calculated MACs of Bi_2O_3 samples correlated to three different energies (shown in Table 2) were determined using equation (2) in section 2.2.6.

The porosities (%) of each synthesized Bi_2O_3 film is another important parameter when preparing the Bi_2O_3 films for X-ray attenuation measurement (shown in Table S1), and it can be determined using equation (5) [33],

$$\text{Porosity (\%)} = (1 - D_B / D_T) \times 100 \quad (5)$$

where D_B represents the bulk density of Bi_2O_3 (1.05 g/cm^3), and D_T is the true density of the synthesized Bi_2O_3 films.

Fig. 7 showed that there was a good agreement between the theoretical and experimental MAC related to bulk Bi_2O_3, especially at 24 and 29 keV. Compared to BM-MP1.2, BM-NP0.8 showed higher MACs as the X-ray energy increased (Table 2). A distinct difference in the porosities (Table S1) between BM-MP1.2 (47.24%) and BM-NP0.8 (37.13%) showed that low porosity resulted in increased MACs, due to less agglomeration occurring in nanoparticles [34]. While BM-MW1.3 can achieve the same MACs (128.35, 67.31 and 40.02 cm^2/g, respectively) with the BM-NP0.8 at three energies, which is higher than theoretical MAC obtained from XCOM. Overall, HT-NF0.4 with the lowest porosity (36.75%) showed the greatest X-ray attenuation with a significate increase of MACs compared to the data from XCOM, thus indicating that porosity is an important factor when preparing the X-ray shielding materials. The previous evidence proves that SAVR plays another key role in improving the properties of nanomaterials, such as increasing reaction efficiency and surface absorption, which is calculated based on the distinct geometrical shapes such as nano-cubes, cylinders and spheres [35].

This study emphasizes the importance that the morphological transformation from wire-like (1.30 ± 0.13 μm) to flower-like (830 ± 30 nm) structures can have positive effects on the enhancement of X-ray attenuation. Importantly to note, the calculation based on XCOM database is limited as it can only simulate the ideal situation of the regular distribution in materials with standardized geometry, such as cubic and spherical structures.

4. Conclusion

This work presents an insight study on influence of Bi_2O_3 particle size and morphological variations. Nanoflower Bi_2O_3 film (HT-NF0.4) provided the most significant X-ray attenuation performance compared to all prepared samples, indicating the synergy effects of both particle size and morphologies impact on low energies (14–29 keV) of X-ray attenuation. Comparison between different shapes with particle size variations indicated that the smaller particle-size (nanoparticles), higher SARV and lower porosity (nanoflowers) provided more effective X-ray attenuation, which should be taken into account when designing Pb-alternative protection garments. However, more studies are needed to optimize nanoparticle size and shape related to their production costs, scalability and the durability of Bi_2O_3 films. Moreover, the differences occurring between the data calculated from XCOM database and measured from the experiments showed the limitation of simulation as it can only calculate the ideal condition of the regular distributions in materials with standardized geometry. Advanced simulation such as a Monte Carlo would be a great approach to identify the possible variations.

Table 2
Mass Attenuation Coefficient (MAC) at different X-ray energies for the five synthesized Bi_2O_3 samples.

Film	MAC (cm^2/g)		
	14 kV	24 kV	29 kV
Bulk Bi_2O_3	107.92	57.43	34.83
BM-MP1.2	108.91	57.58	34.01
BM-NP0.8	128.35	67.31	40.02
HT-MW1.3	128.10	67.32	39.22
HT-NF0.4	165.23	79.79	46.07

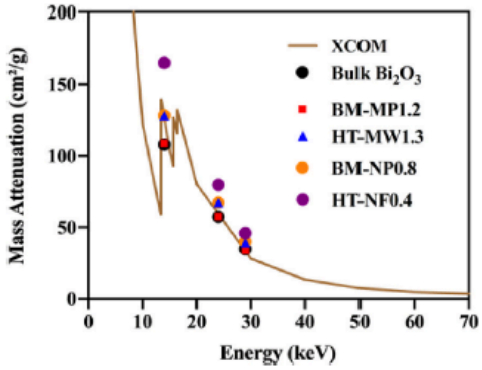

Fig. 7. Mass Attenuation Coefficient of bulk Bi_2O_3 obtained from XCOM, compared to the values of each experimental sample (obtained from their transmission measurements).

CRediT authorship contribution statement

Le Yu: performed all experiments, Data curation, most data processing, wrote paper. **Ana L.C. Pereira:** modeling study, input in final paper. **Diana N.H. Tran:** Writing - review & editing, review paper. **Alexandre M.C. Santos:** design x-ray experiment, Writing - review & editing, review paper. **Dusan Losic:** Conceptualization, design materials design and concept, review and submit paper.

Declaration of competing interest

The authors declare that they have no known competing financial interests or personal relationships that could have appeared to influence the work reported in this paper.

Acknowledgements

The authors acknowledge the financial support from the ARC Research Hub for Graphene Enabled Industry Transformation, (IH150100003). We thank Australian Microscopy and Microanalysis Research Facility (AMMRF) for the access of SEM and TEM facilities, Mr. Ken Neubauer and Dr. Ashley Slattery for their technical support on SEM and TEM measurements. This work was also supported in part by the São Paulo Research Foundation (FAPESP) under grant# 2018/15842–0.

Appendix A. Supplementary data

Supplementary data to this article can be found online at https://doi.org/10.1016/j.matchemphys.2020.124084.

References

[1] R. Li, Y. Gu, Y. Wang, Z. Yang, M. Li, Z. Zhang, Effect of particle size on gamma radiation shielding property of gadolinium oxide dispersed epoxy resin matrix composite, Mater. Res. Express (2017) 4.

[2] S.A. Hashemi, S.M. Mousavi, R. Faghihi, M. Arjmand, S. Sina, A.M. Amani, Lead oxide-decorated graphene oxide/epoxy composite towards X-Ray radiation shielding, Radiat. Phys. Chem. 146 (2018) 77–85.

[3] H.O. Tekin, V.P. Singh, T. Manici, Effects of micro-sized and nano-sized WO_3 on mass attenauation coefficients of concrete by using MCNPX code, Appl. Radiat. Isot. 121 (2017) 122–125.

[4] I.M. Low, N.Z. Noor Azman, Polymer Composites and Nanocomposites for X-Rays Shielding, 2020.

[5] L. Chang, Y. Zhang, Y. Liu, J. Fang, W. Luan, X. Yang, W. Zhang, Preparation and characterization of tungsten/epoxy composites for γ-rays radiation shielding, Nucl. Instrum. Methods Phys. Res. Sect. B Beam Interact. Mater. Atoms 356–357 (2015) 88–93.

[6] H.A. Maghrabi, A. Vijayan, P. Deb, L. Wang, Bismuth oxide-coated fabrics for X-ray shielding, Textil. Res. J. 86 (2015) 649–658.

[7] N.Z. Noor Azman, S.A. Siddiqui, H.J. Haroosh, H.M. Albetran, B. Johannesen, Y. Dong, I.M. Low, Characteristics of X-ray attenuation in electrospun bismuth oxide/polylactic acid nanofibre mats, J. Synchrotron Radiat. 20 (2013) 741–748.

[8] R. Kunzel, E. Okuno, Effects of the particle sizes and concentrations on the X-ray absorption by CuO compounds, Appl. Radiat. Isot. 70 (2012) 781–784.

[9] L.B.T. La, C. Leatherday, Y.-K. Leong, H.P. Watts, L.-C. Zhang, Green lightweight lead-free Gd_2O_3/epoxy nanocomposites with outstanding X-ray attenuation performance, Compos. Sci. Technol. 163 (2018) 89–95.

[10] B.M. Abunahel, I.S. Mustafa, N.Z. Noor Azman, Characteristics of X-ray attenuation in nano-sized bismuth oxide/epoxy-polyvinyl alcohol (PVA) matrix composites, Appl. Phys. A (2018) 124.

[11] P.I. Kattan, Ratio of Surface Area to Volume in Nanotechnology and Nanoscience Petra Books, Canada, 2011.

[12] L.B. Kong, Z. W, O.K. Tan, Preparation and characterization of $PbZr_{0.52}Ti_{0.48}/O_3$ ceramics from high-energy ball milling powders, Mater. Lett. 42 (2000) 232–239.

[13] L. Yu, Diana N.H. Tran, P. Forward, M.F. Lambert, D. Losic, The hydrothermal processing of iron oxides from bacterial biofilm waste as new nanomaterials for broad applications, RSC Adv. 8 (2018) 34848–34852.

[14] M. Xia, Q. Yao, H. Yang, T. Guo, X. Du, Y. Zhang, G. Li, Y. Luo, Preparation of Bi_2O_3/Al core-shell energetic composite by two-step ball milling method and its application in solid propellant, Materials (2019) 12.

[15] L. Liu, J. Jiang, S. Jin, Z. Xia, M. Tang, Hydrothermal synthesis of β-bismuth oxide nanowires from particles, CrystEngComm 13 (2011).

[16] APRANSA, Aprons for Protection against X-Rays, 2015.

[17] B.O. Elbashir, M.G. Dong, M.I. Sayyed, S.A.M. Issa, K.A. Matori, M.H.M. Zaid, Comparison of Monte Carlo simulation of gamma ray attenuation coefficients of amino acids with XCOM program and experimental data, Results in Physics 9 (2018) 6–11.

[18] N. Demir, U.A. Tarim, M.-A. Popovici, Z.N. Demirci, O. Gurler, I. Akkurt, Investigation of mass attenuation coefficients of water, concrete and bakelite at different energies using the FLUKA Monte Carlo code, J. Radioanal. Nucl. Chem. 298 (2013) 1303–1307.

[19] S. Labib, Preparation, characterization and photocatalytic properties of doped and undoped Bi2O3, Journal of Saudi Chemical Society 21 (2017) 664–672.

[20] K. Shoji, S. Lohrasb, L.G. Austin, The variation of breakage parameters with ball and powder loading in dry ball milling, Powder Technol. 25 (1980) 109–114.

[21] V.-I. Merupo, S. Velumani, K. Ordon, N. Errien, J. Szade, A.-H. Kassiba, Structural and optical characterization of ball-milled copper-doped bismuth vanadium oxide (BiVO4), CrystEngComm 17 (2015) 3366–3375.

[22] R. Irmawati, M.N. Noorfarizan Nasriah, Y.H. Taufiq-Yap, S.B. Abdul Hamid, Characterization of bismuth oxide catalysts prepared from bismuth trinitrate pentahydrate: influence of bismuth concentration, Catal. Today 93–95 (2004) 701–709.

[23] P.L. Guzzo, A.A.A. Tino, J.B. Santos, The onset of particle agglomeration during the dry ultrafine grinding of limestone in a planetary ball mill, Powder Technol. 284 (2015) 122–129.

[24] M.M. Patil, V.V. Deshpande, S.R. Dhage, V. Ravi, Synthesis of bismuth oxide nanoparticles at 100 °C, Mater. Lett. 59 (2005) 2523–2525.

[25] Y. Qiu, D. Liu, J. Yang, S. Yang, Controlled synthesis of bismuth oxide nanowires by an oxidative metal vapor transport deposition technique, Adv. Mater. 18 (2006) 2604–2608.

[26] L. Zhang, Y. Hashimoto, T. Taishi, I. Nakamura, Q.-Q. Ni, Fabrication of flower-shaped Bi2O3 superstructure by a facile template-free process, Appl. Surf. Sci. 257 (2011) 6577–6582.

[27] R. Rajagopal, J. Mona, R.S. Joshee, S.N. Kale, S. Pradhan, A.B. Gaikwad, V. Ravi, La0.67Ce0.03Sr0.3MnO3-coupled microwave assisted ultra-fast synthesis of nanocrystalline Cobalt oxide and Bismuth oxide, Mater. Lett. 62 (2008) 1511–1513.

[28] A.M.C. Santos, M. Mohammadi, S. Afshar V, Energy dependency of a water-equivalent fibre-coupled beryllium oxide (BeO) dosimetry system, Radiat. Meas. 73 (2015) 1–6.

[29] L. Cerrito, Radiation and Detectors, first ed., Springer, 2017.

[30] H. Zarei, S. Saramad, S. Razaghi, Testing CuO nanowires as a novel X-ray to electron converter for gas-filled radiation detectors, J. Instrum. 12 (2017). P10006-P10006.

[31] P. Shende, P. Kasture, R.S. Gaud, Nanoflowers: the future trend of nanotechnology for multi-applications, Artif Cells Nanomed Biotechnol 46 (2018) 413–422.

[32] S.H. Hosseini, S. Noushin Ezzati, M. Askari, Synthesis, characterization and X-ray shielding properties of polypyrrole/lead nanocomposites, Polym. Adv. Technol. 26 (2015) 561–568.

[33] S.-C. Kim, S.-H. Cho, Analysis of the correlation between shielding material blending characteristics and porosity for radiation shielding films, Appl. Sci. 9 (2019).

[34] M.H. Hazlan, M. Jamil, R.M. Ramli, N.Z. Noor Azman, X-ray attenuation characterisation of electrospun Bi2O3/PVA and WO3/PVA nanofibre mats as potential X-ray shielding materials, Appl. Phys. A 124 (2018).

[35] P.I. Kattan, Ratio of Surface Are to Volume in Nanotechnology and Nanoscience, Petra books, 2011.

Supporting Information

Bismuth Oxide Films for X-ray Shielding: Effects of and Particle Size and Structural Morphology

Le Yu,[a,b] Ana L. C. Pereira,[a,b,c] Diana N. H. Tran,[a,b] Alexandre M. C. Santos,[d,e] Dusan Losic[a,b*]

[a] School of Chemical Engineering and Advanced Materials, University of Adelaide, Adelaide, SA 5005, Australia.

[b] ARC Research Hub for Graphene Enabled Industry Transformation, University of Adelaide, Adelaide, SA 5005, Australia.

[c] School of Applied Sciences, University of Campinas (UNICAMP), Limeira, 13484-350, Brazil.

[d] School of Physical Sciences, University of Adelaide, Adelaide, South Australia 5005, Australia.

[e] Department of Medical Physics, Royal Adelaide Hospital, Adelaide, South Australia 5000, Australia.

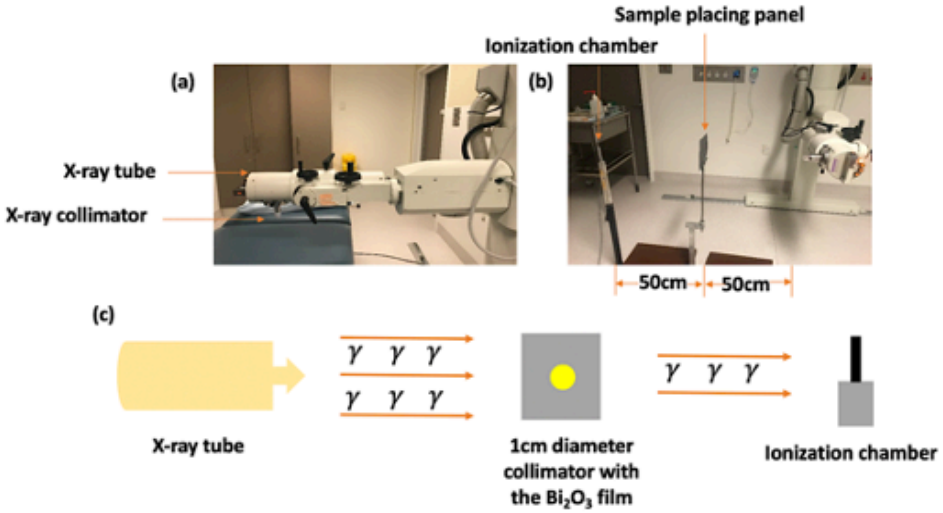

Fig. S1 Schematic illustration of (a) superficial X-ray unit and (b, c) experimental set-up of X-ray transmission testing

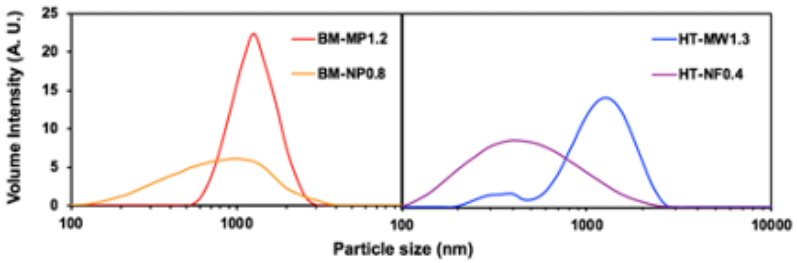

Fig. S2 PSD analysis of BM-MP1.2, BM-NP0.8, HT-MW1.3 and HT-NF0.4

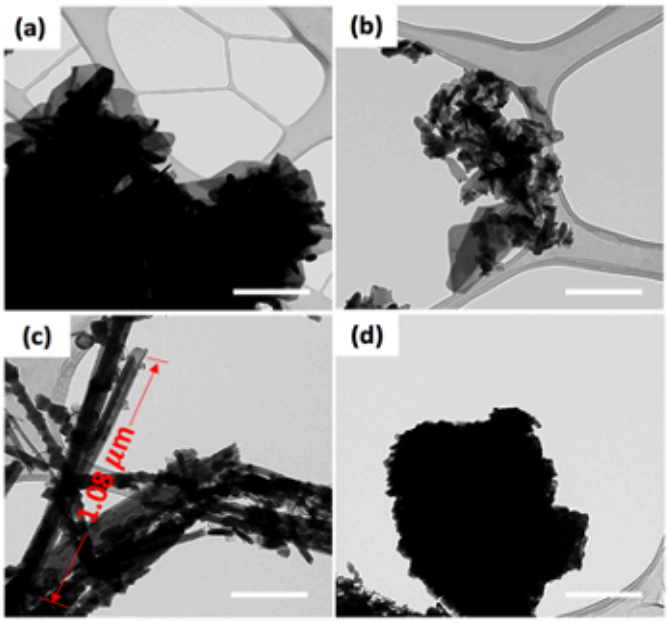

Fig. S3 TEM images of (a-b) BM-MP1.2, BM-NP0.8, and (c-d) HT-MW1.3, and HT-NF0.4 (scale bar = 200 nm)

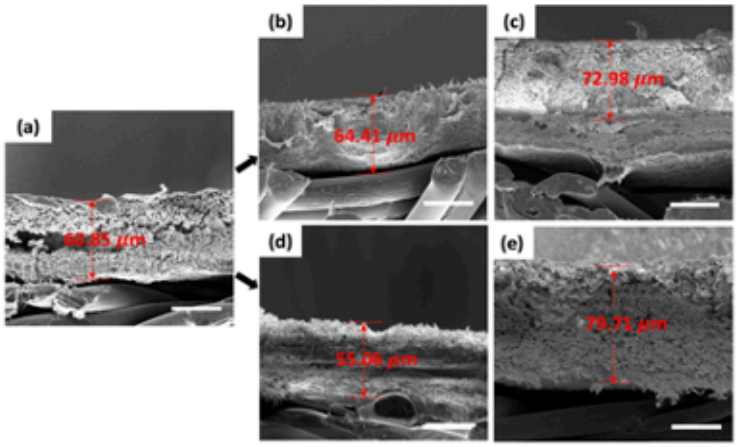

Fig. S4 SEM images on the different thicknesses of (a) bulk Bi_2O_3, (b-c) BM-MP1.2, BM-NP0.8, and (d-e) HT-MW1.3 and HT-NF0.4 (scale bar = 100 μm)

Table S1 Thickness and density of the five synthesized Bi_2O_3 samples

Sample name	Thickness (t) (μm)	Density (ρ) (g/cm^3)	$\rho \times t$ (g/cm^2)	Porosity (%)
Bulk Bi_2O_3	60.85 ± 1.93	1.90 ± 0.09	0.011	44.74 ± 2.14
BM-MP1.2	64.41 ± 2.50	1.99 ± 0.11	0.013	47.24 ± 1.30
BM-NP0.8	72.98 ± 2.95	1.67 ± 0.06	0.012	37.13 ± 1.74
HT-MW1.3	55.06 ± 1.92	2.18 ± 0.07	0.012	51.83 ± 1.26
HT-NF0.4	79.71 ± 1.84	1.66 ± 0.08	0.013	36.75 ± 2.16

Statement of Authorship

Title of Paper	Lightweight bismuth titanate ($Bi_4Ti_3O_{12}$) nanoparticles-epoxy composite for advanced lead-free X-ray radiation shielding
Publication Status	☑ Published ☐ Accepted for Publication ☐ Submitted for Publication ☐ Unpublished and Unsubmitted work written in manuscript style
Publication Details	Yu, L., Yap, P. L., Santos, A., Tran, D., & Losic, D. (2021). Lightweight bismuth titanate ($Bi_4Ti_3O_{12}$) nanoparticle-epoxy composite for advanced lead-free X-ray radiation shielding. *ACS Applied Nano Materials*, 4(7), 7471-7478.

Principal Author

Name of Principal Author (Candidate)	Le Yu		
Contribution to the Paper	Prepared and characterized on all the samples, and interpreted all the data as well as wrote the manuscript.		
Overall percentage (%)	85 %		
Certification:	This paper reports on original research I conducted during the period of my Higher Degree by Research candidature and is not subject to any obligations or contractual agreements with a third party that would constrain its inclusion in this thesis. I am the primary author of this paper.		
Signature		Date	03/03/2022

Co-Author Contributions

By signing the Statement of Authorship, each author certifies that:

i. the candidate's stated contribution to the publication is accurate (as detailed above);

ii. permission is granted for the candidate in include the publication in the thesis; and

iii. the sum of all co-author contributions is equal to 100% less the candidate's stated contribution.

Name of Co-Author	Pei Lay Yap		
Contribution to the Paper	Edited and revised the manuscript.		
Signature		Date	03/03/2022

Name of Co-Author	Alexandre M. C. Santos		
Contribution to the Paper	Co-supervised, performed X-ray irradiations and revised the manuscript.		
Signature		Date	03/03/2022

Please cut and paste additional co-author p

Statement of Authorship

Title of Paper	Lightweight bismuth titanate ($Bi_4Ti_3O_{12}$) nanoparticles-epoxy composite for advanced lead-free X-ray radiation shielding
Publication Status	☑ Published ☐ Accepted for Publication ☐ Submitted for Publication ☐ Unpublished and Unsubmitted w ork w ritten in manuscript style
Publication Details	Yu, L., Yap, P. L., Santos, A., Tran, D., & Losic, D. (2021). Lightweight bismuth titanate ($Bi_4Ti_3O_{12}$) nanoparticle-epoxy composite for advanced lead-free X-ray radiation shielding. *ACS Applied Nano Materials, 4*(7), 7471-7478.

Principal Author

Name of Principal Author (Candidate)	Le Yu		
Contribution to the Paper	Prepared and characterized on all the samples, and interpreted all the data as well as wrote the manuscript.		
Overall percentage (%)	85 %		
Certification:	This paper reports on original research I conducted during the period of my Higher Degree by Research candidature and is not subject to any obligations or contractual agreements with a third party that would constrain its inclusion in this thesis. I am the primary author of this paper.		
Signature		Date	03/03/2022

Co-Author Contributions

By signing the Statement of Authorship, each author certifies that:

i. the candidate's stated contribution to the publication is accurate (as detailed above);

ii. permission is granted for the candidate in include the publication in the thesis; and

iii. the sum of all co-author contributions is equal to 100% less the candidate's stated contribution.

Name of Co-Author	Diana N. H. Tran		
Contribution to the Paper	Co-supervised and revised the manuscript.		
Signature		Date	03/03/2022

Name of Co-Author	Dusan Losic		
Contribution to the Paper	Supervised the development of the work, edited, revised the manuscript and acted as the corresponding author.		
Signature		Date	03/03/2022

Please cut and paste additional co-author panels here as required.

ACS APPLIED NANO MATERIALS

www.acsanm.org Article

Lightweight Bismuth Titanate ($Bi_4Ti_3O_{12}$) Nanoparticle-Epoxy Composite for Advanced Lead-Free X-ray Radiation Shielding

Le Yu, Pei Lay Yap, Alexandre Santos, Diana Tran, and Dusan Losic*

Cite This: ACS Appl. Nano Mater. 2021, 4, 7471−7478 Read Online

ACCESS | Metrics & More | Article Recommendations | Supporting Information

ABSTRACT: Constant exposure to ionizing radiation such as X-rays can be hazardous to human health. Conventional lead (Pb)-based shielding materials are limited by their heaviness and toxicity, and thus, it is imperative to explore lightweight, non-Pb, and promising X-ray protection materials. This work demonstrates the synthesis of bismuth titanate (BTO) particles by a ball-milling process to create a new Pb-free shielding composite using BTO particles with different mass loadings (0−65 wt %) mixed in an epoxy resin (ER) matrix. The surface roughness and hardness properties of the developed BTO-ER composites are investigated to understand their X-ray attenuation ability. The X-ray shielding performance of the prepared BTO-ER composites unveils that the BTO-ER composite with a thickness of ∼2 mm achieves the best X-ray attenuation efficiencies of ∼97 and 95% at 80 and 100 kVp, respectively. The shielding ability of the BTO-ER composite (total weight of 2.2 ± 0.1 g) provides a 0.35 mm Pb equivalent attenuation at the same X-ray energy range, with only half of the weight relative to the 0.35 mm Pb sheet (4.19 g). The outcomes highlight a promising potential for the BTO-based material as a Pb-free X-ray protective material to replace the conventional toxic Pb in designing a safe, affordable, and environmentally friendly diagnostic X-ray protection garment, which also complies with international radiation protection standards.

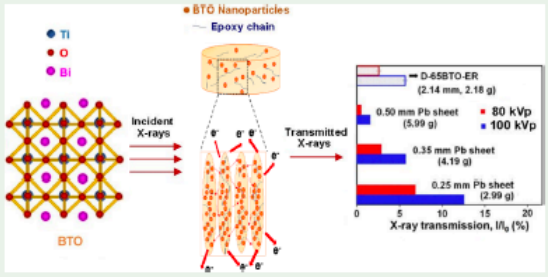

KEYWORDS: *bismuth titanate (BTO), epoxy composite, diagnostic X-ray attenuation, Pb-free shielding material, metal oxide*

1. INTRODUCTION

Effective protection for ionizing radiation, such as X-rays, is highly in demand in the medical field, space, and nuclear industries.[1,2] Since the X-ray shielding ability relies heavily on the density and mass of the absorbing materials, elements with a high atomic number (*Z*) are often utilized for X-ray shielding applications.[1] Lead (Pb) has been renowned as the ideal and conventional material for effective radiation shielding purposes in particular at preventing the penetration of gamma rays and X-rays owing to its high density and high *Z*.[3] Conventional Pb-based shielding materials are made up of Pb powders impregnated with rubber or silicon.[4,5] However, one of the drawbacks about these Pb-based materials is their toxicity and potential to leak due to damages, cracks, and aging of these matrices.[4] It is thus imperative to explore and introduce other less toxic and non-Pb elements with high *Z*, such as bismuth (Bi), tungsten (W), barium (Ba), tin (Sn), cadmium (Cd), gadolinium (Gd), copper (Cu), and titanium (Ti), as Pb alternatives.[6−8] Moreover, most Pb-based shielding materials are bulky and heavy, and the lack of flexibility and lightweight characteristics has hampered their applications in terms of wearable radiation protective garments.[9] Therefore, there is an urgency to create lightweight non-Pb shielding materials with less toxicity to safeguard people from the harmful X-ray radiation.[10] To address these problems, metal oxides containing high-*Z* elements, such as bismuth oxide (Bi_2O_3), tungsten oxide (WO_3), titanium oxide (TiO_2), copper oxide (CuO), and gadolinium oxide (Gd_2O_3), have often been employed for non-Pb radiation shielding applications.[8,11,12] By harnessing the inherent benefits of chemical stability, weight reduction, low cost, and enhanced chemical durability of these metal oxides, a promising radiation protection outcome can be expected to displace the toxic Pb for this application.[13−15]

Formation of a lightweight and Pb-free metal oxide composite is still challenging. Polymers are often used as supporting components benefiting from their flexibility, low manufacturing cost, and strong chemical stability, although they offer negligible contribution toward X-ray attenuation.[16] Nevertheless, the selection of polymers with good thermal and mechanical properties is still critical for the generation of X-ray shielding composites since the radiation heat effects caused by

Received: June 6, 2021
Accepted: June 30, 2021
Published: July 13, 2021

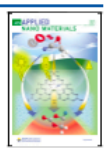

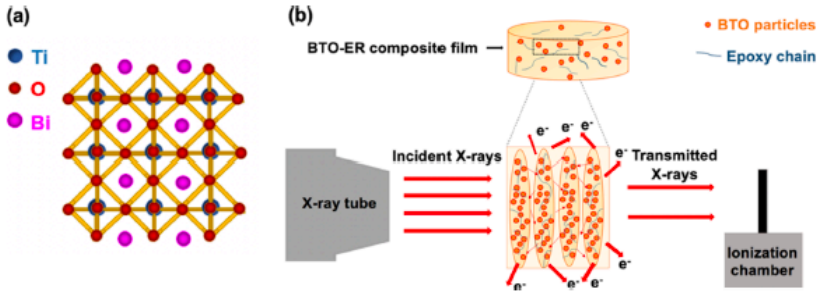

Figure 1. (a) Schematic image of the bismuth titanate structure and (b) schematic illustration of multiple scattering of incoming X-ray photon energy when interacting with the BTO-ER composite film.

the interaction between radiation and the shielding materials can accelerate the aging and cracking of the polymers.[17] For instance, an epoxy polymer is often selected as a supporting matrix for the formation of an effective X-ray shielding composite due to its good thermal stability and its capability to withstand the high energy bombardment caused by X-rays.[4] However, the majority of X-ray shielding composites in the literature are made up of over 50 wt % of polymers only for the supporting purpose.[12,18,19] Higher loading of polymers in the composites may lead to some drawbacks such as increased thickness and potential cracking to the final X-ray shielding composite materials. Therefore, optimizing the weight ratio of the metal oxide and the polymer used in the X-ray shielding composite is required to provide sufficient support for the composite without losing the X-ray attenuation performance.

In addition, to generate a particle-densely packed metal oxide-polymer composite for improved shielding ability, dispersion of these metal-oxide particles and their particle size distribution in the polymer matrix are two important factors to achieve an efficient X-ray protective performance.[20] Recently, the X-ray shielding capacity of the nanoparticle-filled polymer composites has been investigated in transmission mode compared with their microparticle counterparts.[6,21−23] It has been proven that the enhanced X-ray attenuation property can be accredited to the good dispersion and strong affinity of the narrow size range of particles toward their homogeneous distribution in the polymer matrix.[2,7,24−27]

Herein, to address these research gaps and to meet the demand for developing lightweight and Pb-free X-ray shielding materials, a new perovskite-like $Bi_4Ti_3O_{12}$ (BTO) shielding material was engineered by combining two non-hazardous precursors (Bi_2O_3 and TiO_2), which can give rise to effective X-ray shielding ability by harnessing the merits of the binary Bi_2O_3 (high-Z metal compounds)-TiO_2 (enhanced thermal stability and chemical resistance) system.[28] The concept is presented schematically in Figure 1. To achieve thin and highly efficient X-ray shielding materials, BTO particles with narrow sizes were fabricated with a minimal polymer content (only 35 wt % epoxy applied in this work compared to other metal oxide-polymer composites reported so far). The aim of this work is to demonstrate the development of a non-toxic and Pb-free X-ray shielding material using a green, energy-efficient approach for improved X-ray attenuation application. BTO particles were prepared by an optimized ball-milling process (milling duration: 22 h) through mechanically activated synthesis directly from their individual oxide mixture of bulk Bi_2O_3 and TiO_2, which required no additional heating energy and solvents. To demonstrate this concept, epoxy resin (ER) was selected as a lightweight polymer matrix (but this concept is not limited to other polymers).[4] The X-ray attenuation efficiency of the developed BTO-ER composites with different BTO mass loadings (0, 10, 30, 50, and 65 wt %) was investigated with detailed studies performed on their surface roughness and hardness properties. These synthesized BTO-ER composites were then benchmarked with 0.25, 0.35, and 0.5 mm Pb equivalent standard barriers to evaluate their radiation shielding performance (referred to the standard of the International Commission on Radiological Protection).[29−31] This study successfully demonstrated the development of a new lightweight Pb-alternative material through a sustainable and green synthetic approach for X-ray protection application without generation of hazardous side products to the environment.[32]

2. EXPERIMENTAL SECTION

2.1. Materials. Bismuth oxide powder (Bi_2O_3, 99.9%, <4 μm) was provided by Thermo Fisher Scientific (Australia), and titanium oxide powder (TiO_2, 99.9%, <5 μm) in a rutile crystal form was purchased from Aldrich (Australia). Epoxy with two parts (epoxy resin 105 and fast hardener 205) was purchased from West System (Australia). The Pb sheet (0.44 mm, 5 kg) was provided by Midland Lead Australia Pty Ltd. (Australia).

2.2. Synthesis of Bismuth Titanate (BTO) Particles by Ball Milling. BTO particles were prepared from Bi_2O_3 (BO) and TiO_2 (TO) powder by adapting the methodology from a reported work.[33] A predetermined stoichiometric BTO composition, corresponding to the molar ratio of BO and TO powders at 2:3, was added into a zirconium jar together with zirconium grinding balls (3 mm in diameter) at a ball-to-powder weight ratio of 10:1. The milling speed was kept constant at 400 rpm throughout the process with the milling duration varying from 1 to 22 h. After the ball-milling process, the as-prepared samples were recovered by washing with deionized (DI) water and dried at 50 °C overnight for further characterizations and testings.

2.3. Preparation of Bismuth Titanate/Epoxy (BTO-ER) Composites. To fabricate BTO-ER composites, ball-milled BTO powders at different loadings (0, 10, 30, 50, and 65 wt %) were first blended into epoxy resin, followed by mixing with a fast hardener at a mass ratio of 5:1 (epoxy resin to hardener). The mixture was stirred homogeneously for 10 min before casting it into a plastic mold (3.5 cm in diameter) and then left for drying overnight at room temperature (22 ± 2 °C). Samples with different weight percentages of BTO, ER, and their corresponding designations are listed in Table 1.

2.4. Materials Characterization. The synthesized samples were characterized by X-ray diffraction (XRD, Rigaku Miniflex 600, Japan) in a range of 2θ = 10−80° (scan rate of 10° min^{-1}) and Raman spectroscopy (LabRAM HR Evolution, Horiba Jvon Yvon Technol-

https://doi.org/10.1021/acsanm.1c01475
ACS Appl. Nano Mater. 2021, 4, 7471−7478

Table 1. Description of As-Prepared BTO-ER Composites with Different Weight Fractions and Their Corresponding Designations and Mass per Unit Area

composite by weight fraction (wt %)			
bismuth titanate (BTO)	epoxy resin (ER)	composite designation	mass per unit area (g/mm^2)
0	100	ER	0.0012 ± 0.0002
10	90	10BTO-ER	0.0013 ± 0.0002
30	70	30BTO-ER	0.0014 ± 0.0003
50	50	50BTO-ER	0.0022 ± 0.0002
65	35	65BTO-ER	0.0030 ± 0.0003

ogy, Japan) using a 532 nm laser as the excitation source in a range of 50−1000 cm^{-1}. Scanning electron microscopy coupled with energy dispersive X-ray (SEM−EDX, Quanta 450 FEG, FEI, USA; Ultim Max Oxford Instruments, UK) and transmission electron microscopy (TEM, FEI Tecnai G2 Spirit) at accelerating voltages of 10 and 100 kV, respectively, were adopted to study the elemental composition and morphology of the samples. The crystal structure of the obtained BTO sample was further confirmed using a selected area electron diffraction (SAED) technique. Particle size distribution (PSD) was measured using a Zetasizer Nano-ZS (Malvern Analytical Australia, Australia). The top surface roughness was obtained from a 3D optical profilometer (Bruker Contour GT-K, Australia) in vertical scanning interferometry mode with a working distance of 6.7 mm. Shore hardness measurements were performed with a Shore D durometer according to the ASTM D2240 standard.

2.5. X-ray Transmission Performance. X-ray transmission measurements of the controls (air and ER) and as-prepared BTO-ER composite films were determined using a Gulmay D3150 superficial X-ray unit, where the distances between the X-ray tube and the sample holder as well as the sample holder and the detector were both set to 50 cm. The detector used to measure the X-ray transmission was an NE 2571 Farmer-type ionization chamber (Phoenix Dosimetry Ltd., UK). The synthesized BTO-ER composite films with different weight loadings were separately exposed to the X-ray voltage at 80 and 100 kVp (2 and 3 mm Al half value layer) for 0.50 min. X-ray transmission (T) was determined based on eq 1, which can be expressed as the intensity (I) of X-ray after passing through the sample with a thickness (t) compared to the intensity (I_0) of incoming X-ray,[34]

$$T = I/I_0 = e^{-(\mu/\rho)\rho t} \quad (1)$$

where μ/ρ (cm^2/g) is the mass attenuation coefficient of the sample, ρ (g/cm^3) is the density of the sample, and t is the thickness (cm) of the sample.

The density of each BTO-ER composite was calculated using eq 2,

$$\rho = m/V \quad (2)$$

where m (g) is the mass of the sample, and V (cm^3) is the volume of the sample.

2.6. Mass Attenuation Coefficients of the BTO-ER Composites Compared with Pb Sheets. Mass attenuation coefficients (μ/ρ) of the synthesized BTO-ER composites and 0.44 mm Pb sheet were calculated according to eq 3,[35]

$$\mu/\rho = -\ln(T)/\rho t \quad (3)$$

2.7. Benchmarking of Developed Composites with Pb Sheets. X-ray attenuation of pure Pb sheets with different thicknesses (0.25, 0.35, and 0.50 mm) was used as the standard of the International Commission on Radiological Protection,[30,31,36] where Pb equivalence was applied as a term to evaluate the X-ray attenuation performance of the synthesized samples by providing the same X-ray energy conditions.

3. RESULTS AND DISCUSSION

3.1. Characterization of Synthesized BTO Particles. BTO particles were processed directly from their respective metal oxides (TiO_2 and Bi_2O_3) by a mechanochemical process by ball milling, and the optimization of this process was investigated by XRD and Raman analysis through a series of milling times (1−22 h) to monitor the phase evolution of BTO particles. Figure 2a shows the XRD diffractograms of TiO_2 and

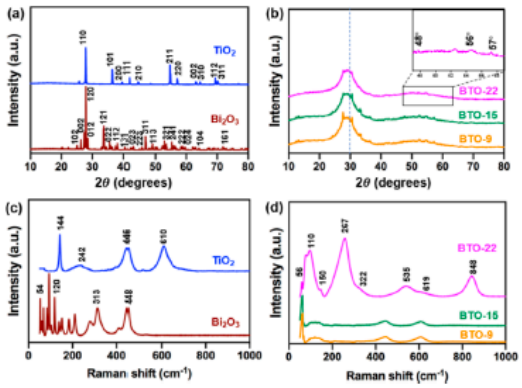

Figure 2. (a, b) XRD profiles and (c, d) Raman spectra of Bi_2O_3, TiO_2 (the precursors), and synthesized BTO particles with different ball-milling times (9, 15, and 22 h), respectively.

Bi_2O_3 (precursors) where the identified peaks (major peaks 2θ = 27°, 36°, and 54°) from TiO_2 can be referenced to the rutile phase,[37] and the peaks (major peak at 2θ = 27°) that arose from Bi_2O_3 confirmed its monoclinic α-phase.[28] Based on the XRD analysis, the individual XRD reflections of the two precursors still remained even after 6 h of ball-milling process (Figure S1). When the milling time was increased to 9 h, all the XRD reflections corresponding to the two precursors diminished significantly alongside the appearance of new and broad peaks, which can be assigned to BTO after 15 h (Figure 2b). Formation of the BTO phase was achieved with a distinguishable amorphous phase obtained when the milling time reached 22 h (Figure 2b). The broadened peaks at 2θ = 30°, 32°, and 39° as well as three new peaks that appeared between 47° and 58° (2θ = 48°, 56°, and 57°) were typical peaks identified for the successful formation of BTO.[33]

Further BTO phase formation was also confirmed by Raman analysis with the presence of peaks at 144, 242, 446, and 610 cm^{-1} representing B_{1g}, two-phonon scattering, E_g, and A_{1g} modes of the rutile TiO_2 phase in Figure 2c, respectively.[37] The strong peaks at 54, 120, 313, and 448 cm^{-1} of Bi_2O_3 were in good agreement with its monoclinic α-phase from the XRD profile.[38] The prepared sample with 22 h of ball milling in Figure 2d showed distinct Raman spectra of the BTO phase compared to the samples at 9 and 15 h milling times, where the sharp mode at 56 cm^{-1} and a peak that arose at 110 cm^{-1} were attributed to the rigid-layer mode and Bi−O vibration, respectively. Raman scattering at 619 and 848 cm^{-1} can be ascribed to the vibration mode in the TiO_6 octahedral phase, while the peak at 535 cm^{-1} represented the opposing excursion of the external apical oxygen of the TiO_6 octahedral phase.[39] Results from both XRD and Raman analysis confirmed the complete formation of the BTO phase optimized with a milling time of 22 h.

https://doi.org/10.1021/acsanm.1c01475
ACS Appl. Nano Mater. 2021, 4, 7471−7478

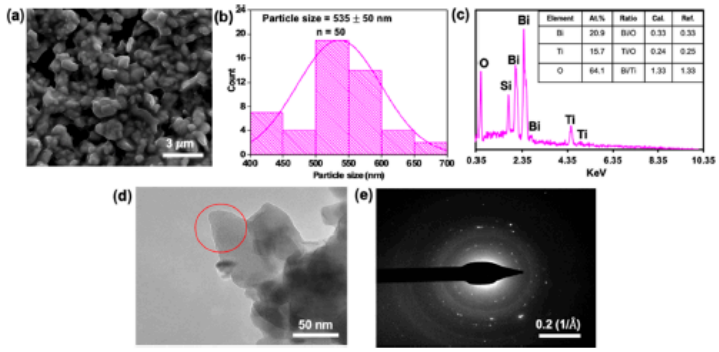

Figure 3. (a) SEM image, (b) PSD based on SEM, (c) EDX analysis, (d) TEM image, and (e) SAED of the synthesized BTO particles.

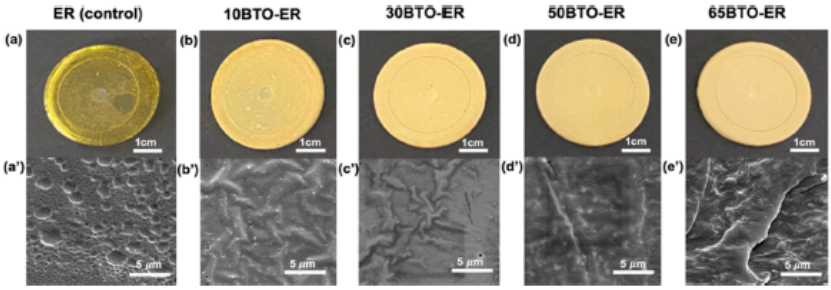

Figure 4. Photographs of (a–e) control epoxy (ER) and synthesized BTO-ER composite films at different loadings of BTO particles including 10BTO-ER, 30BTO-ER, 50BTO-ER, and 65BTO-ER with (a′–e′) their respective SEM images of the top surface.

An SEM image (Figure 3a) of the as-synthesized BTO sample clearly showed the fused irregular structure of BTO particles with agglomeration, which was expected to be resulting from the prolonged ball-milling time (22 h). During the ball-milling process of BTO synthesis, the crystalline coarsening and particle agglomeration are unavoidable because of the interfacial diffusion and reaction, which is common for BTO particles generated from mechanically activated synthesis.[33,40] As per analysis of the SEM structures, the particle size distribution of BTO particles was 535 ±50 nm (Figure 3b), which was in good agreement with the average particle size distribution (475 ± 9 nm) analysis by the dynamic light scattering technique (Figure S4). EDX analysis (Figure 3c) indicated that the characteristic peaks for each element were detected at 2.08, 2.42, and 2.54 keV for bismuth (Bi), 4.51 and 4.96 keV for titanium (Ti), and 0.52 keV for oxygen (O).[41] Silicon was detected (Si, 1.75 keV) due to the use of a silicon wafer during SEM imaging. Meanwhile, the identity of the BTO particles synthesized in a molar ratio of BO to TO at 2:3 was verified with atomic ratios of Bi/O, Ti/O, and Bi/Ti at 0.33, 0.24 and 1.33, respectively. This result (shown as the inset of Figure 3c) was in accord with the atomic ratio of standard BTO powder, supporting the formation of a single phase of BTO as discussed in previous sections.[31,42] Figure 3d showed the TEM image of the synthesized BTO particles, revealing the combination of crystalline particles with the amorphous area as supported by the electron diffraction pattern (Figure 3e) of the synthesized BTO sample containing both diffraction spots (crystalline particles) and halo rings (amorphous phase),[42] which was in good agreement with the XRD study (Figure 2b).

3.2. Characterization of Prepared BTO-ER Composite Films. Figure 4a–e showed the photographs of ER (the control) and four BTO-ER composite films containing 10, 30, 50, and 65 wt % of BTO particles, respectively. Distinguished color changes can be observed on the composite films, from transparent light yellow to opaque yellow with the increment of mass ratios of the BTO particles, showing the increasing hardness from 34.83 ± 1.52 HD (ER) to 84.01 ± 3.60 HD (Figure S2b). SEM images in Figure 3a′–e′ presented the surface structure of the control (ER film) and four as-prepared BTO-ER composite films that varied with different mass loadings. The ER film as depicted in Figure 4a′ showed a morphology similar to a deformed plastic with the presence of micrometer-sized voids on its surface, giving a surface roughness of 1124.58 ± 9.50 nm (Figure S2a).[43] Interestingly, numerous tiny pores and rod-like bubbles were trapped beneath the surface of the 10BTO-ER film (Figure 4b′). This observation could be due to the air trapped within the framework of the film composite during the mixing process. This phenomenon was substantially reduced when the mass loading of BTO particles was increased to 30 wt % (Figure 4c′) with a decreasing surface roughness to 757.52 ± 7.93 nm. One key reason of this morphological change could be related to the successive filling of air sacs within the epoxy polymeric framework by BTO particles.[43] However, BTO particles (white patches) were easily seen to be more uniformly dispersed in the epoxy matrix in the lower mass loading (10–30 wt %) than in the higher mass loading (50–65 wt %). With the increment of BTO particles in the epoxy matrix, the dispersion of the 65BTO-ER film (Figure 3e′) became less uniform with more intense white patches detected on its surface compared to the

https://doi.org/10.1021/acsanm.1c01475
ACS Appl. Nano Mater. 2021, 4, 7471–7478

50BTO-ER film (Figure 3d′) as a result of excessive loading of BTO particles. Compared with others, both surface roughness (1054.46 ± 9.31 nm) and hardness (84.01 ± 3.60 HD) of the 65BTO-ER film became more apparent when BTO particles were increased to 65 wt %, suggesting that the loading threshold was reached. Further observation indicated that no leakage of BTO particles occurred in the 65BTO-ER film due to the strong adhesion between epoxy resin and the hardener, which affixed the BTO powder in the epoxy matrix. Therefore, the maximum mass ratio of the BTO-ER composite was 65:35, which corresponded to the minimal polymer used in this study. However, further kinetic study may need to be conducted for confirmation of the effect on the X-ray shielding property.

3.3. X-ray Transmission Measurement. Figure 5 showed the overall trend of X-ray transmission of the ER (control) and

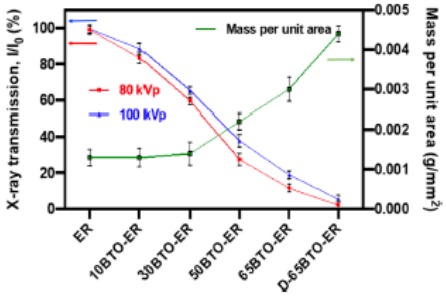

Figure 5. X-ray transmission of ER (control), BTO-ER films with different weight fractions (10, 30, 50, and 65), and the D-65BTO-ER film at 80 and 100 kVp compared with their corresponding mass per unit area.

BTO-ER composite films with different weight fractions compared to their corresponding mass per unit area. A similar trend was observed where an increase in the mass loading of the BTO particles resulted in a decrease in the X-ray transmission (at 80 and 100 kVp). The ER film (control) showed a slight decrease in the X-ray transmission with only 0.96−0.54% for both X-ray energies, which can be regarded as negligible attenuation. With the maximum mass ratio of the BTO-ER composite at 65:35, X-ray transmission of the 65BTO-ER film decreased significantly to 14.90 and 22.97% at 80 and 100 kVp, respectively, showing X-ray attenuation efficiencies at ∼85 and ∼77%, respectively. Further investigation on increasing the thickness (double) of the 65BTO-ER film (denoted as D-65BTO-ER) provided the lowest X-ray transmission values of 2.55 and 5.65% (attenuation efficiencies of ∼97 and 95%), respectively, indicating that the radiation shielding capacity is thickness-dependent as expected.

However, the thickness of a shielding material may vary depending on its density.[44] For the X-ray protective materials, weight is another important parameter that needs to be taken into consideration. Thus, the mass per unit area (g/mm^2) here is considered appropriate as an indication of the weight evaluation for the shielding material composites.[45] The trend of X-ray transmission decreased for both X-ray energies, while the mass per unit area of the BTO-ER films increased. Noticeably, the D-65BTO-ER film showed the best X-ray attenuation performance with the highest mass per unit area at 0.004 g/mm^2, which was slightly lighter than the mass per unit area of a one-layer 0.35 mm Pb sheet (0.005 g/mm^2). However, the weight of the D-65BTO-ER film was 2.2 ± 0.1 g, which was approximately two times lower than a one-layer 0.35 mm Pb sheet (4.19 g).[31]

3.4. Mass Attenuation Coefficient Comparison. The mass attenuation coefficient (μ/ρ) evaluates the attenuation ability of a shielding material (cm^2/g).[46] More specifically, it describes a rate between the X-ray attenuation capacity per unit thickness (cm^{-1}) of a shielding material and the density (g/cm^3) of this material.[46] This value is determined by both the photon energy and the electron density within the shielding material. The probability of a photon being converted to an electron is higher when the electron density within a shielding material is higher.[4] The electron density is mainly determined by the density of a shielding material, which implies that the higher density of a material is more likely to provide more interaction probabilities for the photon energy. According to eq 3 in Section 2.6, the μ/ρ value of each sample can be calculated from the density and thickness (measured and shown in Figure S3) of each composite and is tabulated in Table 2.

Table 2. Thickness and Density of the Six BTO-ER Film Composites and Their Corresponding μ/ρ Values

samples	thickness (μm)	density (g/cm^3)	experimental mass attenuation coefficient (μ/ρ) (cm^2/g)	
			80 kVp	100 kVp
ER	402 ± 2	1.1 ± 0.1	0.6 ± 0.1	0.5 ± 0.1
10BTO-ER	636 ± 2	1.8 ± 0.1	1.6 ± 0.1	1.1 ± 0.1
30BTO-ER	717± 2	1.9 ± 0.1	3.8 ± 0.2	3.1 ± 0.1
50BTO-ER	923 ± 2	1.7 ± 0.1	8.3 ± 0.3	6.2 ± 0.3
65BTO-ER	1516 ± 2	2.0 ±0.1	7.2 ± 0.3	5.4 ± 0.2
D-65BTO-ER	2145 ± 1	2.2 ±0.1	8.1 ± 0.3	6.2 ± 0.2

To compare the shielding ability of each synthesized BTO-ER composite, the μ/ρ values of ER (the control), BTO-ER films with filler loadings from 10 to 65 wt %, and the D-BTO-ER film were calculated for both X-ray energies of 80 and 100 kVp (Figure 6). The ER film displayed the lowest μ/ρ values

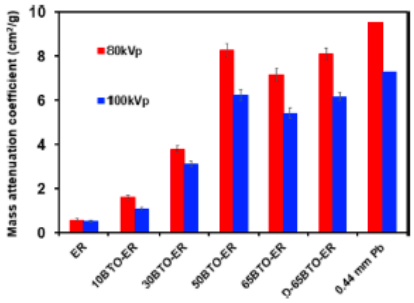

Figure 6. Mass attenuation coefficient (μ/ρ) of ER (control), BTO-ER films with different mass loadings (10, 30, 50, and 65 wt %), and the D-65BTO-ER film compared with 0.44 mm Pb.

(0.6 ± 0.1 and 0.5 ± 0.1 cm^2/g, respectively) among others at X-ray energies of 80 and 100 kVp due to its low-Z element composition and low density (1.1 ± 0.1 g/cm^3). The μ/ρ values of the prepared BTO-ER composites enhanced with the mass loading increasing from 10 to 50 wt % as shown in Figure 6. It is interesting to note that a slight decrease occurred in the

https://doi.org/10.1021/acsanm.1c01475
ACS Appl. Nano Mater. 2021, 4, 7471−7478

μ/ρ value (7.2 ± 0.3 and 5.4 ± 0.2 cm^2/g, respectively) of the 65BTO-ER composite compared to that of the 50BTO-ER composite at 80 and 100 kVp. It can be a result of the significantly increasing surface roughness (shown in Figure S2) of the 65BTO-ER composite. It has been proven that the level of interaction between the polymer (epoxy) matrix and fillers (BTO) led to different surface structural patterns, which played a significant role in the X-ray attenuation ability of the shielding composites at a low X-ray energy.[22] Therefore, the less surface roughness (good dispersion of the particles in a polymer matrix) of the prepared composite corroborated well with the X-ray attenuation performance. Moreover, the D-65BTO-ER composite (highest density at 2.2 ± 0.1 g/cm^3) with a thickness of 2145 ± 1 μm (~2 mm) demonstrated almost the same μ/ρ values (8.1 ± 0.3 and 6.2 ± 0.2 cm^2/g, respectively) as the 50BTO-ER composite at both X-ray energies, which revealed that the ability of X-ray attenuation (at 80 and 100 kVp) mainly depended on (1) the dispersion of the fillers (BTO particles) in a polymer matrix (2) the density and (3) thickness of the shielding materials due to the dominant photoelectric effect at a low X-ray energy.[22,47,48]

Further comparison between D-65BTO-ER and the 0.44 mm Pb sheet showed that the μ/ρ value of the D-65BTO-ER film was slightly lower than that of the 0.44 mm Pb sheet (9.5 and 7.3 cm^2/g, respectively) at both energies of 80 and 100 kVp, thus indicating that the D-65BTO-ER film displayed comparable X-ray attenuation ability with the 0.44 mm Pb sheet. The mechanism related to the enhanced X-ray attenuation capacity of the prepared composites using BTO particles (BTO structure shown in Figure 1a) dispersed in the epoxy matrix can be attributed to several factors. First, the narrow-sized BTO particles increase the effectiveness of the particle distribution in the epoxy matrix.[49] Second, increasing the mass loading of BTO particles in the epoxy matrix can elevate the density of the BTO-ER composite due to an increment in the weight of the composite. This can be explained by the assembly of particles becoming more apparent with the formation of multilayers to fill up the voids within the polymer composite, as supported by the color change and SEM images shown in Figure 4.[23] This increasingly facilitates the multiple scattering of incoming X-ray photon energy, thus leading to the high energy absorption as schematically presented in Figure 1b.[21]

3.5. Benchmarking with Pb Sheets. Pb equivalence is a measure for the radiation attenuation ability of non-Pb shielding materials compared to that of Pb with specific thicknesses (0.25, 0.35, and 0.50 mm).[50] Due to the limitation of the BTO particle loading within the epoxy matrix, the maximum mass loading of BTO in epoxy was 65% to maintain the mechanical property of the polymer (epoxy). To achieve the best X-ray attenuation performance, the optimized weight ratio of the 65BTO-ER composite was doubled, and then it was compared with the X-ray transmission of the standard Pb sheets with different thicknesses (0.25, 0.35, and 0.50 mm) provided at X-ray energies of 80 and 100 kVp.[31] Remarkably, the D-65BTO-ER film exhibited X-ray transmission values of 2.55 and 5.65%, respectively, which were lower than the 0.25 mm Pb sheet (6.68 and 12.57%, respectively) in Figure 7, strongly suggesting that it shielded 50% more than the 0.25 mm Pb at both 80 and 100 kVp. In comparison to the 0.35 mm Pb sheet, the D-65BTO-ER film showed an almost equal X-ray transmission rate (2.86 and 5.73%, respectively) at both 80 and 100 kVp, thus indicating that the X-ray attenuation performance of the D-65BTO-ER film remained slightly superior relative to the 0.35 mm Pb sheet at 80 and 100 kVp. Nevertheless, the 0.50 mm Pb sheet provided better X-ray attenuation than the D-65BTO-ER film at both energies. In terms of material weight as well as the concerns on material safety and sustainability, our developed binary metal-oxide composite still outshines the conventional Pb sheet despite the material thickness. In short, these outcomes confirmed that the D-65BTO-ER film (2.2 ± 0.1 g) with a thickness of ~2 mm was able to provide a 0.35 mm Pb (4.19 g) equivalent attenuation at an energy range of 80 and 100 kVp.

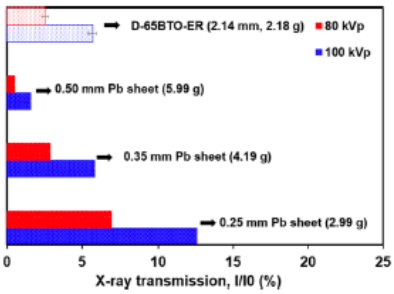

Figure 7. X-ray transmission of the D-65BTO-ER film compared to pure Pb sheets with different thicknesses (0.25, 0.35, and 0.50 mm).

4. CONCLUSIONS

In summary, this work demonstrated the successful development of a new, lightweight, nontoxic, and high-performance X-ray protection material from the design of a BTO-ER film composite by simply adopting an environmentally friendly (minimal polymer) material engineering and processing strategy. The D-65BTO-ER composite with a doubled film thickness proved to be the best X-ray attenuated material with only 2.55 and 5.65% X-ray transmission values at X-ray energies of 80 and 100 kVp, respectively. Moreover, increasing the amount of BTO particles improved the X-ray attenuation ability of the prepared BTO-ER composites due to their increasing densities and thicknesses as well as the enhanced narrow-sized effect toward the polymer. The comparison between the different thicknesses of the Pb sheets demonstrated that the BTO-ER composite with a thickness of ~2 mm and a low mass per unit area of 0.004 g/mm^2 provided a 0.35 mm Pb equivalent attenuation at X-ray energies of 80 and 100 kVp, confirming that this lightweight BTO-ER composite is an effective, Pb-free material for X-ray protection application. The outcomes highlight the promising potential of the developed BTO-based composite as a prominent X-ray shielding candidate to replace toxic Pb-based materials for the new design of a safe, affordable, and environmentally friendly X-ray protection garment.

■ ASSOCIATED CONTENT

Supporting Information

The Supporting Information is available free of charge at https://pubs.acs.org/doi/10.1021/acsanm.1c01475.

Supplementary figures of XRD profiles of BTO-1, BTO-3, and BTO-6 prepared after ball-milling process times of 1, 3, and 6 h; surface roughness (top surface) and shore hardness of ER (the control) and BTO-ER composite films with different mass loadings from 10

https://doi.org/10.1021/acsanm.1c01475
ACS Appl. Nano Mater. 2021, 4, 7471−7478

to 65%; SEM images of ER (control), BTO-ER composite films with different mass loadings from 10 to 65%, and the D-65BTO-ER composite film to indicate the thickness of the respective samples produced; particle size distribution of synthesized BTO nanoparticles determined by a dynamic light scattering technique (PDF)

AUTHOR INFORMATION

Corresponding Author

Dusan Losic − *School of Chemical Engineering and Advanced Materials, University of Adelaide, Adelaide, South Australia 5005, Australia; ARC Research Hub for Graphene Enabled Industry Transformation, The University of Adelaide, Adelaide, South Australia 5005, Australia;* orcid.org/0000-0002-1930-072X; Email: dusan.losic@adelaide.edu.au

Authors

Le Yu − *School of Chemical Engineering and Advanced Materials, University of Adelaide, Adelaide, South Australia 5005, Australia; ARC Research Hub for Graphene Enabled Industry Transformation, The University of Adelaide, Adelaide, South Australia 5005, Australia;* orcid.org/0000-0001-6354-1240

Pei Lay Yap − *School of Chemical Engineering and Advanced Materials, University of Adelaide, Adelaide, South Australia 5005, Australia; ARC Research Hub for Graphene Enabled Industry Transformation, The University of Adelaide, Adelaide, South Australia 5005, Australia*

Alexandre Santos − *School of Physical Sciences, The University of Adelaide, Adelaide, South Australia 5005, Australia; Department of Medical Physics, Royal Adelaide Hospital, Adelaide, South Australia 5000, Australia*

Diana Tran − *School of Chemical Engineering and Advanced Materials, University of Adelaide, Adelaide, South Australia 5005, Australia; ARC Research Hub for Graphene Enabled Industry Transformation, The University of Adelaide, Adelaide, South Australia 5005, Australia;* orcid.org/0000-0002-4023-3373

Complete contact information is available at: https://pubs.acs.org/10.1021/acsanm.1c01475

Author Contributions

The manuscript was written through contributions of all authors. All authors have given approval to the final version of the manuscript.

Notes

The authors declare no competing financial interest.

ACKNOWLEDGMENTS

The authors acknowledge the financial support from the ARC Research Hub for Graphene Enabled Industry Transformation (IH150100003). We thank the Australian Microscopy and Microanalysis Research Facility (AMMRF) for the access of SEM and TEM facilities and Mr. Ken Neubauer and Dr. Ashley Slattery for their technical support on SEM and TEM measurements.

REFERENCES

(1) Wang, Y.; Ding, P.; Xu, H.; Li, Q.; Guo, J.; Liao, X.; Shi, B. Advanced X-ray Shielding Materials Enabled by the Coordination of Well-Dispersed High Atomic Number Elements in Natural Leather. *ACS Appl. Mater. Interfaces* **2020**, *12*, 19916−19926.

(2) Azman, N. Z. N.; Siddiqui, S. A.; Low, I. M. Characterisation of micro-sized and nano-sized tungsten oxide-epoxy composites for radiation shielding of diagnostic X-rays. *Mater. Sci. Eng., C* **2013**, *33*, 4952−4957.

(3) Ambika, M. R.; Nagaiah, N.; Suman, S. K. Role of bismuth oxide as a reinforcer on gamma shielding ability of unsaturated polyester based polymer composites. *J. Appl. Polym. Sci.* **2017**, *134*, 1.

(4) Azman, N. Z. N.; Siddiqui, S. A.; Hart, R.; Low, I. M. Microstructural design of lead oxide-epoxy composites for radiation shielding purposes. *J. Appl. Polym. Sci.* **2013**, *128*, 3213−3219.

(5) More, C. V.; Alsayed, Z.; Badawi, M. S.; Thabet, A. A.; Pawar, P. P. Polymeric composite materials for radiation shielding: a review. *Environ. Chem. Lett.* **2021**, *19*, 2057−2090.

(6) Yaffe, M. J.; Mawdsley, G. E.; Lilley, M.; Servant, R.; Reh, G. Composite materials for x-ray protection. *Health Phys.* **1991**, *60*, 661−664.

(7) Li, R.; Gu, Y.; Wang, Y.; Yang, Z.; Li, M.; Zhang, Z. Effect of particle size on gamma radiation shielding property of gadolinium oxide dispersed epoxy resin matrix composite. *Mater. Res. Express* **2017**, *4*, No. 035035.

(8) Liu, J.-H.; Zhang, Q.-P.; Sun, N.; Zhao, Y.; Shi, R.; Zhou, Y.-L.; Zheng, J. Elevated gamma-rays shielding property in lead-free bismuth tungstate by nanofabricating structures. *J. Phys. Chem. Solids* **2018**, *112*, 185−189.

(9) Tishkevich, D. I.; Grabchikov, S. S.; Lastovskii, S. B.; Trukhanov, S. V.; Zubar, T. I.; Vasin, D. S.; Trukhanov, A. V.; Kozlovskiy, A. L.; Zdorovets, M. M. Effect of the Synthesis Conditions and Microstructure for Highly Effective Electron Shields Production Based on Bi Coatings. *ACS Appl. Energy Mater.* **2018**, *1*, 1695−1702.

(10) Kim, H.; Lim, J.; Kim, J.; Lee, J.; Seo, Y. Multilayer Structuring of Nonleaded Metal (BiSn)/Polymer/Tungsten Composites for Enhanced γ-Ray Shielding. *Adv. Eng. Mater.* **2020**, *22*, 1901448.

(11) Tekin, H. O.; Sayyed, M. I.; Issa, S. A. M. Gamma radiation shielding properties of the hematite-serpentine concrete blended with WO3 and Bi2O3 micro and nano particles using MCNPX code. *Radiat. Phys. Chem.* **2018**, *150*, 95−100.

(12) Mahmoud, M. E.; El-Khatib, A. M.; Badawi, M. S.; Rashad, A. R.; El-Sharkawy, R. M.; Thabet, A. A. Fabrication, characterization and gamma rays shielding properties of nano and micro lead oxide-dispersed-high density polyethylene composites. *Radiat. Phys. Chem.* **2018**, *145*, 160−173.

(13) Mhareb, M. H. A.; Slimani, Y.; Alajerami, Y. S.; Sayyed, M. I.; Lacomme, E.; Almessiere, M. A. Structural and radiation shielding properties of $BaTiO_3$ ceramic with different concentrations of Bismuth and Ytterbium. *Ceram. Int.* **2020**, *46*, 28877−28886.

(14) Sayyed, M. I.; Akman, F.; Kumar, A.; Kaçal, M. R. Evaluation of radioprotection properties of some selected ceramic samples. *Results Phys.* **2018**, *11*, 1100−1104.

(15) Lardhi, S.; Noureldine, D.; Harb, M.; Ziani, A.; Cavallo, L.; Takanabe, K. Determination of the electronic, dielectric, and optical properties of sillenite $Bi_{12}TiO_{20}$ and perovskite-like $Bi_4Ti_3O_{12}$ materials from hybrid first-principle calculations. *J. Chem. Phys.* **2016**, *144*, 134702.

(16) Nambiar, S.; Yeow, J. T. W. Polymer-composite materials for radiation protection. *ACS Appl. Mater. Interfaces* **2012**, *4*, 5717−5726.

(17) Xu, Y.-C.; Zhang, Q.-P.; Liu, J.-H.; Wu, Y.; Liu, L.-P.; Xu, D.-G.; Zhou, Y.-L. $PbWO_4$ nanofibers for shielding gamma radiation: crystal growth, morphology and performance evaluation. *CrystEngComm* **2018**, *20*, 6197−6206.

(18) Yılmaz, S. N.; Güngör, A.; Özdemir, T. The investigations of mechanical, thermal and rheological properties of polydimethylsiloxane/bismuth (III) oxide composite for X/Gamma ray shielding. *Radiat. Phys. Chem.* **2020**, *170*, 108649.

(19) Nambiar, S.; Osei, E. K.; Yeow, J. T. W. Polymer nanocomposite-based shielding against diagnostic X-rays. *J. Appl. Polym. Sci.* **2013**, *127*, 4939−4946.

https://doi.org/10.1021/acsanm.1c01475
ACS Appl. Nano Mater. 2021, 4, 7471−7478

(20) Lopresti, M.; Alberto, G.; Cantamessa, S.; Cantino, G.; Conterosito, E.; Palin, L.; Milanesio, M. Light Weight, Easy Formable and Non-ToxicPolymer-Based Composites for Hard X-rayShielding: A Theoretical and Experimental Study. *Int. J. Mol. Sci.* **2020**, *21*, 833.
(21) Li, Q.; Wei, Q.; Zheng, W.; Zheng, Y.; Okosi, N.; Wang, Z.; Su, M. Enhanced Radiation Shielding with Conformal Light-Weight Nanoparticle-Polymer Composite. *ACS Appl. Mater. Interfaces* **2018**, *10*, 35510−35515.
(22) Yu, L.; Pereira, A. L. C.; Tran, D. N. H.; Santos, A. M. C.; Losic, D. Bismuth Oxide Films for X-ray shielding: Effects of particle size and structural morphology. *Mater. Chem. Phys.* **2021**, *260*, 124084.
(23) Verdipoor, K.; Alemi, A.; Mesbahi, A. Photon mass attenuation coefficients of a silicon resin loaded with WO_3, PbO, and Bi_2O_3 Micro and Nano-particles for radiation shielding. *Radiat. Phys. Chem.* **2018**, *147*, 85−90.
(24) La, L. B. T.; Leatherday, C.; Leong, Y.-K.; Watts, H. P.; Zhang, L.-C. Green lightweight lead-free Gd_2O_3/epoxy nanocomposites with outstanding X-ray attenuation performance. *Compos. Sci. Technol.* **2018**, *163*, 89−95.
(25) Künzel, R.; Okuno, E. Effects of the particle sizes and concentrations on the X-ray absorption by CuO compounds. *Appl. Radiat. Isot.* **2012**, *70*, 781−784.
(26) Azman, N. Z. N.; Musa, N. F. L.; Nik Ab Razak, N. N. A.; Ramli, R. M.; Mustafa, I. S.; Abdul Rahman, A.; Yahaya, N. Z. Effect of Bi_2O_3 particle sizes and addition of starch into Bi_2O_3−PVA composites for X-ray shielding. *Applied Physics A* **2016**, *122*, 1−9.
(27) Tekin, H. O.; Singh, V. P.; Manici, T. Effects of micro-sized and nano-sized WO_3 on mass attenauation coefficients of concrete by using MCNPX code. *Appl. Radiat. Isot.* **2017**, *121*, 122−125.
(28) Gupta, N.; Kaur, A.; Khanna, A.; Gonzàlez, F.; Pesquera, C.; Iordanova, R.; Chen, B. Structure-property correlations in TiO_2-Bi_2O_3-B_2O_3-TeO_2 glasses. *J. Non-Cryst. Solids* **2017**, *470*, 168−177.
(29) Wang, Y.; Zhong, R.; Li, Q.; Liao, J.; Liu, N.; Joshi, N. S.; Shi, B.; Liao, X.; Guo, J. Lightweight and Wearable X-Ray Shielding Material with Biological Structure for Low Secondary Radiation and Metabolic Saving Performance. *Adv. Mater. Technol.* **2020**, *5*, 2000240.
(30) ICPR *The 2007 Recommendations of International Commission on Radiological Protection*. ICPR: 2007.
(31) Scuderi, G. J.; Brusovanik, G. V.; Campbell, D. R.; Henry, R. P.; Kwon, B.; Vaccaro, A. R. Evaluation of non-lead-based protective radiological material in spinal surgery. *Spine J.* **2006**, *6*, 577−582.
(32) Sheldon, R. A. Metrics of Green Chemistry and Sustainability: Past, Present, and Future. *ACS Sustainable Chem. Eng.* **2018**, *6*, 32−48.
(33) Stojanovic, B. D.; Paiva-Santos, C. O.; Jovalekic, C.; Simoes, A. Z.; Filho, F. M.; Lazarevic, Z.; Varela, J. A. Mechanically activating formation of layered structured bismuth titanate. *Mater. Chem. Phys.* **2006**, *96*, 471−476.
(34) Lee, N.; Choi, S. H.; Hyeon, T. Nano-sized CT contrast agents. *Adv. Mater.* **2013**, *25*, 2641−2660.
(35) Viegas, J.; Silva, L. A.; Batista, A. M. S.; Furtado, C. A.; Nascimento, J. P.; Faria, L. O. Increased X-ray Attenuation Efficiency of Graphene-Based Nanocomposite. *Ind. Eng. Chem. Res.* **2017**, *56*, 11782−11790.
(36) ICRP. ICRP Publication 103. *Ann. ICRP* **2007**, *37*, 2−4.
(37) Shaikh, S. F.; Mane, R. S.; Min, B. K.; Hwang, Y. J.; Joo, O. S. D-sorbitol-induced phase control of TiO_2 nanoparticles and its application for dye-sensitized solar cells. *Sci. Rep.* **2016**, *6*, 20103.
(38) Sankar Ganesh, R.; Sharma, S. K.; Abinnas, N.; Durgadevi, E.; Raji, P.; Ponnusamy, S.; Muthamizhchelvan, C.; Hayakawa, Y.; Kim, D. Y. Fabrication of the flexible nanogenerator from BTO nanopowders on graphene coated PMMA substrates by sol-gel method. *Mater. Chem. Phys.* **2017**, *192*, 274−281.
(39) Du, Y. L.; Chen, G.; Zhang, M. S. Grain size effects in $Bi_4Ti_3O_{12}$ nanocrystals investigated by Raman spectroscopy. *Solid State Commun.* **2004**, *132*, 175−179.
(40) Golda, R. A.; Marikani, A.; Padiyan, D. P. Mechanical synthesis and characterization of $Bi_4Ti_3O_{12}$ nanopowders. *Ceram. Int.* **2011**, *37*, 3731−3735.
(41) Lazarevic, Z. Ž.; Stojanovic, B. D.; Romcevic, M. J.; Romcevic, N. Ž. Mechanochemical activation assisted synthesis of bismuth Layered-Perovskite $Bi_4Ti_4O_{12}$. *Sci. Sintering* **2009**, *41*, 19−26.
(42) Stojanović, B. D.; Paiva-Santos, C. O.; Cilense, M.; Jovalekić, Č.; Lazarević, Z. Ž. Structure study of $Bi_4Ti_3O_{12}$ produced via mechanochemically assisted synthesis. *Mater. Res. Bull.* **2008**, *43*, 1743−1753.
(43) da Costa Mattos, H. S.; de Abreu Martins, S. Plastic behaviour of an epoxy polymer under cyclic tension. *Polym. Test.* **2013**, *32*, 1−8.
(44) Azman, N. Z. N.; Siddiqui, S. A.; Hart, R.; Low, I. M. Effect of particle size, filler loadings and x-ray tube voltage on the transmitted x-ray transmission in tungsten oxide-epoxy composites. *Appl. Radiat. Isot.* **2013**, *71*, 62−67.
(45) McCaffrey, J. P.; Tessier, F.; Shen, H. Radiation shielding materials and radiation scatter effects for interventional radiology (IR) physicians. *Med. Phys.* **2012**, *39*, 4537−4546.
(46) Podgoršak, E. B. *Radiation Physics for Medical Physicists*; Springer: 2006.
(47) Li, Z.; Zhou, W.; Zhang, X.; Gao, Y.; Guo, S. High-efficiency, flexibility and lead-free X-ray shielding multilayered polymer composites: layered structure design and shielding mechanism. *Sci. Rep.* **2021**, *11*, 4384.
(48) Low, I. M.; Azman, N. Z. N. *Polymer Composites and Nanocomposites for X-Rays Shielding*; Springer: 2020, DOI: 10.1007/978-981-13-9810-0.
(49) Teh, E. J.; Leong, Y. K.; Liu, Y.; Ong, B. C.; Berndt, C. C.; Chen, S. B. Yield stress and zeta potential of washed and highly spherical oxide dispersions—Critical zeta potential and Hamaker constant. *Powder Technol.* **2010**, *198*, 114−119.
(50) Jayakumar, S.; Saravanan, T.; Philip, J. Thermal Stability and X-ray Attenuation Studies on α-Bi_2O_3, β-Bi_2O_3 and Bi Based Nanocomposites for Radiopaque Fabrics. *J. Nanosci. Nanotechnol.* **2018**, *18*, 3969−3981.

https://doi.org/10.1021/acsanm.1c01475
ACS Appl. Nano Mater. 2021, 4, 7471−7478

Supporting Information

Lightweight Bismuth Titanate ($Bi_4Ti_3O_{12}$) Nanoparticle-Epoxy Composite for Advanced Lead-Free X-ray Radiation Shielding

Le Yu [a,b], Pei Lay Yap [a,b], Alexandre Santos [c,d], Diana Tran [a,b], Dusan Losic [a,b*]

[a] School of Chemical Engineering and Advanced Materials, University of Adelaide, Adelaide, SA 5005, Australia.
[b] ARC Research Hub for Graphene Enabled Industry Transformation, University of Adelaide, Adelaide, SA 5005, Australia.
[c] School of Physical Sciences, University of Adelaide, Adelaide, South Australia 5005, Australia.
[d] Department of Medical Physics, Royal Adelaide Hospital, Adelaide, South Australia 5000, Australia.

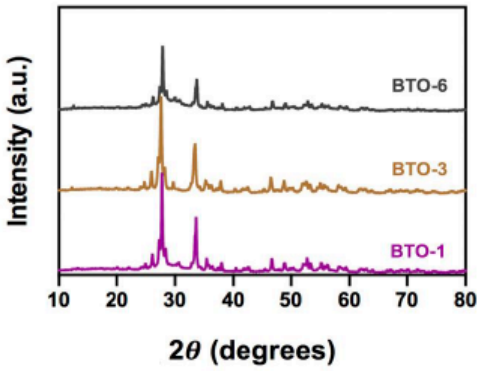

Figure S1. XRD profiles of BTO-1, 3 and 6 prepared after ball milling process of 1, 3 and 6 hours.

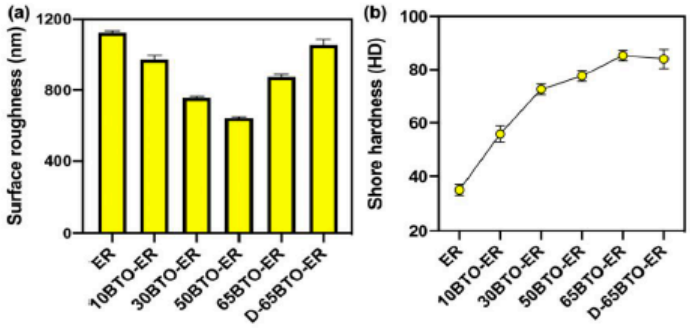

Figure S2. (a) Surface roughness (top surface) and (b) shore hardness of ER (the control) and BTO-ER composite films with different mass loading from 10 – 65 %.

*Corresponding author: Dusan Losic
E-mail address: dusan.losic@adelaide.edu.au

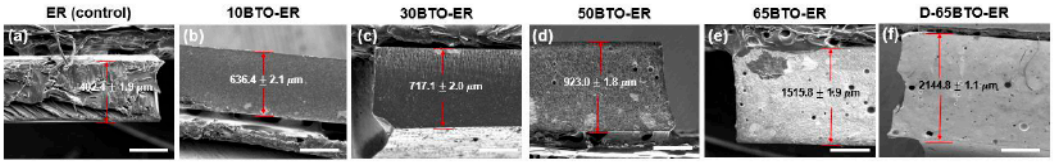

Figure S3. SEM images of (a-f) ER (the control), BTO-ER composite films with different mass loadings from 10-65 % (scale bar = 500 m) and D-65NTO-ER composite film (scale bar = 1mm) to indicate the thickness of the respective samples produced.

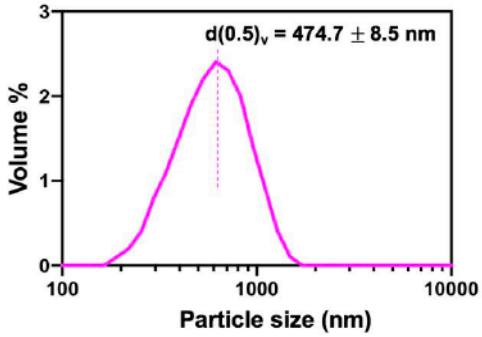

Figure S4. Particle size distribution of synthesized BTO nanoparticles using Dynamic Light Scattering technique.

CHAPTER 4

DEVELOPMENT OF 2D LAYERED MATERIALS FOR LOW-ENERGY X-RAY SHIELDING IMPROVEMENT

Chapter 4 Development of 2D layered materials for low-energy X-ray shielding improvement

Overview and significance of work

This chapter aims to explore the impact of applying 2D layered materials on X-ray attenuation improvement. Bulk and few-layer (exfoliated, FL) 2D material films including antimony (Sb), Mxene and MoS_2 are prepared for the comparison of the low-energy (30 kVp) X-ray shielding effectiveness. Moreover, the influence on X-ray shielding performance using laminated 2D layered structure is investigated at low-energy X-ray. The outcomes showed the significant effect of the layer-structure materials on X-ray attenuation enhancement, providing great potential for the new design of FL-2D materials for the radiation shielding application. The key contribution of this chapter achieves **aim 2,** and two prepared manuscripts are under provisional patent approval (No. AU2021902612):

(1) **Yu, L.**, Douglass, M., Santos, A., Tran, D., & Losic, D. (2022). Two-dimensional (2D) layered molybdenum disulfide (MoS_2) films for high-performing low-energy X-ray radiation shielding. *2D Materials*. **(To be submitted)**

(2) **Yu, L.**, Nine, M. J., Tran, T., Pereira, A. C., Hassan, k., Tran, D., . . . Losic, D. (2022). Layered 2D materials films and their heterolaminates for enhanced low-energy X-Ray radiation shielding. *Advanced Materials*. **(Submitted)**

Provisional patent: Yu L, Losic D, Santos A, Tran D, Tran T and Nine M J (2021). Improved radiation shielding. *University of Adelaide,* (No.AU 2021902612).

Statement of Authorship

Title of Paper	Two-dimensional (2D) layered molybdenum disulfide (MoS2) films for high-performing low-energy X-ray radiation shielding
Publication Status	☐ Published ☐ Accepted for Publication ☐ Submitted for Publication ☑ Unpublished and Unsubmitted work written in manuscript style
Publication Details	Yu, L., Douglass, M., Santos, A., Tran, D., & Losic, D. (2022). Two-dimensional (2D) layered molybdenum disulfide (MoS2) films for high-performing low-energy X-ray radiation shielding. *2D Materials*.

Principal Author

Name of Principal Author (Candidate)	Le Yu		
Contribution to the Paper	Prepared and characterized on all the samples, and interpreted all the data as well as wrote the manuscript.		
Overall percentage (%)	85 %		
Certification:	This paper reports on original research I conducted during the period of my Higher Degree by Research candidature and is not subject to any obligations or contractual agreements with a third party that would constrain its inclusion in this thesis. I am the primary author of this paper.		
Signature		Date	03/03/2022

Co-Author Contributions

By signing the Statement of Authorship, each author certifies that:

i. the candidate's stated contribution to the publication is accurate (as detailed above);

ii. permission is granted for the candidate in include the publication in the thesis; and

iii. the sum of all co-author contributions is equal to 100% less the candidate's stated contribution.

Name of Co-Author	Michael Douglass		
Contribution to the Paper	Edited, performed X-ray irradiations and revised the manuscript.		
Signature		Date	03/03/2022

Name of Co-Author	Alexandre M. C. Santos		
Contribution to the Paper	Co-supervised, performed X-ray irradiations and revised the manuscript.		
Signature		Date	03/03/2022

Please cut and paste additional co-author

Statement of Authorship

Title of Paper	Two-dimensional (2D) layered molybdenum disulfide (MoS2) films for high-performing low-energy X-ray radiation shielding
Publication Status	☐ Published ☐ Accepted for Publication ☐ Submitted for Publication ☑ Unpublished and Unsubmitted work written in manuscript style
Publication Details	Yu, L., Douglass, M., Santos, A., Tran, D., & Losic, D. (2022). Two-dimensional (2D) layered molybdenum disulfide (MoS2) films for high-performing low-energy X-ray radiation shielding. *2D Materials*.

Principal Author

Name of Principal Author (Candidate)	Le Yu		
Contribution to the Paper	Prepared and characterized on all the samples, and interpreted all the data as well as wrote the manuscript.		
Overall percentage (%)	85 %		
Certification:	This paper reports on original research I conducted during the period of my Higher Degree by Research candidature and is not subject to any obligations or contractual agreements with a third party that would constrain its inclusion in this thesis. I am the primary author of this paper.		
Signature		Date	03/03/2022

Co-Author Contributions

By signing the Statement of Authorship, each author certifies that:

i. the candidate's stated contribution to the publication is accurate (as detailed above);

ii. permission is granted for the candidate in include the publication in the thesis; and

iii. the sum of all co-author contributions is equal to 100% less the candidate's stated contribution.

Name of Co-Author	Diana N. H. Tran		
Contribution to the Paper	Co-supervised and revised the manuscript.		
Signature		Date	03/03/2022

Name of Co-Author	Dusan Losic		
Contribution to the Paper	Supervised the development of the work, edited, revised the manuscript and acted as the corresponding author.		
Signature		Date	03/03/2022

Please cut and paste additional co-author panels here as required.

Two-Dimensional (2D) Layered Molybdenum Disulphide (MoS_2) Films for High-Performance Low-Energy X-Ray Radiation Shielding

Le Yu[1,2], Michael Douglass[3,4], Alexandre Santos[3,4], Diana Tran[1,2] and Dusan Losic[*1,2]

[1] School of Chemical Engineering, University of Adelaide, Adelaide, South Australia 5005, Australia.
[2] ARC Research Hub for Graphene Enabled Industry Transformation, University of Adelaide, Adelaide, SA 5005, Australia.
[3] School of Physical Sciences, University of Adelaide, Adelaide, South Australia 5005, Australia.
[4] Department of Medical Physics, Royal Adelaide Hospital, Adelaide, South Australia 5000, Australia.

E-mail: Dusan.losic@adelaide.edu.au

Received
Accepted for publication
Published

Abstract

This paper studies the low-energy X-ray radiation shielding performance of two-dimensional (2D) layered molybdenum disulphide (MoS_2) films with the aim of developing a new generation of high-performance, lightweight, and lead (Pb)-free X-ray shielding materials. The optimization of the MoS_2 composite films was investigated with thicknesses ranging from 110 μm to 1.34 mm followed by the measurement of the low-energy X-ray attenuation performance. A Gulmay D3150 superficial X-ray (SXR) unit was used to investigate the effect of the MoS_2 films on X-ray transmission at 30 kVp, and XCOM program was applied to calculate the X-ray transmission of 0.20 mm Pb for comparison. The results showed that the optimized MoS_2 composite film (1.34 mm) provided similar X-ray transmission to the control Pb sheet (2.17 g) at 30 kVp, and its weight (1.18 g) was 50 % lighter. This new, lightweight, and Pb-free layered MoS_2 (2D) material is potentially effective in providing X-ray shielding performance, as an alternative to the traditional Pb-equivalent materials.

Keywords: low-energy X-ray, shielding, molybdenum disulphide, composites, two-dimensional (2D) materials

1. Introduction

X-ray radiation is of vital importance in many fields, such as radiation therapy and diagnostic imaging, due to its high-penetrative electromagnetic property.[1-3] Currently, the increasing demand on the diagnostic imaging techniques, general computed tomography (CT), mammography, and fluoroscopic examinations have been widely used in the medical fields.[4] Since 2020, the employment of radiologic technologists has increased by 16 %, compared to the average intake in 2018.[5] This growing demand of using X-ray in the medical field causes potential harm for the practitioners who deal with ionizing radiation, especially fluoroscopic examinations.[6] Exposure to a certain amount of penetrative X-ray could cause harmful side effects or even severe cellular damage to living beings.[7] The as-low-as-reasonably-achievable (ALARA) principle for ionizing radiation protection has been established to minimize the doses received by personnel.[8] Meanwhile, application of X-ray radiation protective garment is of great significance to prevent X-ray from the human body for safe implementation.

High atomic number (Z) elements like lead (Pb) are commonly employed for the commercial X-ray protection garments, due to their electron-rich atoms that can attenuate X-ray via the photoelectric effect and Compton scattering.[9, 10] However, it is well-known that Pb is a toxic material, and it has been also banned for use in Europe since 2014 due to healthcare issues.[2] In addition, previous investigations showed that Pb was embedded with other polymers, but the structures of the composites were still detrimental as they easily cracked and aged during the production process. To address this problem, from the last decade, researchers have aimed at replacing Pb with other high-Z materials or with a combination of less toxic Pb compounds.[9] So far, a broad range of synthetic materials with other high-Z elements, such as tin [11], barium (Ba), antimony (Sb), tungsten (W), bismuth (Bi), have been explored to replace Pb for providing effective X-ray attenuation, especially from 40 to 150 kV, due to the strong dependence of the absorption capacity of atomic number on the photoelectric interaction.[4, 12, 13]

The recent discovery of 2D layered materials with their outstanding properies of narrow size, light weight and chemical stability, espeically transition metal dichalcogenide (TMDs) of the form of MX_2 (M = Mo, W and X = S, Se), offered a span-new frontier in the generation of 2D material-based devices for space instrumentation.[14] However, less study is known about the X-ray shielding performance of TMDs and other 2D materials. Moreover, McCaffrey et al. (2007) studied several non-Pb elements ranging from Z = 37 to 88 correlating the X-ray attenuation and materials' properties via a Monte Carlo system. The simulation suggested that these elements, depending on the quality of radiation requiring attenuation, were capable of providing X-ray protection at the energies from 39-205 kV, which provided theoretical evidence to explore other non-Pb materials.[12]

In this paper, it is hypothesized that high-Z, few-layer 2D nanosheets tend to provide advanced X-ray shielding performance. To demonstrate this concept, molybdenum disulphide (MoS_2) with a high Z of Mo at 42 and density of 5.06 g cm^{-3} was investigated as one of the major TMDs for low-energy X-ray shielding application. The effectiveness of the MoS_2 composite films with different thicknesses prepared using carboxymethylcellulose sodium salt (CMC) binder for low-voltage X-ray attenuation was examined. The optimized MoS_2 composite was further compared to a 0.20 mm Pb sheet as a benchmark for evaluation of X-ray shielding performance with a correlation of its weight. The presented results confirmed the proposed concept that this lightweight, Pb-free layered MoS_2 composite had a considerable X-ray shielding performance, as an alternative to the traditional Pb-based materials.

2. Materials and methods

2.1 Materials

Molybdenum disulphide powder (MoS_2, 99.99%, 23 μm) and sodium bromide (NaBr) was purchased from Chem-Supply [15]. Carboxymethylcellulose sodium salt (CMC, high viscosity) was provided by Aldrich Sigma [15]. Hydrophilic PTFE membrane filter (pore size: 0.45 μ m, diameter: 47 mm, thickness: 25 μ m) was purchased from Filter-Bio (China).

2.2 Experimental section

2.2.1 Exfoliation of MoS_2 via ball milling

Bulk MoS_2 powder was exfoliated using a Planetary Ball Mill PM 200 (Retsch, Australia) with zirconium balls (3 mm in diameter). NaBr was added to facilitate the process of the ball milling with a weight ratio of NaBr: MoS_2 at 20:1, and the weight ratio of balls to powder was also 20:1. After the dry ball milling process, NaBr in the as-prepared mixture was removed by washing several times using distilled (DI) water with the aid of a centrifuge (Sigma, Australia, 4200rpm) and then dried in oven at 50℃ overnight for the further step.

2.2.2 MoS_2 composite films preparation

Bulk and ball-milled (exfoliated) MoS_2 were dispersed with DI water and then bath-sonicated for 1 h, respectively. CMC solution (0.5 wt.%) was added to the as-prepared MoS_2 solution with the optimized weight ratio. The mixture was then stirred constantly for 3 h at the room temperature (20 ± 2 ℃) followed by vacuum filtration onto the membrane. The prepared composite film was then dried for 12 h in air at the room environment (20 ± 2 ℃).

2.2.3 Characterization on MoS_2 composite films

The synthesized MoS_2 composite films were characterized by a Scanning Electron Microscopy coupled with Energy Dispersive X-ray (SEM-EDX, FEI Quanta 450, USA; Ultim Max Oxford Instruments, UK) for surface morphology, composite thickness, and elemental analysis. SEM was also performed in backscattered electron (BSE) mode to evaluate the homogeneity of the composite material at an accelerating voltage of 10 kV. Transmission Electron Microscopy (TEM, FEI Tecnai G2 Spirit) at an accelerating voltage of 100 kV to study the number of the layers of the exfoliated MoS_2. X-ray diffractometer (XRD, Rigaku Miniflex 600, Japan) for the measurements of the crystalline forms in the composites were collected in the range of 2θ = 20-80° (scan rate of 10℃ min^{-1}). Chemical structure of the prepared samples was determined using Fourier Transform Infrared spectroscopy (FTIR, Nicolet 6700 Thermo Fisher, Australia) under transmission mode at 4000-400 cm^{-1}. Particle size distribution (PSD) was measured using a Zetasizer Nano-ZS (Malvern Analytical Australia, Australia). The vibrational characterization and layer identification of bulk and exfoliated MoS_2 were analyzed by Raman spectroscopy (LabRAM HR Evolution, Horiba Jvon Yvon Technology, Japan) using 532 nm laser as the excitation source in the range of 300-500 cm^{-1}. A 50× objective was used with the laser powder kept at 100% and all spectra were collected using an acquisition time of 1 s for 3 accumulations. The total composite film thickness (t_{CompM}) was calculated as equation (1),

$$t_{CompM} = t_{Comp} + t_M \quad (1)$$

where t_{Comp} is the composite thickness and t_M is the membrane thickness given as 25 μm.

2.2.4 X-ray transmission measurement

X-ray attenuation is the reduction of the intensity of X-ray when it travels through matter.[16] The properties of the controls (air and membrane) and as-prepared MoS_2 composite samples were measured using a Gulmay D3150 superficial X-ray (SXR) unit as shown in figure 1(a). The distances between the X-ray tube and the material sample, and the material sample to the detector were both set to 50 cm (figure 1(b)). The detector used to measure the transmission was a NE 2571 farmer type ionization chamber (Phoenix Dosimetry Ltd, UK). The samples were exposed to the X-ray voltage at 30 kVp (0.20 mm Al HVL) for 0.50 mins with the material sample placed over a collimator of diameter 1 cm (figure 1(c)). The X-ray transmission was calculated as the charge collected by the ionization chamber with the sample divided by the transmission dose without the sample. Each sample was measured three times and determined by the arithmetic mean.

The X-ray attenuation of an X-ray beam through any material can be estimated as a function of the linear attenuation coefficient (μ) as equation (2),[17]

$$I = I_0\, e^{-ut} \quad (2)$$

where I and I_0 are the final X-ray intensity after the attenuation by the sample and the X-ray intensity

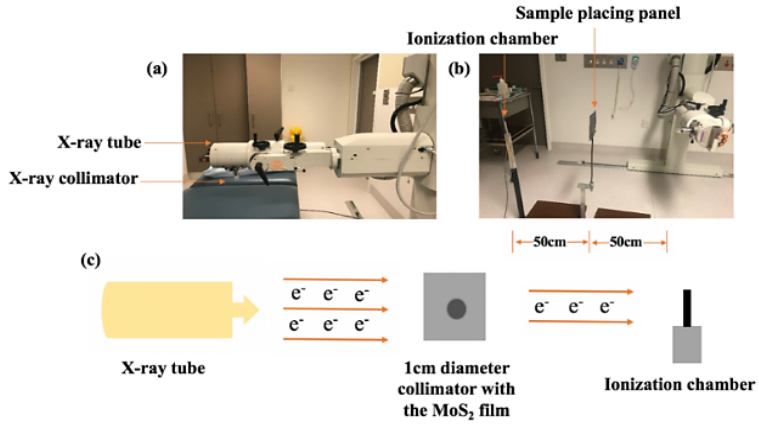

Figure 1 Photographs of the (a) superficial X-ray unit, (b) X-ray attenuation testing set-up and (c) schematic illustration of the X-ray attenuation measurement on MoS_2 composite film.[1]

before passing through the sample, respectively, and t is the material thickness (mm). The X-ray transmission (T) can be expressed as equation (3),

$$T = (I / I_0) \times 100\% \quad (3)$$

The theoretical X-ray transmission of 0.20 mm Pb for the comparison is calculated from the mass attenuation coefficient (μ/ρ) evaluated using XCOM program.[18]

3. Results and discussion

3.1 Characterization of exfoliated MoS_2 and MoS_2 composite films

A facile and effective ball-milling method was employed to exfoliate a large quantity of MoS_2 into small-layered sheets as shown in figure 2(a). SEM image confirmed the presence of the sheet-like MoS_2 with significant changes in the particle size distribution. In figure 2(b), the large layered MoS_2 sheets with particle size of 22.02 μm (figure 2(d)) was exfoliated into small and irregular sheets (figure 2(c)). More information about the exfoliated MoS_2 was obtained using TEM technique (inset of figure 2(c)), showing few-layer MoS_2 nanosheets with reduced particle size (432.10 nm) as shown in figure 2(e). This significant change of morphological geometry suggests successful delamination of MoS_2 sheets via the ball milling process. EDX analysis was performed to evaluate whether additional elements were generated during ball-milling procedure.[19] As depicted in figure 2(b', c'), the elemental composition of both bulk and exfoliated MoS_2 indicated only the presence of Mo and S as major elements, there were no additional alterations in the material after the ball milling process.

XRD patterns of the MoS_2 sheets before and after the dry ball milling process were presented in figure 3(a). Bulk MoS_2 sheets exhibited the presence of typical peaks at 2θ = 14°, 29°, 32°, 35°, 39°, 44°, 49°, 56° and 58° corresponding to their diffraction planes of (002), (004), (100), (102), (103), (006), (105), (106), and (110), respectively. These observed XRD peaks were in good agreement with the standard pattern of 2H phase MoS_2 (JCPDS-37-1492).[20] After 18 h of ball milling process, a decrease in intensity with an increase in width of the major peak (2θ = 14°) and the disappearance of the remaining peaks represented successful exfoliation of MoS_2.[21] FTIR spectra indicated that a characteristic peak at 470 cm^{-1} was detected in both the bulk and exfoliated MoS_2 powder (figure 3(b)). A decreasing intensity of this peak in the exfoliated MoS_2 could be contributed to the smaller thickness of the sheets after ball milling.[22]

Raman analysis is one of non-destructive techniques to study the crystallinity and defect level of 2D materials, where the Raman bands of 2D materials are significantly dependent on the number of layers.[23] In figure 3(c), bulk MoS_2 presented two typical bands at 373.12 cm^{-1} and 399.96 cm^{-1}, corresponding to E^1_{2g} (in-plane vibrations between two sulphur atoms and molybdenum atom) and A_{1g} (out-of-plane vibrations between sulphur atoms in the opposite direction) modes, respectively.[24] Raman spectrum of the exfoliated MoS_2 confirmed that bulk MoS_2 was successfully converted to exfoliated MoS_2, where the typical A_{1g} and E^1_{2g} peaks of exfoliated MoS_2 were significantly weakened and blue-shifted by ~2 cm^{-1} relative to those of bulk MoS_2, due to the thickness and lateral size reduction.[25] The frequency difference ($\Delta\omega$)

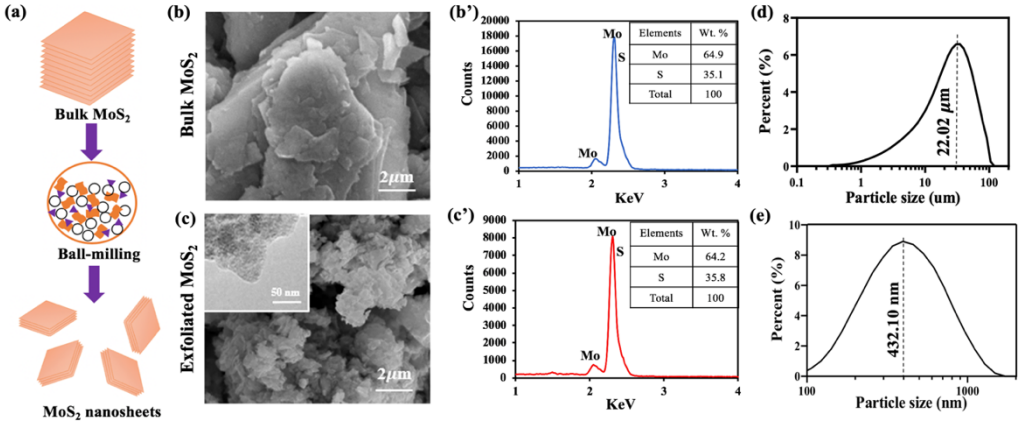

Figure 2 (a) Schematic illustration of MoS_2 by ball-milling, (b, c) SEM images (scale bar = 2 μm) and (b', c') EDX spectrum, (d, e) particle size distribution (PSD) of bulk and exfoliated MoS_2, inset of (c) is TEM image of the exfoliated MoS_2 nanosheets (scale bar = 50 nm).

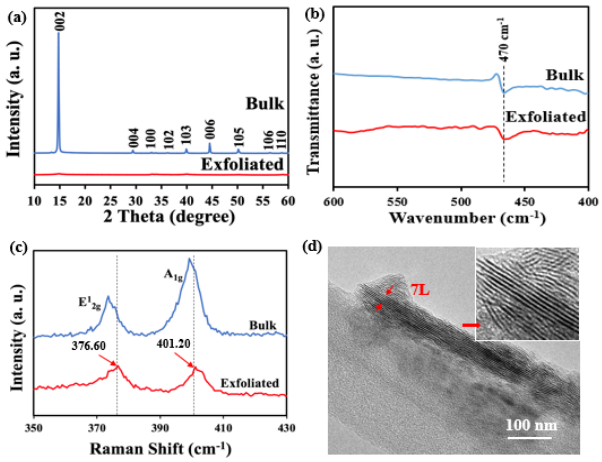

Figure 3 (a) XRD pattern, (b) FTIR spectra, (c) Raman spectra of bulk and exfoliated MoS_2, (d) TEM image of few-layer MoS_2 (scale bar = 100 nm), inset of (d) is a zoom-in image of seven-layer structure.

between E^1_{2g} (376.60 cm^{-1}) and A_{1g} (401.20 cm^{-1}) of exfoliation MoS_2 was 24.60 cm^{-1}, which was applied to the identification of the layer number (N) as shown in equation (4),[26]

$$\Delta\omega\ (A_{1g} - E^1_{2g}) = 25.80 - 8.40/N \qquad (4)$$

The calculated N of exfoliated MoS_2 was reduced up to 7 layers, providing the evidence of the successful delamination of the bulk MoS_2 and confirmed by TEM image in figure 3(d) as 7 layers.

The cross-section of bulk MoS_2 composite film was composed of irregular MoS_2 sheets with a random arrangement, showing a thickness of 111.05 μm (figure 4(a)). Adding the same amount of the exfoliated MoS_2 in the composite film showed a multilayered stacking, cross-sectional structure with a decreased thickness (87.07 μm) in figure 4(b). This is due to the fact that the nano-size MoS_2 sheets could enhance the molecular interaction between the filler (MoS_2) and the binder (CMC) by weakening the chemical and intermolecular forces of the filler, which provided a dense and smooth coverage and also reduced the voidage of the film.[27] EDX analysis showed that the addition of CMC as a binder had no effect on the elemental analysis (shown as figure 4(c)), but only held the as-prepared MoS_2 nanosheets together.

3.2 X-ray attenuation measurements

An initial study provided the evaluation of X-ray attenuation ability between bulk MoS_2 film and exfoliated MoS_2 (layered) film. Figure 5 depicted the X-ray transmission of the controls (air and membrane) and as-prepared MoS_2 composite films at the energy of 30 kVp. The membrane did show a slight decrease in the X-ray transmission but only by 1.20 %, while it was negligible, there still was a small effect on the X-ray shielding. Comparing the bulk and exfoliated MoS_2 composites, it clearly illustrated that by decreasing the particle size of MoS_2 from 22.02 μm to 432.10 nm, there was a significant decrease in X-ray transmission from bulk MoS_2 composite (64.10 %) to the exfoliated (55.06 %) at 30 kVp. By providing the same amount of MoS_2 loading, the exfoliated MoS_2 composite film achieved 15 % more of X-ray attenuation enhancement with a lesser thickness (87.07 μm), compared with to its bulk counterpart (111.05 μ m). Generally, photoelectric absorption dominates at the low X-ray energy (less than 200 keV) when the X-ray travels through a shielding material. A photon is completely

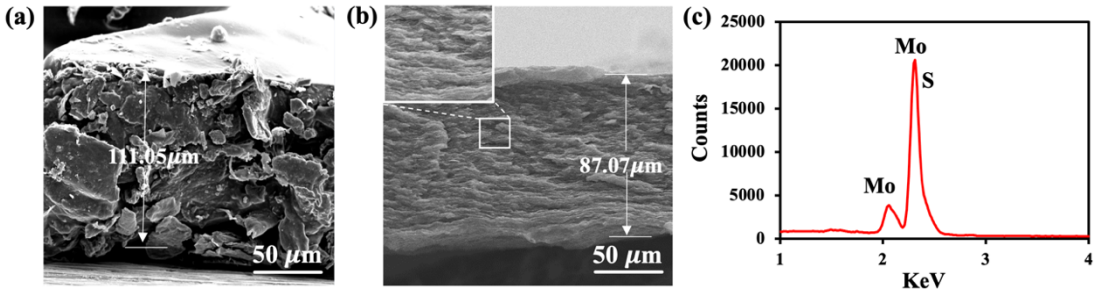

Figure 4 Cross-sectional SEM images of (a, b) bulk and exfoliated MoS_2 composite films showing the corresponding thicknesses (without the membrane) (scale bar = 50 μm), inset of (b) is a zoom-in image of the multilayered structure, and (c) is EDX spectrum of the cross-section (exfoliated MoS_2 composite).

absorbed by the atoms within the shielding material, and a photoelectron is generated and ejected from the material.[4, 28] During this process, the incorporation of nanofillers (exfoliated MoS_2 nanosheets) within the composite materials has high potential to enhance the X-ray absorption, due to the high surface-to-volume ratio of the nanomaterials.[1] Importantly to note, the formation of the multilayered (exfoliated) MoS_2 film (shown in figure 4(b)) benefited X-ray attenuation ability by facilitating the multiple scattering of incoming X-ray photon energy.[29, 30]

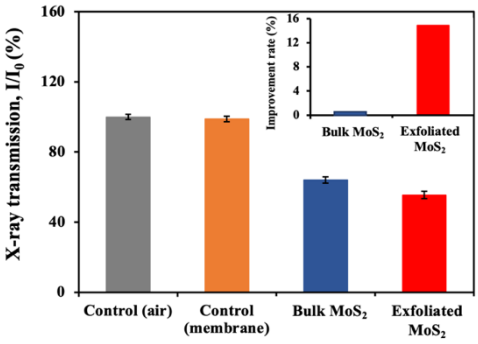

Figure 5 Initial study of X-ray transmission difference between bulk and exfoliated MoS_2 (layered structure) films, and the controls (air and membrane) at X-ray energy of 30 kVp, inset is improvement rate of the exfoliated MoS_2 compared with bulk MoS_2 composite.

3.3 Material thickness and Pb sheet benchmarking

The photon intensity of low-energy X-ray can be attenuated by the photoelectric absorption, which is significantly dependent on the thickness (or density) of the shielding material.[31] Optimization of the material thickness is thus of great importance with the aim of designing a lightweight X-ray shielding composite.[32] Figure 6 demonstrated that by increasing the thickness of the exfoliated MoS_2 composite films from 0.11 mm to 1.34 mm this could effectively attenuate the X-ray transmission down to 0.09 %.

Pb equivalence is a measure for radiation attenuation ability of non-Pb shielding materials compared to that of Pb sheets with specific thicknesses.[30, 33] The X-ray transmission value of the exfoliated MoS_2 composite with the optimized thickness of 1.34 mm was further evaluated with that of 0.20 mm Pb sheet (0.10 %) calculated by XCOM, indicating this optimized exfoliated MoS_2 composite exhibited comparable 0.20 mm Pb-equivalent attenuation at 30 kVp (inset of figure 6). Although the optimized thickness (1.34 mm) was much thicker than the 0.20 mm Pb sheet, the weight of the optimized exfoliated MoS_2 composite film (minus the membranes) at 1.18 g was 50 % lighter than the 0.20 mm Pb (2.17 g).

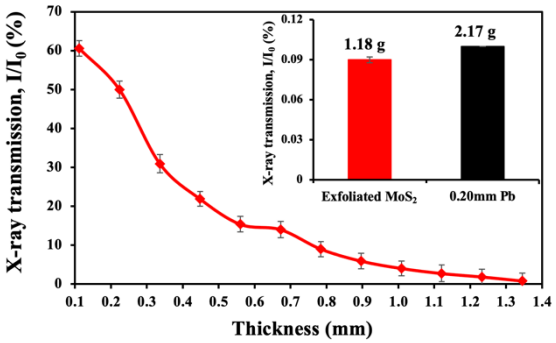

Figure 6 X-ray transmission of the exfoliated MoS_2 composite compared with increasing total composite film thicknesses, inset is the X-ray transmission of the optimized exfoliated MoS_2 composite compared with 0.20 mm Pb sheet.

4. Conclusion

In this work, the use of exfoliated MoS_2 composite was explored for X-ray shielding applications. The optimized weight ratio of layered MoS_2 composite with a thickness of 1.34 mm provided the most effective X-ray shielding performance at the low energy (30 kVp). It also demonstrated that the optimized exfoliated MoS_2 composite with a lightweight of 1.18 g enabled to provide 0.20 mm Pb-equivalent (2.17 g) X-ray attenuation at 30 kVp. In addition, both of MoS_2 and CMC are cheap and environmentally friendly raw materials, which further enhances the potential use as a non-toxic composite. This new, lightweight, non-toxic, layered material composite exhibited its ability as an X-ray shielding alternative to the traditional Pb-based materials, thus providing the evidence for potential low-energy X-ray protection application.

Conflicts of interest

The authors declare no conflict of interest.

Acknowledgements

The authors acknowledge the financial support from the ARC Research Hub for Graphene Enabled Industry Transformation, (IH150100003). We thank Australian Microscopy for the access of SEM, TEM facilities, Mr. Ken Neubauer, Dr. Ashley Slattery for their technical support on SEM and TEM measurements.

Reference

[1]L. Yu, A. L. C. Pereira, D. N. H. Tran, A. M. C. Santos, D. Losic, Materials Chemistry and Physics 2021, 260.
[2]H. A. Maghrabi, A. Vijayan, F. Mohaddes, P. Deb, L. Wang, Fibers and Polymers 2017, 17, 2047.

[3]H. Xu, T. Wang, C. Yang, X. Li, G. Liu, Z. Yang, P. K. Singh, S. Krishnan, D. Ding, Advanced Functional Materials 2018, 28.
[4]C. V. More, Z. Alsayed, M. S. Badawi, A. A. Thabet, P. P. Pawar, Environ Chem Lett 2021, 1.
[5]B. o. L. Statistics, in *Radiologic and MRI Technologists*, US Department of Labor, 2019.
[6]J. Le Heron, R. Padovani, I. Smith, R. Czarwinski, Eur J Radiol 2010, 76, 20.
[7]N. Aral, F. Banu Nergis, C. Candan, Textile Research Journal 2015, 86, 803; Q. Li, R. Zhong, X. Xiao, J. Liao, X. Liao, B. Shi, ACS Appl Mater Interfaces 2020, 12, 54117; D. Fernandez-Antoran, G. Piedrafita, K. Murai, S. H. Ong, A. Herms, C. Frezza, P. H. Jones, Cell Stem Cell 2019, 25, 329.
[8]N. Z. Noor Azman, S. A. Siddiqui, M. Ionescu, I. M. Low, Nuclear Instruments and Methods in Physics Research Section B: Beam Interactions with Materials and Atoms 2012, 287, 120.
[9]S. Nambiar, E. K. Osei, J. T. W. Yeow, Journal of Applied Polymer Science 2013, 127, 4939.
[10]Y. Wang, R. Zhong, Q. Li, J. Liao, N. Liu, N. S. Joshi, B. Shi, X. Liao, J. Guo, Advanced Materials Technologies 2020, 5; N. Lee, S. H. Choi, T. Hyeon, Adv Mater 2013, 25, 2641.
[11]I. Dayana, T. Sembiring, A. P. Tetuko, K. Sembiring, N. Maulida, Z. Cahyarani, E. A. Setiadi, N. S. Asri, M. Ginting, P. Sebayang, Journal of Molecular Liquids 2019, 294.
[12]J. P. McCaffrey, H. Shen, B. Downton, E. Mainegra-Hing, Med Phys 2007, 34, 530.
[13]N. Z. Noor Azman, S. A. Siddiqui, I. M. Low, Applied Physics A 2012, 110, 137; H. A. Maghrabi, A. Vijayan, P. Deb, L. Wang, Textile Research Journal 2015, 86, 649; N. Z. Noor Azman, N. F. L. Musa, N. N. A. Nik Ab Razak, R. M. Ramli, I. S. Mustafa, A. Abdul Rahman, N. Z. Yahaya, Applied Physics A 2016, 122; A. Güngör, İ. K. Akbay, D. Yaşar, T. Özdemir, Progress in Nuclear Energy 2018, 106, 262.
[14]T. Vogl, K. Sripathy, A. Sharma, P. Reddy, J. Sullivan, J. R. Machacek, L. Zhang, F. Karouta, B. C. Buchler, M. W. Doherty, Y. Lu, P. K. Lam, Nat Commun 2019, 10, 1202.
[15]S. Australia, in *Protective clothing and protective devices for gonads*, Vol. 4543.3, AS/NZS, 2000.
[16]J. Viegas, L. A. Silva, A. M. S. Batista, C. A. Furtado, J. P. Nascimento, L. O. Faria, Industrial & Engineering Chemistry Research 2017, 56, 11782.
[17]APRANSA, 2015.
[18]M. J. Berger, J. H. Hubbell, S. M. Seltzer, J. Chang, J. S. Coursey, R. Sukumar, D. S. Zucker, K. Olsen, National Institute of Standards and Technology, U.S. Department of Commerce 2010.
[19]A. Ambrosi, X. Chia, Z. Sofer, M. Pumera, Electrochemistry Communications 2015, 54, 36.
[20]K. Krishnamoorthy, P. Pazhamalai, G. K. Veerasubramani, S. J. Kim, Journal of Power Sources 2016, 321, 112.
[21]G. Liu, N. Komatsu, ChemNanoMat 2016, 2, 500; Y. Li, X. Yin, X. Huang, X. Liu, W. Wu, International Journal of Hydrogen Energy 2020, 45, 16489.
[22]M. A. Santa Ana, E. Benavente, P. Gómez-Romero, G. González, J. Mater. Chem. 2006, 16, 3107; A. Tayyebi, N. Ogino, T. Hayashi, N. Komatsu, Nanotechnology 2020, 31, 075704.
[23]W. L. Zhang, D. Jiang, X. Wang, B. N. Hao, Y. D. Liu, J. Liu, The Journal of Physical Chemistry C 2017, 121, 4989.
[24]H. Sun, H. Liu, Z. Hou, R. Zhou, X. Liu, J.-G. Wang, Chemical Engineering Journal 2020, 387.
[25]C. Han, Y. Zhang, P. Gao, S. Chen, X. Liu, Y. Mi, J. Zhang, Y. Ma, W. Jiang, J. Chang, Nano Lett 2017, 17, 7767.
[26]X. Zhang, X. F. Qiao, W. Shi, J. B. Wu, D. S. Jiang, P. H. Tan, Chem Soc Rev 2015, 44, 2757.
[27]A. P. Kumar, D. Depan, N. Singh Tomer, R. P. Singh, Progress in Polymer Science 2009, 34, 479.
[28]N. Z. Azman, S. A. Siddiqui, I. M. Low, Mater Sci Eng C Mater Biol Appl 2013, 33, 4952.
[29]Q. Li, Q. Wei, W. Zheng, Y. Zheng, N. Okosi, Z. Wang, M. Su, ACS Appl Mater Interfaces 2018, 10, 35510.
[30]L. Yu, P. L. Yap, A. Santos, D. Tran, D. Losic, ACS Applied Nano Materials 2021, 4, 7471.
[31]M. Sharon, M. Sharon, in *Nuclear Chemistry*, 2021, 45.
[32]N. Z. Noor Azman, S. A. Siddiqui, H. J. Haroosh, H. M. Albetran, B. Johannessen, Y. Dong, I. M. Low, J Synchrotron Radiat 2013, 20, 741.
[33]S. Jayakumar, T. Saravanan, J. Philip, J Nanosci Nanotechnol 2018, 18, 3969.

Statement of Authorship

Title of Paper	Internal scattering loss in layered 2D materials films and their hetero laminates for enhanced low-energy X-Ray radiation shielding
Publication Status	☐ Published ☐ Accepted for Publication ☐ Submitted for Publication ☑ Unpublished and Unsubmitted w ork w ritten in manuscript style
Publication Details	Yu, L.; Nine, M. J.; Tung, T. T.; Pereira, A. L. C.; Hassan, K.; Tran, D. N. H.; Santos, A. M. C.; Losic, D.(2022) Internal scattering loss in layered 2D materials films and their hetero laminates for enhanced low-energy X-Ray radiation shielding. *Advanced Materials*.

Principal Author

Name of Principal Author (Candidate)	Le Yu		
Contribution to the Paper	Prepared and characterized on all the samples, and interpreted all the data as well as wrote the manuscript.		
Overall percentage (%)	85 %		
Certification:	This paper reports on original research I conducted during the period of my Higher Degree by Research candidature and is not subject to any obligations or contractual agreements with a third party that would constrain its inclusion in this thesis. I am the primary author of this paper.		
Signature		Date	03/03/2022

Co-Author Contributions

By signing the Statement of Authorship, each author certifies that:

i. the candidate's stated contribution to the publication is accurate (as detailed above);

ii. permission is granted for the candidate in include the publication in the thesis; and

iii. the sum of all co-author contributions is equal to 100% less the candidate's stated contribution.

Name of Co-Author	Md Julker Nine		
Contribution to the Paper	Edited and revised the manuscript.		
Signature		Date	03/03/2022

Name of Co-Author	Tung Tran		
Contribution to the Paper	Edited and revised the manuscript.		
Signature		Date	03/03/2022

Please cut and paste additional co-author panels here as required.

Statement of Authorship

Title of Paper	Internal scattering loss in layered 2D materials films and their hetero laminates for enhanced low-energy X-Ray radiation shielding
Publication Status	☐ Published ☐ Accepted for Publication ☐ Submitted for Publication ☑ Unpublished and Unsubmitted work written in manuscript style
Publication Details	Yu, L.; Nine, M. J.; Tung, T. T.; Pereira, A. L. C.; Hassan, K.; Tran, D. N. H.; Santos, A. M. C.; Losic, D.(2022) Internal scattering loss in layered 2D materials films and their hetero laminates for enhanced low-energy X-Ray radiation shielding. *Advanced Materials*.

Principal Author

Name of Principal Author (Candidate)	Le Yu		
Contribution to the Paper	Prepared and characterized on all the samples, and interpreted all the data as well as wrote the manuscript.		
Overall percentage (%)	85 %		
Certification:	This paper reports on original research I conducted during the period of my Higher Degree by Research candidature and is not subject to any obligations or contractual agreements with a third party that would constrain its inclusion in this thesis. I am the primary author of this paper.		
Signature		Date	03/03/2022

Co-Author Contributions

By signing the Statement of Authorship, each author certifies that:

i. the candidate's stated contribution to the publication is accurate (as detailed above);
ii. permission is granted for the candidate in include the publication in the thesis; and
iii. the sum of all co-author contributions is equal to 100% less the candidate's stated contribution.

Name of Co-Author	Ana L. C. Pereira		
Contribution to the Paper	Edited and revised the manuscript.		
Signature		Date	03/03/2022

Name of Co-Author	Kamrul Hassan		
Contribution to the Paper	Edited and revised the manuscript.		
Signature		Date	03/03/2022

Statement of Authorship

Title of Paper	Internal scattering loss in layered 2D materials films and their hetero laminates for enhanced low-energy X-Ray radiation shielding
Publication Status	☐ Published ☐ Accepted for Publication ☐ Submitted for Publication ☑ Unpublished and Unsubmitted work written in manuscript style
Publication Details	Yu, L.; Nine, M. J.; Tung, T. T.; Pereira, A. L. C.; Hassan, K.; Tran, D. N. H.; Santos, A. M. C.; Losic, D.(2022) Internal scattering loss in layered 2D materials films and their hetero laminates for enhanced low-energy X-Ray radiation shielding. *Advanced Materials*.

Principal Author

Name of Principal Author (Candidate)	Le Yu		
Contribution to the Paper	Prepared and characterized on all the samples, and interpreted all the data as well as wrote the manuscript.		
Overall percentage (%)	85 %		
Certification:	This paper reports on original research I conducted during the period of my Higher Degree by Research candidature and is not subject to any obligations or contractual agreements with a third party that would constrain its inclusion in this thesis. I am the primary author of this paper.		
Signature		Date	03/03/2022

Co-Author Contributions

By signing the Statement of Authorship, each author certifies that:

i. the candidate's stated contribution to the publication is accurate (as detailed above);
ii. permission is granted for the candidate in include the publication in the thesis; and
iii. the sum of all co-author contributions is equal to 100% less the candidate's stated contribution.

Name of Co-Author	Diana N. H. Tran		
Contribution to the Paper	Co-supervised and revised the manuscript.		
Signature		Date	03/03/2022

Name of Co-Author	Alexandre M. C. Santos		
Contribution to the Paper	Co-supervised, performed X-ray irradiations and revised the manuscript.		
Signature		Date	03/03/2022

Please cut and paste additional co-author pa

Statement of Authorship

Title of Paper	Internal scattering loss in layered 2D materials films and their hetero laminates for enhanced low-energy X-Ray radiation shielding
Publication Status	☐ Published ☐ Accepted for Publication ☐ Submitted for Publication ☑ Unpublished and Unsubmitted w ork w ritten in manuscript style
Publication Details	Yu, L.; Nine, M. J.; Tung, T. T.; Pereira, A. L. C.; Hassan, K.; Tran, D. N. H.; Santos, A. M. C.; Losic, D.(2022) Internal scattering loss in layered 2D materials films and their hetero laminates for enhanced low-energy X-Ray radiation shielding. *Advanced Materials*.

Principal Author

Name of Principal Author (Candidate)	Le Yu		
Contribution to the Paper	Prepared and characterized on all the samples, and interpreted all the data as well as wrote the manuscript.		
Overall percentage (%)	85 %		
Certification:	This paper reports on original research I conducted during the period of my Higher Degree by Research candidature and is not subject to any obligations or contractual agreements with a third party that would constrain its inclusion in this thesis. I am the primary author of this paper.		
Signature		Date	03/03/2022

Co-Author Contributions

By signing the Statement of Authorship, each author certifies that:

i. the candidate's stated contribution to the publication is accurate (as detailed above);

ii. permission is granted for the candidate in include the publication in the thesis; and

iii. the sum of all co-author contributions is equal to 100% less the candidate's stated contribution.

Name of Co-Author	Dusan Losic		
Contribution to the Paper	Supervised the development of the work, edited, revised the manuscript and acted as the corresponding author.		
Signature		Date	03/03/2022

Name of Co-Author			
Contribution to the Paper			
Signature		Date	

Please cut and paste additional co-author panels here as required.

Layered 2D Materials Films and Their Heterolaminates for Enhanced Low-Energy X-Ray Radiation Shielding

*Le Yu,[1,2] Md J. Nine, [1,2] Tran T. Tung, Ana C. Pereira, [1,3] Kamrul Hassan,[1,2] Diana Tran, [1,2] Alexandre Santos, [4,5] and Dusan Losic[1,2]**

[1]School of Chemical Engineering and Advanced Materials, The University of Adelaide, Adelaide, SA 5005, Australia

[2]ARC Research Hub for Graphene Enabled Industry Transformation, University of Adelaide, Adelaide, SA 5005, Australia.

[3] School of Applied Sciences, University of Campinas (UNICAMP), Limeira, 13484-350, Brazil

[4] School of Physical Sciences, University of Adelaide, Adelaide, South Australia 5005, Australia.

[5] Department of Medical Physics, Royal Adelaide Hospital, Adelaide, South Australia 5000, Australia.

*Dusan Losic: E-mail: Dusan.losic@adelaide.edu.au

Keywords: 2D materials, multilayered, X-rays, X-rays shielding

Abstract

Protection from ionizing electromagnetic radiation is of great significance for medical, space, nuclear industry, and defence sectors, where the conventional shielding materials have their limitations to provide the required high level of safety. In this paper, we present a new concept using multilayered 2D materials and their heterolaminates for X-ray shielding enhancement, due to the multiple scattering and reflecting of photons between the nano-layered structures. To practically demonstrate this phenomenon, we explored the X-ray shielding performance of the prepared multilayered films composed of exfoliated few-layers 2D sheets of MoS_2, antimony, Mxene and their heterolaminates combinations (MoS_2 +Mxene). These exfoliated films showed significant X-ray shielding enhancement (40-50 %) at lower energy, compared with their bulk structures. Further investigation on X-ray attenuation performance of the laminates (MoS_2+Mxene) films provided promising shielding enhancement. The enhanced shielding efficiency can be explained by the cascade of multiple scattering of X-rays photons within the layered monoatomic 2D sheets. The designed layered structure can offer a promising strategy for the development of new generation of Pb-free shielding materials.

The ionizing radiation emitted from the radioactive substances and natural sources can be classified as α, β, γ, X, or neutron in the form of radiated waves or particles.[1]

Currently, there is a growing demand for applying ionizing radiation (e.g., X-ray) to many different fields, including the defence, nuclear, medical and space sectors.[2] For instance, medical irradiation in the UK is considered as one of the largest artificial sources for radiation exposure, which brings a great concern for human health.[3] An efficient, low-cost and affordable radiation shielding material is in high demand to protect the related practitioners from overexposure to hazardous X-ray (or γ-ray).[4]

For protection of X-ray radiation, metallic lead (Pb) is considered as the conventional shielding material (in its different forms), for examples, Pb bricks, Pb glass and Pb-based garments, to block and absorb most of this radiation.[1, 5] However, Pb-based materials have many disadvantages of being extremely heavy, uncomfortable to wear, highly toxic, non-disposable, and environmentally unsustainable.[6] It is thus of great importance to develop a new generation of lightweight, non-toxic and sustainable Pb-free radiation shielding materials, which comply with the international standards for X-ray radiation protection. To achieve this goal, several materials with high atomic number (Z) and densities, such as tin (Sn), antimony (Sb), tungsten (W)[7] bismuth (Bi) have been explored as new Pb-alternatives.[7, 8] Most of these materials are prepared in different forms, such as polymer-based composites, films, and fabrics that show promising shielding advancements.[9] Although polymer-based composites have been widely used for the formation of lightweight Pb-free X-ray shielding materials, the pin holes and voids within the composites have a negative effect on X-ray attenuation, as the incident X-ray can easily pass through these voids.[10] To solve this problem, a material with a densely packed structure is desirable to stop the penetration of the incident X-ray. A study from our group has showed the advantages of using nanomaterials with high surface-to-volume (SA/V) ratios can provide improved shielding performance.[11] This is due to the fact that the high SA/V nanomaterials are homogenously dispersed in the film to create a densely packed layer.[10] This result also indicated that by designing the internal architecture of the material it is possible to further enhance their radiation shielding performances, compared to their uniform bulk structures.

Since the debut of graphene in 2004, 2D materials have received their designation as "materials of the 21st century",[12] owing to their unique monoatomic 2D structures and outstanding properties, including physical, chemical, electrical, optical, magnetic, thermal, mechanical etc.[12, 13] They have opened a new horizon in materials science and engineering for creating novel materials, properties, and devices for a broad range of

applications.[14] The recent discovery that the combination of two or more 2D materials in the form of laminated structure could generate new and more intriguing properties,[15] which is different from their single-layer structures.[15, 16] This opens unprecedent opportunities toward new discoveries and applications using 2D layered structures.[17, 18] It is reasonable to assume that these 2D materials and their laminated structure may have different impact on radiation shielding properties.[18] For example, the significant effect of 2D layered materials (e.g., graphene[19] and Mxene[20, 21]) towards electromagnetic interference shielding (EMI) was first demonstrated, owing to their unique multilayered structure.[21, 22] To adapt this idea for X-ray shielding application, it is hypothesized that this multilayer structure can increase the probability of X-ray scattering and interaction, leading to the enhanced X-ray shielding ability. Moreover, this phenomenon is not further explored and delivered to practical applications, which can broaden its utilization for the development of new shielding materials that are needed for space exploration, and medical and nuclear industries.

This paper presents the first demonstration for the effect of multilayered 2D material structures and the combination of several 2D materials with a heterolaminated structures on the X-ray shielding performance, because of the multiple scattering and interactions of the incoming X-ray photons occurring within each layer. This phenomenon has been not observed in their uniform bulk structures with the same thickness. The proposed concept is presented in Figure 1. This hypothesis is built on the idea of the unique structural properties of these multilayered films consisting of few-layer 2D material sheets, where each layer can act as a single nanolayered shielding barrier. This multilayered structure of 2D materials towards X-ray radiation is proposed to provide multiple scattering/absorption, leading to increased probability of interaction with X-ray photons, compared to their bulk materials. To demonstrate this behaviour, we prepared these multilayered films that consisted of several 2D materials including few-layer MoS_2, antimony and Mxene, as well as their heterolaminated combinations (MoS_2+Mxene), followed by the investigation on their X-ray shielding performance at low-energy X-ray (30 kVp), compared with their bulk films. The experimental setup is shown in Figure S1.

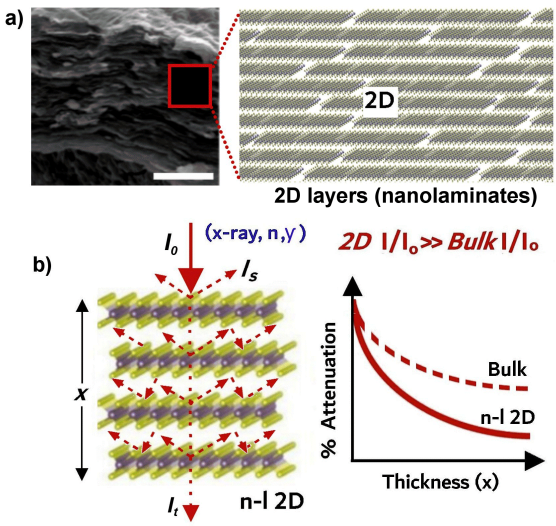

Figure 1. Cross-sectional SEM images of the multilayered structure of 2D film showing aligned layers of 2D nanosheets, which are schematically presented on the right and b) schematic illustration of interaction between X-ray and the layered structure composed of 2D crystals, showing multiple scattering occurred from each layer. The attenuation efficiency of a few-layer 2D material compared to its bulk material with the same thickness (or mass of material) is presented on the right.

Comprehensive characterizations of the synthesized few-layers MoS_2 sheets, antimony and Mxene and their multilayered films are summarized in Figure 2 and Figure S2-S4. A ball-milling method was employed to exfoliate a large quantity of microsized MoS_2 sheets with an average particle size of 22 μm (Figure S2) into few-layers nanosheets with an average particle size of 432 nm (Figure 2(a) and Figure S2). Corresponding SEM and TEM image (Figure S2(a) and Figure 2(a)) confirmed the presence of the sheet-like MoS_2 structure with significant changes in their particle size and morphology. High-resolution TEM showed exfoliated MoS_2 nanosheet with ~ 7 layers (inset of Figure 2(a)), and Raman, XRD, FTIR analysis (Figure S2) exhibited significant difference from bulk MoS_2. Few-layer Mxene were prepared using a common etching process from Ti_3AlC_2 MAX phase materials described in literature. The typical structure of few-layer Mxene was characterized by SEM and TEM are summarized in Figure 2(b). and Figure S2. These images confirmed a typical few-layer structure of Mxene with the dimension of few hundred nanometers. Few-layer antimony (FL-Sb) nanosheets were synthesized in a 4:1 isopropanol/water mixture by exfoliating bulk Sb crystals using a combination of ball milling and ultrasonication, and the structural differences before and after exfoliation are summarized in Figure 2(c) and Figure S3. Their SEM, TEM and AFM images confirmed FL-Sb sheets with lateral sizes in a few-hundred nanometers (Figure 2(c) and Figure S3). It also showed

typical signatures of FL-Sb which agrees with literature (Figure S3). These prepared 2D materials were used to make their multilayered films where a vacuum filtration process was applied to make the assembly of few-layer sheets into a multilayered structure in the film. Their cross-sectional SEM images presented in Figure 2(d-f) of these films confirmed the formation of the multilayered structure, where the thickness of the film could be controlled from tens to several hundreds of microns.

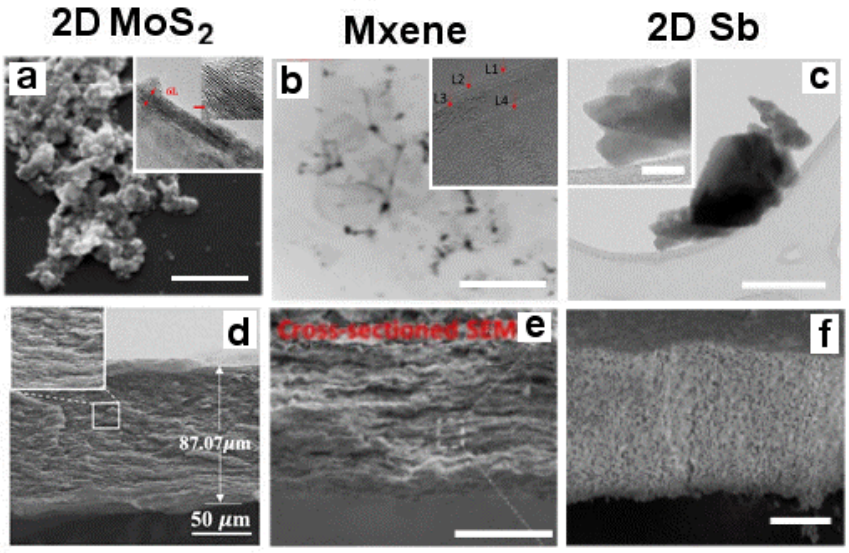

Figure 2. SEM images (scale bar = 1 μm) of the exfoliated nanosheets from the selected 2D materials a) MoS2, b) antimony, and c) Mxene, with their corresponding TEM images (inset of a), b) and c)), and cross-sectional SEM images of the prepared films from d) MoS_2, e) antimony and f) Mxene.

The study on X-ray transmission and the attenuation enhancement of the prepared multilayered MoS_2, Mxene and antimony films compared to their bulk structures is presented in Figure 3 and Table S1. These results clearly showed a significant decrease in X-ray transmission of 2D multilayered films at 30 kVp, compared to their bulk counterparts. Figure 3(b) presented the X-ray attenuation enhancement rate of 46.67 % for MoS_2 film, 37.28 % for 2D antimony film and 41.07 % for Mxene film, compared to their bulk material films. It is worth noting that the mass loading of all the prepared films were the same, therefore the observed results is related to differences in their structures. The obtained results at lower X-ray energy of 30 kVp are presented. However, the X-ray transmission measurements at higher energy of 50 kVp and 80 kVp also showed the same trend in the shielding enhancement but with lower impact (data not shown).

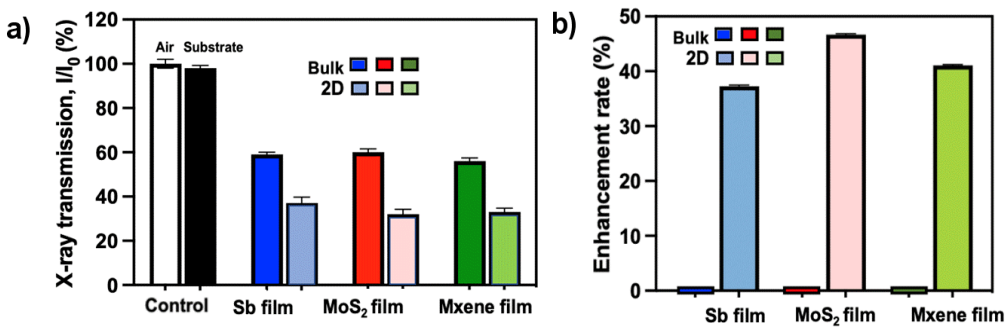

Figure 3. Comparative X-ray transmission results performed at 30 kVp showing difference in X-ray shielding performance between bulk and multi-layered films of selected 2D materials composed of assembled 2D sheets of MoS_2, antimony and Mxene; b) the enhancement rate in % in multilayered films compared to their bulk counterparts. All tested materials were used with the same mass loading.

It is important to state that X-ray shielding is dependent on the thickness of the materials. By increasing the thickness of these 2D multilayered films, it is possible to create a new generation of lightweight X-ray shielding materials that could be comparable with Pb materials. Optimization of X-Ray shielding performance was further demonstrated by controlling the film thickness, by preparing MoS_2 2D films with different thicknesses. Figure S4 presents the X-ray transmission results showing that by increasing the thickness of the MoS_2 films from 0.11 mm to 1.34 mm this could effectively attenuate the X-ray transmission down to 0.09 %. The X-ray transmission value of the exfoliated MoS_2 composite with the optimized thickness of 1.34 mm was further evaluated with that of 0.20 mm Pb sheet indicating this optimized exfoliated MoS_2 composite exhibited comparable 0.20 mm Pb-equivalent attenuation at 30 kVp (inset of Figure S4). Although the optimized thickness (1.34 mm) was much thicker than the 0.20 mm Pb sheet, the weight of the optimized exfoliated MoS_2 composite film (minus the membranes) at 1.18 g was 50 % lighter than the 0.20 mm Pb (2.17 g). This provides outstanding results that is comparable to Pb and very promising for the development of new generation of Pb-free shielding materials.

To further investigate on the potential effect of the laminated structure materials for X-ray radiation shielding applications, laminated 2D films were prepared by combining two or more 2D material sheets followed by testing of the X-ray shielding performance. Figure 4 presents that X-ray transmission results were performed at 30 kVp using the prepared laminated 2D films by the combination of MoS_2 and Mxene, showing further significant enhancement of X-ray attenuation. Comparing between the heterolaminated

film (a combination of 2D MoS_2 (A) and Mxene (B) as double heterolaminated structure (A+B)) and single 2D MoS_2 or 2D Mxene, 12.85 % of X-ray attenuation enhancement was observed compared to 2D MoS_2 and 6.62% compared to 2D Mxene (Figure 4(b-c)). When a quadruple laminated film structure (A+B+A+B) was used with the same mass loading as the individual 2D MoS_2 or 2D Mxene, further significant enhancement of 62.26 % was observed for single 2D MoS_2 and 59.57 % for 2D Mxene. In both cases, the MoS_2 structure was on the top of their laminated films. There was no significant difference when the opposite orientation (Mxene was on the top) was used. Importantly to note, the synergetic effect of the doubled (or quadruple) 2D layered materials needed to be further explored for understanding the mechanism and interaction of X-rays at the interface of these laminated structures. These results suggested another promising strategy to improve the shielding performance of 2D materials has not been explored and considered before.

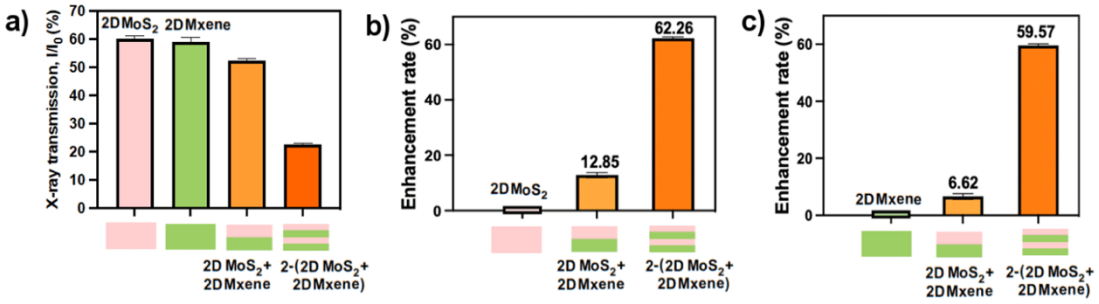

Figure 4. X-ray transmission results performed using 2D heterolaminated structure combined by MoS_2 and Mxene in the forms of double and quadruple laminated films; b) the enhancement rate of heterolaminated films (MoS_2 + Mxene) compared to individual 2D MoS_2 layered film, and c) the enhancement rate of heterolaminated films (MoS_2 + Mxene) compared to individual 2D Mxene layered film. All tested materials were used with the same mass loading and X-ray shielding was performed at 30 kVp.

The results showing the enhanced X-ray shielding of the layered 2D materials and their laminated structures were undoubtfully demonstrated by the presented experiments. However, our attempt to use simulation based on the Monte Carlo system to predict these properties wasn't successful. The main reason is that high complexity of the model needed to be built up for considering the multilayered 2D structure in the film compared with the uniform bulk film. So far, there is no simulation model on 2D materials based on their laminated structure. We expect these models will be developed in the future and will be able to theoretically verify our experimental results. X-ray attenuation is the

process of the X-ray intensity reduction via either absorption or scattering when X-ray photons pass through the shielding material.[23] It involves three interaction mechanisms including (1) photoelectric effect, (2) Compton scattering, and (3) pair production.[24] To explain the observed attenuation results of the 2D layered materials, we assumed that the X-ray shielding performance can be enhanced as a result of multiple scattering and absorption occurring during the incoming X-ray photons that interacted with the multilayered 2D material films. This type of scattering process is not observed within the bulk materials, where most of the deflection occurred on the surface, as schematically presented in Figure 1. The multilayered 2D material films can increase the probability of photoelectric effect within each layer, leading to enhanced X-ray shielding ability.[25] In other word, incident X-ray is absorbed and reflected many times between each layer within the multilayered 2D material films. In terms of the combined layered heterolaminates of two or more 2D material films, the multiple interfaces between each layer of the 2D laminates ensure that X-ray photons can undergo scattering and absorption multiple times as shown in Figure 5. More studies are needed to explore the mechanism of X-ray interactions within these heterolaminated 2D structures.

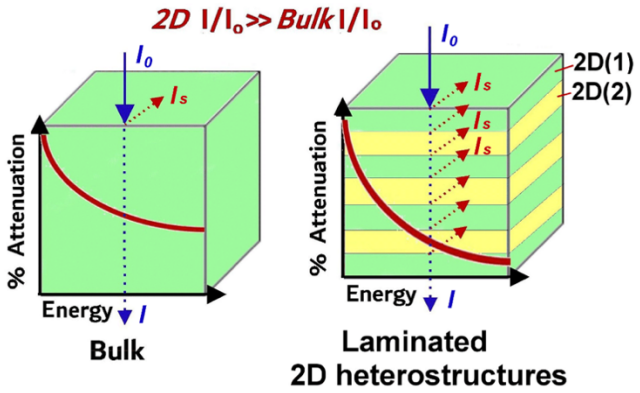

Figure 5. The schematic illustration showing explanation of X-ray shielding on laminated structure combining 2D materials (example: MoS_2 and Mxene) compared with the bulk material (example: only MoS_2).

In summary, it was demonstrated that the films composed of layered 2D materials such as 2D MoS_2, Mxene and antimony and their heterolaminated structure have benefits to attenuate X-ray, due to multiple scattering and absorption within the layered structures. The X-ray shielding performance obtained from the experiments using low-energy X-ray at 30 kVp showed significant enhancement of attenuation of 46.67 % for 2D MoS_2, 37.28 %

for antimony and 41.07 % for Mxene, compared with their bulk counterparts. Significant X-ray shielding enhancement of the double laminated structure by combining MoS_2 and Mxene (2D MoS_2 +2D Mxene +2D MoS_2 +2D Mxene) showed 62.26 % for single 2D MoS_2 and 59.57 % of single 2D Mxene. These results indicated that the layered 2D materials can be a promising candidate for X-ray shielding application. The promising X-ray shielding properties of these laminated 2D materials will open a new horizon for designing an advanced Pb-free shielding material. Further studies based on the theoretical modeling and experimental evidence about these interactions are needed to provide more insights to this mechanism. The presented paper showed another exciting property of 2D materials that can be considered as a new radiation shielding technology.

Experimental Section

Experimental information is available in supporting information.

Supporting Information

Supporting Information is available from the Wiley Online Library or from the author.

Acknowledgements

The authors acknowledge the financial support from the ARC Research Hub for Graphene Enabled Industry Transformation, (IH150100003). We thank Australian Microscopy for the access of SEM, TEM facilities, Mr. Ken Neubauer, Dr. Ashley Slattery for their technical support on SEM and TEM measurements.

References

[1] S. Nambiar, J. T. Yeow, ACS Appl Mater Interfaces 2012, 4, 5717.
[2] Y. R. Uhm, J. Kim, S. Lee, J. Jeon, C. K. Rhee, Industrial & Engineering Chemistry Research 2011, 50, 4478.
[3] J. S. Hughes, S. J. Watson, A. L. Jones, W. B. Oatway, J Radiol Prot 2005, 25, 493.
[4] R. Fazel, H. M. Krumholz, Y. Wang, J. S. Ross, J. Chen, H. H. Ting, N. D. Shah, K. Nasir, A. J. Einstein, B. K. Nallamothu, N Engl J Med 2009, 361, 849.
[5] Q. Li, Y. Wang, X. Xiao, R. Zhong, J. Liao, J. Guo, X. Liao, B. Shi, J Hazard Mater 2020, 398, 122943.
[6] *Radiation Physics for Medical Physicists*, 2016; Q. Li, R. Zhong, X. Xiao, J. Liao, X. Liao, B. Shi, ACS Appl Mater Interfaces 2020, 12, 54117.
[7] Y. Wang, R. Zhong, Q. Li, J. Liao, N. Liu, N. S. Joshi, B. Shi, X. Liao, J. Guo, Advanced Materials Technologies 2020, 5.
[8] Q. Zhang, Q. Liang, Z. Zhang, Z. Kang, Q. Liao, Y. Ding, M. Ma, F. Gao, X. Zhao, Y. Zhang, Advanced Functional Materials 2018, 28; D. He, N. Zhang, A. Iqbal, Y. Ma, X. Lu, Z.-A. Qiao, J.-H. Yu, H. Xu, W. Wang, R. Zhao, X. Li, Z. Zhou, C. Jin, C. M. Koo, C. Wang, Communications Materials 2021, 2.

[9] V. Harish, N. Nagaiah, T. N. Prabhu, K. T. Varughese, Journal of Applied Polymer Science 2010, n/a; S. Verma, M. Mili, C. Sharma, H. Bajpai, K. Pal, D. Qureshi, S. A. R. Hashmi, A. K. Srivastava, Green Chemistry Letters and Reviews 2021, 14, 272.
[10] Y. Kim, S. Park, Y. Seo, Industrial & Engineering Chemistry Research 2015, 54, 5968.
[11] L. Yu, A. L. C. Pereira, D. N. H. Tran, A. M. C. Santos, D. Losic, Materials Chemistry and Physics 2021, 260.
[12] K. S. Novoselov, A. Mishchenko, A. Carvalho, A. H. Castro Neto, Science 2016, 353, aac9439.
[13] S. Manzeli, D. Ovchinnikov, D. Pasquier, O. V. Yazyev, A. Kis, Nature Reviews Materials 2017, 2.
[14] S. Das, M. Kim, J.-w. Lee, W. Choi, Critical Reviews in Solid State and Materials Sciences 2014, 39, 231.
[15] J. Wang, Z. Zhang, J. Zhu, M. Tian, S. Zheng, F. Wang, X. Wang, L. Wang, Nat Commun 2020, 11, 3540.
[16] P. Ares, K. S. Novoselov, Nano Materials Science 2021.
[17] S. Acevedo, L. Giraldo, J. C. Moreno-Pirajan, ACS Omega 2020, 5, 10423.
[18] P. T. Hammond, Advanced Materials 2004, 16, 1271.
[19] C. Pavlou, M. G. Pastore Carbone, A. C. Manikas, G. Trakakis, C. Koral, G. Papari, A. Andreone, C. Galiotis, Nat Commun 2021, 12, 4655.
[20] F. Shahzad, M. Alhabeb, C. B. Hatter, B. Anasori, S. Man Hong, C. M. Koo, Y. Gogotsi, Science 2016, 353, 1137.
[21] T. Yun, H. Kim, A. Iqbal, Y. S. Cho, G. S. Lee, M. K. Kim, S. J. Kim, D. Kim, Y. Gogotsi, S. O. Kim, C. M. Koo, Adv Mater 2020, 32, e1906769.
[22] S.-H. Lee, D. Kang, I.-K. Oh, Carbon 2017, 111, 248; Y. Bhattacharjee, I. Arief, S. Bose, Journal of Materials Chemistry C 2017, 5, 7390.
[23] I. M. Low, N. Z. Noor Azman, *Polymer Composites and Nanocomposites for X-Rays Shielding*, 2020.
[24] E. B. Podgorsak, *Radiation oncology physics*, International Atomic Energy Agency, Vienna 2005.
[25] Z. Li, W. Zhou, X. Zhang, Y. Gao, S. Guo, Sci Rep 2021, 11, 4384.

Supporting Information

Layered 2D Materials Films and Their Heterolaminates for Enhanced Low-Energy X-Ray Radiation Shielding

*Le Yu,[1,2] Md J. Nine, [1,2] Tran T. Tung, Ana C. Pereira, [1,3] Kamrul Hassan,[1,2] Diana Tran, [1,2] Alexandre Santos, [4,5] and Dusan Losic[1,2]**

[1]School of Chemical Engineering and Advanced Materials, The University of Adelaide, Adelaide, SA 5005, Australia

[2]ARC Research Hub for Graphene Enabled Industry Transformation, University of Adelaide, Adelaide, SA 5005, Australia.

[3] School of Applied Sciences, University of Campinas (UNICAMP), Limeira, 13484-350, Brazil

[4] School of Physical Sciences, University of Adelaide, Adelaide, South Australia 5005, Australia.

[5] Department of Medical Physics, Royal Adelaide Hospital, Adelaide, South Australia 5000, Australia.

Experimental Section

***Chemicals and materials**:* Molybdenum disulfide powder (MoS_2, 99.99%, 23 μm) and sodium bromide (NaBr) was purchased from Chem-Supply (Australia). Bulk crystalline antimony (Sb) with 99.9% purity was purchased from Smart Elements, Austria. The Ti_3AlC_2 MAX was supplied by Carbon-Ukraine. Carboxymethylcellulose sodium salt (CMC, high viscosity) was provided by Aldrich Sigma (Australia).

Preparation of few layers 2D materials: Bulk MoS_2 powder was exfoliated using a Planetary Ball Mill PM 200 (Retsch, Australia) with zirconium balls (3 mm in diameter). NaBr was added to facilitate the process of the ball milling with a weight ratio of NaBr: MoS_2 at 20:1, and the weight ratio of balls to powder was also 20:1. After the dry ball milling process, NaBr in the as-prepared mixture was removed by washing several times using distilled (DI) water with the aid of a centrifuge (Sigma, Australia, 4200rpm) and then dried in oven at 50°C overnight for the further step. The synthesis steps of Mxene materials mainly followed a literature guideline.[1] Briefly, the small pieces of Ti_3AlC_2 MAX phase were ground into fine powders using a mortar, and the powders having a particle size of less than 25 μm were selected by a 25 μm sieve and collected for further

use. Lithium fluoride (1.5 g) was added to 20 ml of 9M HCl solution in a reaction vessel under and stirred with a magnetic bar, then 1 gram of Ti_3AlC_2 was slowly added into the solution. The mixture was maintained in an oil bath environment at 35 ºC for 24 h. After the etching reaction was completed, the reacted mixture was subjected to centrifugal washing with deionized H_2O at 3500 rpm for 30 minutes. This washing procedure was repeated 5 to 6 times until the pH value reached around 6, and a relatively pure Ti_3C_2Tx product (Mxene) was obtained. After washing, the product was ultrasonically separated to obtain a two-dimensional layered Mxene material. A small amount of Mxene powder was obtained by drying the raw Mxene material, and its electrical conductivity was tested. Few-layer antimony (FL-Sb) nanosheets were prepared in a 4:1 isopropanol/water mixture by exfoliating bulk Sb crystals using a combination of ball milling and ultrasonication. Bulk Sb crystals were put in a zirconia milling pot with isopropanol/water solvent. The samples were then ball-milled using Retsch planetary ball mill (PM 200) with zirconia balls (1 mm) at 300 rpm for 30 min. After drying, the ball-milled Sb flakes (30 mg) were re-dispersed in 4:1 isopropanol/water mixture (10 mL) for further exfoliation. The exfoliation was carried out in a bath ultrasonication for 40 min. Then the resulting black suspension was centrifuged at 3000 rpm for 3 min, and the dark grey supernatant was recovered.

***Preparation of 2D materials multilayered films and their laminated structures*:** Few-layer exfoliated MoS_2 were dispersed with DI water and then bath-sonicated for 1 h, respectively. CMC solution (0.5 wt.%) was added to the as-prepared MoS_2 solution with the optimized weight ratio to prepare dispersion with known MoS_2 concentration of 10 mg/ml. The mixture was then stirred constantly for 3 h at the room temperature (20 ± 2 ℃) followed by vacuum filtration onto the membrane to prepare MoS_2 films composed of multi layered structures of assembled MoS_2 sheets. The prepared MoS_2 film was then dried for 12 h in air at the room environment (20 ± 2 ℃) and used as freestanding film for X-ray experiments. The mass loading and thickness of the film was measured to be consistent with other prepared films using other 2D material. The Mxene film was produced by the same method of vacuum filtration as following details using Mxene dispersion in deionized water that was sonicated for 1 hour before filtration. Required volumes (2 ml to 8 mL) of as-prepared Mxene solutions were slowly filtrated by a vacuum filtration system to form Mxene layered films on the membranes. The Mxene-deposited membrane connected to the suction filter was placed in a vacuum drying oven and dried

at 40ºC for 12 h. After that, the entire system was taken out from the vacuum drying oven, the suction filter was removed, and then the dried Mxene film was carefully separated from the membrane and used for X-ray measurements. Similar process was applied to make 2D antimony layered films from prepared 2D FL-Sb dispersion with known concentration and volume to achieve with the same mass loading as 2D MoS_2 and 2D Mxene films. Double laminated films of 2D structure were prepared by stacking individual 2D MoS_2 layered film (A) and individual 2D Mxene layered film (B) into one combined structure (A+B). Quadrupole laminated films of 2D structures were prepared by double stacking individual 2D MoS_2 layered films and individual 2D Mxene layered films into the combined structure (A+B+A+B).

Characterization: a scanning electron microscope (SEM-FEI Quanta 450, Japan) in a low vacuum chamber at an accelerating voltage of 5 kV. The average thickness and particle topography of exfoliated FL-Sb was examined using an NT-MDT Ntegra Solaris Atomic Force Microscope (AFM) via tapping mode. NT-MDT SPM Software (Nova 1.0.26) was used for AFM image processing. A particle size analyzer from Malvern instrument (NanoSight NS300) was used to examine the average particle size distribution. A transmission electron microscope (TEM, FEI Titan Themis) was used to acquire nanoscale morphology and elemental analysis of exfoliated substances. Thermogravimetric analysis (TGA) of FL-Sb, PDMS and their composite were studied using Mettler-Toledo TGA/DSC 2, Switzerland in an air atmosphere at a constant heating rate of 5 °C/min. The vibrational stretching modes of different molecular bonds in PDMS modified samples were studied by Fourier transform infrared spectroscopy (FTIR) (Nicolet 6700 Thermo Fisher, USA).

X-ray radiation measurements: X-ray transmission testing was performed using a superficial X-ray tube (SXR) unit (Gulmay D3150, UK) as shown in Figure S7. The distances between the X-ray tube and sample-placing panel and sample-placing panel to the detector were equally 50 cm. The samples were exposed to the X-ray voltage range at 30, 50, 80, 100 kVp, respectively, for 0.50 min with the X-ray transmitted sample placing area of diameter at 1 cm, and the X-ray attenuation performance was evaluated as the transmission dose of samples divided by the transmission dose without the sample. Each sample was measured 3 times and determined by the arithmetic mean. The X-ray attenuation of an X-ray beam is expressed as a function of the linear attenuation coefficient (μ) and calculated using equation and procedure as reported elsewhere.

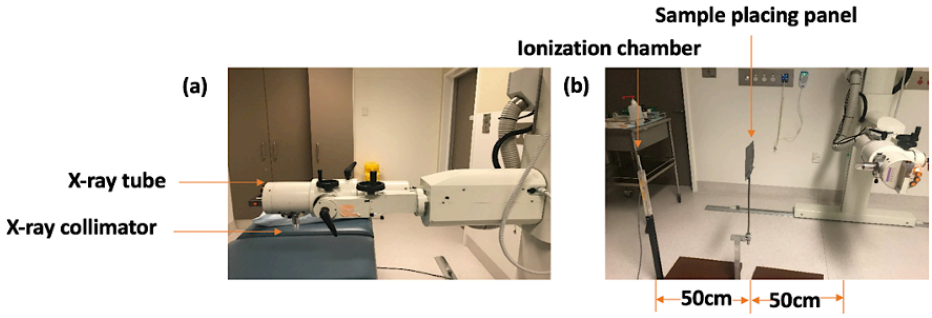

Figure S1. Schematic illustration of (a) superficial X-ray unit, and (b) experimental set-up of X-ray transmission.[2]

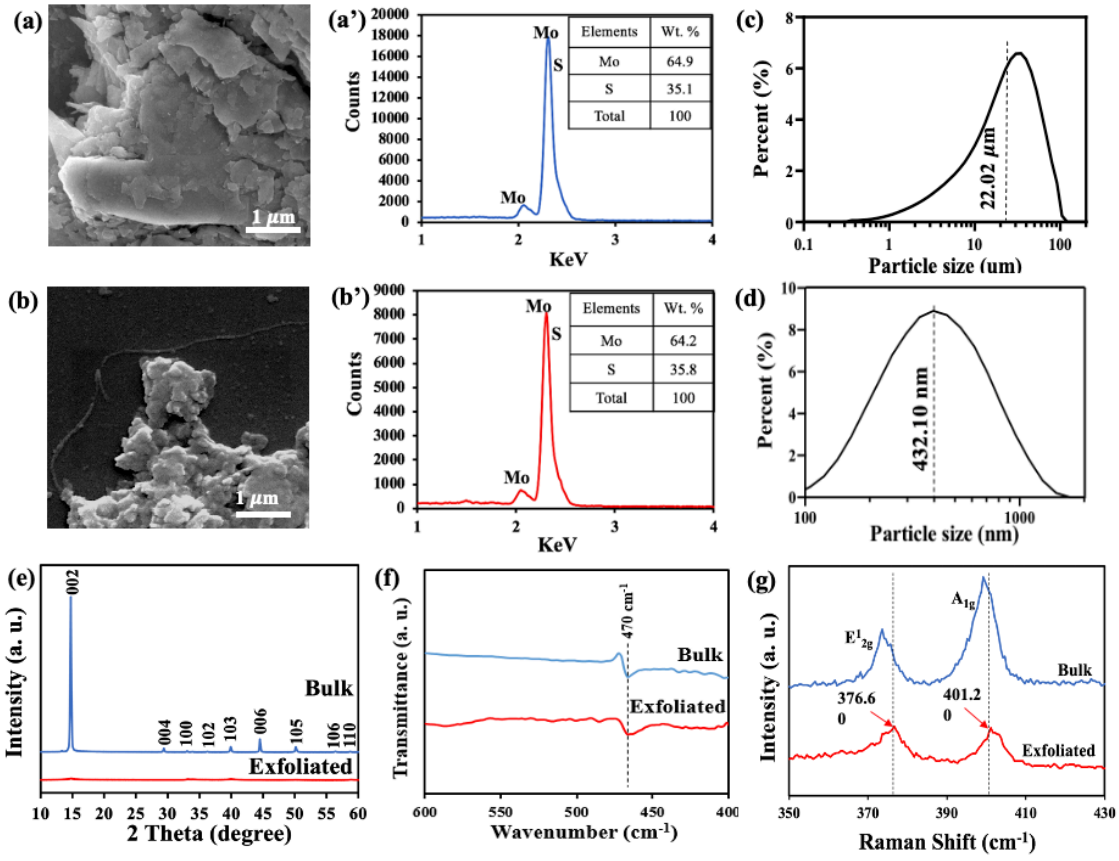

Figure S2. (a, b) SEM images (scale bar = 1 μm), (a', b') EDX spectrum, (c, d) particle size distribution (PSD), (e) XRD patterns, (f) FTIR analysis and (g) Raman analysis of bulk and exfoliated MoS_2, respectively.

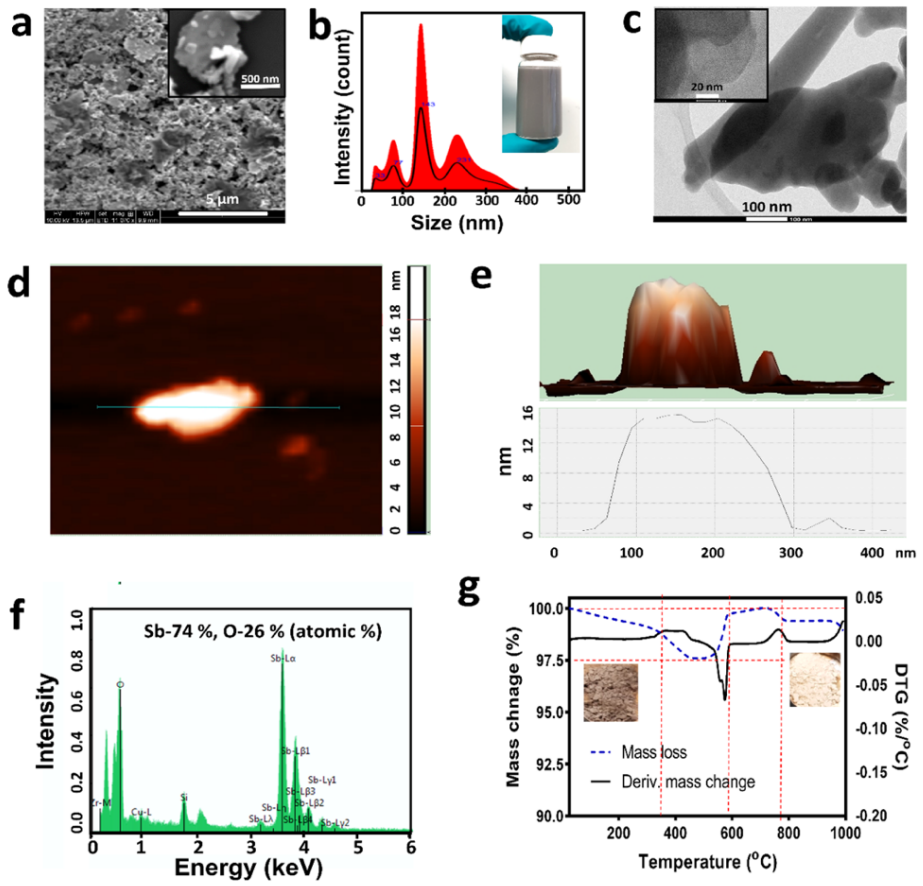

Figure S3. Structural and chemical properties of exfoliated FL-Sb. a) SEM micrograph of FL-Sb, b) Particle size distribution (Inset image-dispersed FL-Sb in Isopropanol), c) high-resolution TEM image of FL-Sb, d) AFM of FL-Sb, e) line profile showing thickness of the FL-Sb, f) EDS spectrum of FL-Sb, g) TGA and DTG of FL-Sb.

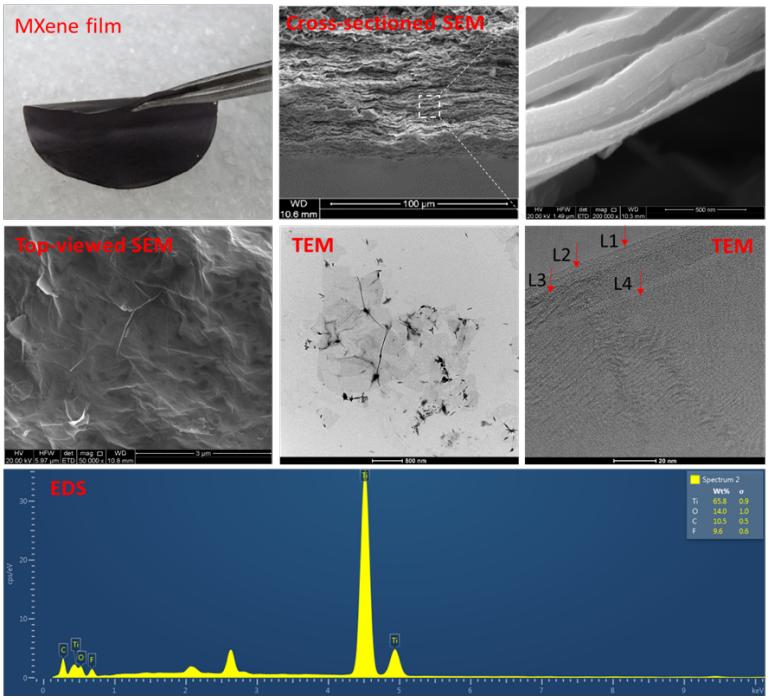

Figure S4. First line from left to right: the freestanding Mxene film, cross-sectional SEM image and zoom-in image of the layers. Second line from left to right: Top-view of Mxene sheets, TEM image and four-layer of Mxene. Third line is the EDS analysis of Mxene sheet.

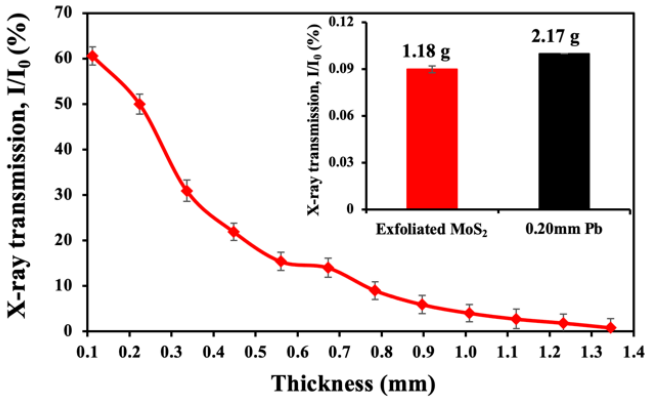

Figure S5. X-ray transmission of the exfoliated MoS_2 film compared with increasing total composite film thicknesses at 30 kVp, inset is the X-ray transmission of the optimized exfoliated MoS_2 film compared with 0.20 mm Pb sheet.

Table S1. X-ray transmission value of the bulk and exfoliated (nano) antimony (Sb), Mxene and molybdenum disulfide (MoS_2) films at 30 kVp. Testing done in triplicate.

Sample name	**X-ray transmission (%)**
Bulk Sb film	59.77 ± 0.02
Nano Sb film	37.90 ± 0.01
Bulk Mxene	56.11 ± 0.01
Nano Mxene	33.20 ± 0.03
Bulk MoS_2	60.56 ± 0.01
Nano MoS_2	32.60 ± 0.02

Table S2. X-ray transmission value of the layered 2D materials at 30 kVp. Testing done in triplicate.

Sample name	**X-ray transmission (%)**
1L (2D MoS_2 + 2D Mxene)	52.29 ± 0.02
2L (2D MoS_2 + 2D Mxene)	22.64 ± 0.01

Reference

[1] K. Hassan, N. Stanley, T. T. Tung, P. L. Yap, H. Rastin, L. Yu, D. Losic, Advanced Materials Interfaces 2021, 8.
[2] L. Yu, A. L. C. Pereira, D. N. H. Tran, A. M. C. Santos, D. Losic, Materials Chemistry and Physics 2021, 260.

CHAPTER 5

DEVELOPMENT OF POLYMER-BASED 2D NANOCOMPOSITES FOR ENHANCED X-RAY SHIELDING PERFORMANCE

Chapter 5 Development of polymer-based 2D nanocomposites for enhanced X-ray shielding performance

Overview and significance of work

The first part of this chapter is to study the synergistic effect of using 2D nanomaterials (graphene and hBN) as reinforcements for polymer-based shielding materials. This work involves the fabrication of FL-hBN via wet chemical exfoliation, preparation of graphene and hBN reinforced MoS_2 nanocomposites for evaluation of X-ray attenuation enhancement as well as their mechanical properties and thermal stability. The key finding proved that graphene and FL-hBN as effective reinforcements can significantly improve the dispersion ability of MoS_2 within the polymer-based composites, leading to enhanced X-ray shielding efficiency as well as improved thermal stability and the hardness of the MoS_2 composites. The second part is to investigate laminated polymer-based composite reinforced with exfoliated 2D antimony for improved shielding ability. The results from this chapter achieve **aim 3:**

(1) **Yu, L.**, Yap, P. L., Tran, D. N. H., Santos, A. M. C., & Losic, D. (2021). High-yield preparation of edge-functionalized and water dispersible few-layers of hexagonal boron nitride (hBN) by direct wet chemical exfoliation. *Nanotechnology, 32*(40). **(Published)**

(2) **Yu, L.**, Yap, P. L., Santos, A., Tran, D., Hassan, k., & Losic, D. (2022). Synergistic effect of graphene and hexagonal boron nitride for significant X-ray shielding enhancement of molybdenum disulfide-epoxy composites. *ACS Applied Materials & Interfaces*. **(Under review)**

(3) Nine, M. J., **Yu, L.**, Pereira, A. L. C., Batmunkh, M., Hassan, K., Santos, A. M. C., . . . Losic, D. (2022). Laminated antimonene as an alternative and efficient shielding strategy against X-ray radiation. Applied Materials Today, *29*, 101556-64. **(Published)**

Statement of Authorship

Title of Paper	High-yield preparation of edge-functionalized and water dispersible few-layers of hexagonal boron nitride (hBN) by direct wet chemical exfoliation
Publication Status	☑ Published ☐ Accepted for Publication ☐ Submitted for Publication ☐ Unpublished and Unsubmitted w ork w ritten in manuscript style
Publication Details	Yu, L., Yap, P. L., Tran, D. N. H., Santos, A. M. C., & Losic, D. (2021). High-yield preparation of edge-functionalized and water dispersible few-layers of hexagonal boron nitride (hBN) by direct wet chemical exfoliation. *Nanotechnology, 32*(40).

Principal Author

Name of Principal Author (Candidate)	Le Yu		
Contribution to the Paper	Prepared and characterized on all the samples, and interpreted all the data as well as wrote the manuscript.		
Overall percentage (%)	85 %		
Certification:	This paper reports on original research I conducted during the period of my Higher Degree by Research candidature and is not subject to any obligations or contractual agreements with a third party that would constrain its inclusion in this thesis. I am the primary author of this paper.		
Signature		Date	03/03/2022

Co-Author Contributions

By signing the Statement of Authorship, each author certifies that:

i. the candidate's stated contribution to the publication is accurate (as detailed above);

ii. permission is granted for the candidate in include the publication in the thesis; and

iii. the sum of all co-author contributions is equal to 100% less the candidate's stated contribution.

Name of Co-Author	Pei Lay Yap		
Contribution to the Paper	Edited and revised the manuscript.		
Signature		Date	03/03/2022

Name of Co-Author	Diana, N. H. Tran		
Contribution to the Paper	Co-supervised and revised the manuscript.		
Signature		Date	03/03/2022

Please cut and paste additional co-author panels here as required.

Statement of Authorship

Title of Paper	High-yield preparation of edge-functionalized and water dispersible few-layers of hexagonal boron nitride (hBN) by direct wet chemical exfoliation
Publication Status	☑ Published ☐ Accepted for Publication ☐ Submitted for Publication ☐ Unpublished and Unsubmitted w ork w ritten in manuscript style
Publication Details	Yu, L., Yap, P. L., Tran, D. N. H., Santos, A. M. C., & Losic, D. (2021). High-yield preparation of edge-functionalized and water dispersible few-layers of hexagonal boron nitride (hBN) by direct wet chemical exfoliation. *Nanotechnology, 32*(40).

Principal Author

Name of Principal Author (Candidate)	Le Yu		
Contribution to the Paper	Prepared and characterized on all the samples, and interpreted all the data as well as wrote the manuscript.		
Overall percentage (%)	85 %		
Certification:	This paper reports on original research I conducted during the period of my Higher Degree by Research candidature and is not subject to any obligations or contractual agreements with a third party that would constrain its inclusion in this thesis. I am the primary author of this paper.		
Signature		Date	03/03/2022

Co-Author Contributions

By signing the Statement of Authorship, each author certifies that:

i. the candidate's stated contribution to the publication is accurate (as detailed above);

ii. permission is granted for the candidate in include the publication in the thesis; and

iii. the sum of all co-author contributions is equal to 100% less the candidate's stated contribution.

Name of Co-Author	Alexandre M. C. Santos		
Contribution to the Paper	Co-supervised, performed X-ray irradiations and revised the manuscript.		
Signature		Date	03/03/2022

Name of Co-Author	Dusan Losic		
Contribution to the Paper	Supervised the development of the work, edited, revised the manuscript and acted as the corresponding author.		
Signature		Date	03/03/2022

Please cut and paste additional co-author panels here as required.

IOP Publishing Nanotechnology
Nanotechnology 32 (2021) 405601 (10pp) https://doi.org/10.1088/1361-6528/ac0931

High-yield preparation of edge-functionalized and water dispersible few-layers of hexagonal boron nitride (hBN) by direct wet chemical exfoliation

Le Yu[1,2], Pei Lay Yap[1,2], Diana N H Tran[1,2], Alexandre M C Santos[3,4] and Dusan Losic[1,2]

[1] School of Chemical Engineering and Advanced Materials, The University of Adelaide, Adelaide, SA 5005, Australia
[2] ARC Research Hub for Graphene Enabled Industry Transformation, The University of Adelaide, Adelaide, SA 5005, Australia
[3] School of Physical Sciences, The University of Adelaide, Adelaide, South Australia 5005, Australia
[4] Department of Medical Physics, Royal Adelaide Hospital, Adelaide, South Australia 5000, Australia

E-mail: dusan.losic@adelaide.edu.au

Received 1 February 2021, revised 6 May 2021
Accepted for publication 8 June 2021
Published 13 July 2021

Abstract

Owing to many fascinating properties including high thermal and chemical stability, excellent electrical insulation, fire-retardant and antibacterial properties, hexagonal boron nitride (hBN) has emerged as a prominent 2D material for broad applications. However, the production of high quality of hBN by chemical exfoliation from its precursor is still challenging. This paper presents a high-yield (+83%), low-cost and energy-efficient wet chemical exfoliation strategy, which produces few-layers (FL, 3–6 layers) of edge-functionalized (OH) hBN nanosheets with uniform size (486 ± 51 nm). This optimized preparation is established based on a comprehensive investigation on the key exfoliation parameters such as exfoliation temperature, time and amount of the oxidant (potassium permanganate). High quality of FL-hBN was confirmed by various characterization techniques including scanning electron microscopy coupled with energy dispersive X-ray, transmission electron microscopy, Raman, Fourier transform infrared spectroscopy, X-ray diffraction and X-ray photoelectron spectroscopy analyses. The outcome of this study paves a promising pathway to effectively produce hBN through a cost-efficient exfoliation approach, which has a significant impact on industrial applications.

Supplementary material for this article is available online

Keywords: hexagonal boron nitride, few-layers hexagonal boron nitride, chemical exfoliation

(Some figures may appear in colour only in the online journal)

1. Introduction

Hexagonal boron nitride (hBN), also known as white graphene, is an analogue of graphene that is made up of alternating sp^2 hybridized nitrogen and boron atoms covalently bonded in a hexagonal planar structure that resembles graphene [1]. Since the successful isolation of graphene (2D) from graphite (3D) in 2004, rapid research progress in graphene materials promotes the emerging development of a broad range of 2D materials including hBN, black phosphorus, Mxene, molybdenum disulfide (MoS_2) and tungsten disulfide (WS_2). Among these 2D materials, h-BN has drawn considerable attention recently due to its exceptional properties such as high thermal conductivity (550 $W\,m^{-1}\cdot K^{-1}$), remarkable oxidation resistance, non-toxicity, excellent mechanical strength (up to 239 $N\,m^{-1}$ with an effective thickness of 0.33 nm) and outstanding chemical

stability, which can be applied as lubricants, light-emitting devices, surface coatings and a platform for graphene electronics [1–4].

In general, the preparation of hBN exfoliation mainly followed and inspired by graphene production methods, which can be performed through the bottom-up approach (precursors are assembled into complex nanostructure) and the top-down approach (chemical exfoliation from bulk hBN materials) [5]. One of the commonly used bottom-up approaches is chemical vapour deposition (CVD), where hBN nanosheets are successfully produced through the absorption of decomposed borazine on the surface of Pt (111) at a temperature range of 800 °C–1200 °C [6]. Although this method can produce high-quality hBN nanosheets with a high crystalline structure, it is very expensive to operate and involves high temperature, which also fails to achieve large-scale production.

Chemical exfoliation still remains the most promising strategy to effectively prepare single- or few-layer 2D materials in low cost and large scale [1]. For instance, high yield (42%) of FL-hBN nanosheets was obtained using monoethanolamine aqueous solution as the exfoliating agent [7]. By adapting improved Hummers' method of graphene oxide, use of the combined chemical precursors (phosphoric acid, sulphuric acid, potassium permanganate and hydrogen peroxide) demonstrated the effective preparation of mono- to FL-hBN with low yield (6%–25%) [8, 9]. However, it is surprising to find that only few studies have reported towards improving the exfoliation process of hBN compared to graphene. Significant research gap is identified with lack of understanding towards the optimized conditions to produce high-quality hBN using key parameters, such as reaction temperature, exfoliation time, concentration of the oxidants and quality (e.g. number of layers, thickness) of obtained hBN materials. Unlike graphene, the research studies on exfoliation of hBN are very limited to control the number of layers and lateral size of hBN, and also only few investigations explored the optimization of exfoliation conditions for achieving high-quality hBN with large yield.

To date, critical obstacles including low yield, poor quality of the prepared hBN with a broad distribution of lateral size and uncontrolled number of layers are yet to be overcome. In fact, the exfoliation of FL-hBN is more challenging compared to graphene due to its stronger lip–lip interactions between the neighbouring hBN basal planes. It appears that it is more difficult to exfoliate bulk h-BN in comparison to 'peeling off' graphene single sheets from graphite [10]. Hence, effective hBN exfoliation strategies to achieve good quality of few-layer hBN sheets are still highly in-demand for many practical and commercial applications of hBN.

To address the limitations in terms of the yield, dispersion ability and quality of the prepared hBN, we report an advanced, low-cost and effective one-step wet chemical exfoliation approach. The proposed approach is based on modified wet exfoliation by using chemical precursors, such as sulphuric acid, potassium permanganate and hydrogen peroxide, to demonstrate the dispersible preparation of edge-oxygen decorated FL-hBN nanosheets with uniform shape, controlled thickness and high yield. A comprehensive study on key exfoliation parameters including reaction temperature (40 °C–75 °C), reaction time (6–24 h) and amount of potassium permanganate ($KMnO_4$/BN ratio 3–6) is systematically investigated to determine the optimum exfoliation conditions of producing a high yield and high quality of edge-functionalized FL-hBN. The outcomes of this study provide valuable contributions towards the development of a low-cost and high-yield method for production of high-quality hBN 2D materials needed for broad applications.

2. Experimental section

2.1. Materials and chemicals

Raw hBN powder (10 μm, c-hBN) was provided by UK Abrasives (UK). Concentrated sulphuric acid (H_2SO_4, 98%) and hydrogen peroxide (H_2O_2, 35%) were purchased from Chem-Supply (Australia). Potassium permanganate ($KMnO_4$, 99%) was purchased from Sigma-Aldrich (Australia). All chemicals were used as received and distilled (DI) water was used throughout the study, unless otherwise stated.

2.2. Preparation of exfoliated hBN (FL-hBN)

FL-hBN was prepared using commercially available bulk hBN (c-hBN) by adapting the modified Hummers' method [9]. Bulk hBN powder (3 g), H_2SO_4 (75 ml) and $KMnO_4$ (18 g or $KMnO_4$/hBN at 6) were first conditioned below 10 °C in the fridge before mixing them homogenously under constant stirring. The green mixture (figure S1(a)) (available online at stacks.iop.org/NANO/32/405601/mmedia) was then heated in an oil bath (75 °C, 24 h) to form a thick paste. After the reaction, the pink thick paste (figure S1(b)) was allowed to cool down to room temperature with subsequent addition of H_2O_2. Resultant product was washed with distilled water using centrifuge at 4200 rpm several times until the supernatant reached pH 7. Obtained product (figure S1(c)) was dried in an oven (50 °C, 24 h) to give white powder for further characterizations. To improve this method, a series of exfoliation conditions with varied amount of $KMnO_4$ (9–18 g or $KMnO_4$/hBN ratio at 3–6), temperature (40 °C–75 °C) and time (6–24 h) were investigated and presented in table S1, supporting information to determine the optimized exfoliation condition.

2.3. Characterizations

Samples were characterized by several analytical techniques including scanning electron microscopy coupled with energy dispersive X-ray (SEM-EDX, Quanta 450 FEG, FEI, USA; Ultim Max Oxford Instruments, UK) and transmission electron microscopy (TEM, FEI Tecnai G2 Spirit) at an accelerating voltage of 30 kV and 100 kV, respectively, to study the morphology and elemental composition of the materials. Atomic force microscopy (AFM, NT-MDT Integra Solaris) was conducted to measure the thickness of the sample layers

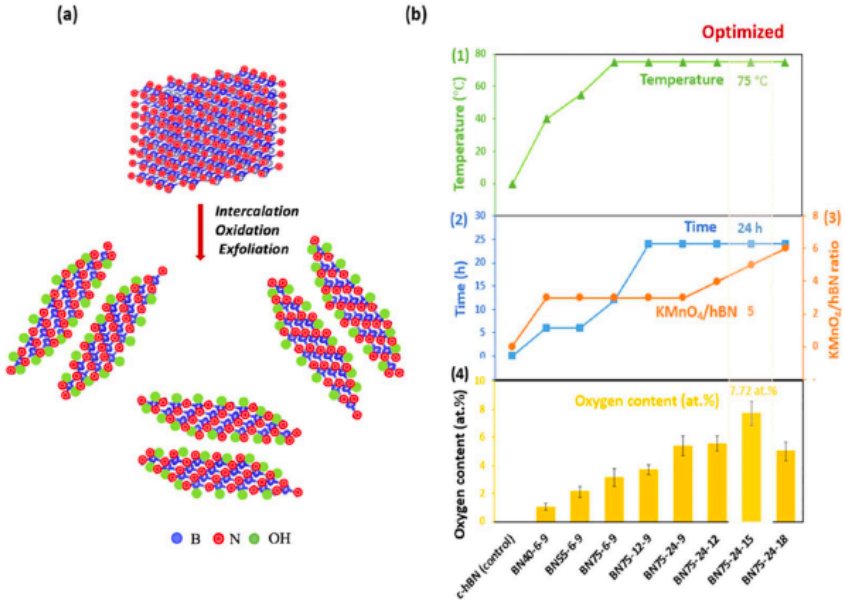

Figure 1. (a) Schematic diagram of the preparation of edge-functionalized FL-hBN exfoliation and (b) parametric study for the optimization of exfoliation conditions (including (1) temperature, (2) time and (3) $KMnO_4$/hBN ratio) and (4) their corresponding oxygen content (at%).

under tapping mode. Chemical structure of the samples was determined using Fourier transform infrared spectroscopy (FTIR, Nicolet 6700 Thermo Fisher, Australia) under transmission mode at 4000–400 cm^{-1}. Number of layers of bulk and exfoliated hBN was confirmed by Raman spectroscopy (LabRAM HR Evolution, Horiba Jvon Yvon Technology, Japan) using 532 nm laser as the excitation source in the range of 1200–1500 cm^{-1}. X-ray diffractograms (XRD, Rigaku MiniFlex 600, USA) were collected at the range of $2\theta = 20°–80°$ (scan rate of 10 °C min^{-1}). Thermal properties of the materials were probed using TGA, 2500 Regulus (Netzsch, Germany) under air atmosphere with the samples heated to 1400 °C at heating rate of 10 °C min^{-1}. Chemical species and surface elemental composition of the samples were confirmed using X-ray photoelectron spectroscopy (XPS, AXIS Ultra_DLD, Kratos, UK) equipped with a monochromatic Al Kα radiation source ($h\nu$ = 1486.7 eV) at 225 W, 15 kV and 15 mA. XPS wide scans were recorded at 0.5 eV step size over −10 to −1100 eV at the pass energy of 160 eV while the narrow scans were collected at a 0.1 eV step size and pass energy of 20 eV. Peak deconvolution was performed using Casa XPS™ software with the core-level spectra involved calibrated to the primary peak (C–C/C–H peak) of adventitious carbon at 284.8 eV.

3. Results and discussion

Significant colour transformation from dark green to pink and finally to white suspension was observed during the exfoliation process (scheme shown in figure 1(a)). To optimize the process, we investigated three key parameters including exfoliation temperature (40°C–75 °C) and time (6–24 h) and the $KMnO_4$/hBN ratio (3–6), followed by monitoring the oxygen level using EDX analysis (table S2). Three characteristic trends as summarized in figure 1(b) were identified towards the optimized conditions: (1) elevating the temperature increased the oxygen content (a gradual increase of 1 atomic % for each temperature rise) (figure 1(b)(1)), (2) increasing reaction time from 6 to 12 h did not result in a significant change in oxygen content (3 at %). However, increment to 5 at% oxygen was recorded when the reaction time was increased to 24 h (figure 1(b)(2)), (3) changing the oxidant ($KMnO_4$) amount showed an unusual trend of oxygen atomic % with $KMnO_4$/hBN mass ratio of 5 (figure 1(b)(3)) demonstrated the highest oxygen content (7.72 at %) (figure 1(b)(4)). The optimized condition ($KMnO_4$/hBN of 5, 75 °C and 24 h) gave rise to the best exfoliated few-layer hBN (labelled as FL-hBN), while the control sample (bulk hBN) was designated as c-hBN in this work. From the perspective of thermodynamics and kinetics, the external heat energy (75°C) used in our exfoliation protocol increased the kinetic energy of the exfoliating agents ($KMnO_4$ and H_2SO_4) and the highly stacked raw hBN sheets during wet chemical exfoliation process. With prolonged exfoliation time (24 h), more oxygen molecules were generated when enough energy was gained by the exfoliating agents with its respective stoichiometric equation described in equation (2). At the same time, we surmised that the weak van der Waals forces between the highly stacked hBN sheets was overcome and the hBN sheets were cut freely from one another under this optimized condition to react with the oxygen molecules produced by the exfoliating agents [9, 11, 12]. As evidenced in the characterization outcomes in the next section, we demonstrated that high quality of hBN nanosheets can be produced by following this wet chemical exfoliation approach. SEM technique

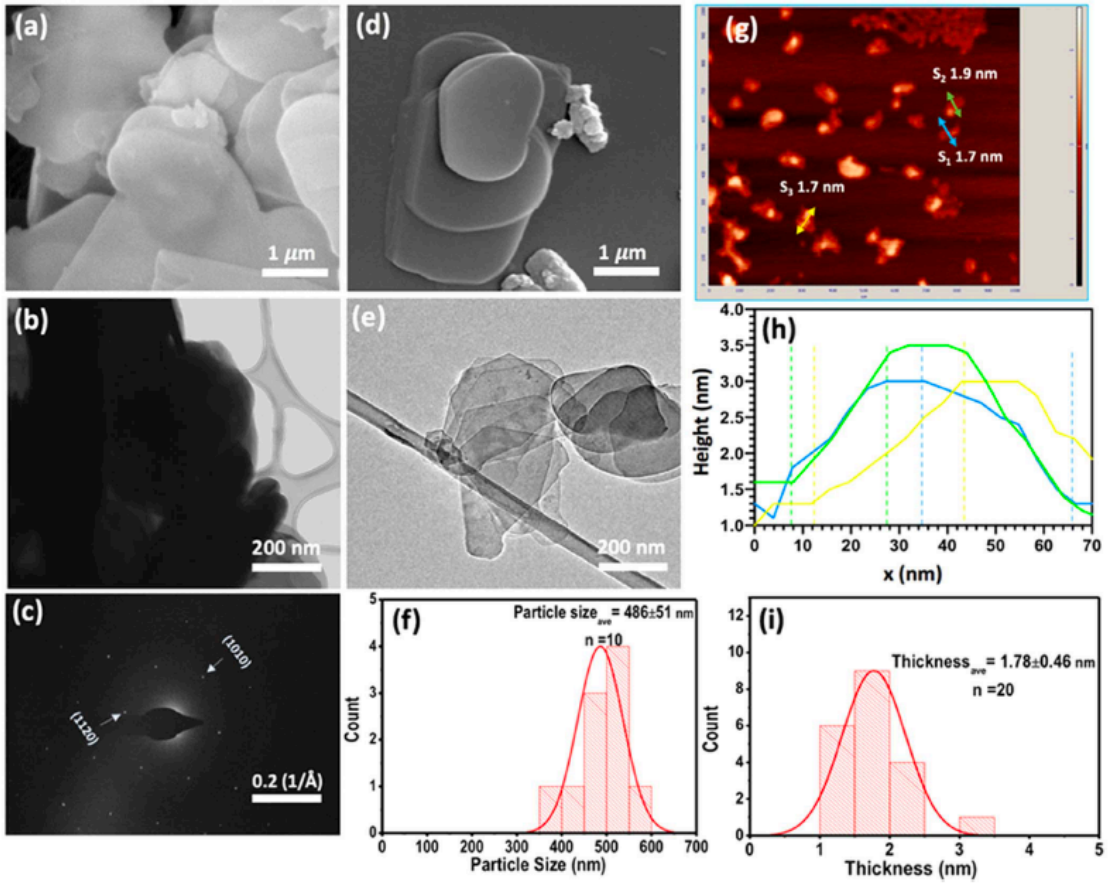

Figure 2. (a) SEM and (b) TEM images of bulk hBN (c-hBN), (c) selected area electron diffraction pattern (SAED) of FL-hBN, (d) SEM and (e) TEM images of exfoliated hBN (FL-hBN), (f) particle size distribution of FL-hBN based on TEM of (e), (g) AFM image with (h) height profiles of three selected examples of FL-hBN, (i) statistical thickness analysis of FL-hBN determined from (g).

was used to confirm the successful isolated hBN nanosheets using optimized conditions. Morphology transition of FL-hBN (figures 2(d)–(e)) was clearly visible from c-hBN (figures 2(a)–(b)). c-hBN exhibited a typical laminated surface structure, consisting of overlapped and highly aggregated sheets that were randomly stacked together [13]. The highly aggregated c-hBN layers were successfully peeled off to few-layer hBN nanosheets as shown in figures 2(a) and (d) after the chemical exfoliation reaction [14]. More information about exfoliated hBN layers were obtained using TEM technique, showing transformation of highly aggregated and randomly stacked c-hBN sheets with the irregular shape (figure 2(b)) to ultrathin and ordered FL-hBN nanosheets with the regular shape (figure 2(e)). The significant change of morphological geometry in terms of the particle size and aggregation suggested successful exfoliation of hBN sheets. TEM investigations and SAED profile of exfoliated hBN revealed typical lattice spacings of 0.218 nm and 0.127 nm that can be indexed to (1010) and (1120) crystal planes, respectively, indicating that the identity of hBN still retained after liquid exfoliation. The SAED profile of FL-hBN (figure 2(c)) suggested that highly crystalline feature of FL-hBN with signally six-fold symmetry observed from the ordered bright spots [15].

Representative AFM image and the statistical analysis of height profile (figures 2(g)–(i)) confirmed that the exfoliated single layer of FL-hBN had an average thickness of 1.78 ± 0.46 nm, revealing that high quality of hBN can be generated using this highly scalable exfoliation approach.

Particle size analysis using dynamic light scattering technique (figure S2) clearly indicated successful exfoliation of c-hBN with drastic reduction of its initial micro-sized bulk hBN size (9.95 μm) to nano-sized FL-hBN (458 nm). This was also in good agreement with the particle size distribution analysis of FL-hBN determined using TEM technique (figure 2(f)) with an average particle size of 486 ± 51 nm.

Figure 3 showed the elemental mapping of FL-hBN sheets via TEM. Both N and B elements were abundantly distributed in the FL-hBN sheets (figures 3(b)–(c)), while O element was found more richly located at the edge of the

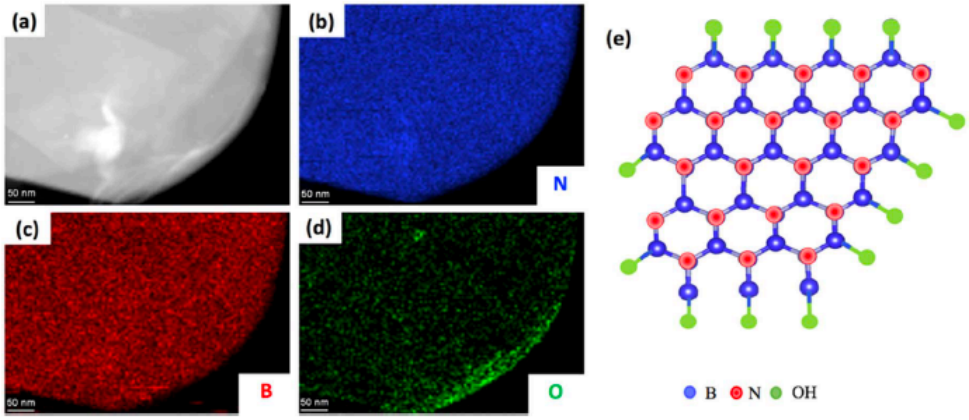

Figure 3. TEM mapping analysis of FL-hBN (a) TEM image of FL-hBN, (b) nitrogen (N), (c) boron (B), (d) oxygen (O), (e) scheme of hBN structure with edge-functionalized OH groups.

sheets (figure 3(d)). The presence of these elements was also confirmed by elemental mapping and EDX analysis from SEM (figure S3), where five selected spots at the centre and at the edge, respectively, were performed on the FL-hBN sheets. table S3 recorded the elemental content of N, B, C and O for each spot. Content of N was consistent among all analysed spots (45.6 ± 0.4 at%–46.2 ± 1.5 at%). While B content was significantly higher at the centre of the sheets (31.3 ± 1.3 at%) than that at the edge area (22.8 ± 1.4 at%), due to the fact that most of cutting B–N bonds near the edge might be prone to attack by the oxygen atoms from hydrolysis during wet chemical exfoliation, and these cut hBN species mostly contained B edges with hydroxyl groups [16, 17]. Remarkably, the O content at the edge of FL-hBN sheets (6.1 ± 0.7 at%) was doubled than that in the centre (2.6 ± 0.4 at%), which indicated that oxygen intercalation using our developed wet chemical exfoliation approach was more likely to occur at the edge of FL-hBN sheets. This result was in good agreement with the TEM mapping analysis provided in figure 3, which confirmed that the oxygen intercalation was more intended to occur at the edge of the FL-hBN sheets.

Effective exfoliation of FL-hBN was further verified by dispersion tests using water and ethanol as dispersing agents. As illustrated in figure S4(a-c), FL-hBN formed a very stable suspension after standing for three days in water compared to bulk hBN, which failed to keep its stability even after standing for 30 min. Typical Tyndall effect with visible light beam was observed on the exfoliated FL-hBN suspension but not on the bulk hBN (figure S4(g)) upon shining of a laser light on both the samples dispersed in water, since the hydroxyl groups from FL-hBN can form the hydrogen bonds with water, thus improving its hydrophilicity [17]. Similar observation monitored for both c-hBN and FL-hBN in the ethanol dispersion showed that the FL-hBN suspension prepared through the optimized wet chemical exfoliation approach was comparatively more stable than c-hBN (figure S4(d-f)).

Raman spectroscopy is commonly used to verify the presence of number of layers of hBN by monitoring the shift of peak position compared to the bulk hBN [8]. Figure 4(a) demonstrated a typical Raman peak of c-hBN at 1365.64 cm^{-1} that represents the E_{2g} vibration mode of h-BN [18]. Notably, Raman peak recorded for FL-hBN was blue shifted to 1367.40 cm^{-1} from bulk hBN, suggesting an decrease in the overall thickness of the analysed FL-hBN nanosheets due to the growing interlayer interaction between the exfoliated layers in the FL-hBN sample [15, 19]. This result was in good agreement with the SEM and TEM images of FL-hBN discussed previously. Evidently, a significant decrease in the intensity with a larger full width at half maximum (FWHM) value was observed for the exfoliated hBN (8.84 cm^{-1}) compared to pristine hBN (8.27 cm^{-1}), which can be attributed to stronger Raman scattering effect experienced by FL-hBN compared to non-exfoliated hBN [15, 20, 21]. This result confirmed that the bulk hBN was exfoliated successfully into few-layer hBN nanosheets as supported by TEM analysis (figure 2(e)).

The XRD plot of bulk hBN revealed a highly crystalline structure in figure 4(b). An intense and sharp peak at 27.21° was common for the crystalline structure of hBN [9]. This peak became weaker for the exfoliated hBN sample, and slightly shifted to 27.46° after the chemical exfoliation process. This shift can be attributed to the increased inter-plane spacing between the exfoliated layers of hBN due to successful intercalation of oxygen, which was in good agreement with the SEM and Raman studies discussed above [14].

Both FTIR spectra (figure 4(c)) of bulk hBN and exfoliated hBN showed two typical peaks at 1378.85 cm^{-1} (in-plane B–N optical modes of sp^2 bonded h-BN) and 781.03 cm^{-1} (B–N–B out-plane bending vibration), indicating that the chemical structure of hBN still preserved even after the chemical modification proposed hereby, which can be well-correlated to the SAED outcome discussed in the previous section [9]. Additionally, two new peaks found in the exfoliated hBN can be assigned to B–O–H (1020.10 cm^{-1}

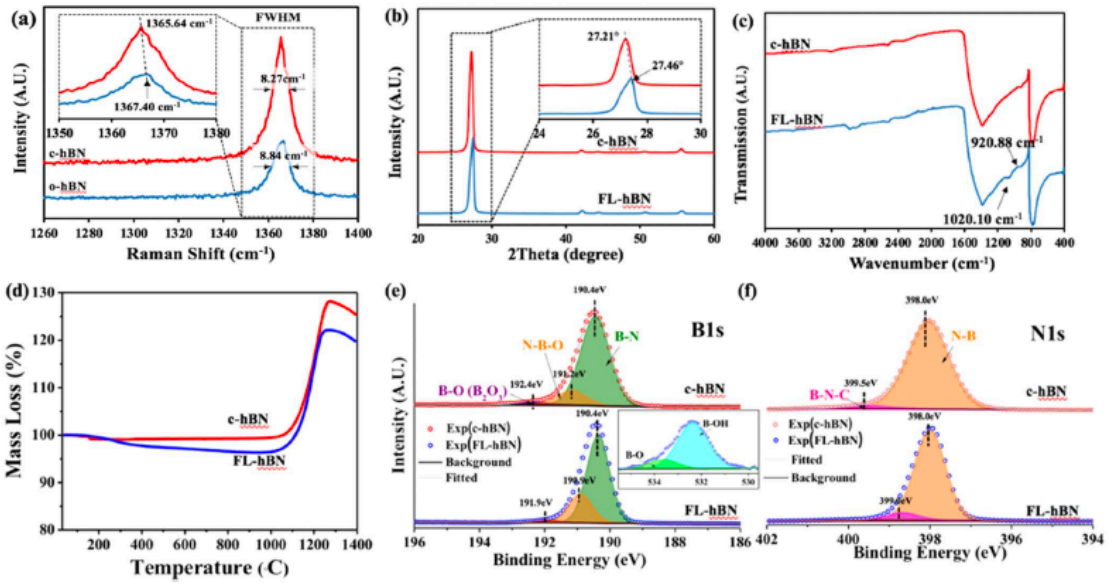

Figure 4. (a) Raman spectra, (b) XRD diffractograms, (c) FTIR, (d) TGA, and XPS fitted narrow curves of (e) B1s with inset of O1s from FL-hBN and (f) N1s for c-hBN and FL-hBN.

and 920.88 cm^{-1}), confirming the successful oxygen intercalation between the hBN layers in FL-hBN [22].

TGA performed in the air atmosphere indicated that mass gain of bulk hBN began at around 1000 °C until a maximum temperature was reached at 1280 °C due to boron trioxide (B_2O_3) formation. This was followed by a slow mass loss to 1400 °C, which can be attributed to the volatilization process of B_2O_3 (figure 4(d)). As evidenced from the literature, the TGA curve of FL-hBN was distinct from the bulk hBN with a prominent temperature delay (1100 °C) in mass gain compared to bulk hBN [14].

Surface elemental composition and presence of chemical species in both bulk and exfoliated hBN were confirmed using XPS technique. Survey spectra of both hBN samples (figure S5) indicated the existence of carbon (C1s) and oxygen (O1s) peaks at around 284.4 eV and 531.9 eV, respectively. Existence of carbon in the commercial hBN was primarily due to the addition of carbon during the BN manufacturing process to inhibit the crystal growth of BN for achieving desired particle size and to improve the purity of the final product formed [23]. Binding energies for survey scanned B1s and N1s peaks of c-hBN at 190.4 eV and 397.9 eV were in good agreement with the reported values [7, 9]. A significant shift of binding energies for B1s and N1s peaks was observed on the survey spectrum of FL-hBN at 189.9 eV and 397.4 eV, respectively, in relative to neat hBN. Chemical composition of c-hBN and FL-hBN (figure S5) showed that calculated B/N atomic ratio of c-hBN (1.03) decreased to 0.90 after chemical exfoliation, indicating a change occurred in the boron percentage. This decrease in boron was due to the additional oxygen and hydroxyl groups in FL-hBN during hBN exfoliation [24]. In order to accurately quantify and compare the oxygen concentration in the two samples, B/O atomic ratio was adopted due to minimum potential contamination that could be introduced to the samples during exfoliation step. Notably, reduction of B/O atomic ratio was identified for exfoliated hBN (15.15) from bulk hBN (15.43), indicating considerable oxygen content has been intercalated between the hBN layers after the exfoliation process. We found that the O content (2.73 at%) in FL-hBN still remained low in XPS analysis (figure S5), although the oxidation reaction introduced was very strong. This could be due to the strong electrostatic attraction between N and B in adjacent the hBN layers, resulting in an increase in interlayer interaction. Thus, it is still challenging to intercalate oxygen between hBN layers [25]. This issue is also evident in most of the studies in literature with only small amount of oxygen found in the exfoliated hBN [12, 26, 27]. However, the elemental quantification from XPS analysis was consistent with the O content (2.6 ± 0.4 at%) at the centre of FL-hBN sheets, compared to higher O content (6.1 ± 0.7 at%) at the edge of exfoliated hBN nanosheets. These outcomes evidently showed that the proposed wet chemical exfoliation method can effectively exfoliate hBN with edge-oxygen insertion from bulk hBN. As depicted in figure 4(e), both c-hBN and FL-hBN were primarily made up of B–N species positioned at 190.4 eV based on the deconvoluted B1s peak. Two oxidized boron species (N–B–O and B–O) were detected at 191.2 eV and 192.4 eV, respectively, from the deconvolution of core B1s peak of c-hBN. Binding energies of oxidized boron species were found to be shifted for exfoliated hBN to 190.9 eV and 191.9 eV recorded [20, 28, 29]. Inset of figure 4(e) demonstrated the narrow O1s peak of FL-hBN that can be deconvoluted to B–OH (532.4 eV) and B–O (533.6 eV) [22].

Table 1. Comparison of yield and properties of hBN prepared using different exfoliation methods.

Method	Exfoliation agent	Amount of agent	Temperature (°C)	Duration (h)	No. of layers	Thickness (nm)	Yield (%)	References
Annealing	NA	—	600	144	Several	NA	NA	[14]
Chemical-assisted annealing	Urea	—	900	5	1-4	0.5–0.9	NA	[5]
Chemical-assisted ball milling	Benzyl benzoate	—	NA	15	<10	2.3–3.7	67	[33]
Chemical-assisted ball milling	Sodium hydroxide (NaOH)	—	NA	24	<10	2.62	18	[25]
Chemical exfoliation	Molten NaOH/KOH	—	180	2	<10	4	0.19	[32]
Chemical exfoliation	NH_4F	—	180	24	NA	1.51	NA	[31]
Chemical exfoliation	Octadecylamine (ODA)	—	160–180	4-6 days	3–20	1–7	10-20	[34]
Compressible flow exfoliation	Gas (He, CO_2, N_2)-solid mixture	50 ml	—	3	6	4.2	10	[35]
Chemical exfoliation	H_2SO_4, H_3PO_4, $KMnO_4$, H_2O_2	H_2SO_4: 120 ml H_3PO_4: 15 ml $KMnO_4$: 6 g H_2O_2: 6 ml	75	12	1-4	4	25	[8]
Chemical exfoliation	H_2SO_4, $KMnO_4$, H_2O_2	H_2SO_4: 25 ml $KMnO_4$: 0.5 g H_2O_2: 10 ml	NA	12	2–3	1.44	6.50	[9]
Chemical exfoliation	H_2SO_4, H_3PO_4, $KMnO_4$, H_2O_2	H_2SO_4/H_3PO_4: 9:1 BN/$KMnO_4$: 1:8	65	24	A few monolayers	3	—	[36]
Chemical exfoliation	H_2SO_4, $KMnO_4$, H_2O_2	H_2SO_4: 75 ml $KMnO_4$: 15 g H_2O_2: 4 ml	75	24	6	1.78 ± 0.46	83.33	This work

Further peak fitting of N1s narrow curve (figure 4(f)) showed two resolved peaks at 398.0 eV and 399.5 eV for bulk hBN; 398.0 eV and 399.0 eV for exfoliated hBN corresponding to N–B and B–N–C peaks, respectively [28]. Complement to all the characterization results, XPS analysis of both bulk and exfoliated hBN clearly demonstrated successful exfoliation and intercalation of oxygen between the bulk hBN layers by adopting the wet chemical exfoliation approach demonstrated in this work.

The yield measurement was determined using the adapted method from the literature [12]. The details of yield measurement was as follow: after wet chemical exfoliation, the sample with the known mass was first dispersed in DI water and bath sonicated for 10 min. This mixture was then allowed to free stand for 24 h to separate the supernatant of FL-hBN nanosheets from the unexfoliated hBN sheets. Finally, these two different layers were individually transferred to a new container and dried in an oven at 50 °C for further characterization (figure S6). The yield of the sample was calculated from equation (1) [30],

$$\text{Yield}(\%) = (\text{mass of FL} - \text{hBN or unexfoliated} - \text{hBN})/\text{mass of bulk hBN}) \times 100\% \quad (1)$$

The calculated yield of FL-hBN was 83.33% (of initial raw hBN mass), indicating that effective expansion of hBN layers using edge-oxygen precursors was an important factor to achieve the high yield and good dispersion ability of few-layer hBN sheets. As reported by Du *et al.*, MnO_2 derived from the reaction between H_2SO_4 and $KMnO_4$ (Equation (2)) was recognized as the key contribution in preventing the BN nanosheets from re-stacking [9]. By optimizing the mass ratio of $KMnO_4$/hBN at 5 in our work, we found that the bulk hBN can be effectively exfoliated into few-layered hBN nanosheets.

$$2H_2SO_4 + 4KMnO_4 = 2K_2SO_4 + 4MnO_2 + 3O_2\uparrow + 2H_2O. \quad (2)$$

In fact, it is still fairly challenging to achieve high quality and large yield of hBN nanosheets with controllable lateral size and number of layers [10]. Several exfoliation strategies such as annealing, mechanical exfoliation, CVD, liquid exfoliation have been reported and summarized in table 1. Our method is able to achieve the highest yield (83.33%) and dispersion ability (up to 3 d) with better control of thickness, lateral size of FL-hBN among other exfoliation methods reported in the literature. Additionally, the exfoliation approach in this work is also relatively energy-efficient (75 °C) compared to majority of exfoliation methods including annealing (600 °C) [14], chemical-assisted annealing (900 °C) [5] and chemical exfoliation (180 °C) [31, 32]. In terms of the quality of the exfoliated hBN, our exfoliation approach demonstrated that few-layer (6 layers) exfoliated hBN nanosheets with uniform shape in nanometer range can be effectively achieved from the initial highly aggregated and irregular hBN flakes, which was hardly accomplished by other methods.

4. Conclusions

A high-yield and efficient wet chemical exfoliation approach for preparation of hBN using a mixture of sulphuric acid, $KMnO_4$ and H_2O_2 to optimize the condition was demonstrated. Through this exfoliation approach, few-layer edge-functionalized hBN nanosheets (6 layers) with the average thickness of 1.78 ± 0.46 nm that is highly dispersible in water was achieved at optimized exfoliation condition (75 °C, 24 h and $KMnO_4$/hBN mass ratio of 5). Successful exfoliation of hBN was confirmed by series of characterization techniques including SEM-EDX, TEM, Raman, TGA, FTIR and XPS analyses. This low-cost and energy-efficient wet chemical exfoliation method promises both high quality and quantity of edge-f hBN with high yield (83.33% of initial raw hBN mass), which opens the door for optical, microelectronics and biomedical applications [37–39, 21].

Acknowledgments

The authors acknowledge the financial support from the ARC Research Hub for Graphene Enabled Industry Transformation, (IH150100003). We thank Australian Microscopy and Microanalysis Research Facility (AMMRF) for the access of SEM, TEM and AFM facilities, Mr Ken Neubauer, Dr Ashley Slattery and Mr Chris Bassell for their technical support on SEM, AFM, TEM and XPS measurements. The XPS analysis was carried out at the Microscopy Australia facilities located at the University of South Australia, infrastructure co-funded by the University of South Australia, the South Australian State Government, and the Australian Federal Governments NCRIS scheme.

Data availability statement

All data that support the findings of this study are included within the article (and any supplementary files).

Conflicts of interest

The authors declare no conflict of interest.

ORCID iDs

Dusan Losic https://orcid.org/0000-0002-1930-072X

References

[1] Wang Z *et al* 2016 Fabrication of boron nitride nanosheets by exfoliation *Chem. Rec.* **16** 1204–15

[2] Chen J, Chen J, Zhang H, Hu M and Li M 2018 Microstructure and mechanical properties of h-BN/Yb4Si2O7N2 composites *J. Adv. Ceram.* **7** 317–24

[3] Falin A *et al* 2017 Mechanical properties of atomically thin boron nitride and the role of interlayer interactions *Nat. Commun.* **8** 15815

[4] Yuan C, Li J, Lindsay L, Cherns D, Pomeroy J W, Liu S, Edgar J H and Kuball M 2019 Modulating the thermal conductivity in hexagonal boron nitride via controlled boron isotope concentration *Commun. Phys.* **2** 1–9

[5] Nag A, Raidongia K, Hembram K P, Datta R, Waghmare U V and Rao C N 2010 Graphene analogues of BN: novel synthesis and properties *ACS Nano* **4** 1539–44

[6] Takahashi T, Itoh H and Takeuchi A 1979 Chemical vapor deposition of hexagonal boron nitride thick film on iron *J. Cryst. Growth* **47** 245–50

[7] Zhang B, Wu Q, Yu H, Bulin C, Sun H, Li R, Ge X and Xing R 2017 High-efficient liquid exfoliation of boron nitride nanosheets using aqueous solution of alkanolamine *Nanoscale Res. Lett.* **12** 596

[8] Bhimanapati G R, Kozuch D and Robinson J A 2014 Large-scale synthesis and functionalization of hexagonal boron nitride nanosheets *Nanoscale* **6** 11671–5

[9] Du M, Wu Y and Hao X 2013 A facile chemical exfoliation method to obtain large size boron nitride nanosheets *CrystEngComm* **15** 1782–6

[10] Zhang K, Feng Y, Wang F, Yang Z and Wang J 2017 Two dimensional hexagonal boron nitride (2D-hBN): synthesis, properties and applications *J. Mater. Chem.* C **5** 11992–2022

[11] Yu H, Zhang B, Bulin C, Li R and Xing R 2016 High-efficient synthesis of graphene oxide based on improved hummers method *Sci. Rep.* **6** 36143

[12] Yuan F, Jiao W, Yang F, Liu W, Liu J, Xu Z and Wang R 2017 Scalable exfoliation for large-size boron nitride nanosheets by low temperature thermal expansion-assisted ultrasonic exfoliation *J. Mater. Chem.* C **5** 6359–68

[13] Zhao G, Zhang F, Wu Y, Hao X, Wang Z and Xu X 2015 One—step exfoliation and hydroxylation of boron nitride nanosheets with enhanced optical limiting performance *Adv. Opt. Mater.* **4** 141–6

[14] Jin H, Li Y, Li X, Shi Z, Xia H, Xu Z and Qiao G 2016 Functionalization of hexagonal boron nitride in large scale by a low-temperature oxidation route *Mater. Lett.* **175** 244–7

[15] Cao C, Xue Y, Liu Z, Zhou Z, Ji J, Song Q, Hu Q, Fang Y and Tang C 2019 Scalable exfoliation and gradable separation of boric-acid-functionalized boron nitride nanosheets *2D Mater.* **6** 035014

[16] Lin Y, Williams T V, Xu T-B, Cao W, Elsayed-Ali H E and Connell J W 2011 Aqueous dispersions of few-layered and monolayered hexagonal boron nitride nanosheets from sonication-assisted hydrolysis: critical role of water *J. Phys. Chem.* C **115** 2679–85

[17] Sainsbury T, Satti A, May P, Wang Z, McGovern I, Gun'ko Y K and Coleman J 2012 Oxygen radical functionalization of boron nitride nanosheets *J. Am. Chem. Soc.* **134** 18758–71

[18] Lin Y, Williams T V, Cao W, Elsayed-Ali H E and Connell J W 2010 Defect functionalization of hexagonal boron nitride nanosheets *J. Phys. Chem.* C **114** 17434–9

[19] Siddiqui G U, Rehman M M, Yang Y-J and Choi K H 2017 A two-dimensional hexagonal boron nitride/polymer nanocomposite for flexible resistive switching devices *J. Mater. Chem.* C **5** 862–71

[20] Li H, Tay R Y, Tsang S H, Zhen X and Teo E H T 2015 Controllable synthesis of highly luminescent boron nitride quantum dots *Small* **11** 6491–9

[21] Zhao H, Ding J and Yu H 2018 The efficient exfoliation and dispersion of hBN nanoplatelets: advanced application to waterborne anticorrosion coatings *New J. Chem.* **42** 14433–43

[22] Lee D and Song S H 2017 Ultra-thin ultraviolet cathodoluminescent device based on exfoliated hexagonal boron nitride *RSC Adv.* **7** 7831–5

[23] Jennifer Klug D K, Murugaiah A and Raman C 2008 *Improved Process for Making Boron Nitride* (USA: W I P Organization)

[24] Cofer C G and Economy J 1995 Oxidative and hydrolytic stability of boron nitride—a new approach to improving the oxidation resistance of carbonaceous structures *Carbon* **33** 389–95

[25] Lee D, Lee B, Park K H, Ryu H J, Jeon S and Hong S H 2015 Scalable exfoliation process for highly soluble boron nitride nanoplatelets by hydroxide-assisted ball milling *Nano Lett.* **15** 1238–44

[26] Rafiei-Sarmazdeh Z, Jafari S H, Ahmadi S J and Zahedi-Dizaji S M 2015 Large-scale exfoliation of hexagonal boron nitride with combined fast quenching and liquid exfoliation strategies *J. Mater. Sci.* **51** 3162–9

[27] Zhi Y R, Yu B, Yuen A C Y, Liang J, Wang L Q, Yang W, Lu H D and Yeoh G H 2018 Surface manipulation of thermal-exfoliated hexagonal boron nitride with polyaniline for improving thermal stability and fire safety performance of polymeric materials *ACS Omega* **3** 14942–52

[28] Uddin M N, Shimoyama I, Baba Y, Sekiguchi T and Nagano M 2005 X-ray photoelectron spectroscopic observation on B–C–N hybrids synthesized by ion beam deposition of borazine *J. Vac. Sci. Technol.* A **23** 497–502

[29] Wang S, Bian C, Jia B, Wang Y and Jing X 2016 Structure and thermal pyrolysis mechanism of poly(resorcinol borate) with high char yield *Polym. Degrad. Stab.* **130** 328–37

[30] Gonzalez Ortiz D, Pochat-Bohatier C, Cambedouzou J, Bechelany M and Miele P 2018 Exfoliation of hexagonal boron nitride (h-BN) in liquide phase by ion intercalation *Nanomaterials* **8** 716–28

[31] Du M, Li X, Wang A, Wu Y, Hao X and Zhao M 2014 One-step exfoliation and fluorination of boron nitride nanosheets and a study of their magnetic properties *Angew. Chem. Int. Ed. Engl.* **53** 3645–9

[32] Li X, Hao X, Zhao M, Wu Y, Yang J, Tian Y and Qian G 2013 Exfoliation of hexagonal boron nitride by molten hydroxides *Adv. Mater.* **25** 2200–4

[33] Li L H, Chen Y, Behan G, Zhang H, Petravic M and Glushenkov A M 2011 Large-scale mechanical peeling of boron nitride nanosheets by low-energy ball milling *J. Mater. Chem.* **21** 11862–6

[34] Lin Y, Williams T V and Connell J W 2009 Soluble, exfoliated hexagonal boron nitride nanosheets *J. Phys. Chem. Lett.* **1** 277–83

[35] Rizvi R *et al* 2018 High-throughput continuous production of shear-exfoliated 2D layered materials using compressible flows *Adv. Mater.* **30** e1800200

[36] Sahu T K, Ranjan P and Kumar P 2021 Chemical exfoliation synthesis of boron nitride and molybdenum disulfide 2D sheets via modified Hummers' method *Emergent Materials* **4** 645–54

[37] Bernhardt N, Kim S, Froch J E, White S J U, Duong N M H, He Z, Chen B, Liu J, Aharonovich I and Solntsev A S 2021 Large few-layer hexagonal boron nitride flakes for nonlinear optics *Opt. Lett.* **46** 564–7

[38] Sharker S M, Alam M A, Shill M C, Rahman G M S and Reza H M 2017 Functionalized hBN as targeted photothermal chemotherapy for complete eradication of cancer cells *Int. J. Pharm.* **534** 206–12

[39] Zhang Y, Choi J R and Park S-J 2017 Thermal conductivity and thermo-physical properties of nanodiamond-attached exfoliated hexagonal boron nitride/epoxy nanocomposites for microelectronics *Composites* A **101** 227–36

[40] Li H, Zhu S, Zhang M, Wu P, Pang J, Zhu W, Jiang W and Li H 2017 Tuning the chemical hardness of boron nitride nanosheets by doping carbon for enhanced adsorption capacity *ACS Omega* **2** 5385–94

Supplementary Information

High-Yield Preparation of Edge-Functionalized and Water Dispersible Few-Layers of Hexagonal Boron Nitride (hBN) by Direct Wet Chemical Exfoliation

Le Yu[1,2], Pei Lay Yap [1,2], Diana N. H. Tran [1,2], Alexandre M. C. Santos [3,4], and Dusan Losic*[1,2]

[1] School of Chemical Engineering and Advanced Materials, The University of Adelaide, Adelaide, SA 5005, Australia

[2] ARC Research Hub for Graphene Enabled Industry Transformation, The University of Adelaide, Adelaide, SA 5005, Australia

[3] School of Physical Sciences, The University of Adelaide, Adelaide, South Australia 5005, Australia.

[4] Department of Medical Physics, Royal Adelaide Hospital, Adelaide, South Australia 5000, Australia.

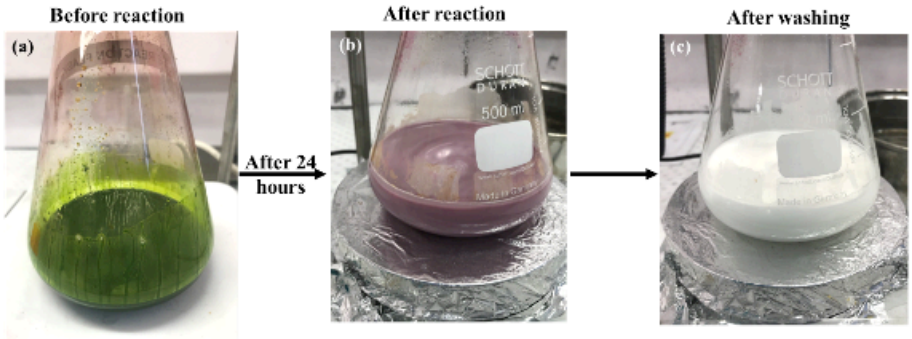

Fig. S1 Photographs of preparation for FL-hBN showing sequential colour changes before turning into the final product

Table S1 Samples prepared at varied exfoliation conditions (temperature, duration and the amount of exfoliating agents)

*Sample	Temp. (°C)	Duration (h)	$KMnO_4$ (g)
BN-40-6-9	**40**	6	9
BN-55-6-9	**55**	6	9
BN-75-6-9	**75**	**6**	9
BN-75-12-9	75	**12**	9
BN-75-24-9	75	**24**	9
BN-75-24-12	75	24	**12**
BN-75-24-15	75	24	**15**
BN-75-24-18	75	24	**18**

Samples are labelled according to varied temperature, duration, and amount of $KMnO_4$ as ***BN-*Temperature-Duration-amount of $KMnO_4$.***

Table S2 EDS analysis for control and other prepared samples (removed carbon elements)

Material	B (at. %) ±0.70	N (at. %) ±0.70	O (at. %) ±0.30
c-hBN	44.37	55.63	0
BN-40-6-9	43.98	54.96	1.06
BN-55-6-9	44.01	53.86	2.13
BN75-6-9	43.90	52.97	3.13
BN-75-12-9	43.42	52.87	3.71
BN-75-24-9	38.38	56.24	5.39
BN-75-24-12	42.37	52.08	5.55
BN-75-24-15	41.56	50.72	7.72
BN-75-24-18	42.09	52.90	5.01

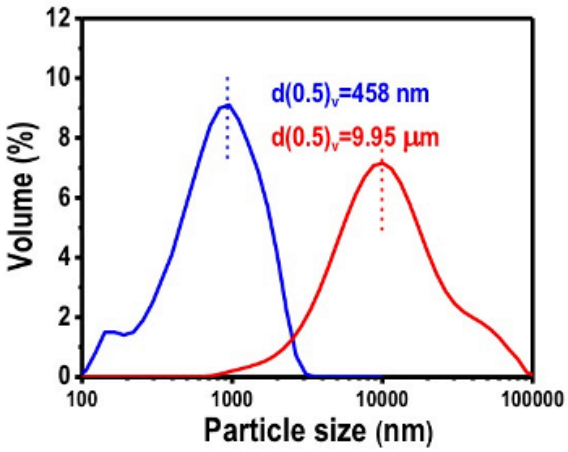

Fig. S2 Particle size analysis of bulk hBN and FL-hBN using dynamic light scattering technique

Statement of Authorship

Title of Paper	Synergistic effect of graphene and hexagonal boron nitride for significant X-ray shielding enhancement of molybdenum disulfide-epoxy composites
Publication Status	☐ Published ☐ Accepted for Publication ☑ Submitted for Publication ☐ Unpublished and Unsubmitted work written in manuscript style
Publication Details	Yu, L., Yap, P. L., Santos, A., Tran, D., Hassan, k., & Losic, D. (2022). Synergistic effect of graphene and hexagonal boron nitride for significant X-ray shielding enhancement of molybdenum disulfide-epoxy composites. *ACS Applied Materials & Interfaces.*

Principal Author

Name of Principal Author (Candidate)	Le Yu		
Contribution to the Paper	Prepared and characterized on all the samples, and interpreted all the data as well as wrote the manuscript.		
Overall percentage (%)	85 %		
Certification:	This paper reports on original research I conducted during the period of my Higher Degree by Research candidature and is not subject to any obligations or contractual agreements with a third party that would constrain its inclusion in this thesis. I am the primary author of this paper.		
Signature		Date	03/03/2022

Co-Author Contributions

By signing the Statement of Authorship, each author certifies that:

i. the candidate's stated contribution to the publication is accurate (as detailed above);

ii. permission is granted for the candidate in include the publication in the thesis; and

iii. the sum of all co-author contributions is equal to 100% less the candidate's stated contribution.

Name of Co-Author	Pei Lay Yap		
Contribution to the Paper	Edited and revised the manuscript.		
Signature		Date	03/03/2022

Name of Co-Author	Alexandre M. C. Santos		
Contribution to the Paper	Co-supervised, performed X-ray irradiations and revised the manuscript.		
Signature		Date	03/03/2022

Please cut and paste additional co-author pa

Statement of Authorship

Title of Paper	Synergistic effect of graphene and hexagonal boron nitride for significant X-ray shielding enhancement of molybdenum disulfide-epoxy composites
Publication Status	☐ Published ☐ Accepted for Publication ☑ Submitted for Publication ☐ Unpublished and Unsubmitted w ork w ritten in manuscript style
Publication Details	Yu, L., Yap, P. L., Santos, A., Tran, D., Hassan, k., & Losic, D. (2022). Synergistic effect of graphene and hexagonal boron nitride for significant X-ray shielding enhancement of molybdenum disulfide-epoxy composites. *ACS Applied Materials & Interfaces*.

Principal Author

Name of Principal Author (Candidate)	Le Yu		
Contribution to the Paper	Prepared and characterized on all the samples, and interpreted all the data as well as wrote the manuscript.		
Overall percentage (%)	85 %		
Certification:	This paper reports on original research I conducted during the period of my Higher Degree by Research candidature and is not subject to any obligations or contractual agreements with a third party that would constrain its inclusion in this thesis. I am the primary author of this paper.		
Signature		Date	03/03/2022

Co-Author Contributions

By signing the Statement of Authorship, each author certifies that:

i. the candidate's stated contribution to the publication is accurate (as detailed above);

ii. permission is granted for the candidate in include the publication in the thesis; and

iii. the sum of all co-author contributions is equal to 100% less the candidate's stated contribution.

Name of Co-Author	Diana N. H. Tran		
Contribution to the Paper	Co-supervised and revised the manuscript.		
Signature		Date	03/03/2022

Name of Co-Author	Kamrul Hassan		
Contribution to the Paper	Edited and revised the manuscript.		
Signature		Date	03/03/2022

Please cut and paste additional co-author panels here as required.

Statement of Authorship

Title of Paper	Synergistic effect of graphene and hexagonal boron nitride for significant X-ray shielding enhancement of molybdenum disulfide-epoxy composites
Publication Status	☐ Published ☐ Accepted for Publication ☑ Submitted for Publication ☐ Unpublished and Unsubmitted w ork w ritten in manuscript style
Publication Details	Yu, L., Yap, P. L., Santos, A., Tran, D., Hassan, k., & Losic, D. (2022). Synergistic effect of graphene and hexagonal boron nitride for significant X-ray shielding enhancement of molybdenum disulfide-epoxy composites. *ACS Applied Materials & Interfaces*.

Principal Author

Name of Principal Author (Candidate)	Le Yu		
Contribution to the Paper	Prepared and characterized on all the samples, and interpreted all the data as well as wrote the manuscript.		
Overall percentage (%)	85 %		
Certification:	This paper reports on original research I conducted during the period of my Higher Degree by Research candidature and is not subject to any obligations or contractual agreements with a third party that would constrain its inclusion in this thesis. I am the primary author of this paper.		
Signature		Date	03/03/2022

Co-Author Contributions

By signing the Statement of Authorship, each author certifies that:

i. the candidate's stated contribution to the publication is accurate (as detailed above);

ii. permission is granted for the candidate in include the publication in the thesis; and

iii. the sum of all co-author contributions is equal to 100% less the candidate's stated contribution.

Name of Co-Author	Dusan Losic		
Contribution to the Paper	Supervised the development of work, edited, revised the manuscript and acted as the corresponding author.		
Signature		Date	03/03/2022

Name of Co-Author			
Contribution to the Paper			
Signature		Date	

Please cut and paste additional co-author panels here as required.

ACS Applied Materials & Interfaces

Synergistic Effect of Graphene and Hexagonal Boron Nitride for Significant X-ray Shielding Enhancement of Molybdenum Disulfide-Epoxy Composites

Journal:	*ACS Applied Materials & Interfaces*
Manuscript ID	Draft
Manuscript Type:	Article
Date Submitted by the Author:	n/a
Complete List of Authors:	Yu, Le; The University of Adelaide, chemical engineering Yap, Pei; The University of Adelaide, School of Chemical Engineering & Advanced Materials Santos, Alexandre ; University of Adelaide, School of Chemical Engineering Tran, Diana N.H.; University of Adelaide, School of Chemical Engineering Hassan, Kamrul; The University of Adelaide, School of Chemical Engineering and Advanced Materials Losic, Dusan; University of Adelaide, School of Chemical Engineering

Synergistic Effect of Graphene and Hexagonal Boron Nitride for Significant X-ray Shielding Enhancement of Molybdenum Disulfide-Epoxy Composites

Le Yu [a,b], *Pei Lay Yap* [a,b] *Alexandre Santos* [c,d,e], *Diana Tran* [a,b], *Kamrul Hassan* [a,b], *Dusan Losic* [a,b*]

[a] School of Chemical Engineering and Advanced Materials, The University of Adelaide, Adelaide, SA 5005, Australia.
[b] ARC Research Hub for Graphene Enabled Industry Transformation, The University of Adelaide, Adelaide, SA 5005, Australia.
[c] School of Physical Sciences, The University of Adelaide, Adelaide, South Australia 5005, Australia.
[d] Department of Medical Physics, Royal Adelaide Hospital, Adelaide, South Australia 5000, Australia.
[e] Australian Bragg Centre for Proton Therapy and Research, Adelaide, SA, Australia 5000.

ABSTRACT Constant exposure to the ionizing radiation such as X-rays can lead to acute health effects including skin redness, hair loss, radiation burns, or cancer. Conventional lead (Pb) based shielding materials have many limitations because of their heaviness and toxicity, thus it is imperative to replace them by lightweight and non-Pb X-ray protection materials. To address this problem molybdenum disulfide (MoS_2) was introduced as an effective filler to form a lightweight MoS_2-epoxy (MoS_2-EP) X-ray shielding composites. However, the low compatibility between MoS_2 and epoxy matrix has hindered the X-ray shielding performance. To overcome this problem, this paper presents how the combination of graphene (GN) and hexagonal boron nitride (hBN) additives can significantly enhance the X-ray attenuation performance of MoS_2-epoxy composites. The results showed that EP-MoS_2-GN with the same thickness and EP-MoS_2-hBN composite with separated addition of GN and hBN exhibited improved X-ray attenuation ability with X-ray transmission of 3.8 % and 30.1 % at 30 kVp and 80 kVp, respectively. However, by employing equal amount of the GN-hBN mixture, the synergistic effect of EP-MoS_2-GN-hBN composite film was observed with a significant X-ray

shielding enhancement of 52.1 % at 30 kVp and 33.2 % at 80 kVp compared to the EP-MoS_2 composite with the same thickness (~ 2 mm) and density (~ 1 g/cm^3). The synergistic effect of GN-hBN mixture on EP-MoS_2 composite was confirmed using Bliss Independence model. These results were attributed to the molecular bonding of GN or hBN that improved compatibility between MoS_2 and the epoxy matrix and providing some other benefits such as a reduced surface roughness (0.46 μm) and improved composite hardness (65.7 HD). The significance of this work is in providing a new strategy using combined GN and/or hBN into other high-Z compounds-polymer composites for development new advanced non-Pb X-ray shielding applications.

KEYWORDS: graphene, hBN, X-ray shielding, epoxy-based composites, synergistic effect

1. INTRODUCTION

Electromagnetic radiation (X-ray) is widely applied to many non-destructive materials testing, including medical radiotherapy, medical diagnosis, and geological exploration.[1] Unfortunately, carcinogenic hazards caused from X-ray have been recognized by the International Committee on Radiological Protection (ICRP), and thus use of the X-ray protective apparel is of great importance to the practitioners working related to X-ray.[2] The mechanism of X-ray attenuation is mainly based on the probability of photoelectric and Compton scattering effects between the incident photons and the shielding materials.[3] Since X-ray contains low-energy photons, the dissipation of the X-ray photon energy is achieved due to the dominant photoelectric effect (mainly dependent on the atomic number (Z) and density).[3-4] Lead (Pb) is therefore widely used as an important shielding material, owing to its high density and high Z that enhances the photoelectric effect by providing more electrons and photon absorption edges.[5-7] However, Pb-based materials normally lack of flexibility, mechanical strength, and chemical stability.[8] Nowadays, Pb-based aprons are commonly used

by the clinical personnel during interventional radiological procedure for the protection from the direct or scattered X-ray. However, the heaviness of these Pb-based aprons hinders the physical movement and causes discomfort wearing experience.[9] Moreover, the severe toxicity of these Pb integrated materials is detrimental to human body and leads to environmental pollution, thus limiting their extensive application.[10] Since 2014, the use of Pb in healthcare has been banned in Europe, leading to high demand for the development of lightweight, non-toxic and Pb-free shielding materials.[11] To meet this demand, several studies have investigated on Pb-alternative materials using other high-Z metals (e.g. bismuth (Bi),[12-13] tungsten (W),[14-15] and barium (Ba),[11, 16]) and their compounds to achieve the efficient X-ray shielding ability.

To reduce the weight of these Pb-free shielding materials, polymer is often introduced as a supporting component to form a lightweight and durable X-ray shielding composite, owing to its unique properties, such as low density, durability, low manufacturing cost, and flexibility in fabrication.[17] Many researchers have explored a wide range of the polymetric matrices (e.g. polyvinyl chloride (PVC), polymethyl methacrylate (PMMA), and natural rubber (NR)) filled with different high-Z metals and metal oxides to fabricate polymer-based composites for X-ray shielding.[18] However, the use of polymers has the limits due to their low mechanical characteristics and low density.[19] The improved mechanical property of a polymetric matrix can be achieved with the reinforcement of nanofillers by having large aspect ratios.[20] For example, 20 wt. % of nanosized lead oxide (Pb_3O_4) was integrated with ethylene propylene diene terpolymer (EPDM) provided 0.65 mm Pb-equivalent X-ray attenuation ability at the high energy of 120 kGy by showing 50 % improvement in maximum strain at break and stress, compared to EPDM only.[21] Another study explored nanosized tungsten oxide (WO_3) with epoxy (EP) proved that addition of 10 wt.% WO_3 nanoparticles can attenuate 98 % X-ray at 40 kV with 38 % of composite hardness enhancement, compared to neat EP.[6]

Among these polymers, EP is commonly employed as a supportive matrix for fabricating a Pb-free shielding composite, due to its good thermal stability that can resist high-energy X-ray bombardment from medical imaging.[4] A previous investigation on the nanosized gadolinium oxide (Gd_2O_3, 400 nm)-EP composite (thickness at 8 mm) for the high-energy X-ray shielding (60-120 kVp) showed 0.5 mm Pb-equivalent X-ray attenuation performance in the range of 60-80 kVp.[22] Our recent study using nanosized bismuth titanate ($Bi_4Ti_3O_{12}$, 500 nm)-EP composite with a thickness of 1 mm successfully achieved 0.35 mm Pb-equivalent X-ray attenuation at 80-100 kVp.[23] Despite the promising outcomes attained by the non Pb-based composites in X-ray attenuation, these Pb-free shielding composites are still impeded by inhomogeneous dispersion and poor distribution of active components in the polymeric matrix.[16] Formation of large voids, sedimentation and segregation led to reduced uniformity of polymer-based composites, which had a negative impact on X-ray attenuation.[24] To overcome these problems, many attempts were taken to develop the reinforced polymer-based composites against X-ray radiation. Graphene oxide (GO) was first considered a potential two-dimensional (2D) material to be applied as an effective reinforcement, since it can be integrated easily with many high-density materials (e.g. Pb) for homogeneous distribution of these materials within the polymers.[15] The effect of functionalized graphene oxide (GO)-polyvinylidene fluoride (PVDF) nanocomposite on X-ray attenuation coefficient was investigated at X-ray energy of 6.9 keV. The results demonstrated that the addition of functionalized GO (1.88 wt.%) into PVDE matrix had four times higher value of X-ray attenuation coefficient, compared to PVDF only. Importantly, the presence of functionalized GO in a polymeric matrix can effectively improve the radiation resistance of PVDF by preventing it from the radiation-oxidation reaction.[25] Later on, Pb_3O_4 decorated GO-EP composites towards X-ray shielding performance were studied with different filler loadings (5 wt.% and 10 wt.% of GO). The outcomes proved that Pb_3O_4-EP composite containing 10 wt.% GO (thickness of 6 mm) achieved 124.3, 124.6 and 103.6%

improvement in the X-ray attenuation at 40 kVp, 60 kVp and 80 kVp, respectively, compared to the neat EP. Moreover, the addition of GO can enhance the mechanical properties of the Pb_3O_4-EP composites, showing improved hardness (0.9 kg·f/mm^2), contact angle (27.8 °) and glass transition temperature (53.2 ℃).[26]

Molybdenum disulfide (MoS_2), with a high Z of Mo at 42 and high density of 5.06 g/cm^3,[27] holds great potential to form a lightweight EP-MoS_2 composite for effective X-ray shielding performance. However, low compatibility between MoS_2 and EP matrix is manifested by the poor dispersion (sedimentation) of MoS_2 particles with the presence of large voids and extreme cracks within the EP matrix. A previous study on the X-ray absorption abilities of high-density polyethylene (HDPE) composites filled with the microsized tungsten (W) powder and MoS_2 powder proved that the equal amount (45 wt.%) of HDPE-MoS_2 composite (the intensity at 4.2 for 80 kVp) exhibited less X-ray absorption compared to the HDPE-W composite (the intensity at 3.5 for 80 kVp), which could be attributed to the significant agglomeration and less uniformity of MoS_2 within the HDPE-MoS_2 composite. To improve the compatibility of MoS_2 within the polymeric matrix, graphene (GN) is introduced to reinforce the EP-based X-ray shielding composites, due to its high aspect ratio providing the homogeneous distribution for various nanoparticles.[28-29] More importantly, graphene has an efficient X-ray attenuation ability (50 %) at the low energy (<10 keV) with very low filler content (<2 %) within the polymer.[30,25] In addition, hexagonal boron nitride (hBN, recognized as white graphene) having a hexagonal crystal structure similar to graphene was applied for improving the mechanical and chemical properties of the polymer-based composite, due to its stiffness and high thermal stability.[31]

In this paper, we present a study to demonstrate how the incorporation of pristine GN (defect-free) and hBN additives and their combination in the EP-MoS_2 composite can significantly enhance X-ray shielding performance. It is hypothesized that the addition of GN or hBN sheets

can provide multitude benefits to the EP-MoS_2 composite including: (1) improved distribution of MoS_2 particles within the composite, (2) strengthened mechanical property, (3) increased thermal stability, and (4) enhanced X-ray attenuation ability that can be further improved by synergetic impact when these two materials are combined. To demonstrate this concept, a comprehensive study was performed by preparing MoS_2 (nanosheets)-EP composites with the addition of GN, hBN and their combination, followed by testing their X-ray shielding performances under X-ray energies of 30 kVp and 80 kVp. All the prepared composites were characterized by a broad range of characterization to confirm their structural, chemical, thermal and mechanical properties. To confirm and understand the synergistic effect of GN and hBN on the EP-MoS_2 composite for X-ray shielding enhancement, the obtained X-ray shielding results were evaluated using Bliss Independence model. The outcome from these study showing significant X-Ray shielding enhancement of EP-MoS_2 composite using EP-MoS2 composite using GN and hBN will offer a new approach for the development of the Pb-free inorganic-polymer composites with superior X-ray shielding performance. This concept will also open a new path to integrate GN and/or hBN (other 2D materials) into other polymer-based composites for the design of the effective X-ray protective materials with improved mechanical, thermal and chemical properties.

2. EXPERIMENTAL SECTION

2.1. Materials

Molybdenum disulfide (MoS_2) and hexagonal boron nitride (hBN) nanosheets were provided from our previous work.[32] Pristine graphene (GN) with an average particle size of ~ 5 μm was provided by First Graphene Ltd. Epoxy (EP) with two parts (epoxy resin 105 and fast hardener 205) was purchased from West System. All the chemicals were used as received and distilled (DI) water was used throughout the study, unless otherwise stated.

2.2. Preparation of molybdenum disulfide (MoS_2) nanosheets and hexagonal boron nitride (hBN) nanosheets

The MoS_2 nanosheets were prepared by a dry ball milling process as reported in our previous work.[33] The hBN nanosheets were synthesized by a direct wet chemical exfoliation method as reported in our previous work.[32]

2.3. Synthesis of epoxy/molybdenum disulfide (EP-MoS_2), epoxy/molybdenum disulfide/graphene (EP-MoS_2-GN), epoxy/molybdenum disulfide/ hexagonal boron nitride (EP-MoS_2-hBN) and ER-MoS_2-GN-hBN composites

To synthesize the EP-MoS_2 composite (the control), the as-prepared MoS_2 nanosheets (60 wt.%) were first blended into the epoxy, followed by mixing with a fast hardener at a mass ratio of 5:1 (epoxy resin to hardener). The mixture was then casted in a plastic mould (3.5 cm in diameter) and set for 24 h at room temperature (20 ± 2 °C). In addition, the EP-MoS_2 composites containing GN or hBN were prepared by subsequently mixing with 16 wt.% of GN or hBN. The EP-MoS_2 composite containing mixed GN and hBN at equal amount (8 wt.%) was synthesized for further investigation on their synergistic effect towards X-ray attenuation improvement. Further details of the prepared samples with their corresponding designations are listed in Table 1.

Table 1. List of as-prepared EP-MoS_2 composites with addition of GN and hBN and their corresponding weight fraction.

Composite designation	Composite by weight fraction (%)		
	MoS_2	GN	hBN
EP	-	-	-
EP-MoS_2	100	-	-
EP-GN	-	100	-
EP-hBN	-	-	100
EP-MoS_2-GN	84	16	-
EP-MoS_2-hBN	84	-	16
EP-MoS_2-GN-hBN	84	8	8

Note: the mass of EP is consistent for all the prepared composites.

2.4. Materials characterization

The synthesized samples were characterized by X-ray diffractometer (XRD, Rigaku Miniflex 600, Japan) in the range of $2\theta = 20\text{-}80°$ (scan rate of 10 ° min^{-1}). Scanning Electron Microscopy coupled with Energy Dispersive X-Ray (SEM-EDX, Quanta 450 FEG, FEI, USA; Ultim Max Oxford Instruments, UK) was adopted to study the elemental composition and morphology of the samples. Particle size distribution (PSD) was measured using a Zetasizer Nano-ZS (Malvern Panalytical Australia, Australia). Thermal stability and properties of the synthesized materials were probed using TGA Q500 (TA Instruments, USA) under air atmosphere with the samples heated to 1000 °C at heating rate of 10 °C min^{-1}. The surface roughness of the composites was obtained from a 3D optical profilometer (Bruker Contour GT-K, Australia), using vertical scanning interferometry (VSI) mode with a working distance of 6.7 mm. Shore hardness measurements were performed with a shore D durometer according to the ASTM D2240 standard. X-ray Photoelectron Spectroscopy (XPS, AXIS Ultra DLD, Kratos, UK) with a monochromatic Al Kα radiation source (hv =1486.7 eV) was used to examine the chemical species and the surface elemental composition of the synthesized composites at 225 W, 15 kV and 15 mA. XPS survey scans were collected at 0.5 eV step size over -10 to 1100 eV at 160 eV pass energy. The narrow scans were collected at 0.1 eV step size and pass energy of 20 eV. All the core-level spectra were referenced to the primary peak (C-C/C-H peak) of adventitious carbon at 284.8 eV. Peak deconvolution was performed using Casa XPS™ software and fitted using a Shirley background correction method. The splitting between the Mo $3d_{3/2}$ and $3d_{5/2}$ peaks was fixed at 3.18 eV.

2.5. X-ray transmission measurements

X-ray attenuation is the reduction of the intensity of X-ray when it travels through matter.[25] The properties of the controls (EP, EP-GN, EP-hBN films) and as-prepared composite films (EP-MoS_2, EP-MoS_2-GN, EP-MoS_2-hBN and EP-MoS_2-GN-hBN) were measured using a Gulmay D3150 superficial X-ray (SXR) unit. The distances between the X-ray tube and the

material sample, and the material sample to the detector were both set to 50 cm. The detector used to measure the transmission was a NE 2571 farmer type ionization chamber (Phoenix Dosimetry Ltd, UK). The samples were exposed to the respective X-ray voltage at 30 kVp (0.2 mm Al) and 80 kVp (2 mm Al) for 0.50 mins with the material sample placed over a collimator of diameter 1 cm. The X-ray transmission was calculated as the charge collected by the ionization chamber with the sample divided by the transmission dose without the sample. Each sample was measured three times and determined by the arithmetic mean.

The X-ray attenuation of an X-ray beam through any material can be estimated as a function of the linear attenuation coefficient (μ) as equation (1),[34]

$$I = I_0 e^{-ut} \quad (1)$$

where I and I_0 are the final X-ray intensity after the attenuation by the sample and the X-ray intensity before passing through the sample, respectively, and t is the material thickness (mm). The X-ray transmission (T) can be expressed as equation (2),[35]

$$T = (I / I_0) \times 100\% \quad (2)$$

The density (g/cm^3) of each sample can be calculated as equation (3),

$$\rho = m / V \quad (3)$$

where m is the mass (g) of the sample and V is volume (cm^3) of the sample.

3. RESULTS AND DISCUSSION

3.1. Characterization of molybdenum disulfide (MoS_2), hexagonal boron nitride (hBN) and graphene (GN) and their epoxy composites

To confirm the morphological and chemical properties of the as-prepared MoS_2 nanosheets, few-layer graphene (FL-GN) and hBN nanosheets, the comprehensive characterizations (including XRD, Raman analysis, FESEM and TEM images, and PSD technique) were performed and presented in Figure. 1 and Figure. S1. The morphological structure of the synthesized MoS_2 nanosheets was studied using FESEM (Figure. 1(a-1)), showing a large

quantity of the irregularly aggregated particles with the average particle size of 432 nm, which was verified by TEM image in Figure. 1(a-2). Moreover, Figure. 1(b-1) exhibited that the SEM image of the pristine graphene sheets were at a few micrometres (Figure. 1(b-3)) with a smooth surface decorated by the distinct folded edges as shown in Figure. 1(b-2). More detailed characteristics about graphene sheets can be viewed in our previous work.[36] The as-prepared hBN nanosheets presented a layered plate-like morphology (Figure. 1(c-1) with an average size distribution of 458 nm as shown in Figure. 1(c-3). Further details can be viewed in our previous work.[32] This observation was confirmed using TEM technique, indicating the ultrathin and ordered few-layer hBN nanosheets (Figure. 1(c-2)) with a clear and regular shape.

The crystallinity and phase purity of the prepared MoS_2, hBN and GN nanosheets were examined using X-ray diffraction. Figure. S1(a) revealed the crystalline phase of the synthesized MoS_2, showing the characteristic peaks located at 2θ = 14°, 29°, 32°, 33°, 35°, 39°, 44°, 49°, 58° and 60° corresponding to their diffraction planes of (002), (004), (100), (101), (102), (103), (006), (105), (110), and (008), respectively. The observed XRD peaks were in good agreement with the standard pattern of 2H phase MoS_2 (JCPDS-37-1492).[37] The sharp and well-defined peaks of (002), (100), (101) and (004) planes in the XRD pattern (Figure S1(b)) corresponded to hexagonal phase boron nitride (JCPDS-034-0421),[38] and the two characteristic peaks at 2θ values of 26°, 54° were assigned to the (002) plane of graphene.[39]

Raman spectroscopy results the synthesized MoS_2 nanosheets presented presented in Figure S1(c) showed two typical Raman bands at 376.6 cm^{-1} and 401.2 cm^{-1}, corresponding to E^1_{2g} (in-plane vibrations between two sulphur atoms and molybdenum atom) and A_{1g} (out-of-plane vibrations between sulphur atoms in the opposite direction) modes, respectively.[40] The Raman spectrum of the graphene and hBN presented Figure. S1(d) showed the characteristic peaks at 1351.8 cm^{-1}, 1577.5 cm^{-1} and 2717.3 cm^{-1}, which can be attributed to the D mode, G mode and D' (2D) mode of the graphitic system, respectively.[39, 41] Moreover, the peak at 1360.1 cm^{-1} can

be attributed to the vibrational mode (E_{2g}) of hBN, due to the in-plane vibration of the sp^2 hybridized B-N=B bond,[42] and this narrow and intense peak of hBN indicated the low concentration of the defect structure.[43] The results obtained from Raman spectrum were in good agreement with their corresponding XRD patterns.

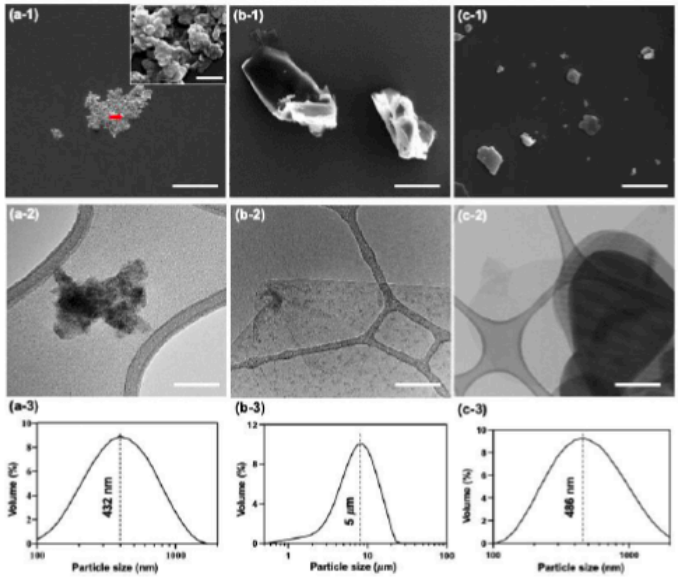

Figure 1. SEM images (scale bar = 10 μm) and TEM images (scale bar = 50 nm) and PSD of the synthesized (a-(1-3)) MoS_2 nanosheets, (b-(1-3)) FL-GN sheets and (c-(1-3)) hBN nanosheets, respectively, and inset of Figure. (a-1) is the high-magnification SEM image (as indicated in the red arrow) of MoS_2 nanosheets (scale bar = 500 nm).

The XRD results of the controls (EP, EP-GN and EP-hBN) and the prepared EP-MoS_2, EP-MoS_2-GN, EP-MoS_2-hBN and EP-MoS_2-GN-hBN composites presented In Figure 2a-c showed a typically broad peak at 2θ value around 22°, as a result of the amorphous structure of epoxy matrix.[44] The humped peak from 10° to 28° caused by scattering of the epoxy molecules,[45]narrowed the characteristic peak of (002) plane observed in both EP-GN (2θ = 26°) and EP-hBN (2θ = 27°) composites, while the remaining peaks were the same as their powdered forms as shown in Figure. S1(b), respectively. The disappearance of the typical MoS_2 peak (2θ = 14°) in the EP-MoS_2 composite was attributed to the broad overlapping peak

of the cured epoxy, and rest of the characteristic peaks of MoS_2 was the same as seen in Figure. S1(a). XRD pattern of EP-MoS_2-GN-hBN composite in Figure. 2(c) showed all the characteristic peaks at $2\theta = 22°, 27°, 32°, 33°, 35°, 39°, 44°, 49°, 54°, 58°$ and 60°, conforming the presence of these fillers (MoS_2, GN and hBN) in an epoxy matrix.

XPS survey analyses of the as-synthesized EP-based composites are illustrated in Figure. 2(d) with their normalized relative atomic composition tabulated in Table S1. Among the detected elements in all the composites, carbon is the major contributing element, followed by oxygen, since epoxy molecules are typically made up of oxygen bonded to carbon framework. The surface elemental composition of the key elements including carbon (C1s at ~ 285 eV), oxygen (O1s at ~532.5 eV), nitrogen (N1s at ~398.5 eV), molybdenum (Mo3d at ~233 eV), sulfur (S2p at ~162.5 eV) and boron (B1s at ~191.0 eV) at varied concentrations confirmed the presence of each chemical species in each epoxy composite system. As presented in Figure 2d, XPS survey scans of both EP control and EP-GN composites contain only C1s, O1s with trace amount of N1s and Si2p elements detected in the composite systems. Integration of hBN and MoS_2 nanosheets in the composite systems were verified by their resulting components including B1s, N1s and Mo3d, S2p, respectively, in the prepared composites. EP-MoS_2-GN-hBN composite exhibited a relative concentration of 57.3 at % of C1s, 14.8 at % of O1s, 13.0 at % of N1s, 2.1 at % of Mo3d, 5.8 at % of S2p and 7.0 at % of B1s, indicating the successful incorporation of the active component and additives in the EP composite. Note that elements such as sodium, bromine, chlorine and etc, were also detected at negligible amount as impurities in these samples. Detailed narrow scans of the C1s spectrum on the hybrid system (EP-MoS_2-GN-hBN) evidently showed that it has a chemical-rich environment with two main carbon peaks at ~284.8 eV and ~286.6 eV that can be deconvoluted into six components including C=C (284.7eV), C-C (285.2 V), C-N (286.0 eV), C-O (286.5 eV), C=O (287 eV) and O-C=O (288 eV). The high-resolution spectral region with two main set of signals that give

rise to Mo3d (~229.8 eV and ~232.9 eV) and S2s peaks (~227.0 eV) with no peak at 228 eV detected for metallic phase (Mo^0), confirmed the presence of molybdenum in the semiconducting phase of MoS_2.[46-47] Fitting of the Mo3d peaks led to three doublets with the first pair located at 229.8 eV and 232.9 eV, corresponding to the characteristic binding energies of Mo^{4+} (charged state of Mo in MoS_2) for $Mo3d_{5/2}$ and $Mo3d_{3/2}$ spin-orbit states, respectively.[48-50] The second doublets due to the presence of Mo^{6+} of MoO_3 or MoO_x for $Mo3d_{5/2}$ and $Mo3d_{3/2}$ were visible at 232.6 eV and 235.7 eV, respectively.[49-50] Small satellite peaks corresponding to its oxide were also found at 234.0 eV and 237.0 eV, indicating a slight oxidation of MoS_2 resulting from the surface oxidation of MoS_2 in air.[47, 51] Existence of hBN as an additive in the hybrid system was validated with the appearance of peaks arising from ~187.8 eV, ~188.9 eV, 191.1 eV and 191.9 eV attributed to B-B, B-C, B-N and B-O species, respectively.[32, 52]

TGA characterization results described the thermal properties of the EP-based composites including control epoxy (EP), EP-GN, EP-hBN, EP-MoS_2 and EP-MoS_2-GN-hBN presented in Figure 2(f) showed that neat EP was completely burned in air with two major decomposition events, which can be observed by its first derivative of TGA (DTG) plot with a mass loss of the maximum temperature (T_{max}) peaks found at 360.3 °C and 585.5 °C. The first thermal decomposition event can be ascribed to the breakdown of the epoxy network, while the second event could be due to the degradation of the benzene ring in the cured epoxy molecules. A slight mass loss (~ 5 %) before 300 °C could be linked to the homolytic scission of chemical bonds in the epoxy network.[53] EP-hBN composite exhibited a similar thermal decomposition pattern as neat EP with only 10 % residue remaining after 1000 °C. hBN is a highly thermal stable material, therefore mass changes only when the heating temperature is beyond 1000 °C.[32] Meanwhile, the DTG curve of EP-GN composite showed T_{max} peaks at three temperature ranges: 350-450 °C, 450-650 °C and > 650 °C with complete thermal degradation.

Apart from the first two DTG peaks that can be related to the thermal decomposition of epoxy resin, the distinctive T_{max} at 680 °C corresponded to the sp^2-hybridized carbon of few-layer graphene (FL-GN), confirming the integration of GN in the epoxy system.[36] In contrast, TGA-DTG graph of EP-MoS_2 composite showed multiple mass loss stages at 350-450 °C due to decomposition of the epoxy network, MoO_3 and SO_2, 450-650 °C for the breakdown of benzene ring in the epoxy network, and the sublimation of MoO_3 above 700 °C. Presence of MoO_3 is common within the MoS_2 nanosheets as evidenced in the XPS results.[54] Addition of GN and hBN as fillers in the EP-MoS_2-GN-hBN hybrid system was confirmed by its TGA-

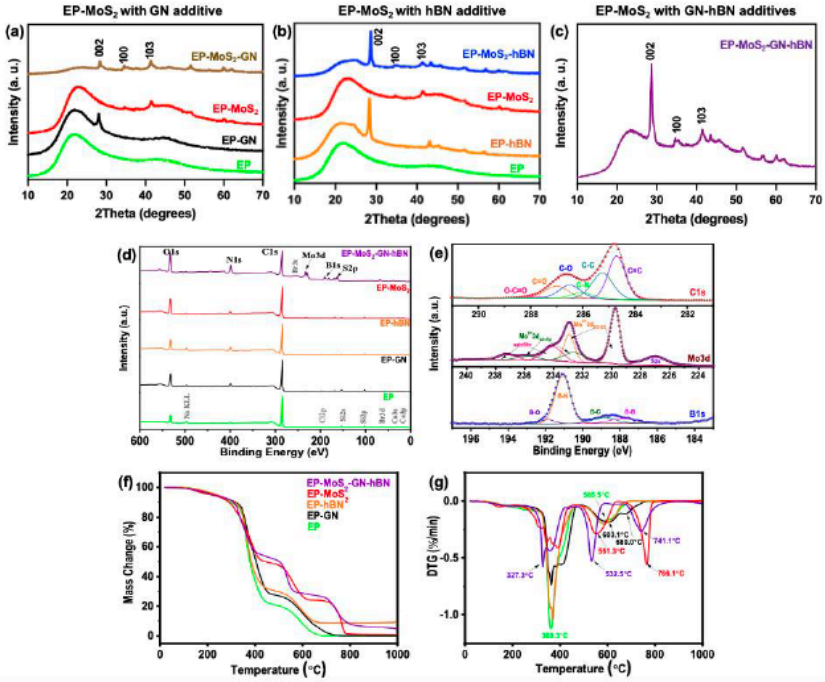

Figure. 2 XRD patterns of the as-prepared EP-MoS_2 composites with (a) GN additive, (b) hBN additive, and (c) with the combination of GN and hBN additives, (d) XPS survey curves, (f) TGA and (g) DTG curves analysis of as-synthesized epoxy composites (EP, EP-GN, EP-hBN, EP-MoS_2 and EP-MoS_2-GN-hBN), and (e) XPS high-resolution plots of C1s, Mo3d and B1s of EP-MoS_2-GN-hBN composite

DTG profile as illustrated (in purple) in Figure 3(g). Changes in DTG peak shape and slight T_{max} shifts were observed with about 5 % residue remaining after the oxidative pyrolysis, which

could be attributed to the hBN nanosheets. The systematic thermal investigations suggested that (1) successful incorporation of hBN and GN as the additives in the EP-MoS_2-GN-hBN composite, and (2) the combined addition of GN and hBN was beneficial in improving the thermal stability of the EP-MoS_2 composite.

The surface morphology of the controls (EP, EP-GN and EP-hBN) and the prepared composites (EP-MoS_2, EP-MoS_2-GN, EP-MoS_2-hBN and EP-MoS_2-GN-hBN) are presented in Figure S2 with their respective photographs of each prepared film (inset of Figure. S2). The SEM image of the EP film in Figure. S2(a) showed a deformed plastic morphology with the presence of micrometre-sized voids on its surface, giving the highest average surface roughness at 1.12 μm (Figure. S3(a)). In contrast, the EP-GN composite had a smoother surface showing several white particles (Figure. S2(b)), while EP-hBN composite (Figure. S2(c)) exhibited a uniformly dispersed structure with an average surface roughness of 0.32 μm (Figure. S3(a)). EP-MoS_2 composite in Figure S2(d) composed of significant agglomeration of MoS_2 nanosheets underneath the epoxy matrix, leading to an increased average surface roughness of 0.53 μm (Figure. S3(a)). This is due to the fact that excessive self-bonding and stacking of MoS_2 nanosheets largely hindered the interaction between the nanofillers and the polymeric matrix.[55] To improve the compatibility and surface roughness of the MoS_2 nanosheets towards the polymeric EP matrix, GN (16 wt.%) was acted as a surfactant to bond MoS_2 surface with the polar tails from epoxy matrix,[16] showing a homogenously-dispersed surface with minimal pits (Figure. S2(e)). EP-MoS_2-hBN composite showed a rough, crack-like surface as a result of polymer deformation (Figure. S2(f)), due to the stiffness of hBN from strong electrostatic bonding between the basal place of hBN and the polymer matrix.[56] To investigate the effect of GN and hBN in the EP-MoS_2 composite for X-ray shielding performance, EP-MoS_2-GN-hBN composite was fabricated and determined using SEM, showing wrinkle-like surface structure (Figure. S2(g)) with an improved average surface roughness of 0.46 μm (Figure. S3(a)). This

strongly suggested that well-dispersed MoS_2 nanosheets in the epoxy matrix was achieved with the aid of both GN and hBN.

To further verify the effect of GN and hBN as nanofillers in the EP-MoS_2 composite, cross-sectional SEM images of the EP, EP-MoS_2 and EP-MoS_2-GN-hBN composite films (Figure. 3(a-c)) were obtained using backscattered electron (BSE) mode to determine the distribution of each element within the prepared films. Figure. 3(a) showed a typical structure of epoxy (control) with minor features (including bubbles, pits, and debris). After the addition of MoS_2, MoS_2 sedimentation with the formation of voids and cracks in epoxy matrix was observed in EP-MoS_2 composite (Figure. 3(b)). This is a common phenomenon of incompatibility within inorganic-epoxy composites, leading to the reduction of mechanical properties (average hardness of 52.5 HD), compared to ER-GN (average hardness of 57.5 HD) and ER-hBN (average hardness of 59.5 HD) composites (Figure. S3(b)), which contain only one nanofiller.[16] To solve this problem, both GN and hBN were employed as reinforcements to bond the MoS_2 nanosheets with epoxy. As shown in Figure. 3(c), less aggregation of MoS_2 nanosheets was observed with aid from both GN and hBN sheets, showing improved dispersion within the epoxy matrix. The elemental distribution of EP-MoS_2-GN-hBN composite film obtained from mapping analysis also confirmed this result (shown in Figure. 3(c1-6)). Its increased average hardness at 65.7 HD (shown as Figure. S3(b)) was also attributed to the strong interfacial reaction between the GN-hBN combination and epoxy.[28, 57-58] Figure. 3(d) illustrated the structural differences of the cross-sectional SEM images (Figure. 3(a-c) and elemental distribution (Figure. 3(c1-6)) of the EP film to the successfully synthesised EP-MoS_2-GN-hBN film.

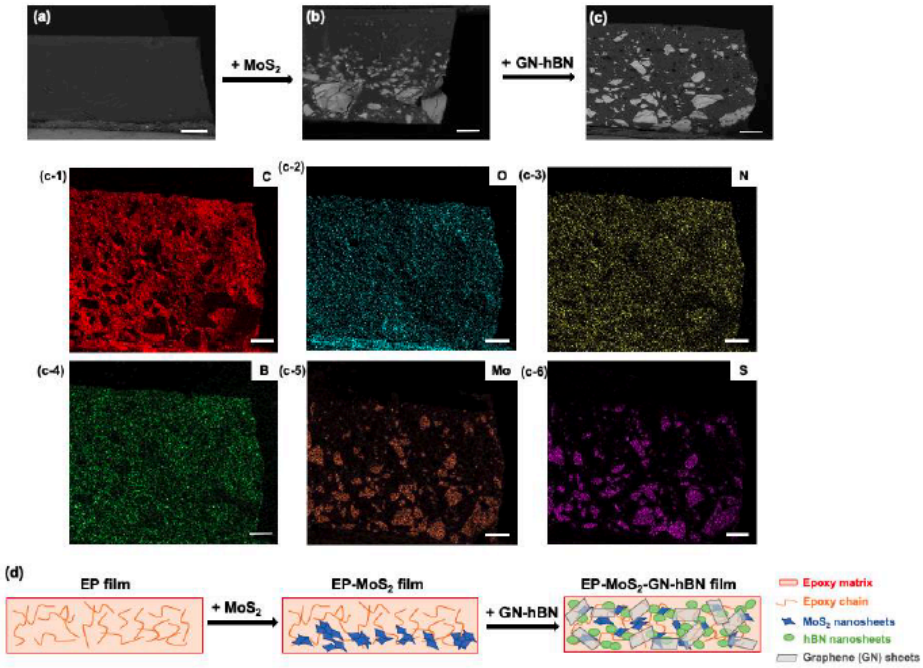

Figure. 3 Cross-sectional BSE-SEM images of (a) EP film (control), (b) EP-MoS_2 composite film, (c) EP-MoS_2-GN-hBN composite film (scale bar = 500 μm), (c-(1-6)) mapping analysis of cross-sectional SEM image of EP-MoS_2-GN-hBN composite film (scale bar = 500 μm), and (d) schematic illustration of the structure changes from EP film to EP-MoS_2-GN-hBN film.

3.2. X-ray transmission measurements

To investigate the influence of individual additives (GN, hBN) within the EP-MoS_2 composite towards X-ray attenuation, X-ray transmission measurements of the controls (EP, EP-GN and EP-hBN) and the EP-MoS_2 composites with each additive (GN, hBN) were performed at X-ray energies of 30 kVp and 80 kVp as presented in Figure. 4. In the initial experiment, the EP film showed the highest X-ray transmission of 87.6 % and 98.9 % at both 30 kVp and 80 kVp, indicating its X-ray attenuation efficiency of ~ 12 % and ~ 1 %, respectively, which can be neglected. Both EP-GN and EP-hBN films obtained similar X-ray attenuation ability, showing X-ray transmission of ~ 64-62 % at 30 kVp and ~ 89-90 % at 80 kVp, respectively. Noticeably, there was a significant decrease in the X-ray transmission of the EP-MoS_2 film, showing the respective X-ray transmission values of 11.7 % at 30 kVp and

45.1 % at 80 kVp. This result was due to the dependence of photon interaction on higher atomic number (Z) of the shielding material (MoS_2) when the photoelectric effect is predominant at the low energy region (< 100 keV).[59] With the addition of GN, X-ray transmission of EP-MoS_2-GN was ~ 1.3 times lower than the EP-MoS_2 composite (Figure. 4(a)), since GN can be used as a stiff filler to reinforce the composite with superior mechanical properties (average composite hardness at 60.7 HD shown as Figure. S3(b)). The strong sp^2 carbon bond (confirmed in Figure. 2) of GN is able to facilitate the homogenous dispersion (average surface roughness at 0.40 μm) of MoS_2 within the epoxy matrix by preventing aggregation within the polymer-based composite.[60] However, by replacing GN with equal amount of hBN, the EP-MoS_2-hBN composite provided the best X-ray attenuation performance, showing X-ray transmission of 7.1 % at 30 kVp and 34.3 % at 80 kVp, respectively (Figure. 4b). This result was attributed to the improved dispersion of MoS_2 within the EP matrix, because of the strong covalent bond between B and N atoms (confirmed in Figure. 2) favoured reinforcement towards polymeric composites.[19] Another aspect that signified the use of hBN was its reduced particle size (486 nm referred to [32]) towards the enhanced interaction within the epoxy matrix, leading to the improved dispersion within EP-MoS_2 composite benefiting X-ray attenuation.[61]

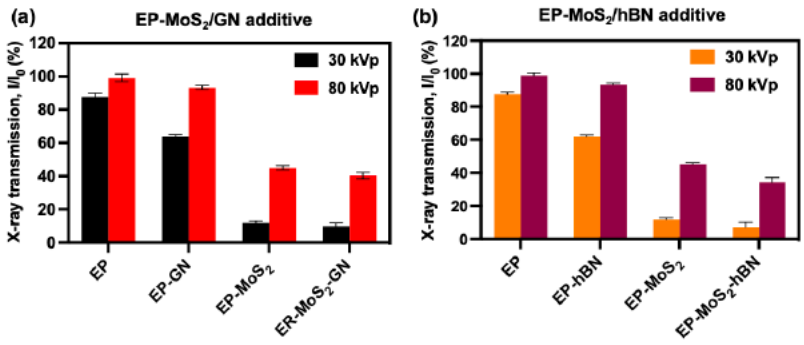

Figure 4 Comparative study on X-ray transmission of the prepared EP-MoS_2 composite with individual additives ((a) EP-MoS_2-GN and (b) EP-MoS_2-hBN), and the controls (EP, EP-GN and EP-hBN) at X-ray energies of 30 kVp and 80 kVp.

3.3. Synergistic effect of graphene (GN) and hexagonal boron nitride (hBN) additives

Following our remarkable enhanced shielding performance after the incorporation of graphene and hBN as individual additive in the EP-MoS_2 composites in the previous experiments, further investigation on the effect of GN and hBN mixture on the X-ray attenuation performance of EP-MoS_2 composite was carried out and presented in Figure 5(a). At both X-ray energies of 30 kVp and 80 kVp, there was a significant linear decrease in the X-ray transmission among the prepared samples. By employing equal amounts of the GN-hBN mixture as their individual counterparts, it was apparent that the EP-MoS_2-GN-hBN composite film achieved the lowest X-ray transmission (5.6 % at 30 kVp and 30.1 % at 80 kVp).

Figure. 5(b) showed improvement percentages of as-prepared EP-MoS_2-GN, EP-MoS_2-hBN and EP-MoS_2-GN-hBN composites compared to EP-MoS_2 composite at X-ray energies of 30 kVp and 80 kVp. By elevating the X-ray energy from 30 kVp to 80 kVp, a decreasing trend was observed on all fabricated composites, since the increment of X-ray energy reduced the photoelectric effect on X-ray attenuation performance.[62] By providing the same composite thickness at ~ 2 mm (obtained from SEM images in Figure. 3 and Figure. S4) and density at ~ 1 g/cm^3 (calculated from equation 3) as shown in Table S2, it is interesting to notice that EP-MoS_2-hBN showed double increment in X-ray shielding improvement compared to EP-MoS_2-GN at 30 kVp. However, this effect of X-ray shielding improvement became insignificant when X-ray energy increased to 80 kVp, due to weakened photoelectric effect on X-ray attenuation. Moreover, EP-MoS_2-GN-hBN showed the most significant X-ray shielding improvement of 52.1 % at 30 kVp and 33.2 % at 80 kVp. This result proved that the use of GN-hBN mixture imposed a greater impact on the X-ray attenuation ability at 30 kVp and 80 kVp, owing to improved dispersion and compatibility of MoS_2 nanosheets within epoxy matrix.[63] Moreover, the addition of GN-hBN mixture into EP-MoS_2 composite not only can

facilitates the uniform dispersion within EP matrix, but also improves thermal stability and strengthen mechanical property of the EP-based material.

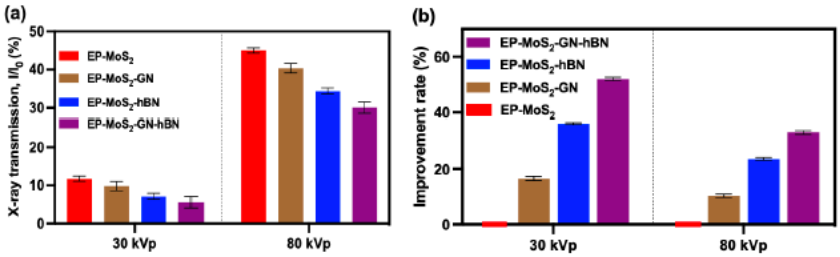

Figure 5 (a) X-ray transmission of EP-MoS_2 (control), EP-MoS_2-GN, EP-MoS_2-hBN and EP-MoS_2-GN-hBN composites, (b) X-ray improvement percentages of EP-MoS_2-GN, EP-MoS_2-hBN, EP-MoS_2-GN-hBN compared to EP-MoS_2 (control) with the same composite thickness (2 mm) and density (1 g/cm^3) at 30 kVp and 80 kVp.

To explain the synergistic effect of GN and hBN additives on the radiation shielding performance, two additional EP-MoS_2 composites were prepared by employing 8 wt.% GN and 8 wt.% hBN (denoted as EP-MoS_2-0.08GN and EP-MoS_2-0.08hBN), respectively. Their X-ray shielding efficiencies were further compared with the value of EP-MoS_2-GN-hBN composite (Figure. S5). Synergy is defined as the effect of two or more agents working as a combination, which is greater than the expected additive effect of the above-mentioned agents.[64] Bliss Independence was herein adapted as one of the commonly used models for determining the synergistic effect in the drug and medical field.[65] Equation (3) is applied to prove whether the synergistic effect is achieved.[66]

$$E_c = E_a + E_b \cdots\cdots E_n \quad (3)$$

where E_c is the effect produced by the combination of compounds A and B, at dose a and b. E_a is the effect of compound A at dose a and E_b is the effect of compound B at dose b. This equation is used as the reference for how the combination of both compounds A and B acts when no synergy is achieved. If the combination of effect is greater than what it is expected, synergy is declared.[67]

Figure 6 presented the results on the improvement percentages of X-ray transmission for EP-MoS_2-0.08GN, EP-MoS_2-0.08hBN and EP-MoS_2-GN-hBN composites at both 30 kVp and 80 kVp, compared to EP-MoS_2 composite, which was obtained from X-ray transmission for the four above-mentioned composites (Figure. S5). At low X-ray energy of 30 kVp, improvement percentages of EP-MoS_2-0.08GN and ER-MoS_2-0.08hBN were 8.3 % and 23.2 %, respectively. The effect of X-ray attenuation improvement for the combination (EP-MoS_2-GN-hBN, 52.1 %) was ~1.6 times greater than the additive effect of both EP-MoS_2-0.08GN and EP-MoS_2-0.08hBN (8.3 % + 23.2 % = 31.5 % < 52.1 %), suggesting that a synergistic effect for the combination of GN-hBN was achieved. The same result was obtained at high X-ray energy of 80 kVp, conforming that this synergistic effect was also attainable at higher X-ray energy. The slight decrease in the synergistic effect on X-ray attenuation ability was probably due to the minor aggregation of MoS_2 nanosheets within the EP-GN-hBN composite (Figure. 3(c)). The slightly broad particle size distribution of MoS_2 nanosheets could be another impact on X-ray shielding performance.

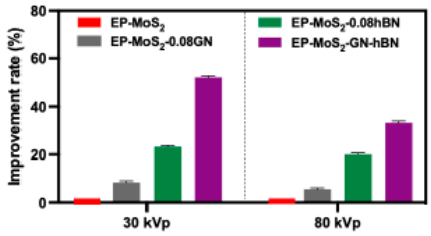

Figure 6 X-ray improvement percentages of EP-MoS_2-0.08GN, EP-MoS_2-0.08hBN, EP-MoS_2-GN-hBN compared to EP-MoS_2 (control) at 30 kVp and 80 kVp.

Previous studies have explored the effect of GO as additive within the polymer-based composites for X-ray shielding enhancement as shown in Table 2. The strong interaction between oxygen-containing groups from GO (e.g. carbonyl groups) and polymers led to improved dispersion of the fillers (effective X-ray shielding materials) within the polymeric matrix.[68] Our work demonstrated that the combination of GN and hBN as additives within the

EP-MoS_2 composite (average thickness at 2 mm) can significantly enhance 70 % of the X-ray attenuation compared to neat EP matrix. It should be highlighted that with only thickness of 2 mm, our developed composite with the addition of GN-hBN mixture could achieve 70 % improvement of X-ray attenuation at 80 kVp in relative to neat EP, which is more superior than majority of the thicker composites listed in Table 2. This promising outcome revealed that the integration of GN-hBN mixture into a polymer-based material paves a new direction for the enhancement of X-ray shielding.

Table 2 Comparison of the effect of additives on polymer-based composites towards X-ray shielding improvement

Active component	Polymer	Additive	Weight fraction of additive (%)	Thickness of composite (mm)	X-ray energy (kVp)	Improvement rate of X-ray attenuation	Reference
Pb_3O_4	Epoxy (EP)	GO	10	6	80	98 % compared to neat EP	26
W-Bi-Sn	Polyaniline (PANi)	GO	10	9	80	6% compared to the same composite with the thickness of 3 mm	69
Iron tungsten nitride (ITN)	PANi	GO	15	1.2	60	60 % compared to neat PANi	70
MoS_2	EP	GN-hBN	16	2	80	70 % compared to neat EP	Our work

4. CONCLUSION

In this work, we successfully demonstrated a significant enhancement of X-Ray radiation shielding of EP-MoS_2 composites with the addition of GN and/or hBN nanofillers and their combination. The synthesis of these composites is confirmed by XRD, SEM, XPS and TGA analysis showing structural and chemical composition of EP-MoS2-GN-hBN composite and their individual components. The X-ray shielding performance study confirmed that adding hBN alone was able to offer ~ 2 times greater improvement in X-ray attenuation at 30 kVp, compared with GN. Remarkably, combination of GN and hBN in the EP-MoS_2 composite with an overall composite thickness of 2 mm, exhibited synergistic effect that significantly

improved X-ray attenuation (52.1 %), compared to the ER-MoS_2 composite showing this concept with mixing two additives can be successfully to enhance the X-ray attenuation at both 30 kVp and 80 kVp, It is important to state these additives also improved the composite hardness and thermal stability performance. These unexpected results are explained due the molecular bonding of GN or hBN that improves compatibility between MoS_2 and the epoxy matrix, optimizing their dispersion and distribution in the matrix that have significant impact on shielding performance. The key findings from this work also provided profound insight on the introduction of GN and/or hBN into other high-Z compounds-polymer composites for development of new generation of Pb-free X-ray shielding protectant that can be used across broad sectors.

ASSOCIATED CONTENT

Supporting Information

The Supporting Information is available free of charge at XXX.

Supplementary Figures of XRD patterns and Raman spectra of the synthesized MoS_2 nanosheets, GN sheets and hBN nanosheets, cross-sectional BSE-SEM images and top-surface SEM images of the prepared composites, surface roughness and shore hardness of the prepared composites, X-ray transmission of EP-MoS_2, EP-MoS_2-0.08GN, EP-MoS_2-0.08hBN and EP-MoS_2-GN-hBN composites at 30 kVp and 80 kVp.

AUTHOR INFORMATION

Corresponding Author

*E-mail: dusan.losic@adelaide.edu.au

NOTES

The authors declare no competing financial interest.

ACKNOLEDGEMENTS

The authors acknowledge the financial support from the ARC Research Hub for Graphene Enabled Industry Transformation, (IH150100003). We thank Australian Microscopy and Microanalysis Research Facility (AMMRF) for the access of SEM facilities, Mr. Ken Neubauer for their technical support on SEM measurements, we also thank OptoFab node of Australian National Fabrication Facility for the access of 3D optical profilometer, Mr. Alson Kwun Leung Ng for his technical support on surface roughness measurement.

REFERENCES

(1) Li, Z.; Zhou, W.; Zhang, X.; Gao, Y.; Guo, S. High-efficiency, flexibility and lead-free X-ray shielding multilayered polymer composites: layered structure design and shielding mechanism. *Sci Rep* **2021**, *11* (1), 4384, DOI: 10.1038/s41598-021-83031-4.
(2) ICRP *Radiological protection of people and the enviroment in the event of a large nuclear accident*; 2020; p 4.
(3) Wang, Y.; Ding, P.; Xu, H.; Li, Q.; Guo, J.; Liao, X.; Shi, B. Advanced X-ray Shielding Materials Enabled by the Coordination of Well-Dispersed High Atomic Number Elements in Natural Leather. *ACS Appl Mater Interfaces* **2020**, *12* (17), 19916-19926, DOI: 10.1021/acsami.0c01663.
(4) Azman, N. Z. N.; Siddiqui, S. A.; Hart, R.; Low, I. M. Microstructural design of lead oxide-epoxy composites for radiation shielding purposes. *Journal of Applied Polymer Science* **2013**, *128* (5), 3213-3219, DOI: 10.1002/app.38515.
(5) Tishkevich, D. I.; Grabchikov, S. S.; Lastovskii, S. B.; Trukhanov, S. V.; Zubar, T. I.; Vasin, D. S.; Trukhanov, A. V.; Kozlovskiy, A. L.; Zdorovets, M. M. Effect of the Synthesis Conditions and Microstructure for Highly Effective Electron Shields Production Based on Bi Coatings. *ACS Applied Energy Materials* **2018**, *1* (4), 1695-1702, DOI: 10.1021/acsaem.8b00179.
(6) Azman, N. Z.; Siddiqui, S. A.; Low, I. M. Characterisation of micro-sized and nano-sized tungsten oxide-epoxy composites for radiation shielding of diagnostic X-rays. *Mater Sci Eng C Mater Biol Appl* **2013**, *33* (8), 4952-7, DOI: 10.1016/j.msec.2013.08.023.
(7) McCaffrey, J. P.; Tessier, F.; Shen, H. Radiation shielding materials and radiation scatter effects for interventional radiology (IR) physicians. *Med Phys* **2012**, *39* (7), 4537-46, DOI: 10.1118/1.4730504.
(8) Harish, V.; Nagaiah, N.; Prabhu, T. N.; Varughese, K. T. Preparation and characterization of lead monoxide filled unsaturated polyester based polymer composites for gamma radiation shielding applications. *Journal of Applied Polymer Science* **2009**, *112* (3), 1503-1508, DOI: 10.1002/app.29633.
(9) Abdel-Aziz, M. M.; Badran, A. S.; Abdel-Hakem, A. A.; Helaly, F. M.; Moustafa, A. B. Styrene–butadiene rubber/lead oxide composites as gamma radiation shields. *Journal of Applied Polymer Science* **1991**, *42* (4), 1073-1080, DOI: 10.1002/app.1991.070420420.
(10) Shao, P.; Liang, D.; Yang, L.; Shi, H.; Xiong, Z.; Ding, L.; Yin, X.; Zhang, K.; Luo, X. Evaluating the adsorptivity of organo-functionalized silica nanoparticles towards heavy metals: Quantitative comparison and mechanistic insight. *J Hazard Mater* **2020**, *387*, 121676, DOI: 10.1016/j.jhazmat.2019.121676.
(11) Maghrabi, H. A.; Vijayan, A.; Mohaddes, F.; Deb, P.; Wang, L. Evaluation of X-ray radiation shielding performance of barium sulphate-coated fabrics. *Fibers and Polymers* **2017**, *17* (12), 2047-2054, DOI: 10.1007/s12221-016-5850-z.
(12) Abunahel, B. M.; Mustafa, I. S.; Noor Azman, N. Z. Characteristics of X-ray attenuation in nano-sized bismuth oxide/epoxy-polyvinyl alcohol (PVA) matrix composites. *Applied Physics A* **2018**, *124* (12), DOI: 10.1007/s00339-018-2254-5.

(13) Jayakumar, S.; Saravanan, T.; Philip, J. Thermal Stability and X-ray Attenuation Studies on alpha-Bi(2)O(3), beta-Bi(2)O(3) and Bi Based Nanocomposites for Radiopaque Fabrics. *J Nanosci Nanotechnol* **2018**, *18* (6), 3969-3981, DOI: 10.1166/jnn.2018.15237.
(14) Tekin, H. O.; Singh, V. P.; Manici, T. Effects of micro-sized and nano-sized WO3 on mass attenauation coefficients of concrete by using MCNPX code. *Appl Radiat Isot* **2017**, *121*, 122-125, DOI: 10.1016/j.apradiso.2016.12.040.
(15) Verdipoor, K.; Alemi, A.; Mesbahi, A. Photon mass attenuation coefficients of a silicon resin loaded with WO3, PbO, and Bi2O3 Micro and Nano-particles for radiation shielding. *Radiation Physics and Chemistry* **2018**, *147*, 85-90, DOI: 10.1016/j.radphyschem.2018.02.017.
(16) Lopresti, M.; Palin, L.; Alberto, G.; Cantamessa, S.; Milanesio, M. Epoxy resins composites for X-ray shielding materials additivated by coated barium sulfate with improved dispersibility. *Materials Today Communications* **2021**, *26*, DOI: 10.1016/j.mtcomm.2020.101888.
(17) Harish, V.; Nagaiah, N.; Prabhu, T. N.; Varughese, K. T. Thermo-mechanical analysis of lead monoxide filled unsaturated polyester based polymer composite radiation shields. *Journal of Applied Polymer Science* **2010**, n/a-n/a, DOI: 10.1002/app.32265.
(18) More, C. V.; Alsayed, Z.; Badawi, M. S.; Thabet, A. A.; Pawar, P. P. Polymeric composite materials for radiation shielding: a review. *Environ Chem Lett* **2021**, 1-34, DOI: 10.1007/s10311-021-01189-9.
(19) Bhattacharya, M. Polymer Nanocomposites-A Comparison between Carbon Nanotubes, Graphene, and Clay as Nanofillers. *Materials (Basel)* **2016**, *9* (4), DOI: 10.3390/ma9040262.
(20) Salavagione, H. J.; Martínez, G.; Gómez, M. A. Synthesis of poly(vinyl alcohol)/reduced graphite oxide nanocomposites with improved thermal and electrical properties. *Journal of Materials Chemistry* **2009**, *19* (28), DOI: 10.1039/b904232f.
(21) Özdemir, T.; Güngör, A.; Akbay, I. K.; Uzun, H.; Babucçuoglu, Y. Nano lead oxide and epdm composite for development of polymer based radiation shielding material: Gamma irradiation and attenuation tests. *Radiation Physics and Chemistry* **2018**, *144*, 248-255, DOI: 10.1016/j.radphyschem.2017.08.021.
(22) La, L. B. T.; Leatherday, C.; Leong, Y.-K.; Watts, H. P.; Zhang, L.-C. Green lightweight lead-free Gd 2 O 3 /epoxy nanocomposites with outstanding X-ray attenuation performance. *Composites Science and Technology* **2018**, *163*, 89-95, DOI: 10.1016/j.compscitech.2018.05.018.
(23) Yu, L.; Yap, P. L.; Santos, A.; Tran, D.; Losic, D. Lightweight Bismuth Titanate (Bi4Ti3O12) Nanoparticle-Epoxy Composite for Advanced Lead-Free X-ray Radiation Shielding. *ACS Applied Nano Materials* **2021**, *4* (7), 7471-7478, DOI: 10.1021/acsanm.1c01475.
(24) Huang, G.; Huo, S.; Xu, X.; Chen, W.; Jin, Y.; Li, R.; Song, P.; Wang, H. Realizing simultaneous improvements in mechanical strength, flame retardancy and smoke suppression of ABS nanocomposites from multifunctional graphene. *Composites Part B: Engineering* **2019**, *177*, DOI: 10.1016/j.compositesb.2019.107377.
(25) Viegas, J.; Silva, L. A.; Batista, A. M. S.; Furtado, C. A.; Nascimento, J. P.; Faria, L. O. Increased X-ray Attenuation Efficiency of Graphene-Based Nanocomposite. *Industrial & Engineering Chemistry Research* **2017**, *56* (41), 11782-11790, DOI: 10.1021/acs.iecr.7b02711.
(26) Hashemi, S. A.; Mousavi, S. M.; Faghihi, R.; Arjmand, M.; Sina, S.; Amani, A. M. Lead oxide-decorated graphene oxide/epoxy composite towards X-Ray radiation shielding. *Radiation Physics and Chemistry* **2018**, *146*, 77-85, DOI: 10.1016/j.radphyschem.2018.01.008.
(27) Jaishankar, M.; Tseten, T.; Anbalagan, N.; Mathew, B. B.; Beeregowda, K. N. Toxicity, mechanism and health effects of some heavy metals. *Interdiscip Toxicol* **2014**, *7* (2), 60-72, DOI: 10.2478/intox-2014-0009.
(28) Park, Y. T.; Qian, Y.; Chan, C.; Suh, T.; Nejhad, M. G.; Macosko, C. W.; Stein, A. Epoxy Toughening with Low Graphene Loading. *Advanced Functional Materials* **2015**, *25* (4), 575-585, DOI: 10.1002/adfm.201402553.
(29) Zandiatashbar, A.; Lee, G. H.; An, S. J.; Lee, S.; Mathew, N.; Terrones, M.; Hayashi, T.; Picu, C. R.; Hone, J.; Koratkar, N. Effect of defects on the intrinsic strength and stiffness of graphene. *Nat Commun* **2014**, *5*, 3186, DOI: 10.1038/ncomms4186.
(30) Chen, C.-Y.; Pu, N.-W.; Liu, Y.-M.; Huang, S.-Y.; Wu, C.-H.; Ger, M.-D.; Gong, Y.-J.; Chou, Y.-C. Remarkable microwave absorption performance of graphene at a very low loading ratio. *Composites Part B: Engineering* **2017**, *114*, 395-403, DOI: 10.1016/j.compositesb.2017.02.016.

(31) Liu, Z.; Li, J.; Liu, X. Novel Functionalized BN Nanosheets/Epoxy Composites with Advanced Thermal Conductivity and Mechanical Properties. *ACS Appl Mater Interfaces* **2020,** *12* (5), 6503-6515, DOI: 10.1021/acsami.9b21467.
(32) Yu, L.; Yap, P. L.; Tran, D. N. H.; Santos, A. M. C.; Losic, D. High-yield preparation of edge-functionalized and water dispersible few-layers of hexagonal boron nitride (hBN) by direct wet chemical exfoliation. *Nanotechnology* **2021,** *32* (40), DOI: 10.1088/1361-6528/ac0931.
(33) Losic, D.; Yu, L.; Tran, D.; Santos, A. Improved Radiation Shielding 2021.
(34) APRANSA, Aprons for Protection Against X-rays. 2015.
(35) Swinehart, D. F. The Beer-Lambert law. *Journal of Chemical Education* **1962,** *39*, 333-35.
(36) Farivar, F.; Yap, P. L.; Hassan, K.; Tung, T. T.; Tran, D. N. H.; Pollard, A. J.; Losic, D. Unlocking thermogravimetric analysis (TGA) in the Figureht against "Fake graphene" materials. *Carbon* **2021,** *179*, 505-513, DOI: 10.1016/j.carbon.2021.04.064.
(37) Krishnamoorthy, K.; Pazhamalai, P.; Veerasubramani, G. K.; Kim, S. J. Mechanically delaminated few layered MoS2 nanosheets based high performance wire type solid-state symmetric supercapacitors. *Journal of Power Sources* **2016,** *321*, 112-119, DOI: 10.1016/j.jpowsour.2016.04.116.
(38) Çelik, O. N.; Ay, N.; Göncü, Y. Effect of Nano Hexagonal Boron Nitride Lubricant Additives on the Friction and Wear Properties of AISI 4140 Steel. *Particulate Science and Technology* **2013,** *31* (5), 501-506, DOI: 10.1080/02726351.2013.779336.
(39) Wang, X.; Zhang, L. Green and facile production of high-quality graphene from graphite by the combination of hydroxyl radicals and electrical exfoliation in different electrolyte systems. *RSC Advances* **2019,** *9* (7), 3693-3703, DOI: 10.1039/c8ra09752f.
(40) Sun, H.; Liu, H.; Hou, Z.; Zhou, R.; Liu, X.; Wang, J.-G. Edge-terminated MoS2 nanosheets with an expanded interlayer spacing on graphene to boost supercapacitive performance. *Chemical Engineering Journal* **2020,** *387*, DOI: 10.1016/j.cej.2020.124204.
(41) Wang, J.; Han, Z. The combustion behavior of polyacrylate ester/graphite oxide composites. *Polymers for Advanced Technologies* **2006,** *17* (4), 335-340, DOI: 10.1002/pat.698.
(42) Guerra, V.; Wan, C.; Degirmenci, V.; Sloan, J.; Presvytis, D.; McNally, T. 2D boron nitride nanosheets (BNNS) prepared by high-pressure homogenisation: structure and morphology. *Nanoscale* **2018,** *10* (41), 19469-19477, DOI: 10.1039/c8nr06429f.
(43) Yu, L.; Pereira, A. L. C.; Tran, D. N. H.; Santos, A. M. C.; Losic, D. Bismuth Oxide Films for X-ray shielding: Effects of particle size and structural morphology. *Materials Chemistry and Physics* **2021,** *260*, DOI: 10.1016/j.matchemphys.2020.124084.
(44) Al-Qadhi, M.; Merah, N.; Gasem, Z. M. Mechanical properties and water uptake of epoxy–clay nanocomposites containing different clay loadings. *Journal of Materials Science* **2013,** *48* (10), 3798-3804, DOI: 10.1007/s10853-013-7180-5.
(45) Prolongo, S. G.; Moriche, R.; Sánchez, M.; Ureña, A. Self-stratifying and orientation of exfoliated few-layer graphene nanoplatelets in epoxy composites. *Composites Science and Technology* **2013,** *85*, 136-141, DOI: 10.1016/j.compscitech.2013.06.015.
(46) Saha, D.; Kruse, P. Editors' Choice—Review—Conductive Forms of MoS2 and Their Applications in Energy Storage and Conversion. *Journal of The Electrochemical Society* **2020,** *167* (12), DOI: 10.1149/1945-7111/abb34b.
(47) Vernickaitė, E.; Lelis, M.; Tsyntsaru, N.; Pakštas, V.; Cesiulis, H. XPS studies on the Mo oxide-based coatings electrodeposited from highly saturated acetate bath. *Chemija* **2020,** *31* (4), DOI: 10.6001/chemija.v31i4.4317.
(48) Syari'ati, A.; Kumar, S.; Zahid, A.; Ali El Yumin, A.; Ye, J.; Rudolf, P. Photoemission spectroscopy study of structural defects in molybdenum disulfide (MoS2) grown by chemical vapor deposition (CVD). *Chem Commun (Camb)* **2019,** *55* (70), 10384-10387, DOI: 10.1039/c9cc01577a.
(49) Kim, I. S.; Sangwan, V. K.; Jariwala, D.; Wood, J. D.; Park, S.; Chen, K. S.; Shi, F.; Ruiz-Zepeda, F.; Ponce, A.; Jose-Yacaman, M.; Dravid, V. P.; Marks, T. J.; Hersam, M. C.; Lauhon, L. J. Influence of stoichiometry on the optical and electrical properties of chemical vapor deposition derived MoS2. *ACS Nano* **2014,** *8* (10), 10551-8, DOI: 10.1021/nn503988x.
(50) Escalera-Lopez, D.; Niu, Y.; Yin, J.; Cooke, K.; Rees, N. V.; Palmer, R. E. Enhancement of the Hydrogen Evolution Reaction from Ni-MoS2 Hybrid Nanoclusters. *ACS Catal* **2016,** *6* (9), 6008-6017, DOI: 10.1021/acscatal.6b01274.

(51) Li, W.; Zhang, Z.; Zhang, W.; Zou, S. MoS2 Nanosheets Supported on Hollow Carbon Spheres as Efficient Catalysts for Electrochemical Hydrogen Evolution Reaction. *ACS Omega* **2017**, *2* (8), 5087-5094, DOI: 10.1021/acsomega.7b00755.
(52) Uddin, M. N.; Shimoyama, I.; Baba, Y.; Sekiguchi, T.; Nagano, M. X-ray photoelectron spectroscopic observation on B–C–N hybrids synthesized by ion beam deposition of borazine. *Journal of Vacuum Science & Technology A: Vacuum, Surfaces, and Films* **2005**, *23* (3), 497-502, DOI: 10.1116/1.1894667.
(53) Gu, H.; Guo, J.; He, Q.; Tadakamalla, S.; Zhang, X.; Yan, X.; Huang, Y.; Colorado, H. A.; Wei, S.; Guo, Z. Flame-Retardant Epoxy Resin Nanocomposites Reinforced with Polyaniline-Stabilized Silica Nanoparticles. *Industrial & Engineering Chemistry Research* **2013**, *52* (23), 7718-7728, DOI: 10.1021/ie400275n.
(54) Li, A.; Xu, W.; Wang, G.; Wang, X. Novel strategy for molybdenum disulfide nanosheets grown on titanate nanotubes for enhancing the flame retardancy and smoke suppression of epoxy resin. *Journal of Applied Polymer Science* **2018**, *135* (15), DOI: 10.1002/app.46064.
(55) Riaz, S.; Park, S.-J. A comparative study on nanoinclusion effect of MoS2 nanosheets and MoS2 quantum dots on fracture toughness and interfacial properties of epoxy composites. *Composites Part A: Applied Science and Manufacturing* **2021**, *146*, DOI: 10.1016/j.compositesa.2021.106419.
(56) Tsuji, Y.; Kitamura, Y.; Someya, M.; Takano, T.; Yaginuma, M.; Nakanishi, K.; Yoshizawa, K. Adhesion of Epoxy Resin with Hexagonal Boron Nitride and Graphite. *ACS Omega* **2019**, *4* (3), 4491-4504, DOI: 10.1021/acsomega.9b00129.
(57) Gao, C.; Zhu, Z.; Shen, Y.; Wang, T.; Xiang, D. Efficient construction of boron nitride network in epoxy composites combining reaction-induced phase separation and three-roll milling. *Composites Part B: Engineering* **2020**, *198*, DOI: 10.1016/j.compositesb.2020.108232.
(58) Chen, J.; Chen, B.; Li, J.; Tong, X.; Zhao, H.; Wang, L. Enhancement of mechanical and wear resistance performance in hexagonal boron nitride-reinforced epoxy nanocomposites. *Polymer International* **2017**, *66* (5), 659-664, DOI: 10.1002/pi.5296.
(59) Eren Belgin, E.; Aycik, G. A.; Kalemtas, A.; Pelit, A.; Dilek, D. A.; Kavak, M. T. Usability of natural titanium-iron oxide as filler material for ionizing electromagnetic radiation shielding composites; preparation, characterization and performance. *Journal of Radioanalytical and Nuclear Chemistry* **2015**, DOI: 10.1007/s10967-015-4643-y.
(60) Bindu Sharmila, T. K.; Antony, J. V.; Jayakrishnan, M. P.; Sabura Beegum, P. M.; Thachil, E. T. Mechanical, thermal and dielectric properties of hybrid composites of epoxy and reduced graphene oxide/iron oxide. *Materials & Design* **2016**, *90*, 66-75, DOI: 10.1016/j.matdes.2015.10.055.
(61) Alavian, H.; Samie, A.; Tavakoli-Anbaran, H. Experimental and Monte Carlo investigations of gamma ray transmission and buildup factors for inorganic nanoparticle/epoxy composites. *Radiation Physics and Chemistry* **2020**, *174*, DOI: 10.1016/j.radphyschem.2020.108960.
(62) Konya, J. *Nuclear and Radiochemistry* Elsevier 2018; Vol. 11.
(63) Rasul, M. G.; Kiziltas, A.; Arfaei, B.; Shahbazian-Yassar, R. 2D boron nitride nanosheets for polymer composite materials. *npj 2D Materials and Applications* **2021**, *5* (1), DOI: 10.1038/s41699-021-00231-2.
(64) Roell, K. R.; Reif, D. M.; Motsinger-Reif, A. A. An Introduction to Terminology and Methodology of Chemical Synergy-Perspectives from Across Disciplines. *Front Pharmacol* **2017**, *8*, 158, DOI: 10.3389/fphar.2017.00158.
(65) Baeder, D. Y.; Yu, G.; Hoze, N.; Rolff, J.; Regoes, R. R. Antimicrobial combinations: Bliss independence and Loewe additivity derived from mechanistic multi-hit models. *Philos Trans R Soc Lond B Biol Sci* **2016**, *371* (1695), DOI: 10.1098/rstb.2015.0294.
(66) Greco, W. R.; Bravo, G.; Parsons, J. C. The search for synergy: a critical review from a response surface perspective. *Pharmacol. Rev.* **1995**, *47*, 331-385.
(67) Goldoni, M.; Johansson, C. A mathematical approach to study combined effects of toxicants in vitro: evaluation of the Bliss independence criterion and the Loewe additivity model. *Toxicol In Vitro* **2007**, *21* (5), 759-69, DOI: 10.1016/j.tiv.2007.03.003.
(68) Gahlot, S.; Kulshrestha, V.; Agarwal, G.; Jha, P. K. Synthesis and Characterization of PVA/GO Nanocomposite Films. *Macromolecular Symposia* **2015**, *357* (1), 173-177, DOI: 10.1002/masy.201400220.

(69) Zarei, M.; Sina, S.; Hashemi, S. A. Superior X-ray radiation shielding of biocompatible platform based on reinforced polyaniline by decorated graphene oxide with interconnected tungsten–bismuth–tin complex. *Radiation Physics and Chemistry* **2021**, *188*, DOI: 10.1016/j.radphyschem.2021.109588.
(70) Hashemi, S. A.; Mousavi, S. M.; Faghihi, R.; Arjmand, M.; Rahsepar, M.; Bahrani, S.; Ramakrishna, S.; Lai, C. W. Superior X-ray Radiation Shielding Effectiveness of Biocompatible Polyaniline Reinforced with Hybrid Graphene Oxide-Iron Tungsten Nitride Flakes. *Polymers (Basel)* **2020**, *12* (6), DOI: 10.3390/polym12061407.

Graphical Abstract

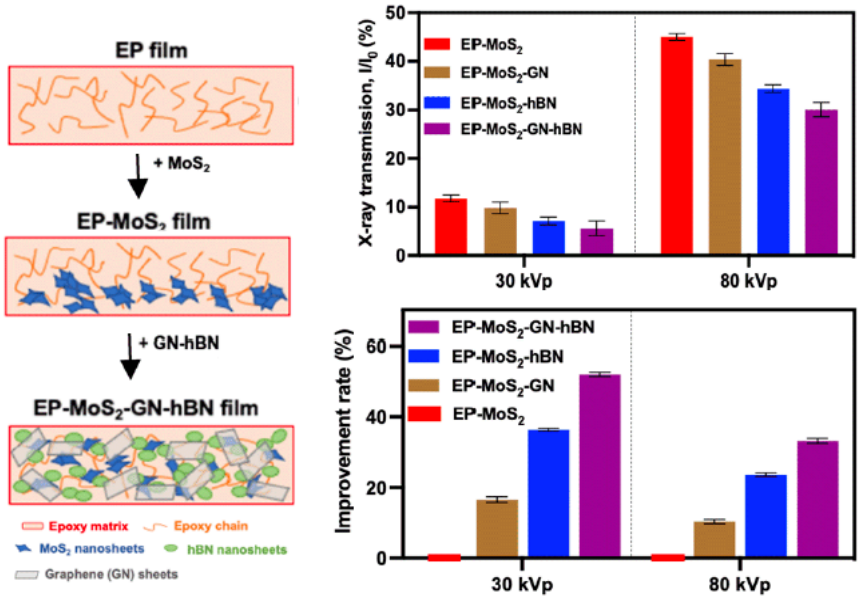

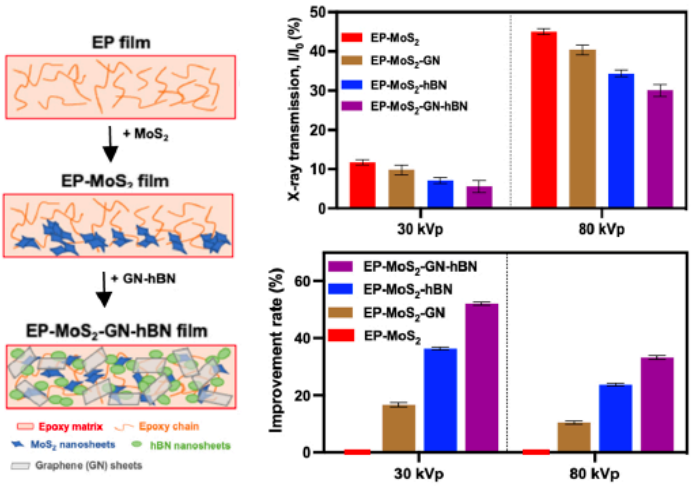

TOC

398x294mm (72 x 72 DPI)

Supporting Information

Synergistic Effect of Graphene and Hexagonal Boron Nitride on Effective X-ray Attenuation Performance of Molybdenum Disulfide (MoS_2)-Epoxy Composites

Le Yu [a,b], *Pei Lay Yap* [a,b] *Alexandre Santos* [c,d,e], *Diana Tran* [a,b], *Kamrul Hassan* [a,b], *Dusan Losic* [a,b*]

[a] School of Chemical Engineering and Advanced Materials, The University of Adelaide, Adelaide, SA 5005, Australia.
[b] ARC Research Hub for Graphene Enabled Industry Transformation, The University of Adelaide, Adelaide, SA 5005, Australia.
[c] School of Physical Sciences, The University of Adelaide, Adelaide, South Australia 5005, Australia.
[d] Department of Medical Physics, Royal Adelaide Hospital, Adelaide, South Australia 5000, Australia.
[e] Australian Bragg Centre for Proton Therapy and Research, Adelaide, SA, Australia 5000.

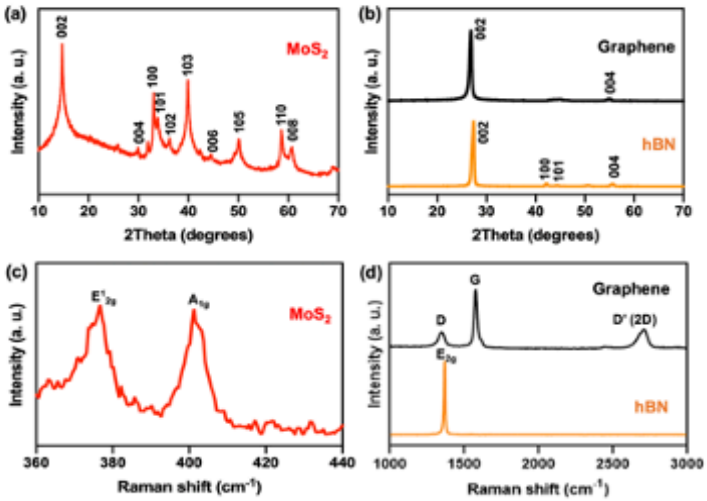

Fig. S1 (a, b) XRD patterns and (c, d) Raman spectra of the synthesized MoS_2 nanosheets, GN sheets and hBN nanosheets, respectively.

Table S1 XPS survey scan of as-synthesized epoxy composites (EP, EP-GN, EP-hBN, EP-MoS_2 and EP-MoS_2-GN-hBN) with their normalized surface atomic composition.

Composites	Normalized Atomic %						
	C1s	O1s	N1s	Si2p	Mo3d	S2p	B1s
EP	85.8	10.6	1.7	2.0	N.A.	N.A.	N.A.
EP-GN	78.5	13.9	5.3	2.4	N.A.	N.A.	N.A.
EP-hBN	79.7	12.2	5.8	1.8	N.A.	N.A.	0.4
EP-MoS_2	78.5	15.7	3.4	1.4	0.2	0.9	N.A.
EP-MoS_2-GN-hBN	57.3	14.8	13.0	N.A.	2.1	5.8	7.0

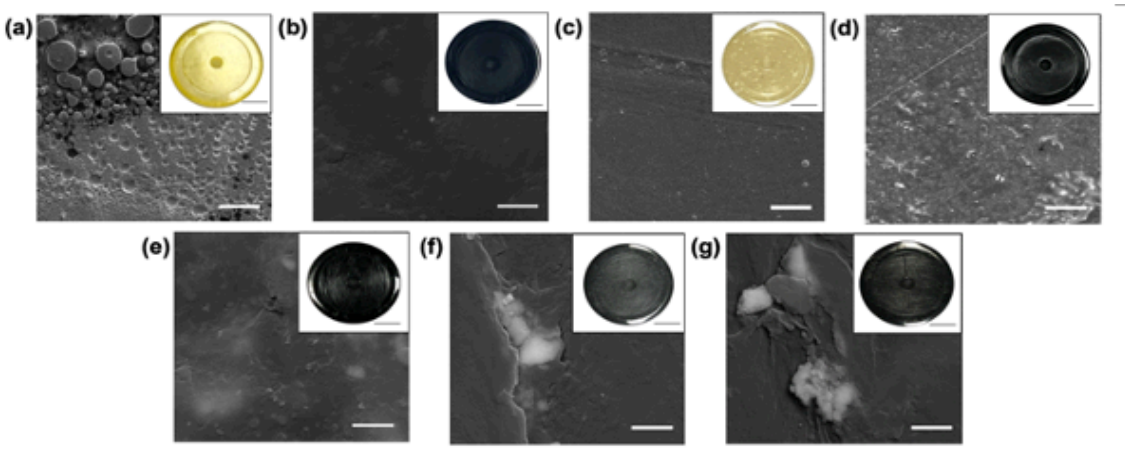

Figure S2 Top-surface SEM images (scale bar = 10 μm) of (a-c) controls (EP, EP-GN, and EP-hBN composites), (d) EP-MoS_2 (e) EP-MoS_2-GN, (f) EP-MoS_2-hBN and (g) EP-MoS_2-GN-hBN composites, inset is their corresponding photographs of the composite films (scale bar = 1 cm).

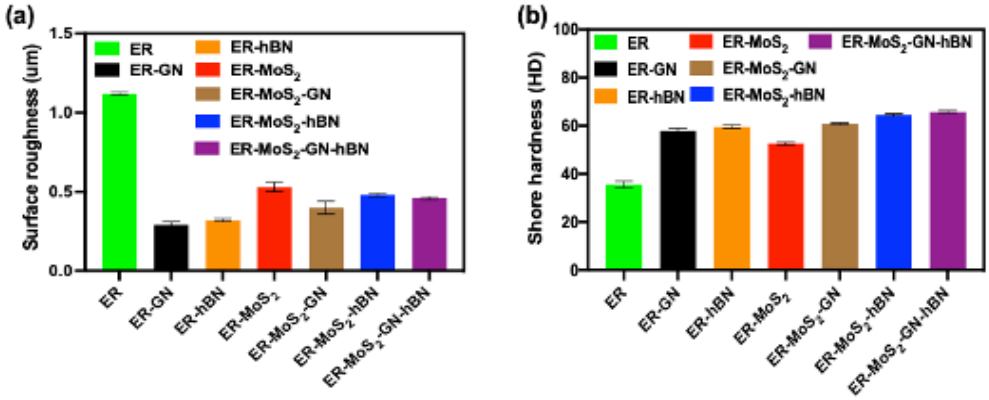

Figure S3 (a) Surface roughness and (b) shore hardness of controls (EP, EP-GN, and EP-hBN composites), EP-MoS_2, EP-MoS_2-GN, EP-MoS_2-hBN and EP-MoS_2-GN-hBN composites.

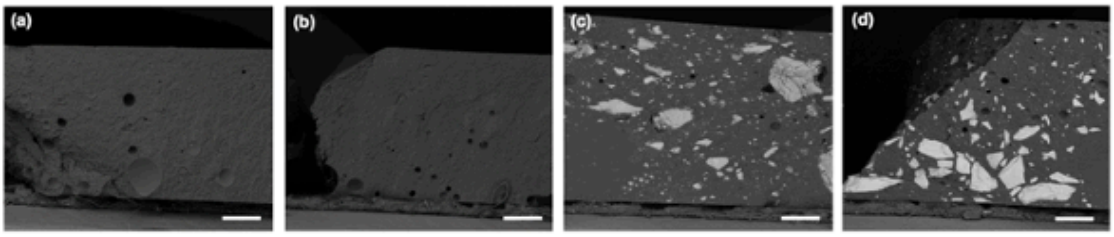

Figure S4 Cross-sectional BSE-SEM images of (a) EP-GN, (b) EP-hBN, (c) EP-MoS_2-GN and (d) EP-MoS_2-hBN composites (scale bar = 500 μm).

Table S2 Thickness and density of controls (EP, EP-GN, EP-hBN composites) and as-prepared EP-MoS_2 composites with addition of GN and hBN

Samples	Weight (g)	Thickness (mm)	Volume (cm^3)	Density (g/cm^3)
EP-GN	1.38 ± 0.01	1.29 ± 0.01	1.24 ± 0.01	1.11 ± 0.02
EP-hBN	1.38 ± 0.02	1.28 ± 0.01	1.23 ± 0.01	1.11 ± 0.01
EP-MoS_2	1.83 ± 0.03	2.07 ± 0.02	1.99 ± 0.02	0.92 ± 0.01
EP-MoS_2-GN	1.95 ± 0.03	2.07 ± 0.02	1.99 ± 0.02	0.98 ± 0.02
EP-MoS_2-hBN	1.95 ± 0.01	2.08 ± 0.01	2.00 ± 0.01	0.97 ± 0.01
EP-MoS_2-GN-hBN	1.96 ± 0.01	2.08 ± 0.01	2.00 ± 0.01	0.98 ± 0.01

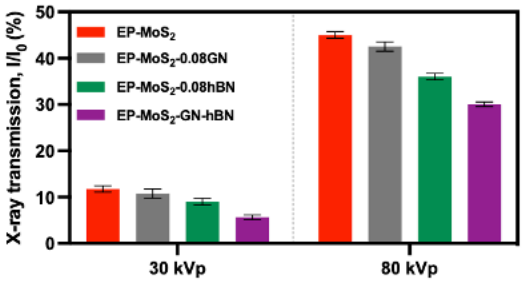

Figure S5 X-ray transmission of EP-MoS_2, EP-MoS_2-0.08GN, EP-MoS_2-0.08hBN and EP-MoS_2-GN-hBN composites at 30 kVp and 80 kVp.

Statement of Authorship

Title of Paper	Laminated-antimonene: An efficient shielding strategy against ionizing radiation.
Publication Status	☐ Published ☐ Accepted for Publication ☐ Submitted for Publication ☑ Unpublished and Unsubmitted w ork w ritten in manuscript style
Publication Details	Nine, M. J., Yu, L., Pereira, A. C., Batmunk, M., Hassan, k., Tran, T., & Losic, D. (2022). Laminated-antimonene: An efficient shielding strategy against ionizing radiation.

Principal Author

Name of Principal Author (Candidate)	Md Julker Nine
Contribution to the Paper	Prepared and characterized on all the samples, and interpreted all the data as well as wrote the manuscript, acted as corresponding author.
Overall percentage (%)	85 %
Certification:	This paper reports on original research I conducted during the period of my Higher Degree by Research candidature and is not subject to any obligations or contractual agreements with a third party that would constrain its inclusion in this thesis. I am the primary author of this paper.
Signature	Date 03/03/2022

Co-Author Contributions

By signing the Statement of Authorship, each author certifies that:

i. the candidate's stated contribution to the publication is accurate (as detailed above);
ii. permission is granted for the candidate in include the publication in the thesis; and
iii. the sum of all co-author contributions is equal to 100% less the candidate's stated contribution.

Name of Co-Author	Le Yu
Contribution to the Paper	Edited and revised the manuscript.
Signature	Date 03/03/2022

Name of Co-Author	Ana L. C. Pereira
Contribution to the Paper	Edited and revised the manuscript.
Signature	Date 03/03/2022

Please cut and paste additional co-author panels here as required.

Statement of Authorship

Title of Paper	Laminated-antimonene: An efficient shielding strategy against ionizing radiation.
Publication Status	☐ Published ☐ Accepted for Publication ☐ Submitted for Publication ☑ Unpublished and Unsubmitted work written in manuscript style
Publication Details	Nine, M. J., Yu, L., Pereira, A. C., Batmunk, M., Hassan, k., Tran, T., & Losic, D. (2022). Laminated-antimonene: An efficient shielding strategy against ionizing radiation.

Principal Author

Name of Principal Author (Candidate)	Md Julker Nine		
Contribution to the Paper	Prepared and characterized on all the samples, and interpreted all the data as well as wrote the manuscript, acted as corresponding author.		
Overall percentage (%)	85 %		
Certification:	This paper reports on original research I conducted during the period of my Higher Degree by Research candidature and is not subject to any obligations or contractual agreements with a third party that would constrain its inclusion in this thesis. I am the		
Signature		Date	03/03/2022

Co-Author Contributions

By signing the Statement of Authorship, each author certifies that:

i. the candidate's stated contribution to the publication is accurate (as detailed above);
ii. permission is granted for the candidate in include the publication in the thesis; and
iii. the sum of all co-author contributions is equal to 100% less the candidate's stated contribution.

Name of Co-Author	Munkhbayar Batmunkh		
Contribution to the Paper	Edited and revised the manuscript.		
Signature		Date	03/03/2022

Name of Co-Author	Kamrul Hassan		
Contribution to the Paper	Edited and revised the manuscript.		
Signature		Date	03/03/2022

Statement of Authorship

Title of Paper	Laminated-antimonene: An efficient shielding strategy against ionizing radiation.
Publication Status	☐ Published ☐ Accepted for Publication ☐ Submitted for Publication ☑ Unpublished and Unsubmitted w ork w ritten in manuscript style
Publication Details	Nine, M. J., Yu, L., Pereira, A. C., Batmunk, M., Hassan, k., Tran, T., & Losic, D. (2022). Laminated-antimonene: An efficient shielding strategy against ionizing radiation.

Principal Author

Name of Principal Author (Candidate)	Md Julker Nine
Contribution to the Paper	Prepared and characterized on all the samples, and interpreted all the data as well as wrote the manuscript, acted as corresponding author.
Overall percentage (%)	85 %
Certification:	This paper reports on original research I conducted during the period of my Higher Degree by obligations or contractual agreements with a thesis. I am the primary author of this paper.
Signature	Date 03/03/2022

Co-Author Contributions

By signing the Statement of Authorship, each author certifies that:

i. the candidate's stated contribution to the publication is accurate (as detailed above);

ii. permission is granted for the candidate in include the publication in the thesis; and

iii. the sum of all co-author contributions is equal to 100% less the candidate's stated contribution.

Name of Co-Author	Tung Tran
Contribution to the Paper	Edited and revised the manuscript.
Signature	Date 03/03/2022

Name of Co-Author	Dusan Losic
Contribution to the Paper	Edited and revised the manuscript.
Signature	Date 03/03/2022

Please cut and paste additional co-author panels here as required.

Applied Materials Today 29 (2022) 101566

Contents lists available at ScienceDirect

Applied Materials Today

journal homepage: www.elsevier.com/locate/apmt

Laminated antimonene as an alternative and efficient shielding strategy against X-ray radiation

Md J. Nine [a,*], Le Yu [a], Ana L.C. Pereira [a,b], Munkhbayar Batmunkh [c], Kamrul Hassan [a], Alexandre M.C. Santos [d,e], Tran T. Tung [a], Dusan Losic [a,*]

[a] School of Chemical Engineering and Advanced Materials, The University of Adelaide, Adelaide, South Australia 5005, Australia
[b] School of Applied Sciences, University of Campinas (UNICAMP), Limeira 13484-350, Brazil
[c] Queensland Micro- and Nanotechnology Centre, School of Environment and Science, Griffith University, Nathan, Queensland 4111, Australia
[d] School of Physical Sciences, University of Adelaide, Adelaide, South Australia 5005, Australia
[e] Department of Medical Physics, Royal Adelaide Hospital, Adelaide, South Australia 5000, Australia

ARTICLE INFO

Keywords:
Lamination
Antimonene
X-ray shield
Radiation protection

ABSTRACT

Scientific research concerning lead (Pb)-free shielding materials and their composites showed great promise in shielding ionising radiation (e.g., X-ray, gamma-ray) applied in medical diagnosis, security screening, space and nuclear industry. However, the typical "blend and mix" composites with imperfect composition due to random particle distribution, morphology, low density, and unwanted micro-crack in an inappropriate matrix could result in poor X-ray attenuation. To address these limitations, we demonstrate a unique laminated architecture using few-layered antimonene (Sb_{FL}) to increase the chances of interaction between ionising radiation and shielding materials. The proposed lamination is a sandwiched structure (PDMS-Sb_{FL}-PDMS) having an identical composition to a conventional form of composite (PDMS/Sb_{FL}). The experiments were carried out within X-ray energy ranging between ~14 and 35 keV (equivalent tube voltage of 30 to 100 kVp), which was further numerically investigated with an extended energy range up to 100 keV. The PDMS-laminated Sb_{FL} with a cotton carrier exhibited an attenuation enhancement of 45% and ~3 times reduced half-value layers (HVL) at high energy (e.g., ~35 keV) X-ray compared to the conventional PDMS/Sb_{FL} composite (13.5 wt% of Sb_{FL}). Using high-density Sb_{FL} nanoflakes in a sandwiched structure demonstrated significant potential to overcome practical challenges (e.g., aggregation, particle distribution, interparticle gaps, cracks) of composites typically employed for shielding ionising radiation.

1. Introduction

Human exposure to different ionising radiations has become very frequent due to their extensive use in medical imaging [1], radiation therapy [2], airport security checking [3], nuclear fuel imaging [4], diagnosis of structural faults [5], as well as in space industries [6]. In brief, the worldwide yearly exercises of ionising radiation related to the medical industry include more than 3600 million diagnostic radiology examinations, 37 million nuclear medicine procedures, and 7.5 million radiation therapy [7]. Uncontrolled exposure to scattered ionising radiation is well documented to have many adverse health impacts, such as an increase in the risk of deadly acute radiation syndrome (e.g., fatigue, loss of appetite) [8,9], risk of long-term effects on the body (e.g., cancer) [10]. Consequently, wearable shielding has become a common practice to protect against X-ray ionising radiation during the procedures, wherein radiographers and patients widely use lead (Pb) aprons [11–13]. However, the findings revealed that a lead apron of 0.5 mm thickness could block just over one-third of the scattered radiation recommended to minimise frequent human exposure to radiation rather than reliance on protection by Pb aprons [11]. Nowadays, Pb is considered to be less desirable material for use in wearable radiation protection due to its heavy weight (~ 4.95 kg apron weight for 0.50 mm Pb), inflexibility, poor durability, and toxicity [14–16]. Therefore, researchers in the field are putting much efforts to develop an efficient and Pb-alternative radiation protection coatings/films.

In this trend, many medium and high-atomic number (Z) elements (tin (Sn) [17], antimony (Sb) [13], iodine (I) [17], barium (Ba) [17], tungsten (W) [18], bismuth (Bi) [19], thorium (Th) [20], uranium (U)

* Corresponding authors.
E-mail addresses: mdjulker.nine@adelaide.edu.au (M.J. Nine), dusan.losic@adelaide.edu.au (D. Losic).

https://doi.org/10.1016/j.apmt.2022.101566
Received 2 April 2022; Received in revised form 25 May 2022; Accepted 16 June 2022
Available online 23 June 2022

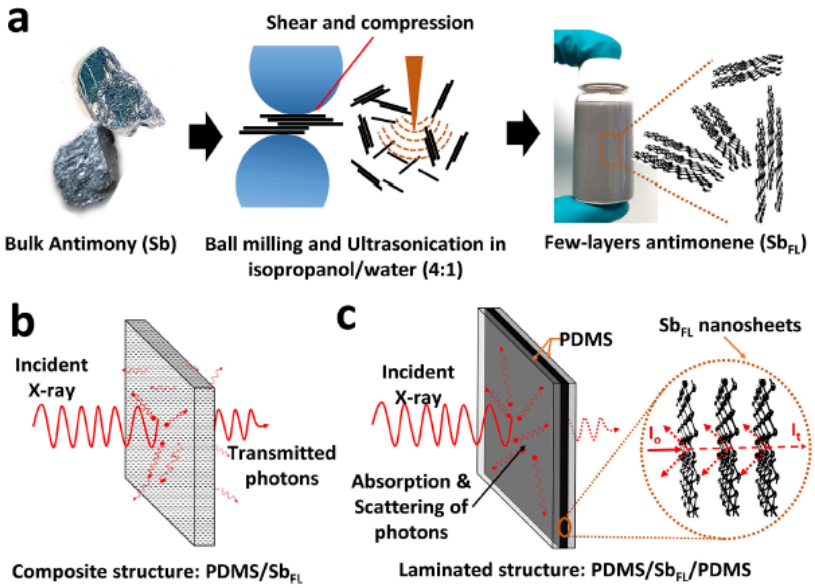

Fig. 1. Schematic representation of the synthesis and film preparation, (a) Mechanical exfoliation of bulk antimony (Sb) combining wet ball-milling and ultrasonication in isopropanol/water (4:1) medium, (b) Conventional PDMS/Sb_{FL} composite structure of X-ray shielding, (c) Laminated approach of X-ray shielding by Sb_{FL} (Sb_{FL} nanoflakes sandwiched between PDMS thin film).

[20], plutonium (Pu) [20], (W-Si) [21] and their oxide compounds such as bismuth(III) oxide (Bi_2O_3) [14,22], copper (II) oxide (CuO) [23], lead (II) oxide (PbO) [22], tungsten oxide (WO_3) [24], cadmium oxide (CdO) [25], gadolinium (III) oxide (Gd_2O_3) [26,27], clay (e.g., dolomite) [28] as well as their blend have been extensively investigated. Recently reported 2D transition metal carbides could be a potential group of materials for enhanced electromagnetic interference (EMI) shielding [29–31]. In addition, a few carbon nanomaterials (e.g., carbon nanotubes (CNTs), graphene) were reported to be effective in EMI shielding [32,33]. The combination of medium and high-Z elements/compounds is an efficient strategy to achieve protection over a broad energy range because of the absorption limit of individual materials against specific energy [13,17,34]. Despite the efforts made for the development of Pb-free protection, the conventional strategy in the fabrication of wearable protective films remained unchanged over many years, which is simply a "blend it and test it" process combining different radiation absorptive materials into polymeric [19,25–27,35,36], or glass matrix [22]. These composites combined with fabrics [14,16], film or paper [18], have been tested to justify their potential for shielding aprons [13, 14,16,37]. A few works reported particle size effect in radiation shielding, wherein nanoparticles perform better than microparticles in polymer composites against low radiation energy range [19,23,24]. In this case, the factual reasons for poor attenuation performance lie in unsuitable particle morphology, distribution, crack formation, and the large interparticle gaps within the conventional form of composites. Although X-ray attenuation depends on the density of materials, it is realized that photon-matter interaction reduces due to numerous interparticle gaps, cracks, and inefficient particle morphology appearing in composites.

To address these problems, we framed an elemental 2D material (e.g., antimonene, a few layers of Sb) [38,39], into film with a compact layered structure laminated with PDMS films. The dense laminated structure is proposed to increase the chance of matter-photons interactions. The proposed fabrication method and working principle are illustrated in Fig. 1a–c. A series of layered films composed of Sb_{FL} were prepared on a cotton carrier and encased in a PDMS mould making the laminated composite to demonstrate the hypothesis shown in Fig. 1c. The X-Ray shielding performances of the proposed laminated sample were conducted to investigate their X-ray attenuation in an experimental energy range between ~14 and 35 keV (equivalent beam energy of 30 to 100 kVp) and compared with the conventional composite structure (schematically illustrated in Fig. 1b). The lower X-ray energy range chosen in this work is based on the X-ray energy frequently used in medical imaging and diagnosis. The simulation results of both composite and laminated samples were performed across a broader energy range (~10 keV up to 120 keV) and compared with experimental results. Relevant photon atomic parameters such as linear attenuation coefficient, half-value layers (HVL), tenth-value layers (TVL), and mass attenuation coefficient were derived and compared. The laminated and layered approach to the structural arrangement of effective shielding materials with larger K-edge values could be future follow-up work to attenuate ionized radiation with higher energy.

2. Materials and methods

2.1. Materials

Bulk crystalline antimony (Sb) with 99.9% purity was purchased from Smart Elements, Austria. The elastomeric polydimethylsiloxane (PDMS) prepolymer (Sylgard 184) with a curing agent was obtained from Dow Corning Corporation (USA). Other chemicals such as Isopropanol (reagent grade, ≥ 99.5%), toluene (anhydrous, 99.8%) were purchased from Merck, Australia. Milli-Q water (PURELAB Option-Q, 18.2 MΩ cm) was used in the experiments. Thin white cotton fabric was purchased from a local supplier, "Lincraft", South Australia.

2.2. Exfoliation of bulk Sb

Few-layer antimonene (Sb_{FL}) nanosheets were prepared in a 4:1 isopropanol/water mixture by exfoliating bulk Sb crystals using a

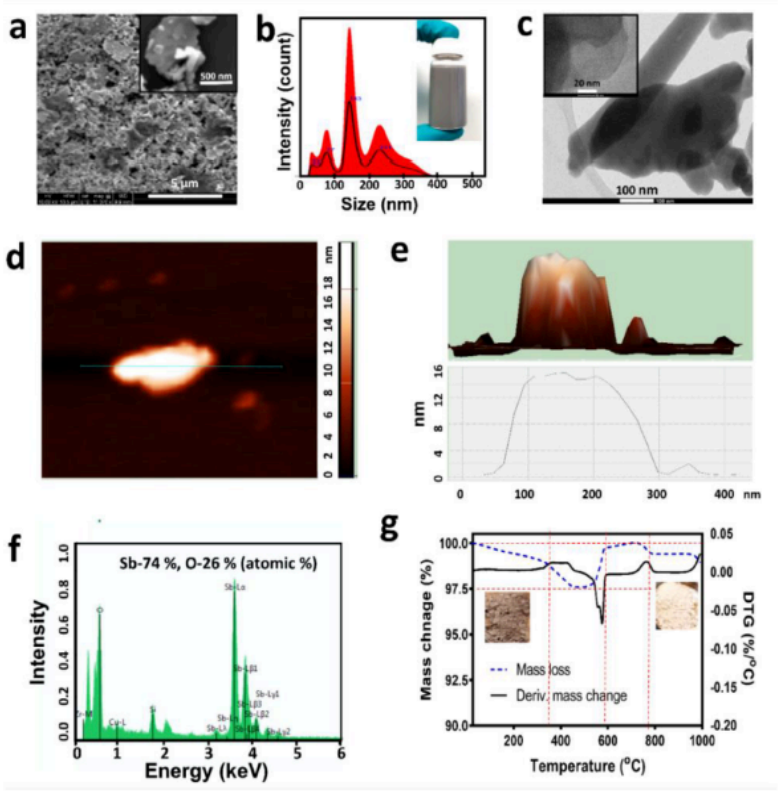

Fig. 2. Structural and chemical properties of exfoliated Sb_{FL}. (a) SEM micrograph of Sb_{FL}, (b) Particle size distribution (Inset image-dispersed Sb_{FL} in Isopropanol), (c) high-resolution TEM image of Sb_{FL}, (d) AFM of Sb_{FL}, (e) line profile showing thickness of the Sb_{FL}, (f) EDX spectrum of Sb_{FL}, (g) TGA and DTG of Sb_{FL}.

combination of ball milling and ultrasonication. Bulk Sb crystals (1 g/pot) were put in a zirconia milling pot (150 ml) with isopropanol/water solvent (50 ml/pot). The samples were then ball-milled using a Retsch planetary ball mill (PM 200) with zirconia balls (3 mm size, 50 ml/pot) at 300 rpm for 3 h. After drying, the ball-milled Sb flakes (10 mg/ml) were re-dispersed in 4:1 isopropanol/water mixture for further exfoliation using a tip-ultrasonication sonicator (Digital Sonifier 450, Branson) for 40 min. Then the resulting black suspension was centrifuged at 3000 rpm for 3 min, and the dark grey supernatant was recovered and oven-dried at 50 °C.

2.3. *Preparation of testing films*

The exfoliated Sb_{FL} powder was further dispersed into toluene by ultrasonication using a tip-sonicator (Digital Sonifier 450, Branson). The Sb_{FL} suspension was added to PDMS prepolymer at three different loading% (4.5 wt%, 9.0 wt%, 13.5 wt%) and mixed in a beaker using an overhead mechanical stirrer (IKA RW20 digital). Once the toluene evaporated, the curing agent was mixed in the beaker to prepare the final PDMS/Sb_{FL} semi-solid composite, which was poured into a Teflon mould (2.5 cm × 2.5 cm) to prepare PDMS/Sb_{FL} films. The thickness of the prepared films (as tabulated in **Table S2**) was maintained by pouring an identical volume of casting materials (e.g., PDMS and PDMS-based composite).

In case of laminated sample, PDMS film with a square size dip (2.5 cm × 2.5 cm × 0.5 mm) in the middle was prepared which was used as negative template. An ethanol soaked wet-cotton fabric (2.5 cm × 2.5 cm) was placed on a negative PDMS template as Sb_{FL} nanosheets carrier. Then, the desired amount of ethanol-based Sb_{FL} suspension was drop cast on the fabrics and allowed to dry at room temperature to fabricate Sb_{FL} films, as shown in Fig. S3. Finally, a measured amount of PDMS prepolymer mixed with a curing agent (part-A and part-B) was poured on the cast film to cover the dip area and thermally cured at 50 °C in the oven for 48 h. (Characterization and X-ray radiation measurement experiment details are provided in **Supporting Information**)

3. Results and discussion

The morphology, elemental analysis, and thermal properties of exfoliated Sb_{FL} sheets are presented in Fig. 2. The morphology of exfoliated bulk-Sb was demonstrated in Fig. 2**a**, wherein the few-layered nano/micro-flakes (confirmed by the inset image) are randomly distributed all over the surface. The flake size distribution of the exfoliated Sb_{FL} was in a broad range between 100 and 300 nm, in which dominated peak counts of particle distribution were determined between 100 and 200 nm, as displayed in Fig. 2**b**. The high-resolution transmission electron microscope (TEM) image in Fig. 2**c** presents exfoliated Sb_{FL} flakes overlapping adjacent layers. The average thickness of random particles was realized by the atomic force microscope (AFM) image demonstrated in Figs. 2**d, e** and **S2**, showing multi-layer exfoliation with approximately 16 nm thick, corresponding to ~35–40 atomic layers Sb_{FL} [40]. The characteristic elemental peaks of Sb_{FL} indicate the presence of oxygen in the materials suggesting the partial oxidation of

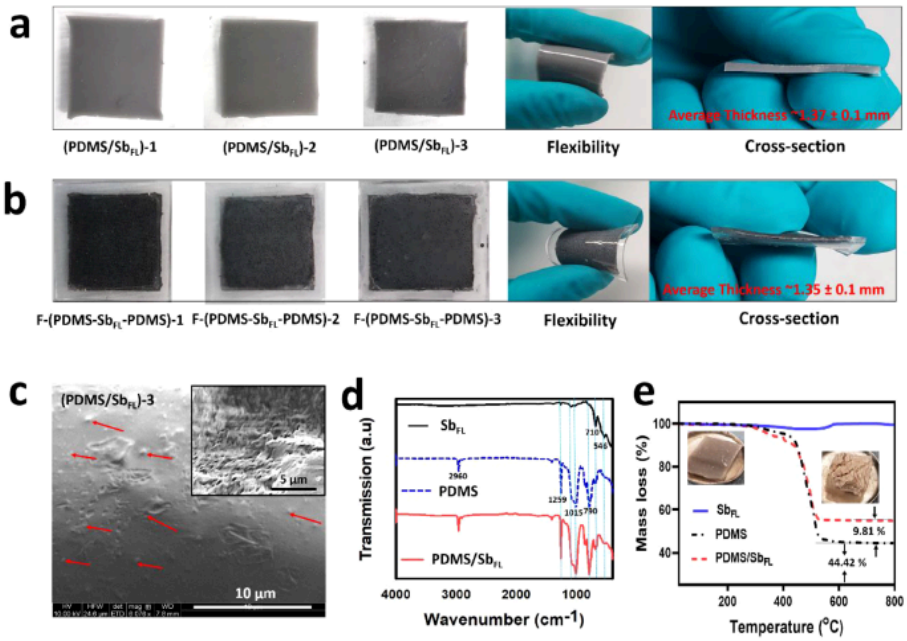

Fig. 3. Prepared films in conventional composite approach and sandwiched structure, (a) Composite films (PDMS/Sb_{FL})-1, (PDMS/Sb_{FL})-2 and (PDMS/Sb_{FL})-3 corresponding to 4.5 wt%, 9 wt% and 13.5 wt%, respectively. The flexibility (inset-middle) of composite films with an average thickness of 1.37± 0.1 mm. (b) Laminated films with intermediate cotton fabric as Sb_{FL} carrier. F-(PDMS-Sb_{FL}-PDMS)-1, F-(PDMS-Sb_{FL}-PDMS)−2 and F-(PDMS-Sb_{FL}-PDMS)-3 corresponding to 4.5 wt%, 9 wt% and 13.5 wt%, respectively. The flexibility (inset-middle) of composite films with an average thickness of 1.35 ± 0.1 mm. (c) SEM of the composite film (PDMS/Sb_{FL})−3. (d) Characteristic FTIR peaks of Sb_{FL}, PDMS and PDMS/Sb_{FL}. (e) Comparative mass-change profile of Sb_{FL}, PDMS and PDMS/Sb_{FL} (Air atmosphere) during thermogravimetric analysis.

Sb_{FL} flakes either during or after the exfoliation (Fig. 2f). Energy-dispersive X-ray spectroscopy (EDX) showed that the quantified atomic composition for oxygen is 26%, while the rest is Sb. Thermal degradation of the Sb_{FL} was demonstrated using thermogravimetric analysis (TGA) and derivative thermogravimetry (DTG), as depicted in Fig. 2g. Although the sample was preheated at 50 °C, it retained approximately ~1.5 wt% of moisture, leaving the sample between 100 and 150 °C. There is still a mass loss of ~2 wt.% between 320 and 580 °C, which might be caused by the unwanted impurities in the sample involved during the exfoliation of Sb_{FL}. The conversion of grey colour Sb_{FL} into white (shown in the inset image) indicates complete oxidation in an air atmosphere at an elevated temperature between 500 and 800 °C. In the third stage, at a temperature around 580 °C, a significant increase in the mass was observed due to the oxidation of Sb_{FL}, resulting in white antimony (III) oxide (Sb_2O_3).

With an intention to improve the ability to attenuate ionizing radiation (e.g., X-ray), laminated film with sandwiched "PDMS-Sb_{FL}-PDMS" structure was proposed in this work as an alternative to the conventional "blend-and-mix" type composite, e.g., "PDMS/Sb_{FL}" wherein both types of the specimen should contain identical composition for comparison. The "PDMS/ Sb_{FL}" composite films with three different weight percentages (4.5 wt%, 9 wt% and 13.5 wt%) of Sb_{FL} were labelled as (PDMS/Sb_{FL})-1, (PDMS/Sb_{FL})-2 and (PDMS/Sb_{FL})-3, respectively, as shown in Fig. 3a. The film fabrication with sandwiched "PDMS-Sb_{FL}-PDMS" structure was challenging as micro-cracks formed in the middle layer caused by thermal shrinkage of Sb_{FL} on PDMS mould, as shown in **Fig. S3a–c**. Toward the tentative formation of the crack-free film, graphene oxide (GO), and rosin were employed as a binder, wherein GO was identified to be a crack enhancer, and rosin influenced the aggregation of Sb_{FL} (**Fig. S3a–c**). Finally, the use of cotton fabric as Sb_{FL} carrier in the laminated samples (F-(PDMS-Sb_{FL}-PDMS)-1, F-(PDMS-Sb_{FL}-PDMS)-2 and F-(PDMS-Sb_{FL}-PDMS)−3) provided crack-free samples as shown in Figs. 3b and **S4b**. For the comparison, these samples of conventional composites and laminated sandwiched structures were prepared with identical wt% of Sb_{FL} and PDMS for each composition, as shown in **Table S2**. The deposition of mid-layer "Sb_{FL}" for the mass of 30 mg, 60 mg and 90 mg (corresponding to 4.5 wt%, 9 wt% and 13.5 wt % of Sb_{FL}) resulted in 51 ± 3 µm, 111 ± 3 µm and 165 ± 3 µm of thickness, respectively (**Fig. S5a–c**). The laminated samples are "Sb_{FL}" loaded cotton fabrics sandwiched by PDMS films, as shown in Fig. 3b. Both composite and laminated films were flexible (inset-middle) with an average thickness of 1.37 ± 0.1 mm and 1.35 ± 0.1 mm, respectively. Fig. 3c displays the surface morphology of composite film (e.g., (PDMS/Sb_{FL})-3), while the inset image with a scratch on it revealed the presence of Sb_{FL} (red-arrow and rough) in the PDMS matrix. The chemical and thermal characteristics of the composite films were demonstrated in Fig. 3d and e. Considering the partial oxidation of Sb_{FL} during ball-milling (Fig. 2f), FTIR characteristic peaks were expected to correspond to Sb—O—Sb and Sb—O vibration bond. According to the literature, four distinct FTIR peaks of Sb_2O_3 could be generated. Herein, a couple of low-intensity peaks at 710 and 546 cm^{-1} could be related to asymmetric bending of Sb—O—Sb and asymmetric stretching of Sb—O bond, respectively, as shown in Fig. 3d [41,42]. PDMS characteristic FTIR peaks at 1259 cm^{-1} correspond to the deformation or in-plane bending of Si—CH_3, and 789–796 cm^{-1} relates to the out-of-plane oscillations of the Si—CH_3 (rocking vibration mode of –CH_3 and stretching vibration of Si—C in Si-CH_3). The FTIR peaks at 1000–1074 cm^{-1} and 2950–2960 cm^{-1} are due to stretching of Si—O—Si and asymmetric stretching in Si—CH_3, respectively [43,44]. Recorded data from thermogravimetric analysis (TGA) of Sb_{FL}, PDMS and PDMS/Sb_{FL} samples

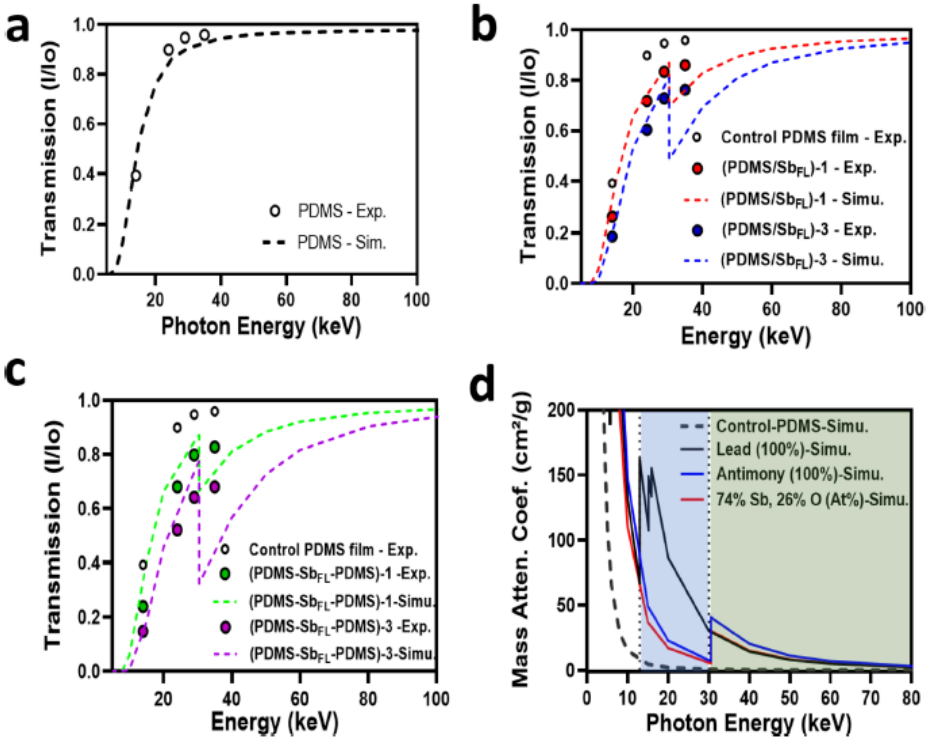

Fig. 4. Comparison of experimental and numerical simulation results of X-ray transmission through Control-PDMS, PDMS/Sb_{FL} composites and laminated samples. (a) PDMS films (1.38 mm thickness), (b) X-ray transmission through composite films ((PDMS/Sb_{FL})-1, and (PDMS/Sb_{FL})-3) (c) X-ray transmission through laminated films ((PDMS-Sb_{FL}-PDMS)-1, and (PDMS-Sb_{FL}-PDMS)-3), (d) Direct comparison of numerically simulated mass attenuation coefficients (pure PDMS, 100% Pb, 100% Sb, and "74% Sb-26% O (atomic%)" with the composite films (experimental) of (PDMS/Sb_{FL})-3 and (PDMS-Sb_{FL}-PDMS)-3.

were plotted in Fig. 3e. Different mass change profiles of Sb_{FL}, PDMS and PDMS/Sb_{FL} specimens were observed while undergoing a thermal degradation in the air atmosphere. Thermal degradation of Sb_{FL} was discussed above in detail, as displayed in Fig. 2g, while a two-stage mass loss was distinguished for PDMS. The 1st stage mass loss took place at an on-set temperature of ~281 °C with a maximum decomposition temperature (T_{max-1}) at 330 °C. With a maximum decomposition, the second stage mass-loss was identified at around 502 °C [45]. An identical mass loss profile was observed for "PDMS/Sb_{FL}" composite except for the additional ~9.81% residual mass due to the presence of oxidised Sb_{FL} (Sb_2O_3). The inset-images in Fig. 3e indicate the physical change before and after thermal decomposition of PDMS/Sb_{FL}.

The transmitted intensity of X-rays (I/I_0) for the samples (control PDMS film, PDMS/ Sb_{FL} composites and laminated "PDMS-Sb_{FL}-PDMS" samples) were examined and analysed both experimentally and numerically, as presented in Fig. 4. Details about the experimental measurements and the simulations are provided in **Section 3.4** of **Supporting Information**. Considering the density of PDMS ($\rho = 0.97$ g/cm^3) film with a measured thickness of 1.38 ± 0.1 mm, X-ray transmission values expected from the simulations are in excellent agreement with the experimental outcome, as shown in Fig. 4a. It is obvious that despite posing ~ 60% attenuation effect at low energy X-ray (14 keV), control PDMS film has an insignificant X-ray attenuation effect at 35 keV, showing ~96% of X-ray transmission at the defined thickness. Fig. 4b displays X-rays transmission through (PDMS/Sb_{FL})-1 (1.38 mm ± 0.1 mm thick composite film, $\rho_{comp-1} = 0.99$ g/cm^3, 95.4 wt% PDMS and 4.6 wt% Sb_{FL}) and (PDMS/Sb_{FL})-3 (1.41 mm ± 0.1 mm thick film, $\rho_{comp-3} = 1.12$ g/cm^3, 86.6 wt% PDMS and 13.4 wt% Sb_{FL}) as a function of the photon energy at 14, 24, 29 and 35 keV.

The measured physical parameters for the films were considered to simulate the transmitted intensity of X-rays photons. The comparison of X-ray transmission values for "PDMS/Sb_{FL}" composites obtained from simulations and the experiments is also in good agreement. The inclusion of 13.4 wt% Sb_{FL} nano/micro flakes in the PDMS matrix posed significant attenuation, which is approximately 20.4% more effective to attenuate high energy (35 keV) X-ray than control PDMS film. Using the measured and calculated density (**Section S1**), a simulation of X-ray transmission was numerically analysed for laminated composites and compared with the experimental outcome, as shown in Fig. 4c. Similar compositions of composites were considered for laminated samples ((PDMS-Sb_{FL}-PDMS)-1 and (PDMS-Sb_{FL}-PDMS)-3). The density of the intermediate Sb_{FL} layer was measured to be $\rho(Sb_{FL}) = 2.14$ g/cm^3, which is much less than the bulk density of Sb ($\rho_{Sb} = 6.697$ g/cm^3). It is important to highlight that the experimental measurements close to the absorption energy (K-shell) of antimony (at 30.5 keV) are not expected to follow precisely the abrupt change in transmission values obtained in simulation. This occurs as the experimental measurements were performed by considering the effective energy of the X-ray beam, which contains a spectrum of peak photon energies instead of a monoenergetic X-ray beam. That explains the inconsistency between experiment and simulation values observed close to the absorption energy in Fig. 4b and c. **Fig. S5** shows dose-dependent X-ray transmission through the specimen of composites and laminated structure (fabrics as a carrier). However, Figs. 4b, c and **S6** displayed a gradual reduction in X-ray transmission with the increase in loading% of Sb_{FL} for both conventional composite structures and laminated samples.

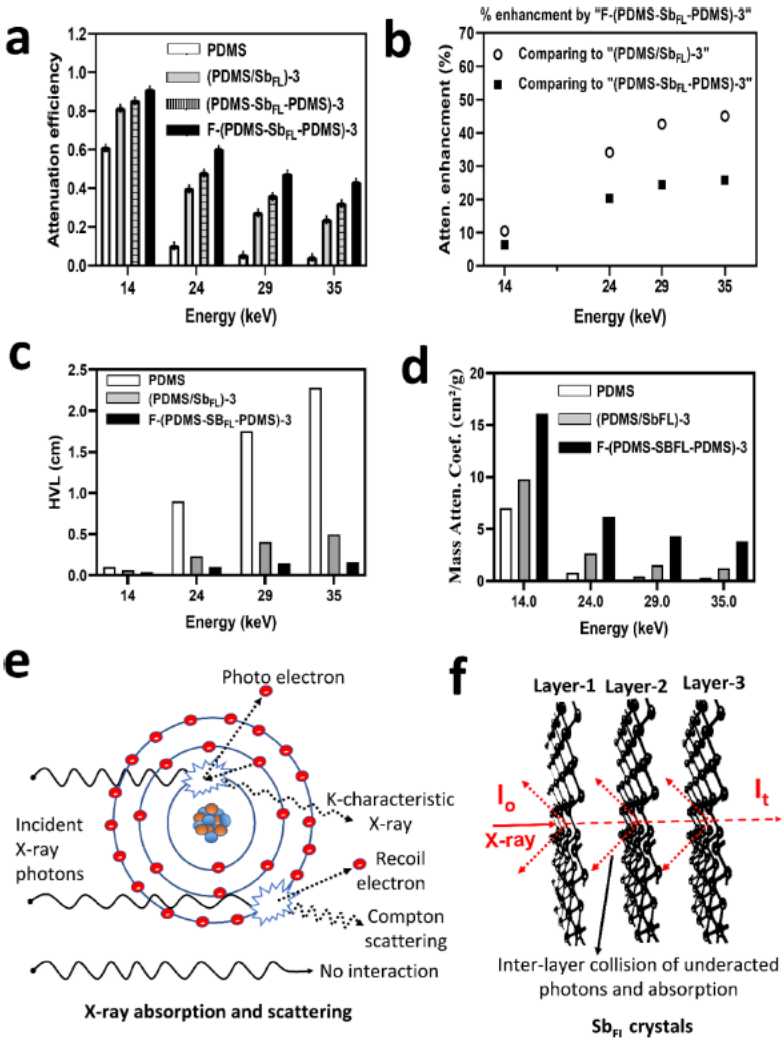

Fig. 5. X-ray attenuation efficiency and enhancement by composite and laminated films (with and without the fabrics carrier) within an energy range between ~14 and 35 keV. (a) Calculated attenuation efficiency obtained by samples of control-PDMS, conventional composite ((PDMS/Sb_{FL})-3), a laminated film without fabrics carrier ((PDMS/Sb_{FL})-3), and laminated film with fabrics carrier (F-(PDMS-Sb_{FL}-PDMS)-3) at different energy band, (b) Enhancement in attenuation by best-performed sample F-(PDMS-Sb_{FL}-PDMS)-3 with respect to (PDMS/Sb_{FL})-3, (PDMS-Sb_{FL}-PDMS)-3 samples. (c) comparison of HVL value for control-PDMS, (PDMS/Sb_{FL})-3, (PDMS-Sb_{FL}-PDMS)-3 samples, (d) comparison of mass attenuation coefficients for control-PDMS, (PDMS/Sb_{FL})-3, (PDMS-Sb_{FL}-PDMS)-3 samples, (e) Generic mechanism of X-ray absorption and scattering, (f) Proposed mechanism of an enhanced interaction between few-layer nanosheets and X-ray.

In Figs. 4d and S7, the NIST XCOM database was used to calculate the total mass attenuation coefficient for control PDMS, lead (Pb, $Z = 82$), antimony (Sb, $Z = 51$), and the composition of Sb_{FL} containing 74% Sb-26% O (atomic%). Pb was used as a reference to investigate theoretical X-ray attenuation imposed by the materials used in this experiment. The attenuation coefficient curve for Sb_{FL} (74% Sb and 26% O) are very close to the curve posed by 100% Sb, which is different from the Pb curve. In Fig. 4d, The discontinuities in the Pb curve (**marked blue shade**) are due to absorption edges (K, L, M) reflecting on the photoelectric absorption. As photoelectric absorption is the dominant process for energies less than 100 keV, the contributions of incoherent scattering and pair production in the nuclear field are less considered. It is noticeable that "Sb" has a slightly better mass attenuation co-efficient than "Pb" after the energy range ~30 keV.

The performance of Pb as a standard X-ray shielding material was compared to relatively low-Z element "Sb" for understanding their effectiveness as a function of the photon energy, as shown in **Fig. S7**. The shielding effectiveness against X-ray radiation of laminated specimen in the presence of a "cotton fabrics carrier" loaded with 13.4 wt% of Sb_{FL} was presented in Fig. 5. Significantly higher transmittance values for both composite and cracked laminated specimens were recorded in contrast to the relatively low X-ray transmission recorded for crack-free laminated nanosheets for the identical loading of Sb_{FL} (Fig. 5a). The attenuation enhancement by "F-(PDMS-Sb_{FL}-PDMS)-3″ was as high as 45% compared to the composite "(PDMS/Sb_{FL})-3″ that is 25.75% more than "(PDMS-Sb_{FL}-PDMS)-3″ when high-energy (35 keV) X-ray is applied as shown in Fig. 5b. It is highly significant that a rising trend of attenuation enhancement posed by "F-(PDMS-Sb_{FL}-PDMS)-3″ was observed with the increase in X-ray energy. The outcome might be explained by the exponential relationship between the number of photons reaching a specific point and the thickness of the shielding material used. Every photon has a different travel range before it interacts with the shielding atom on its way of transmission. In this regard, HVL and TVL are also frequently used photon atomic parameters to quantify both

Table 1
Benchmark comparison in X-ray transmission at an effective energy of 29 keV (tube voltage 80 kVp).

Specimen	Thickness	% Loading	% Transmission	Refs.
Bi_2O_3/PVC composite (loaded in Nylon fabrics)	1.47 mm	23.08 wt %	46	[14]
Bi_2O_3/PDMS	1.3 mm	28.57 wt %	~48 ± 1	[35]
$BaSO_4$/Silicon rubber (Loaded in cotton fabrics)	~0.4 mm	60 wt%	~78.5	[48]
W/Silicon rubber (Loaded in cotton fabrics)	~0.4 mm	60 wt%	~64	[48]
F-(PDMS-Sb_{FL}-PDMS)-3 (Loaded in cotton fabrics)	1.33 mm	13.5 wt %	52.6	This work

the shielding ability of specific objects and the penetrating ability of specific radiations. The HVL and TVL are the thickness of a radiation shielding material that reduces the radiation level by one-half and one-tenth of the initial level, respectively [46]. In Fig. 5**c**, the HVL value was significantly reduced by laminated samples compared to both control-PDMS and composite against broad range X-ray energy. The effective thickness reduction by the laminated sample "F-(PDMS-Sb_{FL}-PDMS)-3″ is ~14 times and ~3 times less than "control-PDMS" and "(PDMS/Sb_{FL})-3″ samples, respectively, at high-energy (35 keV) X-ray. The calculated HVL and TVL values at different X-ray energy have been tabulated in **Table S3**. Similarly, the enhanced mass attenuation coefficient was obtained by laminated sample "F-(PDMS-Sb_{FL}-PDMS)-3″, which is about ~3 times more than conventional composite blends "(PDMS/Sb_{FL})-3″ at 35 keV as presented in Fig. 5**d**. The outcome with enhanced mass attenuation and reduced HVL value posed by the laminated sample can justify the effectiveness of this new structure proposed in this work. The calculated linear attenuation coefficient shows a few degree improvements in attenuation posed by laminated samples, particularly at higher energy, as plotted in Fig. S8. Although the dominant photoelectric effect is highly active within the energy range between 10 and 30 keV, many incident photons generate scattered radiation after interacting with electrons in the atom through Compton scattering (Fig. 5**e**). It seems that the reduced interparticle gap in the laminated Sb_{FL} structure played a significant role in the reduction of scattered ionizing radiation. The use of multiple succeeding layers (Fig. 5**f**) in the few-layer nanosheets of Sb_{FL} could be a promising strategy to attenuate ionizing radiation. The networking of the fabric structure provides better support for the homogeneous distribution of Sb_{FL} in the laminated PDMS film and contributes to minimising voids and cracks, as shown in Fig. 3**c**. Hence, crack-free compact Sb_{FL} nanosheets in the middle of a sandwiched structure may perform better than dispersed Sb_{FL} in the composite within an identical defined volume.

In this work, the best attenuation performance was obtained by developing a crack-free laminated sample (F-(PDMS-Sb_{FL}-PDMS)-3), wherein a cotton fabric was used as a carrier of Sb_{FL} (18.5 mg/cm^2) sandwiched by PDMS-film. The X-ray transmission results at effective energy of 29 keV (tube voltage 80 kVp) posed by the specimen of F-(PDMS-Sb_{FL}-PDMS)-3 were compared (Table 1) with standard 0.18 mm thick Pb sheets equivalent and bismuth oxide/polyvinyl chloride (Bi_2O_3/PVC) composite coated fabrics (Nylon and Polyester) published elsewhere [14,47]. It is noticeable that ~23 wt% of Bi_2O_3/PVC composite coated on Nylon with a thickness of 1.47 mm is reasonably comparable to 13.5 wt% of Sb_{FL} (Sb 74%, O 26% (~Sb_3O)) laminated specimen (F-(PDMS-Sb_{FL}-PDMS)-3) with an approximate thickness of 1.33 mm. However, if the Bi_2O_3/PVC loading is increased to 50% on polyester fabrics with a thickness of just above 1 mm, the coated fabrics transmit 26% of X-ray at 29 keV. The results suggest that four times more loading of a high-Z (Bi = 83) oxide composite (Bi_2O_3/PVC) can generate only two times more effective than the laminated version of relatively low-Z (Sb = 51) compound (Sb_{FL} (Sb_3O)). This comparison reflects a similar outcome achieved in our experiments that the laminated specimen performs ~1.5 times better at an effective X-ray energy of 29 keV than the composite version of the specimen containing an identical loading percentage of Sb_{FL} (13.4 wt%). Similar works based on Bi_2O_3/PDMS (28.57 wt%, 1.3 mm), $BaSO_4$/Silicon rubber (60 wt%, ~0.4 mm), and W/Silicon rubber (60 wt%, ~0.4 mm) composite coated on fabrics performed lower than the outcome of Sb_{FL} (13.4 wt%, 1.33 mm) as enlisted in Table 1.

3. Conclusion

A new and efficient shielding strategy was developed by introducing a laminated Sb_{FL} structure to overcome the drawbacks (e.g., aggregation, poor particle distribution, interparticle gaps, cracks) observed in conventional polymer composites. The lamination of Sb_{FL} nanosheets, loaded on a cotton fabrics carrier of F-(PDMS-Sb_{FL}-PDMS)-3 allows ~35% less X-ray transmission over a broad energy range of X-ray (24–35 keV) compared to the composite (PDMS/ Sb_{FL})-3 prepared by conventional "blend and mix" method. The attenuation enhancement by the proposed laminated sample "F-(PDMS-Sb_{FL}-PDMS)-3″ was 45% more than the conventional form of composite "(PDMS/Sb_{FL})-3″ subjected to high energy X-ray (35 keV). Furthermore, the HVL and TVL thickness were significantly reduced by "F-(PDMS-Sb_{FL}-PDMS)-3″ which is ~3 times less than "(PDMS/Sb_{FL})-3″ at 35 keV. The enhanced attenuation was feasibly posed by the Sb_{FL} nanosheets with reduced interparticle gap and their crack-free lamination, which influenced the interaction between photons and shielding atoms. This new design of shielding materials and achieved preference outcome presented in this work is believed to advance the shielding technology of ionizing radiation.

CRediT authorship contribution statement

Md J. Nine: Conceptualization, Visualization, Methodology, Formal analysis, Writing – original draft. **Le Yu:** Methodology, Writing – review & editing. **Ana L.C. Pereira:** Formal analysis, Writing – review & editing. **Munkhbayar Batmunkh:** Writing – review & editing. **Kamrul Hassan:** Writing – review & editing. **Alexandre M.C. Santos:** Methodology, Resources, Writing – review & editing. **Tran T. Tung:** Writing – review & editing. **Dusan Losic:** Supervision, Resources, Formal analysis, Writing – review & editing.

Declaration of Competing Interest

The authors declare that they have no known competing financial interests or personal relationships that could have appeared to influence the work reported in this paper.

Acknowledgments

The authors thank the support of the Australian Research Council (IH 150100003 ARC Research Hub for Graphene Enabled Industry Transformation). This work was also supported in part by the São Paulo Research Foundation (FAPESP) under Grant# 2018/15842-0. Furthermore, we thank The University of Adelaide for providing access to necessary research facilities and support.

Supplementary materials

Supplementary material associated with this article can be found, in the online version, at doi:10.1016/j.apmt.2022.101566.

References

[1] M. Hoheisel, Review of medical imaging with emphasis on X-ray detectors, Nucl. Instrum. Methods Phys. Res. Sect. A Accel. Spectrom. Detect. Assoc. Equip. 563 (1) (2006) 215–224.
[2] M. Goitein, M. Jermann, The relative costs of proton and X-ray radiation therapy, Clin. Oncol. 15 (1) (2003) S37–S50.
[3] D. Turcsany, A. Mouton, T.P. Breckon, Improving feature-based object recognition for X-ray baggage security screening using primed visualwords, in: Proceedings of the IEEE International Conference on Industrial Technology (ICIT), 2013.
[4] H.M.O.D. Parker, M.J. Joyce, The use of ionising radiation to image nuclear fuel: a review, Prog. Nucl. Energy 85 (2015) 297–318.
[5] P.J. Withers, M. Preuss, Fatigue and damage in structural materials studied by X-ray tomography, Annu. Rev. Mater. Res. 42 (1) (2012) 81–103.
[6] M. Durante, F.A. Cucinotta, Physical basis of radiation protection in space travel, Rev. Mod. Phys. 83 (4) (2011) 1245–1281.
[7] World Health Organization (WHO), Ionizing Radiation, Health Effects and Protective Measures, World Health Organization (WHO), 2016, 29 April.
[8] E.H. Donnelly, et al., Acute radiation syndrome: assessment and management, South. Med. J. 103 (6) (2010) 541–546.
[9] F.A.J. Mettler, A.K. Gus'kova, I. Gusev, Health effects in those with acute radiation sickness from the chernobyl accident, Health Phys. 93 (5) (2007) 462–469.
[10] E.S. Gilbert, Ionising radiation and cancer risks: what have we learned from epidemiology? Int. J. Radiat. Biol. 85 (6) (2009) 467–482.
[11] S.J. Hyun, et al., Efficiency of lead aprons in blocking radiation - how protective are they? Heliyon 2 (5) (2016) e00117.
[12] S.H. Hosseini, M. Askari, S.N. Ezzati, X-ray attenuating nanocomposite based on polyaniline using Pb nanoparticles, Synth. Met. 196 (2014) 68–75.
[13] S. Johansen, et al., Are antimony-bismuth aprons as efficient as lead rubber aprons in providing shielding against scattered radiation? J. Med. Imaging Radiat. Sci. 49 (2) (2018) 201–206.
[14] H.A. Maghrabi, et al., Bismuth oxide-coated fabrics for X-ray shielding, Text. Res. J. 86 (6) (2015) 649–658.
[15] M. Zuguchi, et al., Usefulness of non-lead aprons in radiation protection for physicians performing interventional procedures, Radiat. Prot. Dosim. 131 (4) (2008) 531–534.
[16] S.C. Kim, J.R. Choi, B.K. Jeon, Physical analysis of the shielding capacity for a lightweight apron designed for shielding low intensity scattering X-rays, Sci. Rep. 6 (1) (2016) 27721.
[17] E.W. Webster, Experiments with Medium-Z Materials for Shielding Against Low-Energy X Rays, Radiology 86 (1) (1966) 146.
[18] H. Monzen, et al., Estimation of the shielding ability of a tungsten functional paper for diagnostic x-rays and gamma rays, J. Appl. Clin. Med. Phys. 18 (5) (2017) 325–329.
[19] Q. Li, et al., Enhanced radiation shielding with conformal light-weight nanoparticle–polymer composite, ACS Appl. Mater. Interfaces 10 (41) (2018) 35510–35515.
[20] R.B. Roof, X-ray absorption coefficients of thorium, uranium, and plutonium—experimental determination and theoretical interpretation, Phys. Rev. 113 (3) (1959) 820–825.
[21] M. Kazempour, et al., Assessment of the radiation attenuation properties of several lead free composites by monte carlo simulation, J. Biomed. Phys. Eng. 5 (2) (2015) 67–76.
[22] E.S.A. Waly, G.S. Al-Qous, M.A. Bourham, Shielding properties of glasses with different heavy elements additives for radiation shielding in the energy range 15–300 keV, Radiat. Phys. Chem. 150 (2018) 120–124.
[23] M.Z. Botelho, et al., X-ray transmission through nanostructured and microstructured CuO materials, Appl. Radiat. Isot. 69 (2) (2011) 527–530.
[24] N.Z. Noor Azman, et al., Effect of particle size, filler loadings and x-ray tube voltage on the transmitted x-ray transmission in tungsten oxide—epoxy composites, Appl. Radiat. Isot. 71 (1) (2013) 62–67.
[25] A.M. El-Khatib, et al., Gamma attenuation coefficients of nano cadmium oxide/high density polyethylene composites, Sci. Rep. 9 (1) (2019) 1–11.
[26] L.B.T. La, et al., The interaction between encapsulated Gd_2O_3 particles and polymeric matrix: the mechanism of fracture and X-ray attenuation properties, Colloids Surf. A Physicochem. Eng. Asp. 535 (2017) 175–183.
[27] S. Jayakumar, T. Saravanan, J. Philip, Preparation, characterization and X-ray attenuation property of Gd_2O_3-based nanocomposites, Appl. Nanosci., 7 (8) (2017) 919–931.
[28] H.M.H. Zakaly, et al., Synthesis, optical, structural and physical properties of newly developed dolomite reinforced borate glasses for nuclear radiation shielding utilizations: an experimental and simulation study, Opt. Mater. 114 (2021), 110942 (Amst).
[29] F. Shahzad, et al., Electromagnetic interference shielding with 2D transition metal carbides (MXenes), Science 353 (6304) (2016) 1137–1140.
[30] L. Liang, et al., Promising Ti_3C_2Tx MXene/Ni chain hybrid with excellent electromagnetic wave absorption and shielding capacity, ACS Appl. Mater. Interfaces 11 (28) (2019) 25399–25409.
[31] M. Han, et al., Ti_3C_2 MXenes with modified surface for high-performance electromagnetic absorption and shielding in the X-band, ACS Appl. Mater. Interfaces 8 (32) (2016) 21011–21019.
[32] Q. Song, et al., Carbon nanotube–multilayered graphene edge plane core–shell hybrid foams for ultrahigh-performance electromagnetic-interference shielding, Adv. Mater. 29 (31) (2017), 1701583.
[33] J. Viegas, et al., Increased X-ray attenuation efficiency of graphene-based nanocomposite, Ind. Eng. Chem. Res. 56 (41) (2017) 11782–11790.
[34] M.J. Yaffe, et al., Composite materials for X-ray protection, Health Phys. 60 (5) (1991) 661–664.
[35] S. Nambiar, E.K. Osei, J.T.W. Yeow, Polymer nanocomposite-based shielding against diagnostic X-rays, J. Appl. Polym. Sci. 127 (6) (2013) 4939–4946.
[36] C.V. More, et al., Polymeric composite materials for radiation shielding: a review, Environ. Chem. Lett. 19 (3) (2021) 2057–2090.
[37] H. Mori, et al., Evaluation of the effectiveness of X-ray protective aprons in experimental and practical fields, Radiol. Phys. Technol. 7 (1) (2014) 158–166.
[38] M. Bat-Erdene, et al., Surface oxidized two-dimensional antimonene nanosheets for electrochemical ammonia synthesis under ambient conditions, J. Mater. Chem. A 8 (9) (2020) 4735–4739.
[39] C. Gibaja, et al., Few-layer antimonene by liquid-phase exfoliation, Angew. Chem. Int. Ed. 55 (46) (2016) 14345–14349.
[40] W. Lin, et al., A fast synthetic strategy for high-quality atomically thin antimonene with ultrahigh sonication power, Nano Res. 11 (11) (2018) 5968–5977.
[41] Q. Chen, B. Miao, Q. Ma, Sb_2O_3 functionalized plasmon, photoluminescence and Faraday rotation in glass, J. Non Cryst. Solids 545 (2020), 120251.
[42] K. Kaviyarasu, D. Sajan, P.A. Devarajan, A rapid and versatile method for solvothermal synthesis of Sb_2O_3 nanocrystals under mild conditions, Appl. Nanosci. 3 (6) (2013) 529–533.
[43] M.J. Nine, et al., Facile adhesion-tuning of superhydrophobic surfaces between "lotus" and "petal" effect and their influence on icing and deicing properties, ACS Appl. Mater. Interfaces 9 (9) (2017) 8393–8402.
[44] L.M. Johnson, et al., Elastomeric microparticles for acoustic mediated bioseparations, J. Nanobiotechnol. 11 (1) (2013) 22.
[45] G. Camino, S.M. Lomakin, M. Lazzari, Polydimethylsiloxane thermal degradation part 1. Kinetic aspects, Polymer 42 (6) (2001) 2395–2402 (Guildf).
[46] A. Akkaş, Determination of the tenth and half value layer thickness of concretes with different densities, Acta Phys. Pol. A 129 (4) (2016) 770–772.
[47] G.J. Scuderi, et al., Evaluation of non-lead-based protective radiological material in spinal surgery, Spine J. 6 (5) (2006) 577–582.
[48] N. Aral, F. Banu Nergis, C. Candan, An alternative X-ray shielding material based on coated textiles, Text. Res. J. 86 (8) (2016) 803–811.

Supporting Information

Laminated antimonene as an alternative and efficient shielding strategy against X-ray radiation

Md J. Nine[a]*, Le Yu[a], Ana L. C. Pereira[a,b], Munkhbayar Batmunkh[c], Kamrul Hassan[a], Alexandre Santos[d,e], Tran T. Tung[a], Dusan Losic[a]*

[a]School of Chemical Engineering and Advanced Materials, The University of Adelaide, Adelaide, SA 5005, Australia

[b]School of Applied Sciences, University of Campinas (UNICAMP), Limeira, 13484-350, Brazil

[c]Queensland Micro- and Nanotechnology Centre, School of Environment and Science, Griffith University, Nathan, Queensland 4111, Australia

[d]School of Physical Sciences, University of Adelaide, Adelaide, South Australia 5005, Australia.

[e]Department of Medical Physics, Royal Adelaide Hospital, Adelaide, South Australia 5000, Australia

*Email address: mdjulker.nine@adelaide.edu.au; and dusan.losic@adelaide.edu.au;

Materials and methods.

NIST's XCOM Standard Reference Database: The results from simulations were based on this web database, which can be used to calculate photon cross sections for scattering, photoelectric absorption and pair production, as well as total attenuation coefficients for any element, compound or mixture ($Z \leq 100$), from 1 keV to 100 GeV.

Experimental: The control (air and PDMS) and as-prepared samples were detected for X-ray transmission testing via a superficial X-ray tube (SXR) unit (Gulmay D3150, UK), as shown in **Figure S1**. The distances between the X-ray tube and sample-placing panel as well as between the sample-placing panel and the detector were equally 50 cm. The samples were exposed to the X-ray voltage range at 30, 50, 80, 100 kVp, respectively, for 0.50 min with the X-ray transmitted sample placing an area of diameter at 1 cm, and the X-ray attenuation performance was evaluated as the transmission dose of samples divided by the transmission dose without the sample. Each specimen was measured 3 times and determined by the arithmetic mean.

The X-ray attenuation of an X-ray beam through any material can be expressed as a function of the linear attenuation coefficient (μ) as equation (1),[1]

$$I = I_0 \, e^{-\mu x} \quad (1)$$

Where I and I_0 are the X-ray intensities of the transmitted beam through the samples, and the incident beam (air), respectively, and x is the material thickness (mm). The X-ray transmission (T) can be expressed as equation (2),

$$T = (I / I_0) \times 100\% \quad (2)$$

The measured x-ray energy responses are normalised to the response measured with the highest superficial X-ray energy and plotted against the effective energy of the x-ray beams shown in **Table S1**.[2]

Materials Characterization.

The exfoliated morphology of Sb_{FL} was primarily analysed using a scanning electron microscope (SEM-FEI Quanta 450, Japan) in a low vacuum chamber at an accelerating voltage of 5 kV. The average thickness and particle topography of exfoliated Sb_{FL} was examined using an NT-MDT Ntegra Solaris Atomic Force Microscope (AFM) via tapping mode. NT-MDT SPM Software (Nova 1.0.26) was used for AFM image processing. A particle size analyzer from Malvern instrument (NanoSight NS300) was used to examine the average particle size distribution. A transmission electron microscope (TEM, FEI Titan Themis) was used to acquire nanoscale morphology and elemental analysis of exfoliated substances. Thermogravimetric analysis (TGA) of Sb_{FL}, PDMS and their composite were studied using Mettler-Toledo TGA/DSC 2, Switzerland in an air atmosphere at a constant heating rate of 5 °C/min. The vibrational stretching modes of different molecular bonds in PDMS modified samples were studied by Fourier transform infrared spectroscopy (FTIR) (Nicolet 6700 Thermo Fisher, USA).

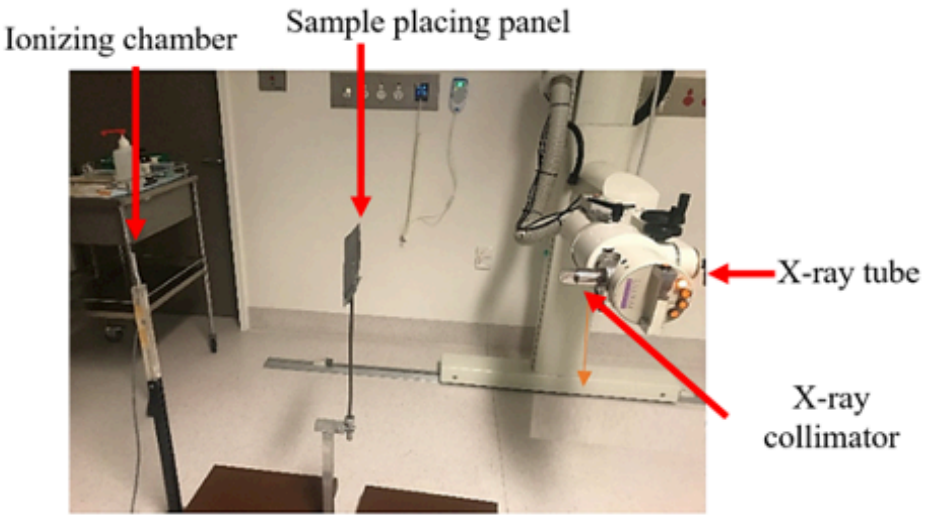

Figure S1. Experimental set-up of X-ray radiation measurement

Observe that we consider here the **effective energy** in keV of the X-ray beam, which was transformed from the tube voltage in kVp, first provided in the experimental data. Tube voltage is the maximum voltage in the X-ray tube, for x-ray beams that contain a spectrum of photon energies, with different X-ray penetration is different for each energy. The effective energy of an X-ray spectrum is the energy of a mono-energetic beam of photons that would have the same penetrating ability (HVL) as the spectrum of photons. The effective energy is generally close to 30% or 40% of peak energy, but its exact value depends on the shape of the spectrum. These values (Table S1) were obtained from reference Santos et.al,[2] for this same experimental set-up and X-ray tube.

Table S1. The effective energies used in this work for the various beam qualities.[2]

Therapy unit	Beam quality	Effective energy (keV)
Superficial X-ray unit	30 kVp – 0.2 mm Al HVL	14
	50 kVp – 1 mm Al HVL	24
	80 kVp – 2 mm Al HVL	29
	100 kVp – 3 mm Al HVL	35

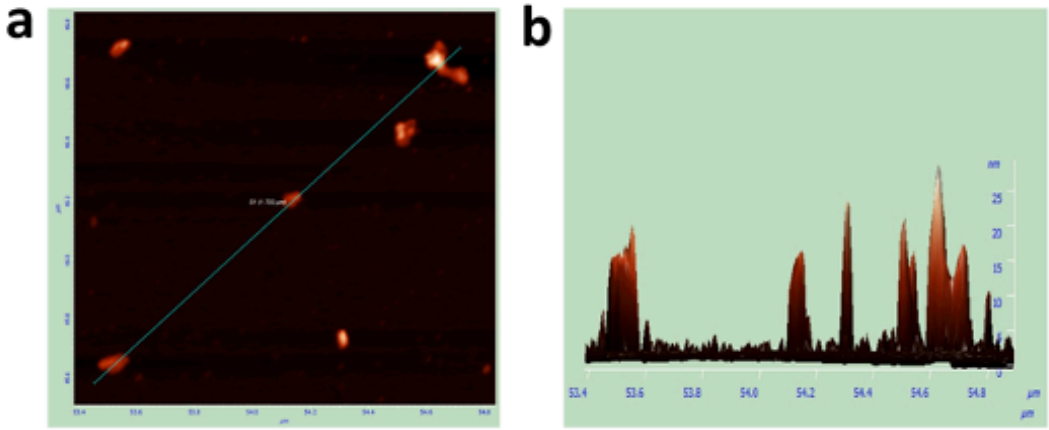

Figure S2. Probing multiple Sb_{FL} nanosheets in AFM to measure the average thickness.

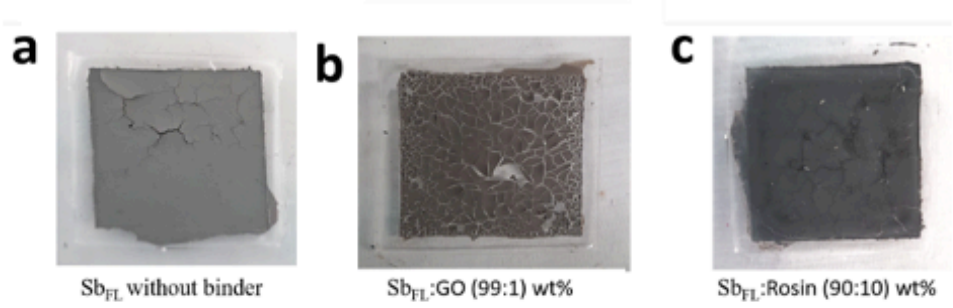

Figure S3. A few examples of failed approaches towards forming a crack-free Sb_{FL} film. a) Sb_{FL} (without binder), b) Sb_{FL} film with 1 wt% graphene oxide (GO) as a binder, c) Sb_{FL} film with 10 wt% gum-rosin as a binder.

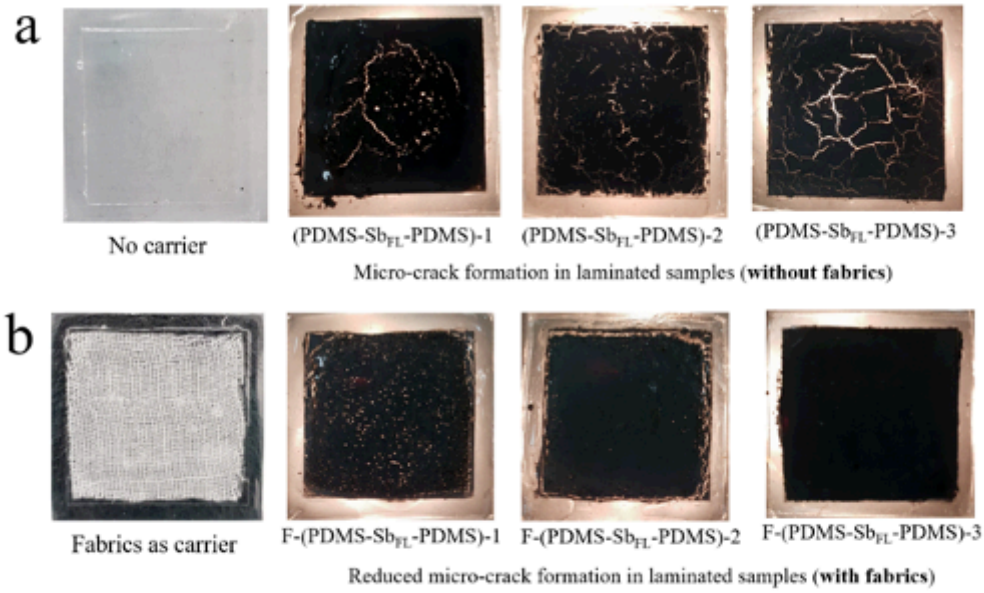

Figure S4. Formation of crack-free films using PDMS lamination. a) Photos of laminated films without fabric carrier at different Sb_{FL} loading %, b) Photos of laminated films with cotton fabric as Sb_{FL} nanosheets carrier ($Sb_{FL}$was loaded on cotton at different wt%).

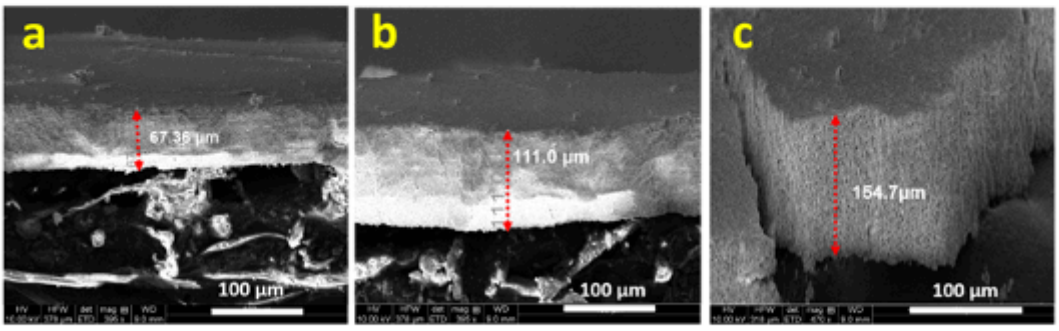

Figure S5. Cross-sectional SEM of fabricated Sb_{FL} films at deferent mass deposition. a) thickness of Sb_{FL} film (30 mg) deposited on 22 mm × 22 mm area, b) thickness of Sb_{FL} film (60 mg) deposited on 22 mm × 22 mm area, c) thickness of Sb_{FL} film (90 mg) deposited on 22 mm × 22 mm area.

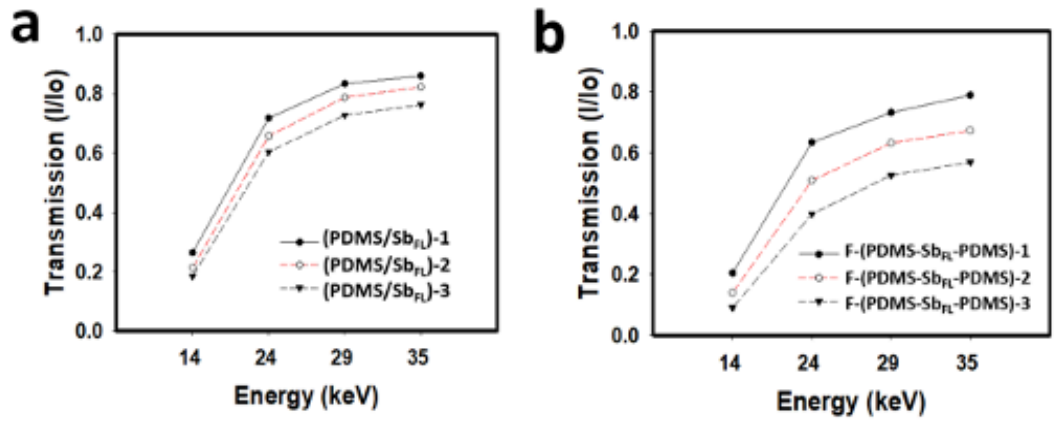

Figure S6. Dose-dependent X-ray transmission of the composite and laminated structure, a) X-ray transmission of conventional blended composites of "**PDMS/Sb$_{FL}$**" for different loading % of Sb$_{FL}$, b) X-ray transmission of laminated "**F-(PDMS-Sb$_{FL}$-PDMS)**" samples (with fabrics) at different wt% of Sb$_{FL}$.

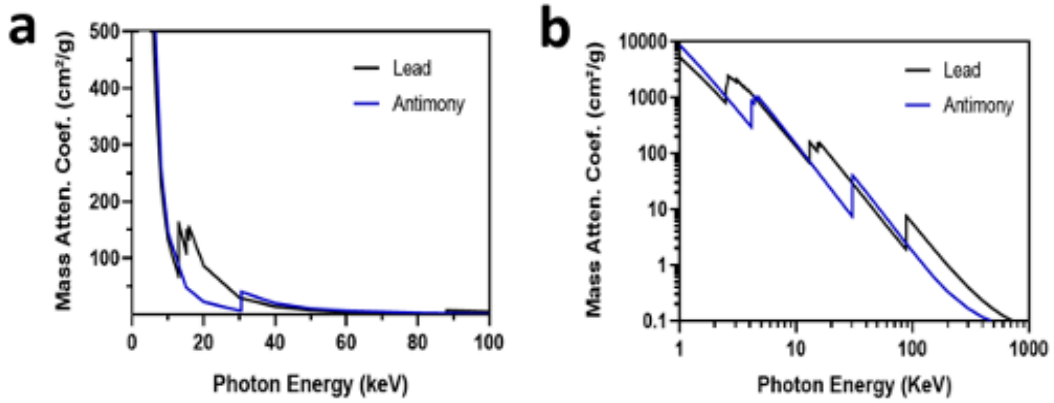

Figure S7. Direct comparison of the total mass attenuation coefficient for Lead (Pb) and antimony (Sb), as a function of the photon energy in keV, in (a) linear scale up to 100 keV and (b) logarithmic scale in a broader energy range.

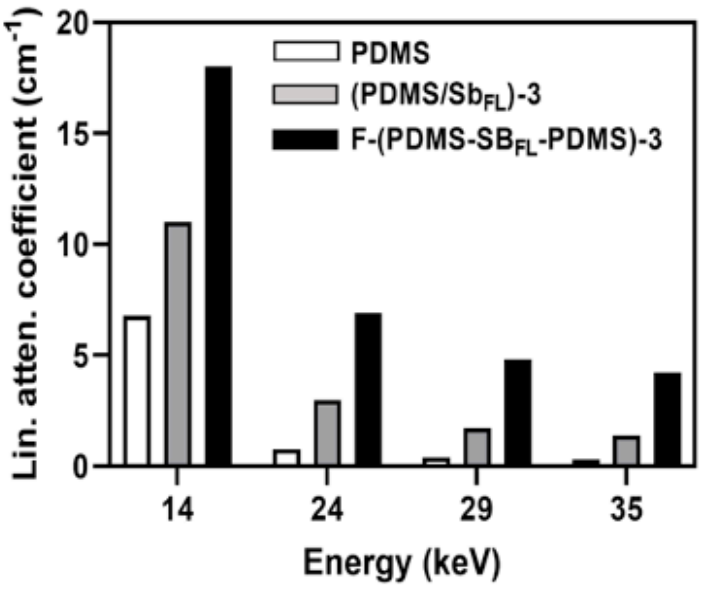

Figure S8. Direct comparison of the linear attenuation coefficient for control-PDMS film, blended composites of "**PDMS/Sb_{FL}-3**" and laminated "**F-(PDMS-Sb_{FL}-PDMS)-3**" samples.

Table S2. Experimental Results of PDMS control, composite and final set of laminated films.

Sample	**Loading of Sb_{FL} (wt%)**	**Thickness (mm)**	**X-ray Transmission %**			
			14 keV	24 keV	29 keV	35 keV
Control PDMS film		1.38 ± **0.1**	39.232	89.852	94.702	95.868
(PDMS/Sb_{FL})-1	4.5	1.38 ± **0.1**	29.357	75.034	86.755	88.786
(PDMS/Sb_{FL})-2	9	1.41 ± **0.1**	26.536	71.801	83.444	86.003
(PDMS/Sb_{FL})-3	13.5	1.40 ± **0.1**	21.446	65.784	78.808	82.293
F-(PDMS-Sb_{FL}-PDMS)-1	4.5	1.37± **0.1**	20.464	63.449	75.828	78.921
F-(PDMS-Sb_{FL}-PDMS)-2	9	1.29 ± **0.1**	14.018	50.921	63.245	67.285
F-(PDMS-Sb_{FL}-PDMS)-3	13.5	1.33 ± **0.1**	9.125	39.874	52.649	56.914

Section S1. Calculated and measured density of materials taken into account for simulation

PDMS (C_2H_6OSi) density: $\rho_{PDMS} = 0.97$ g/cm³

Antimony (Sb) bulk density: $\boldsymbol{\rho}_{Sb} = 6.697$ g/cm³

Packing density as Sb_{FL} (74% Sb and 26% O (Atomic%), Sb_3O): $\boldsymbol{\rho}_{film} = 2.14$ g/cm³

Section S2. Transmission as a function of the material's thickness

The X-ray transmission T = I / I_0 through a homogeneous material of thickness x decays exponentially as:

$$T = \frac{I}{I_0} = e^{-\mu x} \quad \text{(S1)}$$

Where I is the intensity of photons transmitted across some distance x , I_0 the initial intensity of photons, and μ is the linear attenuation coefficient. The linear attenuation coefficient is dependent on the incident X-ray photon energy.

Since a linear attenuation coefficient is $I = I_0 e^{-\mu x}$ dependent on the density ρ of a material, the mass attenuation coefficient (μ/ρ, in units of cm²/g) is often reported for convenience (as obtained from the XCOM/NIST database). Normalizing μ by dividing it by the density of the element or compound will produce a constant value for a particular element or compound. To convert a mass attenuation coefficient (μ/ρ) to a linear attenuation coefficient (μ), multiply it by the density of the material:

$$\mu = (\mu/\rho) * \rho \quad \text{(S2)}$$

Section S2.1. Simulations – case of PDMS only

With the density ρ for the PDMS ($\boldsymbol{\rho}_{PDMS} = 0.97$ g/cm³), the measured thickness of the PDMS control sample ($x = 1.38$ mm,) and the NIST's XCOM database value for the mass attenuation

coefficient for PDMS at different energies, we calculate the transmitted intensity of X-rays photons (I/I_0) using eq. S1.

Section S2.2. Simulations - Case of Composites

Considering the density ρ for composites (e.g. $\rho_{comp\text{-}1}$ = 1.02 g/cm^3 and $\rho_{comp.3}$ = 1.12 g/cm^3), we proceed to obtain the linear attenuation coefficient $\mu = (\mu/\rho) * \rho$ as a function of energy, where the values of (μ/ρ) are obtained from NIST/XCOM for the case of "MIXTURE" - having 95.5% of PDMS and 4.5% of oxidized Antimonene (Sb_3O) for composite 1; and 86.5% PDMS and 13.5% oxidized Antimonene (Sb_3O) for composite 3. Then, for the two corresponding thickness x of the composites (x_1 = 1.38 mm and x_3 = 1.40 mm), we calculate the transmitted intensity I/I_0 of X-rays photons using eq.S1.

Section S2.3. Case of Laminated Antimonene films

PDMS has a much lower mass attenuation coefficient compared to Antimonene film due to the lower atomic numbers of the atoms in the PDMS composition (C_2H_6OSi). However, in our samples, PDMS is much thicker than the Antimonene films, and because of that, it also has a significant (not negligible) attenuation, as observed in the experimental results for PDMS control sample. Therefore, the simulation for these cases needs to take into account both contributions (PDMS + Antimonene film) in the following way.

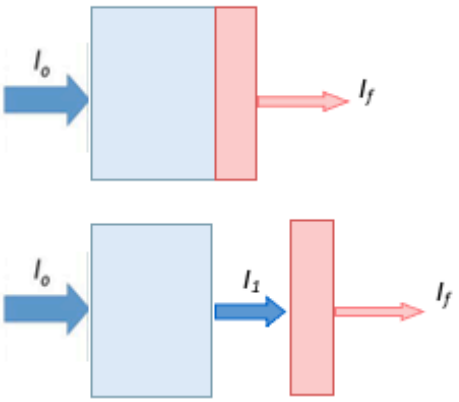

We simulate the transmission throughout only PDMS, T_{PDMS} = I_1 /I_0, and we simulate the transmission through the Antimonene film: T_{film} = I_f/ I_1 (both at the correct thickness for each case), and then we can obtain the transmission through the two materials, T_{total}, by multiplying one by the other:

$$T_{total} = \frac{I_f}{I_0} = \frac{I_f}{I_1} \times \frac{I_1}{I_0} = T_{Sb_{FL}} \times T_{PDMS} \qquad (S3)$$

For each film, we consider the exact thickness of PDMS and of the Antimonene film, as enlisted in Table S1, and the respective densities. We can simulate the transmission for film + PDMS using eq. S3, and compare it with the total experimental transmission.

An example of laminated Sb_{FL}, $T_{total} = T_{Sb_{FL}} \times T_{PDMS}$ for the simulation 1.14 mm of PDMS and 165 μm of Antimonene F-(PDMS-Sb_{FL}-PDMS)-3.

$$T_{film} = \frac{I_f}{I_1} = \frac{(I_f/I_0)}{(I_1/I_0)} = \frac{T_{total}}{T_{PDMS}} \quad \text{(S4)}$$

Section S3. Calculation of linear attenuation coefficient (μ), half value layer (HVL), tenth value layers (TVL), mass attenuation coefficient ($^{\mu}/_{\rho}$)

As mentioned in "Section S1", the exfoliated packing density of few layered antimonene (Sb_{FL}) was measured as 2.14 g/cm³ and the **PDMS** (C_2H_6OSi) density was ρ_{PDMS} = 0.97 g/cm³.

The fabrication of blended composite and laminated samples at different wt% of Sb_{FL}

The "PDMS/ Sb_{FL}" composite films with three different weight percentages (4.5 wt%, 9 wt% and 13.5 wt%) of Sb_{FL} were labelled as (PDMS/Sb_{FL})-1, (PDMS/Sb_{FL})-2 and (PDMS/Sb_{FL})-3, respectively. The laminated samples were having similar composition of the composite samples mentioned above except ultra-thin cotton fabrics as Sb_{FL} carrier. The laminated samples with three different weight percentages (4.5 wt%, 9 wt% and 13.5 wt%) of Sb_{FL} nanosheets were labelled as F-(PDMS-Sb_{FL}-PDMS)-1, F-(PDMS-Sb_{FL}-PDMS)-2 and F-(PDMS-Sb_{FL}-PDMS)-3. The composites and laminated samples were considered to be equivalent in weight and density if the weight of ultrathin cotton is ignored. There, the density of the both composite and laminated samples were determined as below;

$\rho_{(PDMS/Sb_{FL})-1} = \rho_{F-(PDMS-Sb_{FL}-PDMS)-1}$ = 1.0226 g/cm³.

$\rho_{(PDMS/Sb_{FL})-2} = \rho_{F-(PDMS-Sb_{FL}-PDMS)-2}$ = 1.0753 g/cm³.

$\rho_{(PDMS/Sb_{FL})-3} = \rho_{F-(PDMS-Sb_{FL}-PDMS)-3}$ = 1.1279 g/cm³.

Linear attenuation coefficient (μ) was calculated using eq. S5.

$$\text{Linear attenuation coefficient } (\mu) = -\frac{\ln(\frac{I}{I_0})}{x} \quad \text{cm}^{-1} \qquad \text{(S5)}$$

Where, I/I_0 is transmitted intensity of X-rays photons, x is thickness of experimental sample in cm.

The half value layers (HVL) and tenth value layers (TVL) are the thickness of a radiation shielding or absorber materials that reduces the radiation level by a factor of one-half and one tenth of the initial level, respectively [3].

HVL and TVL were calculated as below;

$$\text{HVL} = \frac{\ln 2}{\mu} \text{ cm, where } \mu \text{ is linear attenuation coefficient.} \qquad \text{(S6)}$$

$$TVL = \frac{\ln 10}{\mu} \text{ cm, where } \mu \text{ is linear attenuation coefficient.} \quad \text{(S7)}$$

Mass attenuation coefficient (μ/ρ) was calculated by dividing linear attenuation coefficient with the determined density mentioned above for each different sample.

Table S3. Calculated photon atomic parameter from experimental results of control-PDMS, composite and final set of laminated films.

Samples	Thickness (mm)	Energy (keV)	X-ray transmission (I/Io)	Linear attenuation (μ) cm^{-1}	HVL (ln 2/μ) cm	TVL (ln 10/μ) cm	Mass attenuation (μ/ρ) cm2/g
PDMS only	1.38 ± 0.1	14	0.392	6.786	0.102	0.339	6.996
		24	0.899	0.772	0.898	2.984	0.795
		29	0.947	0.395	1.757	5.835	0.407
		35	0.959	0.303	2.285	7.590	0.313
(PDMS/SbFL)-1	1.38 ± 0.1	14	0.293	8.896	0.078	0.259	8.704
		24	0.75	2.085	0.333	1.105	2.040
		29	0.867	1.034	0.670	2.226	1.012
		35	0.887	0.869	0.798	2.650	0.850
(PDMS/SbFL)-2	1.41 ± 0.1	14	0.265	9.352	0.074	0.246	8.700
		24	0.718	2.333	0.297	0.987	2.170
		29	0.834	1.278	0.542	1.801	1.189
		35	0.86	1.062	0.653	2.168	0.988
(PDMS/SbFL)-3	1.40 ± 0.1	14	0.214	11.013	0.063	0.209	9.772
		24	0.658	2.990	0.232	0.770	2.653
		29	0.788	1.702	0.407	1.353	1.510
		35	0.823	1.391	0.498	1.655	1.235
F-(PDMS-SbFL-PDMS)-1	1.37± 0.1	14	0.205	11.567	0.060	0.199	11.318
		24	0.634	3.326	0.208	0.692	3.255
		29	0.758	2.080	0.333	1.107	2.036
		35	0.789	1.730	0.401	1.331	1.693
F-(PDMS-SbFL-PDMS)-2	1.29 ± 0.1	14	0.14	15.241	0.045	0.151	14.178
		24	0.509	5.235	0.132	0.440	4.870
		29	0.632	3.557	0.195	0.647	3.309
		35	0.673	3.070	0.226	0.750	2.856
F-(PDMS-SbFL-PDMS)-3	1.33 ± 0.1	14	0.091	18.022	0.038	0.128	16.091
		24	0.399	6.908	0.100	0.333	6.168
		29	0.526	4.830	0.143	0.477	4.313
		35	0.569	4.240	0.163	0.543	3.785

Reference.

1. APRANSA, *Aprons for Protection Against X-rays*. 2015.

2. Santos, A.M.C., M. Mohammadi, and S. Afshar V, *Energy dependency of a water-equivalent fibre-coupled beryllium oxide (BeO) dosimetry system.* Radiation Measurements, 2015. **73**: p. 1-6.

3. Akkaş, A., Determination of the tenth and half value layer thickness of concretes with different densities. Acta Physica Polonica A, 2016. 129(4): p. 770-772.

CHAPTER 6

APPLICATION OF THE DESIGNED POLYMER-BASED 2D OXIDE COATED TEXTILE FOR X-RAY SHIELDING

Chapter 6 Application of the designed polymer-based 2D oxide for X-ray shielding

Overview and significance of work

This chapter introduces the best shielding materials selected the previous studies in chapter 3, 4, and 5 to fabricate a lightweight, Pb-free coated textile for X-ray protection. The new design of the sandwich-structure coated textile was prepared using nanosized $Bi_4Ti_3O_{12}$ composite, followed by determination of chemical properties, thermal stability, and X-ray attenuation ability. The key finding indicated that the sandwich-structure $Bi_4Ti_3O_{12}$ composite coated textile can achieve 0.35 mm Pb equivalent X-ray shielding ability at 80 kVp. This study on the structure design of 2D metal oxide composite coated textile provides new solution of fabrication of light, flexible and effective Pb-free shielding fabrics. The results from this work achieve **aim 4** with one paper:

(1) **Yu, L.**, Yap, P. L., Santos, A., Tran, D., & Losic, D. (2022). Lightweight polyester fabric with elastomic bismuth titanate composite for high-performing lead-free X-ray shielding. *Advanced Engineering Materials*. **(Under review)**

Statement of Authorship

Title of Paper	Lightweight polyester fabric with elastomic bismuth titanate composite for high-performing lead-free X-ray shielding
Publication Status	☐ Published ☐ Accepted for Publication ☑ Submitted for Publication ☐ Unpublished and Unsubmitted w ork w ritten in manuscript style
Publication Details	Yu, L., Yap, P. L., Santos, A., Tran, D., & Losic, D. (2022). Lightweight polyester fabric with elastomic bismuth titanate composite for high-performing lead-free X-ray shielding. *Advanced Engineering Materials*.

Principal Author

Name of Principal Author (Candidate)	Le Yu		
Contribution to the Paper	Prepared and characterized on all the samples, and interpreted all the data as well as wrote the manuscript.		
Overall percentage (%)	85 %		
Certification:	This paper reports on original research I conducted during the period of my Higher Degree by Research candidature and is not subject to any obligations or contractual agreements with a third party that would constrain its inclusion in this thesis. I am the primary author of this paper.		
Signature		Date	03/03/2022

Co-Author Contributions

By signing the Statement of Authorship, each author certifies that:

i. the candidate's stated contribution to the publication is accurate (as detailed above);

ii. permission is granted for the candidate in include the publication in the thesis; and

iii. the sum of all co-author contributions is equal to 100% less the candidate's stated contribution.

Name of Co-Author	Pei Lay Yap		
Contribution to the Paper	Edited and revised the manuscript.		
Signature		Date	03/03/2022

Name of Co-Author	Alexandre M. C. Santos		
Contribution to the Paper	Co-supervised, performed X-ray irradiations and revised the manuscript.		
Signature		Date	03/03/2022

Please cut and paste additional co-author pa

Statement of Authorship

Title of Paper	Lightweight polyester fabric with elastomic bismuth titanate composite for high-performing lead-free X-ray shielding
Publication Status	☐ Published ☐ Accepted for Publication ☑ Submitted for Publication ☐ Unpublished and Unsubmitted w ork w ritten in manuscript style
Publication Details	Yu, L., Yap, P. L., Santos, A., Tran, D., & Losic, D. (2022). Lightweight polyester fabric with elastomic bismuth titanate composite for high-performing lead-free X-ray shielding. *Advanced Engineering Materials*.

Principal Author

Name of Principal Author (Candidate)	Le Yu		
Contribution to the Paper	Prepared and characterized on all the samples, and interpreted all the data as well as wrote the manuscript.		
Overall percentage (%)	85 %		
Certification:	This paper reports on original research I conducted during the period of my Higher Degree by Research candidature and is not subject to any obligations or contractual agreements with a third party that would constrain its inclusion in this thesis. I am the primary author of this paper.		
Signature		Date	03/03/2022

Co-Author Contributions

By signing the Statement of Authorship, each author certifies that:

i. the candidate's stated contribution to the publication is accurate (as detailed above);

ii. permission is granted for the candidate in include the publication in the thesis; and

iii. the sum of all co-author contributions is equal to 100% less the candidate's stated contribution.

Name of Co-Author	Diana N. H. Tran		
Contribution to the Paper	Co-supervised and revised the manuscript.		
Signature		Date	03/03/2022

Name of Co-Author	Dusan Losic		
Contribution to the Paper	Supervised the development of work, edited, revised the manuscript and acted as the corresponding author.		
Signature		Date	03/03/2022

Please cut and paste additional co-author p

Advanced Engineering Materials

Lightweight Polyester Fabric with Elastomeric Bismuth Titanate Composite for High-Performing Lead-Free X-ray Shielding

--Manuscript Draft--

Manuscript Number:	
Article Type:	Research Article
Corresponding Author:	Dusan Losic, PhD The University of Adelaide Adelaide, SA AUSTRALIA
Corresponding Author E-Mail:	dusan.losic@adelaide.edu.au
Order of Authors:	Le Yu
	Pei Lay Yap
	Alexandre Santos, Dr
	Diana Tran, Dr
	Dusan Losic, PhD
Keywords:	X-ray shielding enhancement; coated textile; bismuth titanate; sandwich structure
Section/Category:	
Abstract:	To protect the workers from overexposure to X-ray radiation, conventional lead (Pb)-based aprons are widely applied to many medical institutions and nuclear industries. However, these Pb-based aprons have many disadvantages such as the heaviness, toxicity and discomfort wearing experience so there is a strong demand for the replacement using lightweight, Pb-free, and flexible X-ray shielding materials. In this study, a new solution using the sandwich-composite structure with textile with polyester fabric with elastomeric bismuth titanate Composite is explored to develop the superior X-ray shielding materails. To demonstrate this concept, nanosized bismuth titanate (BTO) was used as an effective shielding component, which was blended with polydimethylsiloxane (PDMS) to form a PDMS/BTO composite. The sandwich-structure PDMS/BTO coated polyester fabric (SL-PDMS/BTO-PES) was then fabricated using 2 [[EQUATION]] coated PES fabrics and compressed together. X-ray transmission of these SL-PDMS/BTO-PES fabrics with an average thickness at 1.1 [[EQUATION]] m was measured at 80 kVp and 100 kVp, showing 0.35 mm Pb-equivalent X-ray shielding ability. Moreover, the SL-PDMS/BTO-PES was 42% lighter than 0.35 mm Pb sheet, indicating that this lightweight and flexible sandwich-structure coated PES textile can be potentially engineered in the future for replacing the conventional Pb-vinyl X-ray shielding clothing.
Suggested Reviewers:	Susanna Guatelli, phd University of Wollongong susanna@uow.edu.au Expert on X-ray radiation shielding
Opposed Reviewers:	
Author Comments:	NA
Additional Information:	
Question	Response
Please submit a plain text version of your cover letter here.	Cover letter is attached
Do you or any of your co-authors have a conflict of interest to declare?	No. The authors declare no conflict of interest.

WILEY-VCH

Lightweight Polyester Fabric with Elastomeric Bismuth Titanate Composite for High-Performing Lead-Free X-ray Shielding

*Le Yu, Pei Lay Yap, Alexandre Santos, Diana Tran, Dusan Losic**

Le Yu, Pei Lay Yap, Diana Tran, Dusan Losic*

School of Chemical Engineering and Advanced Materials, The University of Adelaide, Adelaide, SA 5005, Australia.
ARC Research Hub for Graphene Enabled Industry Transformation, The University of Adelaide, Adelaide, SA 5005, Australia.
E-mail: Dusan.losic@adelaide.edu.au

Alexandre Santos

School of Physical Sciences, The University of Adelaide, Adelaide, South Australia 5005, Australia.
Department of Medical Physics, Royal Adelaide Hospital, Adelaide, South Australia 5000, Australia.
Department of Medical Physics, Royal Adelaide Hospital, Adelaide, South Australia 5000, Australia.

Keywords: X-ray shielding enhancement, coated textile, bismuth titanate, sandwich structure

Abstract To protect the workers from overexposure to X-ray radiation, conventional lead (Pb)-based aprons are widely applied to many medical institutions and nuclear industries. However, these Pb-based aprons have many disadvantages such as the heaviness, toxicity and discomfort wearing experience so there is a strong demand for the replacement using lightweight, Pb-free, and flexible X-ray shielding materials. In this study, a new solution using the sandwich-composite structure with textile with polyester fabric with elastomeric bismuth titanate Composite is explored to develop the superior X-ray shielding materails. To demonstrate this concept, nanosized bismuth titanate (BTO) was used as an effective shielding component, which was blended with polydimethylsiloxane (PDMS) to form a PDMS/BTO composite. The sandwich-structure PDMS/BTO coated polyester fabric (SL-PDMS/BTO-PES) was then fabricated using 2 × coated PES fabrics and compressed together. X-ray transmission of these SL-PDMS/BTO-PES fabrics with an average thickness at 1.1 μm was measured at 80 kVp and 100 kVp, showing 0.35 mm Pb-equivalent X-ray shielding ability. Moreover, the SL-PDMS/BTO-PES was 42 % lighter than 0.35 mm Pb sheet, indicating that this lightweight and

flexible sandwich-structure coated PES textile can be potentially engineered in the future for replacing the conventional Pb-vinyl X-ray shielding clothing.

1. Introduction

X-ray electromagnetic radiation is widely applied in radiotherapy, medical imaging, and material characterization, due to high-energy electromagnetic property.[1] So far, the growing demand of applying X-ray, especially in the medical field has brought potential harm for practitioners, due to their frequent exposure to X-ray.[2] The employment rate of radiology occupation has been estimated to increase by 9 % between 2014 and 2024.[3] Previous reports from International Commission on Radiological Protection (ICRP) revealed that the long-term exposure to high-energy radiation led to irreversible health issues (e.g. carcinogenetic disease),[4] thus the use of X-ray protective material is of great significance for the practitioners' safety.

Materials with high atomic number (Z) elements are often used for effective X-ray shielding application, owing to their electron-rich atoms that increase the probability of X-ray attenuation by the photoelectric effect.[5] Lead (Pb, Z = 81) is therefore employed as an ideal X-ray shielding material, due to its high density and high attenuation coefficient.[6] Historically, the conventional radiation shielding apparels were constructed from polymer, rubber, or vinyl binders embedded with Pb powder or lead oxide (Pb_3O_4).[7, 8] The conventional Pb-based apron composed of the Pb impregnated sheets enveloped by the nylon or polyester fabric as casing.[9] This casing filled with Pb sheets has added extra heaviness on the final product, leading to severe back pain or fatigue during the long-term wearing. However, toxicity, poor flexibility, heaviness, and discomfort wearing experience of using Pb-based protective apparel have caused health and environmental concerns,[7, 10] which has been banned for use in Europe since 2014.[11] Moreover, Pb-based protective apparels that compose of the thin-layered Pb sheets can easily develop cracks and holes, due to poor durability.[11]

To address these problems, many studies have been focused on the development of the non-Pb, lightweight and flexible X-ray shielding materials. The compounds that contain other high-Z elements (including bismuth (Bi), tungsten (W), and barium (Ba), tin (Sn), and antimony (Sb)) were explored to replace Pb as effective X-ray attenuating materials.[13, 14] Currently, these studies have been mainly focused to develop lightweight, Pb-free X-ray shielding composites in combination with various polymeric matrixes such as epoxy and polyesters. . The X-ray attenuation of the microsized bismuth oxide (Bi_2O_3) filled with epoxy composites

were studied at X-ray energies of 40-120 kVp, showing that the Bi_2O_3 (70 wt.%)-epoxy composite with a thickness of 8 mm provided nearly the same X-ray attenuation ability (90 %) as Pb glass at 120 kVp. However, a marked decrease in the flexural strength was found with the increment of Bi_2O_3 loading reached to 30 wt.%, due to significant agglomeration of the microsized Bi_2O_3 particles within the epoxy-based composite.[15] Azman et al. investigated the effect of particle size of tungsten oxide (WO_3) on the X-ray attenuation using WO_3-epoxy composites at a different set of X-ray energy (40-120 kVp), indicating that the nanosized WO_3-epoxy composite showed 3 times better in X-ray attenuation compared with its microsized counterpart, due to improved dispersion ability.[16] Since then, the polymer-based nanocomposites have been widely applied for X-ray shielding improvement with reduced weight and enhanced durability.[17] Recently, in our study on the impact of the particle size and morphology effect on Bi_2O_3 films on X-ray shielding enhancement, it was found that the Bi_2O_3 film with nanoflower (~ 400 nm) particle morphologies gave the best X-ray shielding performance (45.93 % and 47.49 % improvement at 30 kVp, respectively) compared to the microwire (~ 1.30 μm) and spherical nanoparticle (~ 830 nm) Bi_2O_3 film, due to its large surface-to-volume ratio.[6] Nowadays, nanocomposites have been extensively explored for new design of the lightweight radiological protective garments, which can be great potential to replace the conventional Pb-based aprons.[18]

To reduce the weight of the X-ray protective apparel with the comparable Pb-equivalent X-ray shielding performance, incorporation of Pb-free metal powders into the polymeric yarn was first developed. Earlier study tended to use Sn (80 wt.%) and Bi (20 wt.%) embedded in a protective clothing for evaluation of X-ray shielding effectiveness at 60 kVp and 120 kVp. However, the Sn-Bi combination embedded clothing (at the thickness of 0.41 mm) provided 32 % less protection compared with 0.35 mm Pb sheet at 120 kVp.[19] In addition, it was found that adequately higher amount of the metal powders were used within the polymeric fabric to achieve the effective attenuation as Pb, which was much costly. Another study has been reported using barium sulphate ($BaSO_4$)-silicon rubber (SR) composite coated cotton fabric for X-ray shielding performance, compared to the Bi-SR and W-SR composites coated cotton fabrics. It was found that $BaSO_4$-SR coated fabric with a thickness of 2.81 mm only showed 90 % X-ray attenuation at 100 kVp, which was less effective than the Bi-SR (99 %) and W-SR (95 %) composites coated fabrics.[20] Bi_2O_3 was then introduced as a Pb-alternative to develop an X-ray protective textile, showing that Bi_2O_3 (50 wt.%) coated polyester fabric with a thickness of 1.33 mm provided 92 % X-ray attenuation at 80 kVp.[21] However, the one-side

coating technique made this X-ray protective textile less resistant to laundry and less durable for bending and folding.

To address these problems, in this study we presented a new solution (a sandwich-structure: one textile sheet-polymer-based nanocomposite-one textile sheet) for coated X-ray protective textile using compressed layer-by-layer coating technique, compared with the casing structure of the commercial Pb-based protective apron (as shown in Fig. 1). It is hypothesized that this sandwiched polymer-based nanocomposite coated textile will be able to provide improved resistance to avoid crack mitigation without scarifying the high flexibility of the textile for the superior X-ray shielding performance.

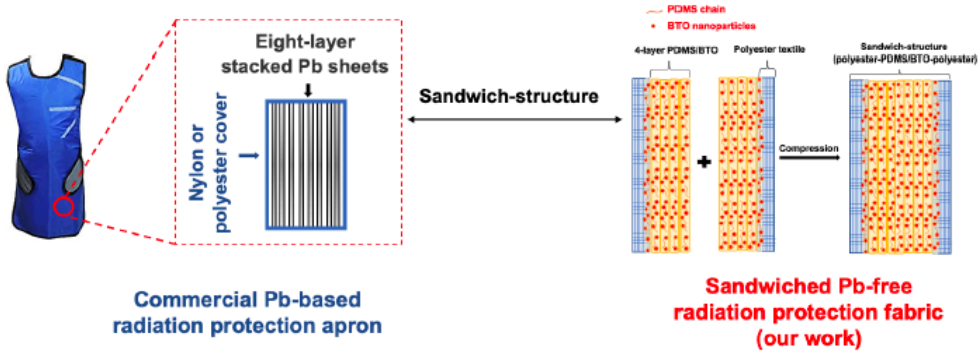

Fig. 1 Schematic illustration of commercial Pb-based radiation protection apron compared to the sandwich-structure of the PDMS-BTO composite coated PES fabric.

To demonstrate this concept, nanosized bismuth titanate (BTO) is used as an effective X-ray attenuating component as proven by our previous work.[22] Polydimethylsiloxane (PDMS) is applied as a supporting polymer for formation of the X-ray protective nanocomposite, owing to its thermoset property, non-toxicity, cost-effectiveness, flexibility and easy handling to coat on any even and uneven surface, which is suitable for adhesion on the surface of the textiles.[23, 24] A polyester fabric is selected as a coating substrate, as it is commonly used in the commercial X-ray protective garments.[25] In addition, the woven structure of PES fabric can offer its benefit as reinforcement in the polymer-based composites, due to its good mechanical property.[25] In our study, a lightweight, flexible, non-toxic, and Pb-free coated PES textile sandwiched with PDMS/BTO composite is fabricated using a compressed layer-by-layer coating process for the promising X-ray shielding application. Importantly, the X-ray attenuation effectiveness of this sandwiched PDMS/BTO composite coated PES fabric is investigated at X-ray energies of 80 kVp and 100 kVp, and this result is then evaluated using the standard Pb sheets with three different thicknesses (0.25 mm, 0.35 mm, and 0.50 mm). The

outcomes from this study will provide new alternatives to Pb-free materials to significantly reduce the weight of Pb impregnated materials with superior X-ray attenuation ability, which potentially can be engineered in the future for replacing the conventional Pb-vinyl apparel.

2. Results and Discussion

2.1. Characterization of Bismuth Titanate (BTO) Nanoparticles

Fig. 2 presents the structural and chemical properties of the synthesized BTO nanoparticles used in this study characterized by XRD, Raman, PSD analysis and SEM technique. The broad XRD peaks at 2θ = 30°, 32° and 39° as well as three new peaks appeared between 47° to 58° (2θ = 48°, 56° and 57°) were identified for BTO phase in Fig. 2(a).[26] Fig. 2(b) presented a distinct Raman spectrum, where the sharp mode at 56 cm^{-1} and a peak arose at 110 cm^{-1} were attributed to the rigid-layer (RL) mode and Bi-O vibration, respectively. Raman scattering at 619 and 848 cm^{-1} can be ascribed to the vibration mode in the TiO_6 octahedral; while the peak at 535 cm^{-1} represented the opposing excursion of the external apical oxygen of the TiO_6 octahedral phase.[27] Results from both XRD and Raman analysis confirmed the successful formation of the BTO phase. SEM image (Fig. 2(c)) of the as-synthesized BTO sample clearly showed the fused irregular structure of BTO particles with the agglomeration, which could result from the prolonged ball milling time. As per analysis of the SEM structures, the particle size distribution of BTO particles was 535.40 ± 50 nm (Fig. 2(d)), which was in good agreement with the average particle size distribution. The detailed characterization of BTO nanoparticles can be reviewed in our previous work.[22]

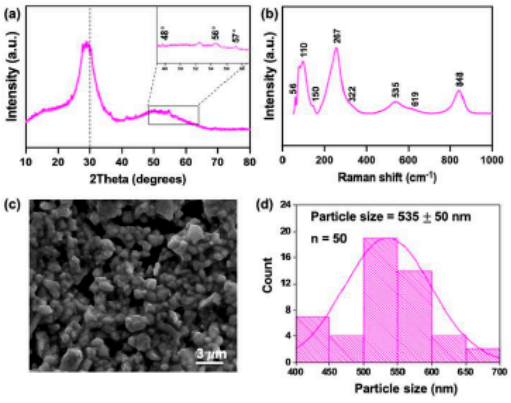

Fig. 2 (a) XRD pattern, (b) Raman spectra, (c) SEM image (scale bar = 3 μm) and (d) PSD analysis of the synthesized BTO nanoparticles.

2.2. Characterization of the PDMS/BTO composite coated PES fabrics

Surface morphology of the prepared PDMS/BTO coated PES fabrics with increased number of layers (1L, 2L, 4L and 6L, L = layer) were obtained using SEM to determine the maximum coating layers onto one single PES fabric as show in Fig. 3(a-e). Fig. 3(a) showed a typical structure of a woven polyester fabric with interlacing micron-sized rod-like fibres in a weft pattern at an average surface roughness at 32.2 μm (shown in Fig. S1).[28] After applying 1L PDMS/BTO composite, it was easy to observe that a thin-layer of the composite enveloped the PES fibres (Fig. 3(b)), and several debris underneath the PDMS matrix were attributed to the slight aggregation of BTO nanoparticles. Compared to 2L composite PES sample (Fig. 3(c)), the 4L coated PES fabric (4L-PES-PDMS/BTO) exhibited a much smoother surface with no significant aggregation observed in micron scale (Fig. 3(d)), showing the lowest average surface roughness at 5.5 μm in Fig. S1. In Fig. 3(e), 6L-PES-PDMS/BTO fabric composed of a more wrinkle-like structure with several small debris under the coating surface. Moreover, the uneven-distributed BTO nanoparticles underneath the PDMS matrix showed increased surface roughness of 8.1 μm (Fig. S1), indicating that the limitation of the coating layers for the PES fabric had been reached. The results obtained from both SEM and surface roughness measurement suggested that the use of the 4L PDMS/BTO composite (4L-PES-PDMS/BTO) was the maximum coating layer for a single polyester sheet. This finding was also supported with the observation from the photographs (Fig. 3a'-e') of the prepared PDMS/BTO coated PES fabrics with increased layers.

To successfully fabricate a sandwich-structure PDSM/BTO coated PES fabric (denoted as SL-PES-PDMS/BTO), 2 × 4L PDMS/BTO coated PES fabrics were compressed together as the scheme shown in Fig. 1. The cross-sectional SEM image of successfully synthesized SL-PES-PDMS/BTO showed densely stacked PDMS/BTO layers covered with two PES fabrics at the average thickness of 1.1 mm (Fig. 3(f)), which was in good agreement with the thickness measurement (Fig. 3(g)). The highly bending SL-PES-PDMS/BTO showed in Fig. 3(h), indicating that this densely packed PDMS/BTO composite between two PES fabrics can still maintain its flexibility.

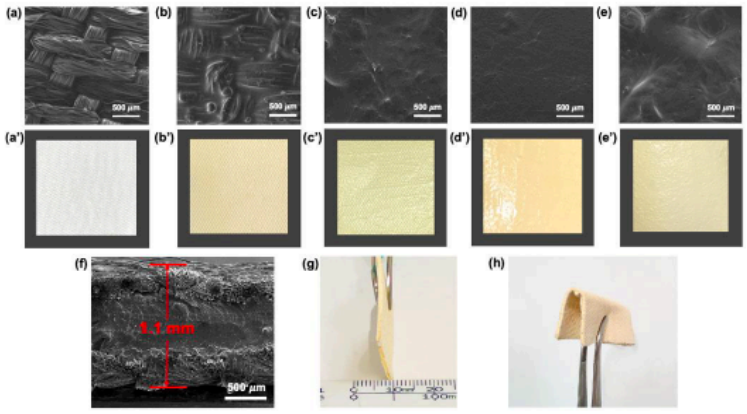

Fig. 3 Top-sectional SEM images of (a) polyester fabric (PES, control), and PDMS/BTO coated PES fabric with different coating layers, including (b) 1L-PES-PDMS/BTO, (c) 2L-PES-PDMS/BTO, (d) 4L-PES-PDMS/BTO and (e) 6L-PES-PDMS/BTO with (a'-e') their corresponding photographs; (f) cross-sectional SEM image (scale bar = 500 μm), (g) the thickness measurement, and (h) high flexibility of prepared SL-PES-PDMS/BTO.

The chemical and thermal properties of the synthesized SL-PES-PDMS/BTO were determined using XRD and TGA-DTG analysis. XRD patterns of controls (PES, PES-PDMS) and SL-PES-PDMS/BTO were present in Fig. 4(a). The typical reflection peaks of PES at 2θ = 18°, 23° and 26° corresponded to (100), (002) and (101) planes of woven polyester fabric.[29] After coating with 1L PDMS onto PES fabric, a broad peak located at 12° was attributed to amorphous phase of PDMS.[30] A series of XRD peaks incorporating six characteristic peaks of BTO nanoparticles (indicated as square shape) and four additional peaks resulting from PES-PDMS composite (symbolized by solid triangle and asterisk) suggested successful synthesis of sandwich-like PDMS/BTO coated PES fabric (SL-PES-PDMS/BTO). The elemental analysis of SL-PES-PDMS/BTO sample obtained from EDX mapping technique (Fig. S2) was in good agreement with the XRD analysis and SEM image, showing well distribution of BTO nanoparticles within PDMS matrix and tightly imbedded with PES sheets.

The thermal behaviour and thermal stability of the uncoated and coated PES fabrics were examined using thermogravimetric and its first derivative analysis (TGA-DTG) under air atmosphere as depicted in Fig. 4 (b) and (c). Uncoated PES control fabric showed two typical mass loss stages as evidenced by its two distinct temperature of maximum mass decomposition (T_{max}) at 432.7 °C and 537.8 °C. The first stage contributing to primary mass loss (~ 78%) at around 300-460 °C that can be attributed to the degradation of polyester framework to form styrene, phthalic anhydride, CO and CO_2. This was followed by a minor mass loss of ~18% at 460-600°C for the char oxidation stage, leaving behind 3.9 % residue.[31] PES fabric coated

with PDMS exhibited its mass decomposition with major depolymerization temperature between 400-750 °C. The DTG curve of the PDMS coated PES fabric has an additional DTG peak at ~ 743 °C apart from two DTG peaks slightly right shifted to 437.6 °C and 567.6 °C in relative to uncoated PES material. Majority of the PDMS have converted to cyclic oligomers through unzip degradation at 400-500 °C (~ 60 %), forming cyclic siloxanes intermediate, followed by rearrangement degradation of Si-O-Si bonds in the siloxane backbone and heterolytic cleavage beyond 500 °C (~ 16 %), leading to cyclic siloxanes and short moieties.[32] Meanwhile, BTO coated fabric demonstrated the lowest mass decomposition among the tested samples with > 60 % residue remained after thermal decomposition at 1000 °C. Its primary mass loss accounted for ~28 % at 400-530 °C can be linked to the degradation of $BiONO_3$ to Bi_2O_3, followed by two minor mass losses with their DTG peaks at 532.6 °C and 722.6 °C due to thermal decomposition of PDMS coated PES fabric.[33] This result not only confirmed the successful coating of BTO onto the PES-PDMS fabric as discussed in previous section, but also approved the enhanced thermal stability of SL-PES-PDMS/BTO up to 1000 °C.

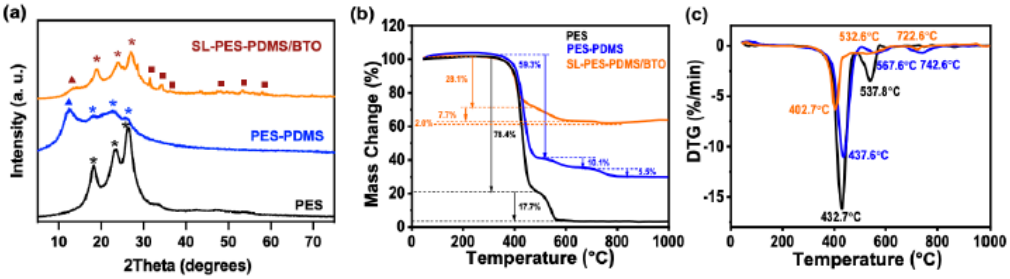

Fig. 4 (a) XRD patterns, (b) TGA analysis and (c) DTG analysis of the controls (PES fabric and PES-PDMS) and the prepared SL-PES-PDMS/BTO.

2.3. X-ray shielding performance of the sandwich-structure textile

Generally, the incident X-ray photons possess a high degree of directivity while passing through the coated attenuating materials, which could impact on the X-ray transmission values.[34, 35] To be specific, the incident X-ray photons will firstly interact from the front layer of PDMS/BTO composite to the PES fabric cover when the coated layer faces to the incoming X-ray (Fig. S3(a-1)), and vice versa. To understand the impact of the directivity (the frontside and backside) of the PDMS/BTO coated textiles towards X-ray attenuation efficiency, X-ray transmission measurements of the frontside and backside of the coated PES fabrics were performed under 80 kVp and 100 kVp (the scheme as shown in Fig. S3(a)). Fig. S3(b) exhibited that the overall trend of photon transmittance decreased sharply with an increase in the

PDMS/BTO coating layers at both X-ray energies. The polyester fabric (control) was negligibly affected by X-ray attenuation at both 80 kVp and 100 kVp, showing that ~ 99.9 % of X-ray intensity was transmitted. This is due to the gaps generated between the woven structure of the polyester textile that allowed easy penetration of the incident X-ray photons.[36] Generally, X-ray attenuation strongly depends on the photon energy of X-ray and thickness of the shielding materials.[37] By elevating the average thicknesses of the coated PES fabrics from ~ 0.4 mm (1L) to ~ 0.8 mm (6L) obtained from Fig. S4, X-ray transmission values of the PDMS/BTO coated PES decreased significantly from ~ 59 % and ~ 41 % up to ~ 14 % and ~ 19 %, at X-ray energies of 80 kVp and 100 kVp, respectively. This remarkable outcome could be explained by the effective coating of PDMS/BTO that not only closed the weft gaps of PES, but also acted as a shield by covering the PES surface to prevent the penetration of X-ray photons. Despite the 6L-PES-PDMS/BTO presented the lowest X-ray transmission (~ 14 % at 80 kVp and ~ 19 % at 100 kVp), the uneven distribution of BTO nanoparticle within PDMS matrix and the highest average surface roughness (8.1 μm) from the previous results indicated the significantly reduced mechanical properties of 6L-PES-PDMS/BTO. To achieve the effective X-ray attenuation ability without sacrificing the mechanical properties, the 4L PDMS/BTO coating on a single PES fabric was selected for further synthesis of the sandwich-structure shielding material. The X-ray transmission of back-side coated textiles in Fig. S3(c) suggested that there were insignificant differences (~ 1 %) compared with front-side coated samples, which can be negligible. This provided evidence for our design of the sandwich-structure (PES sheet-PDMS/BTO filler-PES sheet) X-ray shielding material.

Mass attenuation coefficient (μ/ρ) is used to evaluate the X-ray shielding ability of the developed shielding materials with different densities.[35, 37] More specifically, it describes a rate between X-ray attenuation capacity per unit thickness (cm^{-1}) of a shielding material and the density (g/cm^3) of this material. Fig. 5 presented mass attenuation coefficient of SL-PES-PDMS/BTO sample compared with the commercial 0.44 mm Pb sheet (the μ/ρ value was measured and referred to our previous work[22]). Importantly, the calculated μ/ρ value of our sandwich-structure textile from equation (3) showed 12.1 $\pm$ 0.1 cm^2/g and 9.3 $\pm$ 0.1 cm^2/g at 80 kVp and 100 kVp, respectively. The obtained results were slightly higher than that of 0.44 mm Pb sheet (8.1 cm^2/g and 6.2 cm^2/g, respectively), showing the superior X-ray shielding ability of the sandwich-structure PDMS/BTO coated textile at both 80 kVp and 100 kVp.

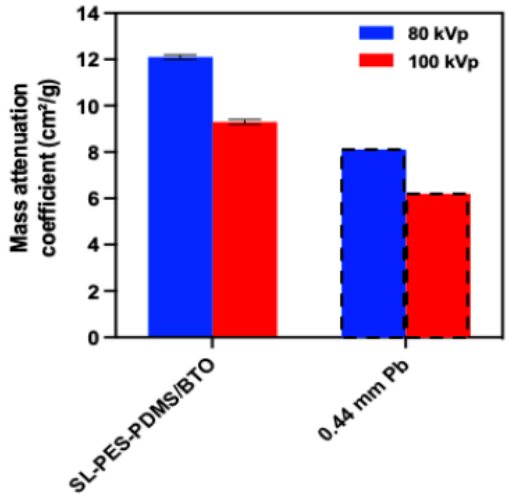

Fig. 5 Mass attenuation coefficients of SL-PES-PDMS/BTO compared with the commercial 0.44 mm Pb sheet at 80 kVp and 100 kVp.

To further evaluate the X-ray attenuation ability of the prepared SL-PES-PDMS/BTO, the X-ray transmission value of SL-PES-PDMS/BTO was further compared with that of Pb sheets with the specific thicknesses (0.25 mm, 0.35 mm, and 0.50 mm), according to the standard of International Commission on Radiological Protection.[38, 39] In Fig. 6, the transmitted X-ray intensity ratio of SL-PES-PDMS/BTO was evaluated with 0.25 mm, 0.35 mm, and 0.50 mm pure Pb sheets (calculated from 0.44 mm Pb sheet measured under 80 kVp and 100 kVp). The SL-PES-PDMS/BTO at its thickness of 1.1 mm achieved the lowest X-ray transmission of ~ 6 % and ~ 11 %, showing X-ray attenuation efficiency of ~ 94 % and ~ 88 % at both 80 kVp and 100 kVp, respectively. Remarkably, this result showed twice lower X-ray transmission value compared to 0.25 mm Pb sheet. In addition, SL-PES-PDMS/BTO with the weight of 2.81 g was able to provide comparable X-ray attenuation ability as 0.35 mm Pb sheet at both X-ray energies of 80 kVp and 100 kVp. Further calculation based on 0.35 mm Pb using the same sheet dimension as our sample (3.5 cm × 3.5 cm) had an equivalent weight of 4.86 g (Pb sheet), which was ~ 42 % heavier than the weight of SL-PES-PDMS/BTO (2.81 g). As the commercial Pb-free aprons are 20-40 % lighter than their standard Pb-based aprons,[40] this lightweight (42 % lighter than 0.35 mm Pb sheet) SL-PES-PDMS/BTO with 0.35 mm Pb-equivalent X-ray shielding ability can be considered as a competent Pb-alternative shielding material.

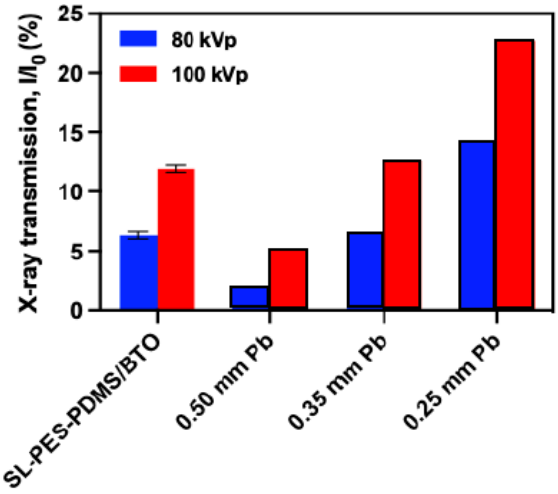

Fig. 6 Benchmarking of SL-PES-PDMS/BTO with the Pb sheets at different thicknesses (0.25 mm, 0.35 mm, and 0.50 mm).

Table 1 summarized the comparison of our results with other coated textile samples for X-ray shielding performance (energy at 80 kVp). Among the materials, our developed sandwich-structure PDMS/BTO coated PES fabric has its potential for providing superior X-ray attenuation ability. This thinnest (1.1 μm), and lighted (2293.8 g/m^2) coated PES fabric can be potentially engineered in the future for replacing the conventional Pb-vinyl apparel.

Table 1 Comparison of thickness, weight, and X-ray attenuation performance (at 80 kVp) of X-ray shielding materials

High Z materials	Textile matrix	Thickness (mm)	Mass per unit area (g/m^2)	Major results	References
Bi_2O_3	Polyester	1.33	2907.0	X-ray transmission of 8 %	[21]
$Bi_2O_3/BaSO_4$	Polyester/viscose	1.8	Reduced 30 % of 0.35 mm Pb	equivalent to 0.35 mm Pb	[14]
Bi_2O_3/La_2O_3	Leather	1.4	-	mass attenuation coefficient at 16.9 cm^2/g	[41]
$Bi_2O_3/BaSO_4$	Nylon	1.46	2321.8	X-ray transmission of 55.6 %, mass attenuation coefficient at 9.6 cm^2/g	[11]
Bi/I	Leather	2.0	-	mass attenuation coefficient at 28 cm^2/g, equivalent to 0.25 mm Pb	[2]
$Bi_4Ti_3O_{12}$	Polyester	1.1	2293.8 Reduced 42 % of 0.35 mm Pb	X-ray transmission of ~ 6 %, mass attenuation coefficient at 12.1 cm^2/g, equivalent to 0.35 mm Pb	Our work

2.4. Mechanism of X-ray shielding enhancement by sandwiched structure

Predominant photoelectric effect with the partial Compton scattering occurs at low-energy X-ray (e.g. 80 kVp and 100 kVp).[42] In our work, the sandwich-structure shielding textile was synthesized using PDMS/BTO composite as an effective filler (Fig. 7(a)). As an example, when the incident X-ray passes through the sandwich-structure PES-PDMS/BTO composite, majority of the transmitted X-ray photons from the first layer (PES textile) are largely absorbed

by the second layer (PDMS/BTO composite) due to the high-Z dependent photoelectric effect, with the partial reflectance from the surface illustrated as Fig. 7(a). With the benefit of increased thickness of the composite using layer-by-layer coating technique, it significantly increases probability of photoelectric effect within the material. In other word, the incident X-ray has been absorbed and reflected several times within the composite, leading to enhanced X-ray attenuation ability (releasing much lower electron energy at the end).[45]

In addition, when incident X-ray interacts with the shielding material, each atom within the material undergoes reflection due to Compton scattering, and the secondary X-ray is then generated by photoelectric effect (Fig. 7(b)).[42] The increased composite thickness of the shielding material can effectively attenuate these secondary X-ray.[43] However, the weight of the material can grow sharply by elevating the composite thickness, which is opposite to our goal to develop lightweight shielding material. Moreover, each component (effective shielding compounds) has their own absorption limits during photoelectric effect occurring. To address these problems, this sandwiched structure can be complementarity of the absorption limits of each component, by creating multiple interfaces for increasing probability of photoelectric effect.

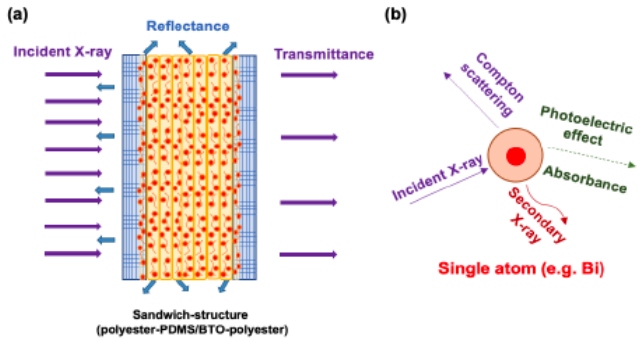

Fig. 7 (a) schematic diagram of X-ray photon attenuation mechanism within the sandwiched structure, and (b) X-ray attenuation occurred on a single atom.

3. Conclusion

The concept of textile shielding material composed of a coated PES fabric sandwiched with the PDMS/BTO composite for X-ray attenuation enhancement is successfully demonstrated. The key results from this study indicated that this successfully synthesized sandwich-structure PDMS/BTO coated textile with the thickness of 1.1 μm provided 0.35 mm Pb equivalent X-ray attenuation ability (~ 94 % and ~ 88 % at both 80 kVp and 100 kVp, respectively), suggesting that this synthesized material complied with medical X-ray protection standards

(AS/NZS 4543.3:2000).[44] Moreover, the weight of this PDMS/BTO coated textile was significantly lighter (42 %), compared with 0.35 mm Pb sheet, proving that the X-ray shielding apparel can be based on a coated fabric rather than Pb-based vinyl sheets which can be described as a significant advancement. On the other hand, this sandwich-structure textile significantly increases probability of photoelectric effect, leading to X-ray attenuation improvement. This proved X-ray attenuation effectiveness of the sandwich structure can be adapted to other polymeric composites and coated fabrics, which offers a new approach for manufacture of non-toxic, lightweight, and flexible radiation protection garments. This design when practically applied in wearable form has potential to provide many practical advantages and reduce probability of occupational injuries occasionally occurred with Pb based shielding aprons.

4. Experimental Section

4.1. Materials

Bismuth oxide powder (Bi_2O_3, 99.9%, <4 μm) was provided by Thermo Fisher Scientific and titanium oxide powder (TiO_2, 99.9%, < 5 μm) in a rutile crystal form was purchased from Aldrich. Polyester fabric (PES, 100 % polyester, 195 g/m^2, 0.3 mm thickness) was purchased from Spotlight. Polydimethylsiloxane (PDMS, SILASTIC, MDX4-4210) was used as a base matrix (part A), and the curing agent consisted of an inhibitor and a siloxane crosslinker (part B). Both part A and part B were provided from Dupont (USA). 0.44 mm Pb sheet (5 kg) was provided by Midland Lead Australia Pty Ltd.

4.2. Synthesis of Bismuth Titanate (BTO) Nanoparticles by Ball Milling

Bismuth titanate (BTO) nanoparticles were synthesized from our previous work.[22] In brief, BTO nanoparticles were prepared using a ball milling process with a predetermined stoichiometric BTO composition, corresponding to the molar ratio of Bi_2O_3 (BO) and TiO_2 (TO) powders at 2:3.

4.3. Fabrication of sandwich-structure PDMS/BTO composite coated PES fabric

To fabricate a sandwich-structure PDMS/BTO composite coated PES fabric, 2 × individual PDMS/BTO coated polyester textiles were prepared using a layer-by-layer coating technique and then compressed together as shown in Fig. 1. The details of the preparation of an individual PDMS/BTO composite coated PES fabric were described as follows: the ball milled BTO nanoparticles (50 wt.%) were first blended into the PDMS matrix, followed by mixing with a

curing agent at a mass ratio of 10: 1 (PDMS to curing agent). The suspension was stirred homogenously before it was applied onto a polyester fabric (3.5 cm × 3.5 cm) and then cured in an oven at 65 ℃ for 4 h. To investigate the maximum coating layers onto a single PES fabric, PDMS/BTO composite coated PES fabric with different layers (2L, 4L, 6L) were further fabricated. The same procedure as stated above were repeated on a cured one-layer PDMS/BTO coated PES fabric with the same composite loading for each layer. The maximum layer of the PDMS/BTO coated PES fabric was determined by characterization with XRD, SEM, and surface roughness measurement. The description of the as-prepared samples is listed in Table 2

Table 2 Description of the as-prepared PDMS/BTO composite coated polyester fabrics

Sample Name	Coated layers (L)	Weight (g)	Thickness (mm)	Average mass per unit area (g/m^2)	Sample designation
Neat polyester (control)	0	0.26	-	-	PES
PDMS/BTO coated on polyester	1	0.67 ± 0.01	0.38 ± 0.04	546.9	1L-PES-PDMS/BTO
	2	1.06 ± 0.02	0.46 ± 0.03	865.3	2L-PES-PDMS/BTO
	4	1.75 ± 0.02	0.66 ± 0.02	1428.6	4L-PES-PDMS/BTO
	6	2.19 ± 0.03	0.79 ± 0.06	1783.7	6L-PES-PDMS/BTO
	8	2.81 ± 0.03	1.10 ± 0.05	2293.8	SL-PES-PDMS/BTO

Note: PDMS/BTO represents the mixture of PDMS and BTO

4.4. Materials characterization

The synthesized samples were characterized by X-ray diffractometer (XRD, Rigaku Miniflex 600, Japan) in the range of 2θ = 20-80° (scan rate of 10 ° min^{-1}). Scanning Electron Microscopy coupled with Energy Dispersive X-Ray (SEM-EDX, Quanta 450 FEG, FEI, USA; Ultim Max Oxford Instruments, UK) was adopted to study the elemental composition and morphology of the samples. Thermal stability and properties of the synthesized materials were probed using TGA STA 449 F5 Jupiter (Netzsch, Germany) under air atmosphere with the samples heated to 1000 ˚C at a heating rate of 10 ˚C min^{-1}. The surface roughness was obtained from a 3D optical profilometer (Bruker Contour GT-K, Australia), using vertical scanning interferometry (VSI) mode with a working distance of 6.7 mm.

4.5. X-ray transmission measurement

X-ray attenuation is the reduction of the intensity of X-ray when it travels through matter.[45] The X-ray transmission of the as-prepared samples were measured using a Gulmay D3150 superficial X-ray (SXR) unit. The distances between the X-ray tube and the material sample, and the material sample to the detector were both set to 50 cm. The detector used to measure the transmission was a NE 2571 farmer type ionization chamber (Phoenix Dosimetry Ltd, UK).

The samples were exposed to the respective X-ray voltage at 80 kVp (2 mm Al HVL) and 100 kVp (3 mm Al HVL) for 0.50 mins with the material sample placed over a collimator of diameter 1 cm. The X-ray transmission was calculated as the charge collected by the ionization chamber with the sample divided by the transmission dose without the sample. Each sample was measured three times and determined by the arithmetic mean.

The X-ray attenuation of an X-ray beam through any material can be estimated as a function of the linear attenuation coefficient (μ) as equation (1),[46]

$$I = I_0 \, e^{-ut} \quad (1)$$

where I and I_0 are the final X-ray intensity after the attenuation by the sample and the X-ray intensity before passing through the sample, respectively, and t is the material thickness (mm). The X-ray transmission (T) can be expressed as equation (2),[47]

$$T = (I / I_0) \times 100\% \quad (2)$$

4.6. Mass attenuation coefficients

Mass attenuation coefficients (μ/ρ) of the synthesized coated samples were calculated according to equation (3),[45] and further compared with the commercial 0.44 mm Pb sheet.

$$\mu/\rho = - \ln (T) / \rho t \quad (3)$$

where ρ is the density of the material (g/cm^3).

4.7. Benchmarking of the developed X-ray shielding textile with Pb sheets

X-ray attenuation of pure Pb sheets with different thicknesses (0.25 mm, 0.35 mm and 0.50 mm) were used as the standard of International Commission on Radiological Protection,[38, 48] where Pb equivalent was applied as a term to evaluate X-ray attenuation performance of the synthesised samples by providing the same X-ray energy conditions.

Supporting Information

Supporting Information is available from the Wiley Online Library.

Acknowledgements

The authors acknowledge the financial support from the ARC Research Hub for Graphene Enabled Industry Transformation, (IH150100003). We thank Australian Microscopy and Microanalysis Research Facility (AMMRF) for the access of SEM facilities, Mr. Ken Neubauer for their technical support on SEM measurements, we also thank OptoFab node of Australian

National Fabrication Facility for the access of 3D optical profilometer, Mr. Alson Kwun Leung Ng for his technical support on surface roughness measurement.

Note

The authors declare no competing financial interest.

References

[1] Y. C. Kim, K. H. Kim, D. Y. Son, D. N. Jeong, J. Y. Seo, Y. S. Choi, I. T. Han, S. Y. Lee, N. G. Park, Nature 2017, 550, 87.
[2] Y . Wang, R. Zhong, Q. Li, J. Liao, N. Liu, N. S. Joshi, B. Shi, X. Liao, J. Guo, Advanced Materials Technologies 2020, 5.
[3]U. S. D. o. Labor, *Occupational outlook handbook*, Radiologic and MRI Technologists 2015.
[4]ICRP, Vol. 49, 2020, 4.
[5]N. Lee, S. H. Choi, T. Hyeon, Adv Mater 2013, 25, 2641.
[6]L. Yu, A. L. C. Pereira, D. N. H. Tran, A. M. C. Santos, D. Losic, Materials Chemistry and Physics 2021, 260.
[7]K. K. Kadyrzhanov, D. I. Shlimas, A. L. Kozlovskiy, M. V. Zdorovets, Journal of Materials Science: Materials in Electronics 2020, 31, 11729.
[8]M. Mirzaei, M. Zarrebini, A. Shirani, M. Shanbeh, S. Borhani, Textile Research Journal 2017, 89, 63; J. P. McCaffrey, E. Mainegra-Hing, H. Shen, Med Phys 2009, 36, 5586.
[9]X. Xray, 2014.
[10]Q. Li, Q. Wei, W. Zheng, Y. Zheng, N. Okosi, Z. Wang, M. Su, ACS Appl Mater Interfaces 2018, 10, 35510.
[11]H. A. Maghrabi, A. Vijayan, F. Mohaddes, P. Deb, L. Wang, Fibers and Polymers 2017, 17, 2047.
[12]I. Dayana, T. Sembiring, A. P. Tetuko, K. Sembiring, N. Maulida, Z. Cahyarani, E. A. Setiadi, N. S. Asri, M. Ginting, P. Sebayang, Journal of Molecular Liquids 2019, 294.
[13]B. M. Abunahel, I. S. Mustafa, N. Z. Noor Azman, Applied Physics A 2018, 124; H. O. Tekin, V. P. Singh, T. Manici, Appl Radiat Isot 2017, 121, 122; K. Verdipoor, A. Alemi, A. Mesbahi, Radiation Physics and Chemistry 2018, 147, 85; M. Lopresti, L. Palin, G. Alberto, S. Cantamessa, M. Milanesio, Materials Today Communications 2021, 26; A. J. Mieszawska, W. J. Mulder, Z. A. Fayad, D. P. Cormode, Mol Pharm 2013, 10, 831; Q. Zhang, Q. Liang, Z. Zhang, Z. Kang, Q. Liao, Y. Ding, M. Ma, F. Gao, X. Zhao, Y. Zhang, Advanced Functional Materials 2018, 28.
[14]S. Pulford, M. Fergusson, The Journal of The Textile Institute 2016, 107, 1610.
[15]N. Z. Noor Azman, S. A. Siddiqui, I. M. Low, Applied Physics A 2012, 110, 137.
[16]N. Z. Noor Azman, S. A. Siddiqui, R. Hart, I. M. Low, Appl Radiat Isot 2013, 71, 62.
[17]V. Harish, N. Nagaiah, T. N. Prabhu, K. T. Varughese, Journal of Applied Polymer Science 2009, 112, 1503; N. Z. N. Azman, S. A. Siddiqui, R. Hart, I. M. Low, Journal of Applied Polymer Science 2013, 128, 3213.
[18]K. Günther, C. Giebing, A. Askani, T. Leisegang, M. Krieg, Y. Kyosev, T. Weide, B. Mahltig, Materials Chemistry and Physics 2015, 167, 125.
[19]H. Schlattl, M. Zankl, H. Eder, C. Hoeschen, Med Phys 2007, 34, 4270.
[20]N. Aral, F. Banu Nergis, C. Candan, Textile Research Journal 2015, 86, 803.
[21]H. A. Maghrabi, A. Vijayan, P. Deb, L. Wang, Textile Research Journal 2015, 86, 649.
[22]L. Yu, P. L. Yap, A. Santos, D. Tran, D. Losic, ACS Applied Nano Materials 2021, 4, 7471.
[23]T. Fujii, Microelectronic Engineering 2002, 61-62, 907.

[24]D. C. Duffy, J. C. McDonald, O. J. Schueller, G. M. Whitesides, Anal Chem 1998, 70, 4974.
[25]N. D. Yılmaz, G. M. Arifuzzaman Khan, in *Mechanical and Physical Testing of Biocomposites, Fibre-Reinforced Composites and Hybrid Composites*, 2019, 13.
[26]B. D. Stojanovic, C. O. Paiva-Santos, C. Jovalekic, A. Z. Simoes, F. M. Filho, Z. Lazarevic, J. A. Varela, Materials Chemistry and Physics 2006, 96, 471.
[27]Y. L. Du, G. Chen, M. S. Zhang, Solid State Communications 2004, 132, 175.
[28]L. Liu, W. Weng, J. Zhang, X. Cheng, N. Liu, J. Yang, X. Ding, Journal of Materials Chemistry A 2016, 4, 12981.
[29]Z. Zhao, J. Zhou, T. Fan, L. Li, Z. Liu, Y. Liu, M. Lu, Materials Chemistry and Physics 2018, 203, 89.
[30]P. Ferreira, A. Carvalho, T. R. Correia, B. P. Antunes, I. J. Correia, P. Alves, Sci Technol Adv Mater 2013, 14, 055006.
[31]E. Kandare, B. K. Kandola, D. Price, S. Nazaré, R. A. Horrocks, Polymer Degradation and Stability 2008, 93, 1996.
[32]S. M. N. Al-Ajrash, C. Browning, R. Eckerle, L. Cao, Materials Advances 2021, 2, 1083.
[33]A. E. Nogueira, E. Longo, E. R. Leite, E. R. Camargo, Ceramics International 2015, 41, 12073.
[34]H. Huasi, in *Advances in Composite Materials for Medicine and Nanotechnology*, 2011.
[35]Z. Li, W. Zhou, X. Zhang, Y. Gao, S. Guo, Sci Rep 2021, 11, 4384.
[36]R. Perumalraj, G. Nalankilli, B. S. Dasaradan, Journal of Reinforced Plastics and Composites 2010, 29, 2992.
[37]D. He, Y. Ma, R. Zhao, J. Qiu, B. Sun, H. Wang, M. Yang, X. Jia, X. Li, Y. Li, X. Lu, C. Wang, Advanced Materials Interfaces 2021, 8.
[38]G. J. Scuderi, G. V. Brusovanik, D. R. Campbell, R. P. Henry, B. Kwon, A. R. Vaccaro, Spine J 2006, 6, 577.
[39]ICRP, ICRP 2007, 103.
[40]R. G. Dixon, V. Khiatani, J. D. Statler, E. M. Walser, M. Midia, D. L. Miller, G. Bartal, J. D. Collins, K. A. Gross, M. S. Stecker, B. Nikolic, S. Society of Interventional Radiology, C. Health, J Vasc Interv Radiol 2017, 28, 195.
[41]Q. Li, R. Zhong, X. Xiao, J. Liao, X. Liao, B. Shi, ACS Appl Mater Interfaces 2020, 12, 54117.
[42]H. Yu, X. Chen, Y. Zhou, D. Chen, L. Zhang, Appl Radiat Isot 2020, 156, 108785.
[43]B. Bartholet, Journal of Aerospace 2004, 113, 359.
[44]S. Australia, in *Protective clothing and protective devices for gonads*, Vol. 4543.3, AS/NZS, 2000.
[45]J. Viegas, L. A. Silva, A. M. S. Batista, C. A. Furtado, J. P. Nascimento, L. O. Faria, Industrial & Engineering Chemistry Research 2017, 56, 11782.
[46]APRANSA, 2015.
[47]D. F. Swinehart, Journal of Chemical Education 1962, 39, 333.
[48]ICPR, Vol. 103, ICPR 2007; ICRP, Ann. ICRP 2007, 37, 2.

Supporting Information

Lightweight Polyester Fabric Sandwiched with Elastomeric Bismuth Titanate Composite for High-Performing Lead-Free X-ray Shielding

*Le Yu, Pei Lay Yap, Alexandre Santos, Diana Tran, Dusan Losic**

Le Yu, Pei Lay Yap, Diana Tran, Dusan Losic*

School of Chemical Engineering and Advanced Materials, The University of Adelaide, Adelaide, SA 5005, Australia.
ARC Research Hub for Graphene Enabled Industry Transformation, The University of Adelaide, Adelaide, SA 5005, Australia.
E-mail: Dusan.losic@adelaide.edu.au

Alexandre Santos

School of Physical Sciences, The University of Adelaide, Adelaide, South Australia 5005, Australia.
Department of Medical Physics, Royal Adelaide Hospital, Adelaide, South Australia 5000, Australia.
Department of Medical Physics, Royal Adelaide Hospital, Adelaide, South Australia 5000, Australia.

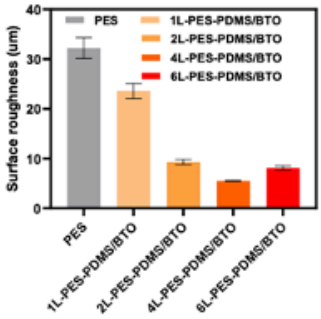

Fig. S1 Surface roughness of polyester fabric (PES, control), and PDMS/BTO coated PES fabric with different coating layers (1L, 2L, 4L and 6L), respectively.

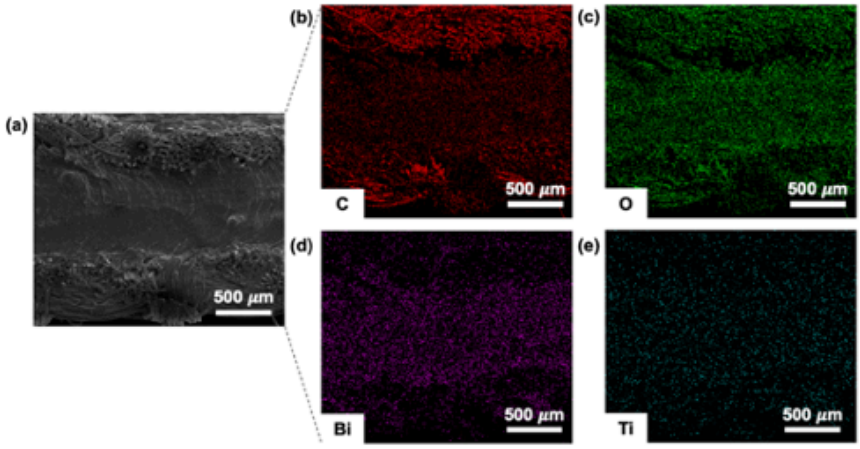

Fig. S2 (a) Cross-sectional SEM image of SL-PES-PDMS/BTO for mapping analysis (scale bar = 500 μm), and mapping distribution of (b) carbon (c), (c) oxygen (O), (d) bismuth (Bi), and (e) titanium (Ti).

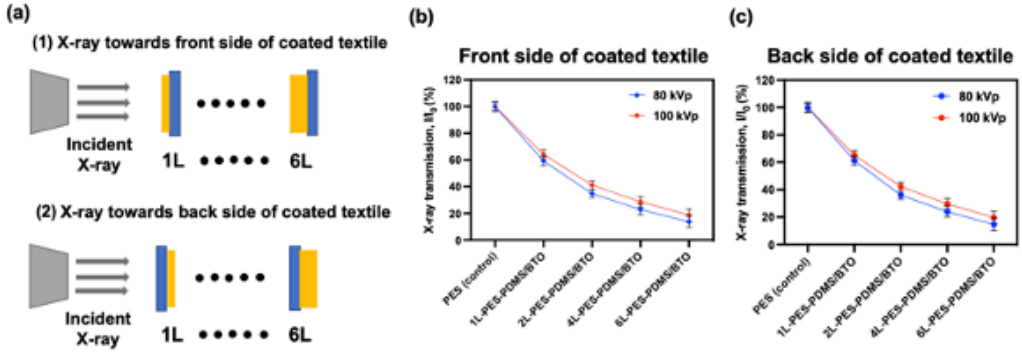

Fig. S3 (a) Schematic illustration and X-ray transmission values towards (b) front and (c) back side of the coated textiles at 80 kVp and 100 kVp

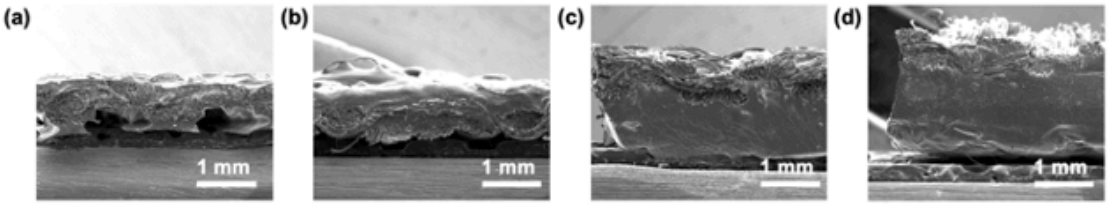

Fig. S4 Cross-sectional SEM images (scale bar = 1 mm) of (a) 1L-PES-PDMS/BTO, (b) 2L-PES-PDMS/BTO, (c) 4L-PES-PDMS/BTO, and (d) 6L-PES-PDMS/BTO.

CHAPTER 7

CONCLUSION, CHALLENGES AND FUTURE PERSPECTIVES

Chapter 7 Conclusion, challenges, and future perspectives

Overview and significance of work

This chapter includes the summary of the development of 2D composite materials for advanced X-ray shielding application, and it also highlights the future challenges of engineering a lightweight, non-toxic, and environmentally friendly Pb-free shielding materials for commercializing X-ray shielding apparels. This section presents the key findings and the future direction of the development of a new generation of 2D materials-based Pb-free X-ray shielding materials.

7.1. Conclusion

This thesis aims to provide a comprehensive study on a new generation of 2D and their composite materials for X-ray shielding applications. In essence, this thesis is devoted to the development of lightweight, non-toxic, environmentally friendly, and high-performing X-ray shielding materials using 2D materials in the form of films, composites, and textiles. The key findings from this research are summarized below:

Chapter 3 investigates the effect of particle size distribution and structural morphology on X-ray shielding improvement of the metal oxide materials. This chapter contributes to two research papers, including (1) an insight study on influence of the particle size and morphological variations towards X-ray shielding performance of the Bi_2O_3 films, and (2) the dosage effect of the $Bi_4Ti_3O_{12}$ (BTO) nanocomposites towards the X-ray shielding performance. The key results from this chapter are listed below:

- The nanoflowered Bi_2O_3 film with the smallest particle size (~ 388 nm) and the highest SA/V ratio (22.07 μm^{-1}) achieved the best X-ray attenuation performance at the energy range of 30 kVp, 50 kVp, and 80 kVp.
- The reduced particle-size nanomaterials with the large SA/V ratio have a significant effect on X-ray shielding, especially for the low-energy range, which can be considered when designing a Pb-free protection material.
- The perovskite-structure BTO nanoparticles are fabricated using the mechanochemical process. The synthesized BTO-epoxy composite with a thickness of ~ 2mm achieved ~ 95 % of X-ray attenuation efficiency at 100 kVp.
- The X-ray shielding effectiveness of the prepared BTO-epoxy composite (total weight of 2.18 $\pm$ 0.11 g) provided 0.35 mm Pb equivalent attenuation at 80 kVp and 100 kVp, with half of the weight relative to 0.35 mm Pb sheet (4.19 g). The results highlighted a promising potential for the BTO-based material as a lightweight, non-toxic X-ray protection material to replace Pb.

Significance of these findings:

- This chapter provides a new insight on the influence of particle size and morphology on X-ray shielding performance, which has not been explored properly before.
- The outcomes of this study will provide new knowledge on greater understanding of the influence of shapes and particle size towards X-ray shielding performance.

- The better understanding of this knowledge can be beneficial for designing new generation of Pb-free shielding materials.

Chapter 4 unveils a new concept of applying 2D layered materials for low-energy X-ray attenuation improvement. To demonstrate this concept, the first study from this chapter aims to explore the X-ray shielding ability between the bulk and the exfoliated (few-layer, FL) MoS_2 films at low-energy X-ray of 30 kVp. The second study aims to demonstrate a new concept that the 2D layered materials and their heterostructures in the form of multilayered films can significantly improve X-ray attenuation performance, due to the multiple scattering and absorption of the X-ray photons between each nanolayered structure. The key results from this chapter are listed below:

- The FL-MoS_2 (particle size of ~ 430 nm) film provided greater X-ray attenuation ability, showing ~ 15 % of X-ray shielding improvement, compared to the bulk MoS_2 (particle size of ~ 23 μm) film at 30 kVp.
- The results showed that the optimized MoS_2 composite film (1.34 mm) provided similar X-ray transmission to the 0.20 mm Pb sheet (2.17 g) at 30 kVp, and its weight (1.18 g) was 50 % lighter. This new, lightweight, and Pb-free layered MoS_2 (2D) material is potentially effective in providing X-ray shielding performance, as an alternative to the traditional Pb-equivalent materials.
- The exfoliated FL-2D material films (MoS_2, antimony, Mxene) exhibited 30-50 % of X-ray shielding enhancement at 30 kVp, compared to their bulk counterparts.
- Further investigation on the heterostructure in the form of multilayered films unveiled that the two layers (2L) of the combined heterolaminated structure (MoS_2 + Mxene) had ~ 62% and ~ 60% X-ray attenuation enhancement at 30 kVp, compared to the single MoS_2 and Mxene film, respectively. This outcome shows the advantages of the 2D layered structure towards X-ray shielding improvement, which provides a new technology for designing a Pb-free X-ray shielding material.

Significance of these findings:

- This chapter presents a new concept and discovery for improved X-ray shielding performance using layer-structure 2D materials, which has yet been reported.
- The outstanding X-ray attenuation performance of this designed layer-structure 2D materials provides new technique for the development of Pb-alternative shielding materials.

- The layer-structure 2D sheets that enhance X-ray shielding efficiency by the interlayer scattering multiple times open a pathway for applying a new technique to the material design.

Chapter 5 exhibits the development of polymer-based 2D nanocomposites for X-ray shielding reinforcement. The first part of this chapter aims to study the effect of 2D nanomaterials on X-ray shielding improvement using pristine graphene and exfoliated hBN as additives. The second part of this chapter presents the study on X-ray shielding of the high-density FL-antimony lamellar composite in a sandwich structure compared to the conventional FL-antimony composite at 30, 50, 80 and 100 kVp. The key results from this chapter are listed below:

- The exfoliated hBN using the direct wet chemical exfoliation process produced high-yield, few-layer (3-6 layers), and edge-functionalized hBN nanosheets with a uniform particle size of ~ 486 nm. This result paves a promising pathway to effectively synthesize hBN nanosheets via this cost-efficient exfoliation method.
- By proving the same composite thickness at ~ 2mm, the MoS_2-epoxy composites with the respective addition (16 wt.%) of graphene and hBN achieved ~ 16 % and ~ 37 % of X-ray improvement at 30 kVp, compared to the MoS_2-epoxy composite itself. Importantly, the addition of the graphene-hBN mixture within the MoS_2-epoxy composite obtained ~ 52 % of X-ray improvement at the same energy.
- This synergistic effect of graphene-hBN mixture with a significant X-ray attenuation enhancement provides a new strategy for the reinforcement of other high-Z compounds-polymer composites towards X-ray shielding application.
- X-ray attenuation efficiency of the FL-antimony lamellar composite provided up to 45 % of X-ray shielding improvement, compared to the conventional FL-antimony composite.
- This new design concept provides significant potential to overcome the “blend and mix” technique, which can be employed for the development of an advanced Pb-free X-ray shielding composite.

Significance of these findings:

- This chapter brings great potential for employing 2D materials, especially carbon-based 2D materials for X-ray shielding improvement.

- Graphene and hBN acted as reinforcement towards polymer-based composites, which can be adapted to other high-Z compound composites.
- This study brings an opportunity to other carbon-based 2D materials as reinforcements for enhanced X-ray shielding performance with increased thermal stability as well as mechanical properties.

Chapter 6 explores the new design of the polymer-based 2D oxide composite coated textile for X-ray shielding application. The work creates a sandwich-structure BTO-PDMS composite coated polyester fabrics for fabrication of a highly flexible, non-toxic, high-performing Pb-free shielding material. The key results from this chapter are listed below:

- The effective attenuating filler of this sandwich-structure coated polyester (PES) fabric was a PDMS matrix filled with BTO nanoparticles. This synthesized coated PES fabric with a thickness of 1.1 mm provided 0.35 mm Pb-equivalent X-ray shielding ability at both 80 kVp and 100 kVp.
- This sandwich-structure coated fabric showed a high flexibility with a total weight of 2.81 g, which is 42 % lighter than a 0.35 mm Pb sheet (providing the same dimension of the sheet).
- This sandwich-structure design can significantly improve the X-ray shielding, due to the reflection and absorption of the incident X-ray multiple times with the densely packed BTO-PDMS composite sealed with two pieces of PES fabrics.
- This sandwich-structure design offers a new approach for manufacturing a flexible, lightweight, non-toxic Pb-free textile material to replace the conventional Pb-based shielding garment.

Significance of these findings:

- This chapter brings a new idea for developing a 2D material coated fabric for X-ray shielding application.
- This sandwiched coated fabric provides a new solution for the development of other polymer-based textiles, which can be employed as a new technique for the synthesis of X-ray shielding material.
- The design of this sandwich-structure coated textile can be adapted to further commercialization of Pb-free radiation shielding apparels.

7.2. Challenges and future perspectives

This PhD thesis has made a great contribution to the development of new generation of 2D materials for ionizing electromagnetic shielding applications. This work also signifies the advanced X-ray shielding materials designed using the different techniques with various forms of the 2D layered films, nanocomposites, and coated fabrics. Herein, there are several points for the future research direction and challenges listed as follows:

- This thesis only provides important insights on the influence of particle size and morphology on X-ray shielding performance, which has not been explored before.
- The comprehensive study on the mechanism of these nanomaterials with shape variations towards X-attenuation needs to be explored.
- The theoretical data obtained from XCOM comparing the experimental data has its limitation of the simulation system, as it only can set up an ideal condition for a regular distribution of the nanomaterials with a standardized geometry. A proper computing simulation using Monte Carlo system is highly recommended in the future work.
- As more than 99 % of the kinetic energy from the incident X-ray is converted to heat, the effect of heat on the properties of the polymer-based composite has not been investigated. The X-ray irradiation correlated to the time differences has to be performed for determining the degradation condition of the polymers. This will provide the guidance for development of the polymer-based shielding composite.
- As the photoelectric effect is dominant in the low-energy X-ray range (<100 KeV), the dissipation probability of X-ray photons is significantly dependent on the atomic number and the density of the materials. However, the mechanism of the heterostructure materials with multilayered 2D sheets is still not clear. The secondary scattered X-ray generated from the reflection of each layer has not been determined yet. The future work should conduct this experiment with a proper setup for secondary scattered X-ray measurements.
- There is still a synthetic challenge for production of graphene oxide and hBN using wet-chemical exfoliation, due to generation of the wastewater streams. A ‘zero-waste’ method needs to be explored for sustainability of graphene oxide/hBN production.
- There are still many 2D materials with excellent physical and chemical properties that need to be explored for X-ray shielding application. For instance, other high-Z 2D

materials with high density, non-toxicity and low manufacturing cost have not been studied.

- For manufacturing a Pb-free X-ray shielding apparel, the sustainability and durability measurement of the designed X-ray shielding textile needs to be conducted.
- To scale up the developed X-ray shielding materials from this study, optimization of the manufacturing procedure is highly recommended before commercializing the Pb-free shielding materials.
- The new concepts of X-ray shielding enhancement from this study can be adapted to other radiation (e.g., γ-ray) shielding applications, which can be applied to the field of space exploration and nuclear industry.
- Designing a practical radiation protection garment for application across different sectors (nuclear plants, defence, and medical clinics) using the developed 2D materials and their composites is highly recommended as the next step for commercialization purposes.